CHARMONIUM SPECTROSCOPY FROM RADIATIVE DECAYS

OF THE J/ψ AND ψ' *

John Erthal Gaiser

Stanford Linear Accelerator Center
Stanford University
Stanford, California 94305

August 1982

---
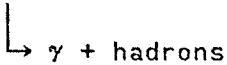
* Ph.D. dissertation.
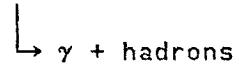
ABSTRACT

The Crystal Ball NaI(Tl) detector was used to study the photon spectra from the following inclusive charmonium decays:

$$e^+e^- \to J/\psi$$
$$\hookrightarrow \gamma + hadrons$$

$$e^+e^- \to \psi'$$
$$\hookrightarrow \gamma + hadrons$$

Data were collected at the Stanford Linear Accelerator Center's electron-positron colliding beam machine, SPEAR, intermittently over a two and half year period, beginning at the end of 1978. The Cystal Ball detector consists of a highly segmented array of 732 NaI(Tl) crystals (16 radiation lengths) covering $\simeq 98\%$ of 4π steradians, and is used to measure the photon energies, directions, and lateral shower distributions. Centrally located spark and proportional chambers are used for charged particle recognition. As a result, this detector is excellently suited for studying the radiative transitions among the charmonium family of states: i) from ψ' to the triplet P states, $\chi(3415)$, $\chi(3510)$, and $\chi(3550)$; ii) from ψ' and J/ψ to the singlet S state $\eta_c(2984)$; and iii) from ψ' to the radially excited singlet S state $\eta_c'(3592)$.

The analysis of $1.8 \cdot 10^6$ ψ' and $2.2 \cdot 10^6$ J/ψ decays yields the following spectrum of states: $\chi_0(3418)$, $\chi_1(3512)$, $\chi_2(3558)$, $\eta_c(2984)$, and $\eta_c'(3592)$, each with a ± 4 MeV error on its mass. The branching ratios are measured to be: $B(\psi' \to \gamma\chi_{0,1,2}) = (9.9 \pm 0.5 \pm 0.8)\%$,

$(9.0\pm0.5\pm0.7)\%$, and $(8.0\pm0.5\pm0.7)\%$, respectively; $B(\psi'\to\gamma\eta_c) = (0.28\pm0.06)\%$ and $B(J/\psi\to\gamma\eta_c) = (1.27\pm0.36)\%$; and $B(\psi'\to\gamma\eta_c') = (0.5-1.2)\%$ at the 90% confidence level. Values for the natural line widths are obtained: $\Gamma(\chi_{0,1,2}) = (13.5-20.4)$ MeV, < 3.8 MeV, $(0.85-4.9)$ MeV, respectively (90% C.L.); $\Gamma(\eta_c) = (11.5+4.5/-4.0)$ MeV; and $\Gamma(\eta_c') < 7$ MeV (90% C.L.). The cascade product branching ratios $B(\psi'\to\gamma\chi_J)\cdot B(\chi_J\to\gamma J/\psi)$ were measured for $J = 1$ and 2 to be: $(2.56\pm0.12\pm0.20)\%$ and $(0.99\pm0.10\pm0.08)\%$, respectively. No signal was seen for the $J = 0$ transition, with an upper limit above its previously measured product branching ratio. The results of this analysis are compared with the predictions of the charmonium models.

ACKNOWLEDGEMENTS

For Debbie and John

You are never given a wish without also being given the power to make it true. You may have to work for it, however.

Richard Bach — "Illusions"

CONTENTS

LIST OF TABLES

LIST OF FIGURES

Chapter I

CHARMONIUM

The initial discovery and ongoing unraveling of the charmonium family of states has proved highly significant in the advancement of high energy particle physics. A tremendous effort in obtaining experimental observations and in refining the charmonium model has been underway since the discoveries[1-4] of J/ψ and ψ′ in 1974. This report describes a detailed experimental investigation of charmonium via the inclusive radiative decays of ψ′ and J/ψ:

$$
\begin{array}{ll}
e^+e^- \rightarrow J/\psi & e^+e^- \rightarrow \psi' \\
\quad \llcorner\!\!\rightarrow n\gamma + \text{hadrons} & \quad \llcorner\!\!\rightarrow n\gamma + \text{hadrons}
\end{array}
\qquad (I-1)
$$

The data were collected at the Stanford Linear Accelerator Center's electron-positron colliding beam machine (SPEAR) over a two and a half year period beginning at the end of 1978.

Basically the charmonium theory[5] describes a system of bound states composed of a charmed quark (c) and antiquark ($\bar{c}$) interacting via the strong color force (also see Appendix A). In its most naive form, the model assumes that the interaction is static and may be described by an instantaneous nonrelativistic potential. As the current theory of the strong color interaction, i.e., quantum chromodynamics or QCD, does not allow for an exact calculation of the static potential, both empirical and theory inspired interaction models have been devised. The most

advanced form of the model includes relativistic corrections to the dynamics of the interaction and to the kinematics, in addition to higher order terms from QCD perturbation theory. Currently the experimental results bear out the predictions of the charmonium model to a high degree. This has not always been the case.

The J/ψ(3095) was simultaneously discovered by two generically different experiments. One research group[1] at Brookhaven National Laboratory observed a peak in their e^+e^- invariant mass distribution at 3.1 GeV, in the reaction $p+B_e \rightarrow e^+e^-X$. The Mark I group[2] at SLAC's SPEAR facility witnessed a dramatic rise in the $e^+e^- \rightarrow$ hadron and lepton pair cross sections at 3.105±0.003 GeV center of mass. The SPEAR results indicated an unexpectedly narrow resonance which was immediately confirmed by experiments[3] at the ADONE e^+e^- storage ring at Frascati. Within a month a second narrow resonance[4] was observed by the Mark I at 3.695±0.004 GeV, designated as the ψ'(3684). From this point on the e^+e^- colliding beam machines completely dominated the picture.

Concurrent with the experimental discoveries were the theoretical predictions[6] that a whole family of narrow $c\bar{c}$ mesons should exist below the ψ' state. Figure 1 details the positronium-like spectrum expected by the early charmonium models. A great deal of excitement centered around the prospect of seeing a photon spectrum resulting from decays of the massive 3.7 GeV ψ' with characteristic monochromatic signals so familiar to atomic and nuclear physics, but unheard of in high energy physics. From the point of view of the charmonium model, the photon signals would result from radiative transitions between the family members as indicated in Figure 1. In particular, six states were

expected to lie below the ψ'. The three triplet ^3P_J states (triplet, since they have a total spin of 1 allowing for a triplet of spin orientations) should lie between the J/ψ and ψ'. At their mass center of gravity is expected the singlet $^1P_1$ state (total spin = 0). At about 100 MeV below the ψ' and J/ψ would lie their hyperfine split partners, the two singlet $^1S_0$ states. In this picture the experimentally observed states J/ψ and ψ' correspond to the ground state and first excited triplet $^3S_1$ states of the theory.[7] Single gamma transitions between some of these states are forbidden by symmetry and conservation laws. However, there are still about 14 allowed transitions, depending on the mass of the singlet $^1P_1$ state.

The HEPL-Penn experiment,[8] running concurrently with the Mark I at SPEAR, used two large cylindrical NaI(Tl) crystals (30 inches in diameter and 20 radiation lengths deep) to measure the inclusive photon spectrum at ψ'. The analysis of their data (integrated luminosity[9] of 98 nb^{-1}) was hindered by a low photon detection efficiency (of order 1%) and an inability to untangle overlapping photons in the large crystals.[10] Not seeing statistically significant signals, they placed upper limits on possible radiative transitions. Their limits ranged from a factor of $2\frac{1}{2}$ to 5 below the naive model predictions for the largest ψ' radiative decay rates, $\psi' \rightarrow \gamma^3P_J$, which were typically predicted to be 15%-30% per transition.

By 1976, analyses of exclusive decays of the ψ' by several experiments[11-13] established the existence of three states intermediate to J/ψ and ψ', later referred to as $\chi_0(3415)$, $\chi_1(3510)$, and $\chi_2(3555)$. A careful analysis[13,14] of photons converted in the beam pipe passing
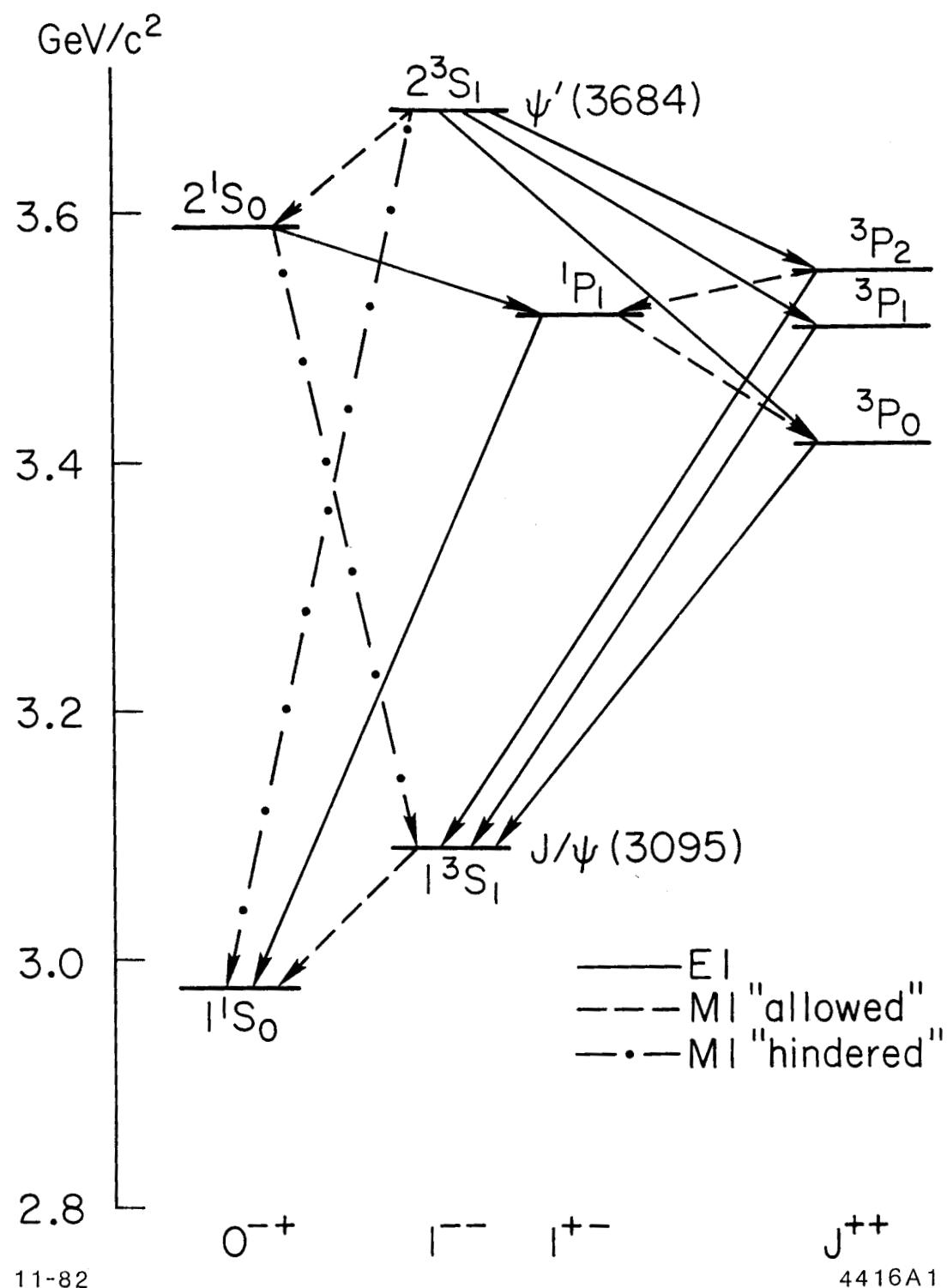
Figure 1: Charmonium Spectrum Predicted by the Early Model.
The states are identified by the modified spectroscopic notation, $n^{2S+1}L_J$, where n is the radial quantum number (1,2,...), L is the orbital angular momentum (0,1,...,n), S is the total spin (0 or 1), and J is the total angular momentum (L-1, L, or L+1 if L > 0, or S if L = 0). The total angular momentum, space parity (P), and charge parity (C) are indicated at the bottom of the figure for the various family groups. Also shown are the electric dipole (E1) and magnetic dipole (M1) radiative transitions.

- 4 -

through the Mark I magnetic field and tracking chambers from $309 \cdot 10^3$ ψ' decays, yielded a spectrum for photons with energies above $\simeq 200$ MeV. A significant γ signal was seen corresponding to the transition $\psi' \to \gamma \chi_0$ at $\simeq 260$ MeV. The branching ratio at $(7.5 \pm 2.6)\%$, turned out to be slightly greater than the HEPL-Penn upper limit, and a factor of 2-4 below naive model predictions.

Meanwhile, an improved NaI(Tl) detector[15] was installed at the SPEAR east pit in an experiment designated as SP-27. They obtained integrated luminosities of $\simeq 600$ nb^{-1} and $\simeq 100$ nb^{-1} at the ψ' and J/ψ respectively. Their apparatus employed two segmented arrays of 19 NaI(Tl) crystals each for their photon energy measurements. The segmentation proved to be a powerful improvement over the HEPL-Penn experiment, since it allowed rejection of events with another photon shower nearby. Their data from ψ' decays yielded a spectrum with clear structure. Three sharp peaks indicated the transitions from ψ' to the three χ_J states. In addition, a broad signal was seen corresponding to the two overlapping doppler broadened transitions $\chi_{1,2} \to \gamma$J/ψ. The SP-27 branching ratio for the χ_0 transition, at $(7.2 \pm 2.3)\%$, agreed with the Mark I value. The other two transitions for χ_1 and χ_2 were essentially the same at $(7.1 \pm 1.9)\%$ and $(7.0 \pm 2.0)\%$, respectively. Transitions to other states from either J/ψ or ψ' were not seen in the SP-27 spectra.

Aside from the inclusive photon process, the search for new charmonium states included the investigation of basically three other decay channnels: i) the radiative cascade decay, $\psi' \to \gamma X \to \gamma\gamma$J/$\psi \to \gamma\gamma \ell^+ \ell^-$, where the lepton, ℓ, can be either an electron or a muon, ii) the three photon final state, ψ' or J/$\psi \to \gamma X \to 3\gamma$, or iii) hadronic

decays, J/ψ or $\psi' \rightarrow \gamma X \rightarrow \gamma$ + hadrons, where the state X is observed in the invariant mass of the hadron system. The states χ_0, χ_1, and χ_2 were seen by their hadronic decays,[11] while only the χ_1 and χ_2 were observed in cascade decays.[12,13] Initially, some evidence for a ψ' hyperfine partner (the 2^1S_0 called the η_c') was reported[13] at a mass of 3455 MeV in the cascade process by the Mark I detector. This observation was not confirmed by a subsequent experiment[16] (the DESY-Heidelberg collaboration) independently investigating the radiative cascade process. However, the DESY-Heidelberg group presented evidence for an alternative intermediate state at 3591 MeV as a possible η_c' candidate. In addition, they reported a product branching ratio for the ψ' cascade decay involving the χ_0, which was previously unmeasured.

It was hoped that the three photon final state would be particularly well suited for the η_c and η_c' search, since the 2γ branching ratios for these pseudoscalar particles might be large. The DASP collaboration,[17] using a nonmagnetic detector, observed a 5 standard deviation signal in their highest $\gamma\gamma$ invariant mass distribution at 2.83±0.03 GeV, in the decay J/$\psi \rightarrow 3\gamma$. They measured a product of branching ratios, B(J/$\psi \rightarrow \gamma$X(2830))·B(X(2830)$\rightarrow \gamma\gamma$) = (1.2±0.5)·10^{-4}. This state, X(2830), immediately became a candidate for the theory's J/ψ hyperfine partner (the 1^1S_0 state called η_c).

The historical situation at the end of 1978, which also marked the start of the Crystal Ball experiment at SPEAR, is summarized in Figure 2. Those charmonium states directly produced in e$^+$e$_-$ annihilation,[7] J/ψ and ψ', are assigned the quantum numbers of the photon (J(PC) $\equiv$ 1(--)) and are displayed centrally in the figure. They correspond to the

triplet $^3S_1$ states of the charmonium theory. The three χ_J states are shown on the right side of the figure. The preferred quantum numbers for the χ states, indirectly inferred[11] from their hadronic decay patterns and mass ordering, identified them with the theory's triplet ^3P_J states. The three remaining experimental observations are shown on the left side of the figure. Since they were observed in radiative decays of the triplet S states, with charge parity C = -1, they became candidates for positive C parity states. Possible correspondence with charmonium theory was to identify the state at 2830 MeV with the η_c and the 3591 MeV state with the η_c', ie. the two singlet $^1S_0$ states. The unconfirmed observation at 3455 MeV had no logical place in the model.

The situation at that time seemed to present the charmonium model with an insurmountable challenge.[5,18] If the X(2830) is identified as the theory's η_c, with a 265 MeV hyperfine splitting, then the theory predicts a rate for J/$\psi \rightarrow \gamma$ X(2830) to be an order of magnitude greater than the 90% confidence level upper limit[15] provided experimentally by SP-27, at 2.0%. Also the inferred lower limit for X(2830) $\rightarrow \gamma\gamma$, obtained from the DASP rate for J/$\psi \rightarrow \gamma$X(2830) $\rightarrow 3\gamma$, divided by the SP-27 upper limit for J/$\psi \rightarrow \gamma$X(2830), was about five times greater than predicted by the charmonium model. In addition the model could not survive[18] such a large hyperfine splitting as seen for the X(2830). As for the state at 3591 MeV seen by the DESY-Heidelberg group, their reported branching ratio product for $\psi' \rightarrow \gamma$X(3591) $\rightarrow \gamma\gamma$J/ψ is many orders of magnitude greater than predicted by the model, if this state is taken to be the η_c'.
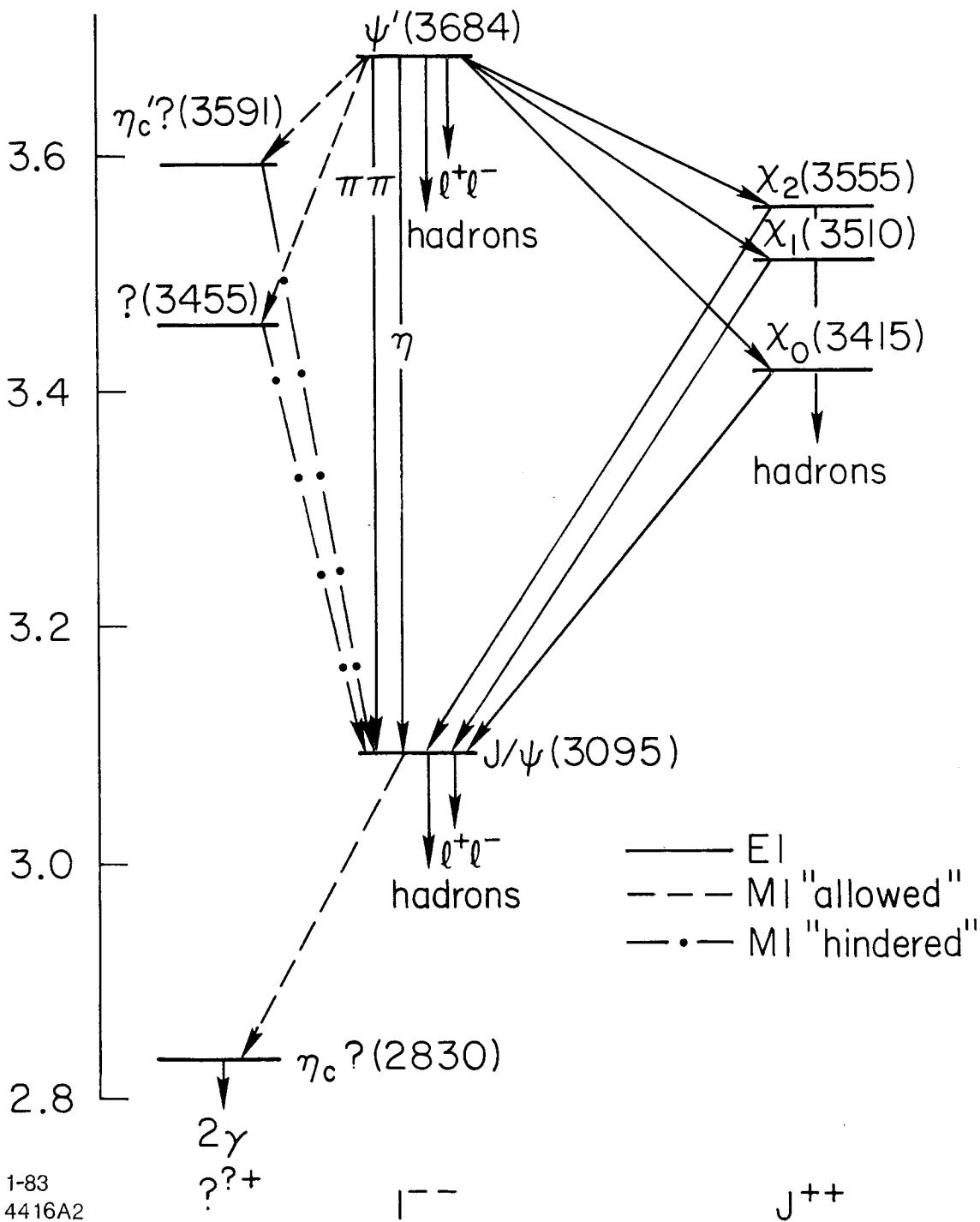
Figure 2: Charmonium Spectrum at the End of 1978.
Only the quantum numbers for the J/ψ and ψ' were known, J(PC) = 1(--),
while those for the χ_J states were indirectly inferred from their
hadronic decay patterns and mass ordering. The states at 3455 MeV and
3591 MeV (not confirmed in later experiments) were seen only in the
cascade decay channel, leading to the C = +1 assignment. Likewise, the
2830 MeV state (also not confirmed in a subsequent experiment) was seen
in the radiative decay of the J/ψ and necessarily had C = +1. The other
quantum numbers for these three observations were not known.

By early 1979 the Crystal Ball had obtained enough data at the J/ψ to report[19,20] on the channel $J/\psi \rightarrow 3\gamma$. Their upper limit for the 3γ branching ratio product at X(2830) is more than 5 times below the DASP measurement. Later in 1979 the Crystal Ball[19,21-23] and the Mark II detector,[24] which was running concurrently with the Crystal Ball at SPEAR, presented results from investigations of the cascade channel in $\simeq 10^6$ ψ' decays. The three χ_J states were seen clearly, while both the Mark I state at 3455 MeV and the DESY-Heidelberg state at 3591 MeV were not confirmed. These experiments set upper limits on the cascade product branching ratios significantly below the values reported by the two earlier experiments. This left the theory with no candidates for the pseudoscalar singlet $^1S_0$ states.

Subsequently, a candidate for the spin singlet ground state $\eta_c(2984)$ was observed in the inclusive photon spectra from ψ' and J/ψ decays by the Crystal Ball.[25] This state was confirmed in exclusive decays of the ψ' by the Mark II experiment.[26] Then in 1981, with double their sample of ψ' decays, the Crystal Ball reported[27] evidence for an $\eta_c'(3592)$ candidate seen in the ψ' inclusive photon spectrum.

The remaining chapters will present the final results of an analysis of the inclusive radiative decays of $1.8 \cdot 10^6$ ψ' and $2.2 \cdot 10^6$ J/ψ decays, using the Crystal Ball detector. The corresponding integrated luminosities are 3452 nb^{-1} at the ψ' and 768 nb^{-1} at the J/ψ. Strong evidence will be presented for an $\eta_c(2984)$ and $\eta_c'(3592)$ candidate. Measurements of the radiative transition rates to the χ_0, χ_1, χ_2, η_c, and η_c' states will be given, as well as measurements of the state's natural line widths.

REFERENCES

1. J. J. Aubert et al., Phys. Rev. Lett. **33**, 1404 (1974).

2. J.-E. Augustin et al., Phys. Rev. Lett. **33**, 1406 (1974).

3. C. Bacci et al., Phys. Rev. Lett. **33**, 1408 (1974).

4. G. S. Abrams et al., Phys. Rev. Lett. **33**, 1453 (1974).

5. Several excellent reviews of the charmonium model are: T. Appelquist, R. M. Barnett, and K. Lane, Ann. Rev. Nucl. Part. Sci. **28**, 387 (1978); V. A. Novikov et al., Phys. Rep. **41C**, 1 (1978); M. Krammer and H. Krasemann, DESY Report 79/20, 1979; M. Shifman et al., Nucl. Phys. **B147**, 385, 448 (1979); W. Buchmüller and S.-H. H. Tye, Phys. Rev. **D25**, 132 (1981); E. D. Bloom, "Quark-Antiquark Bound State Spectroscopy and QCD," Proceedings of Summer Institute on Particle Physics, July 27-August 7, 1981, SLAC Report No. 245, January, 1982; A. Martin, "New Particle Spectroscopy," in Proceedings of XXIth International Conference on High Energy Physics, Paris, France, July 26-31, 1982, to be published. Also see Appendix A.

6. T. Appelquist and H. Politzer, Phys. Rev. Lett. **34**, 43 (1975); A. De Rujula and S. L. Glashow, Phys. Rev. Lett. **34**, 46 (1975); C. G. Callan, R. L. Kingsley, S. B. Treiman, F. Wilczek, and A. Zee, Phys. Rev. Lett. **34**, 52 (1975); T. Appelquist, A. De Rujula, H. Politzer, and S. L. Glashow, Phys. Rev. Lett. **34**, 365 (1975); E. Eichten, K. Gottfried, T. Kinoshita, J. Kogut, K. D. Lane, and T.-M. Yan, Phys. Rev. Lett. **34**, 369 (1975).

7. A. Boyarski et al., Phys. Rev. Lett. **34**, 1357 (1975); V. Lüth et al., Phys. Rev. Lett. **35**, 1124 (1975).

8. J. W. Simpson et al., Phys. Rev. Lett. **35**, 699 (1975).

9. The SPEAR ψ' total cross section was $\simeq 650$ nb.

10. A. D. Liberman, "$\psi(3095)$ and $\psi(3684)$ Results from the HEPL Experiment (SP-16) at SPEAR," 1975 Lepton-Photon Symposium, at the Stanford Linear Accelerator Center, August 21-27, 1975.

11. G. J. Feldman et al., Phys. Rev. Lett. 35, 821 (1975); G. Goldhaber, in Proceedings of the International Conference on Production of Particles with New Quantum Numbers, Madison, Wisconsin, 1976; M. S. Chanowitz and F. J. Gilman, Phys. Lett. 63B, 178 (1976); W. Tanenbaum et al., Phys. Rev. D17, 1731 (1978).

12. W. Braunschweig et al., Phys. Lett. 57B, 407 (1975); W. Tanenbaum et al., Phys. Rev. Lett. 35, 1323 (1975).

13. J. S. Whitaker et al., Phys. Rev. Lett. 37, 1596 (1976).

14. J. S. Whitaker, Ph.D. thesis, Lawrence Berkeley Laboratory Report No. LBL-5518, 1976 (unpublished).

15. C. J. Biddick et al., Phys. Rev. Lett. 38, 1324 (1977).

16. W. Bartel et al., Phys. Lett. 79B, 492 (1978).

17. W. Braunschweig et al., Phys. Lett. 67B, 243 (1977); B. H. Wiik and G. Wolf, "A Review of e^+e^- Interactions," DESY 78/23, May, 1978.

18. M. A. Shifman et al., Phys. Lett. 77B, 80 (1978).

19. E. D. Bloom, "Initial Studies of the Charmonium System Using the Crystal Ball Data at SPEAR," Proceedings of the XIVth Rencontre de Moriond, Les Arcs-Savoie, France, March 11-23, 1979, SLAC-PUB-2598, August, 1980.

20. R. Partridge et al., Phys. Rev. Lett. 44, 712 (1980).

21. M. Oreglia, "Charmonium Studies with the Crystal Ball," in Proceedings of the XVth Rencontre de Moriond: Electroweak and Unified Theory Prediction, Les Arcs, France, March 15-21, 1980,

SLAC-PUB-2529, June, 1980.
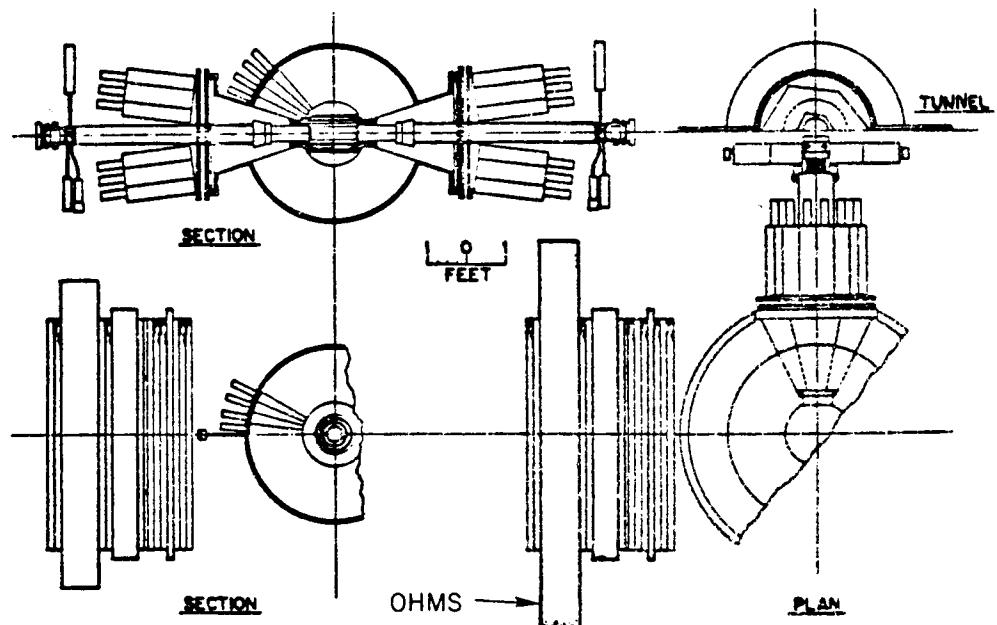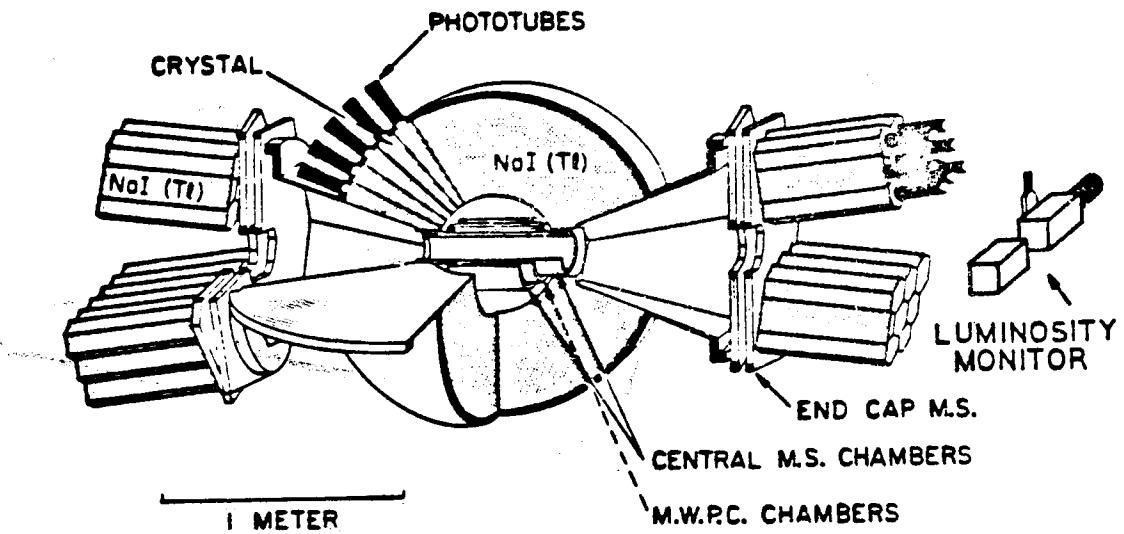
22. M. Oreglia, Ph.D. thesis, Stanford University Report No. SLAC-236, 1980, (unpublished).

23. M. Oreglia et al., Phys. Rev. D25, 2259 (1982).

24. T. Himel, Ph.D. thesis, Stanford University Report No. SLAC-223, October, 1979.

25. E. D. Bloom, "Results from the Crystal Ball Detector at Spear," in Proc. of the 1979 International Symposium on Lepton and Photon Interactions at High Energy, Batavia, Illinois, August 23-29, 1979, SLAC-PUB-2425, November, 1979; R. Partridge et al., Phys. Rev. Lett., 45, 1150 (1980).

26. T. M. Himel et al., Phys. Rev. Lett. 45, 1146 (1980).

27. F. C. Porter, "Recent Result from the Crystal Ball," presented at the SLAC Summer Institute on Particle Physics, Stanford, California, July 27-August 7, 1981, SLAC-PUB-2796, September, 1981; C. Edwards et al., Phys. Rev. Lett. 48, 70 (1982).

Chapter II

THE CRYSTAL BALL DETECTOR

2.1   INTRODUCTION

The real power of the Crystal Ball detector lies in its excellent calorimetry resolution for electromagnetic showering particles, and in its high degree of spatial segmentation. As a total energy calorimeter its sensitivity to electromagnetic energy deposition is essentially 100%, resulting from the 15.7 radiation lengths (L_{rad}) of Thallium doped Sodium Iodide in the central detector, and 20 L_{rad} of NaI(Tl) in the end caps. This is equivalent to about one absorption length of NaI resulting in $\simeq 67\%$ of the final state hadrons interacting in the detector. The remaining $\simeq 33\%$ deposit about 210 MeV as minimum ionizing charged particles (the energy deposition may be less if the particle ranges out, and possibly more if it is negatively charged and interacts with a nucleus). On the average about 50% of the total hadronic energy is measured by the NaI(Tl). Although the efficiency for detecting photonic energy is almost perfect, the detection of individual photons depends on the spatial resolving power of the apparatus. It is with regard to this last issue, i.e., the individual photon detection efficiency, that the high degree of crystal segmentation really pays off. The details of the central ball and associated detector components are shown in Figures 3 and 4 and discussed below.

THE CRYSTAL BALL EXPERIMENT

CRYSTAL

PHOTOTUBES

NaI (Tℓ)

NaI (Tℓ)

LUMINOSITY MONITOR

END CAP M.S.

CENTRAL M.S. CHAMBERS

M.W.P.C. CHAMBERS

I METER

SECTION

FEET

SECTION

OHMS

PLAN
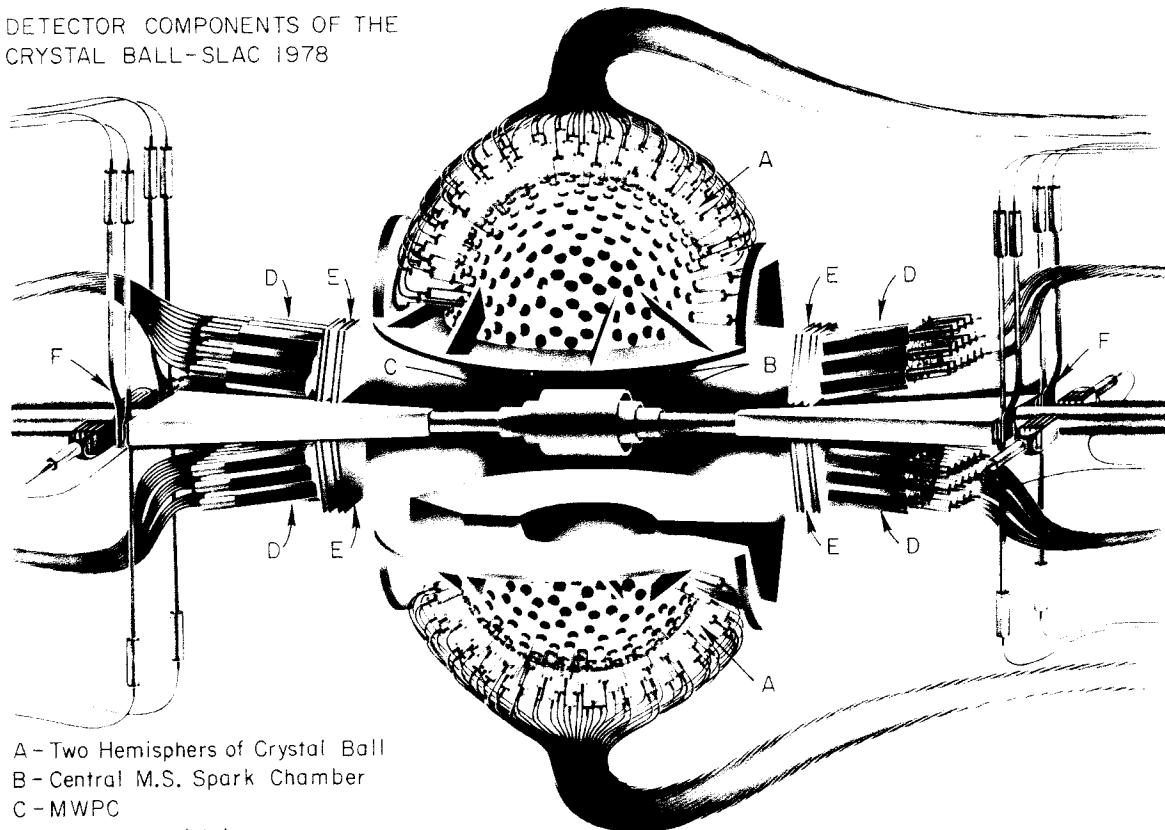
TUNNEL

11-82

4416A57

Figure 3: The Crystal Ball Detector.
The ball hemispheres are shown in their closed position, corresponding
to the detector configuration during data acquisition. Note the two
tunnel regions at the insertion point of the beam pipe.

DETECTOR COMPONENTS OF THE
CRYSTAL BALL-SLAC 1978

A - Two Hemisphers of Crystal Ball
B - Central M.S. Spark Chamber
C - MWPC
D - End Cap NaI(Tℓ)
E - End Cap M.S. Spark Chambers
F - Luminosity Monitor

Figure 4: Artist's Conception of the Crystal Ball.
Here the ball is shown partially open to facilitate the artist's
conception. However, during periods when data were not taken, the two
hemispheres and end caps were "opened" away from the degrading radiation
environment of the beam to protect the critical NaI(Tl).

The Crystal Ball was designed to operate in the center of mass interaction machines, especially e^+e^- colliding beams, where the final state phase space is fairly evenly spread over the near 4π acceptance of the detector. A typical J/ψ or ψ' event, $e^+e^- \rightarrow \simeq 8$ particles, would produce a number of local energy deposits (called bumps) in the NaI(Tl). The number would depend on the size of the local energy bumps and on how many of them overlapped within the spatial resolving capability of the segmentation. This number would also be modified by additional local energy deposits resulting from final state hadron-nuclear interactions in the scintillator material which would split away (designated as split-offs)[1] from the parent particle's impact point. Each bump with an energy > 10 MeV became a final state particle candidate.

The identification of charged particles with the energy bumps was facilitated by a package of cylindrical magnetostrictive spark chambers and multiwire proportional chambers surrounding the beam pipe. Information from the central tracking chambers was used in the current analysis to separate neutral candidates from charged for the inclusive photon spectra. To achieve the basic design philosophy of the detector, that the apparatus be as close to a 100% active calorimeter as possible, the materials and construction of the central chambers were selected to minimize their converter thickness. For a more detailed description of the experiment than what follows, the reader is referred to the list of references,[2-8] while a detailed description of the central magnetostrictive spark chambers may be found in Appendix B.

2.2 EXPERIMENTAL LAYOUT

The SPEAR[9] e^+e^- colliding beam facility at the Stanford Linear Accelerator Center is a machine for circulating a single bunch each of electrons and positrons in parallel but opposite oval orbits. The e^- and e^+ bunches are made to collide at the two interaction regions, where a detector can observe the final state and study the physics of the process. The SPEAR ring has $\simeq 30$ meter minor diameter and $\simeq 40$ meter major diameter. The bunch size is typically 2.6 cm long (σ_z) and less than one millimeter in transverse dimension.

The Crystal Ball detector was enclosed in an environmental dry room located in the SPEAR east interaction region (IR). Located directly adjacent to the east IR was the experiment control room, which housed the data processing electronics, the trigger electronics, the PDP 11/T55 data acquisition computer, and operator's console. The detector proper consisted of the following elements, as shown in Figures 3 and 4.

1) The Central Ball with 672 NaI(Tl) crystals.
2) The Central Tracking Chambers Package.
3) The End Caps: tracking chambers and 60 NaI(Tl) crystals.
4) The Luminosity Monitor.
5) The Outer Hadron-Muon Separator (OHMS).

Since the NaI is hygroscopic and its optical properties would be irreparably damaged if exposed to even a small amount of surface hydration, the central NaI was hermetically sealed in two hemispherical containers. The end cap crystals were individually sealed in thin walled stainless steel enclosures. As an added precaution the dry room maintained a constant temperature of (20 ± 1)°C and a low humidity (dew-point of -42°C) environment for the detector. Aside from

safeguarding the integrity of the NaI crystals, the dry room added to the stability of the combined NaI and photomultiplier tube (PMT) temperature sensitive output signals. The data from the OHMS part of the detector were not used in the analysis for this study. Located outside the dry room were the 500 KeV proton Van de Graaff accelerator used for energy calibration of the NaI(Tl), and the prepulser, pulser, and high voltage power supplies used for the spark chambers.

Data at the two resonances were collected over a period from November, 1978 to April, 1981. The histories of the J/ψ and ψ' runs are summarized in Figure 5. During this period a wiggler magnet system was installed at SPEAR. This system was designed to increase the beam current ceiling and thereby the luminosity, in addition to increasing the synchrotron light available to the Stanford Synchrotron Radiation Laboratory, which was also conducting experiments at SPEAR. Data were taken with the wiggler magnet both on and off. A quantitative analysis of the ψ' resonance yield as a function of the wiggler magnet field strength has already been given by M. Oreglia.[2] Table 1 lists the typical beam currents and luminosities observed shortly after injection and the average resonance yields for each run. Based on short term tests the J/ψ yield was found to be best with the wiggler magnet off. A qualitative comparison of the ψ' yield with the wiggler magnet condition, as shown in Table 1, indicates an improved yield with the magnet on.
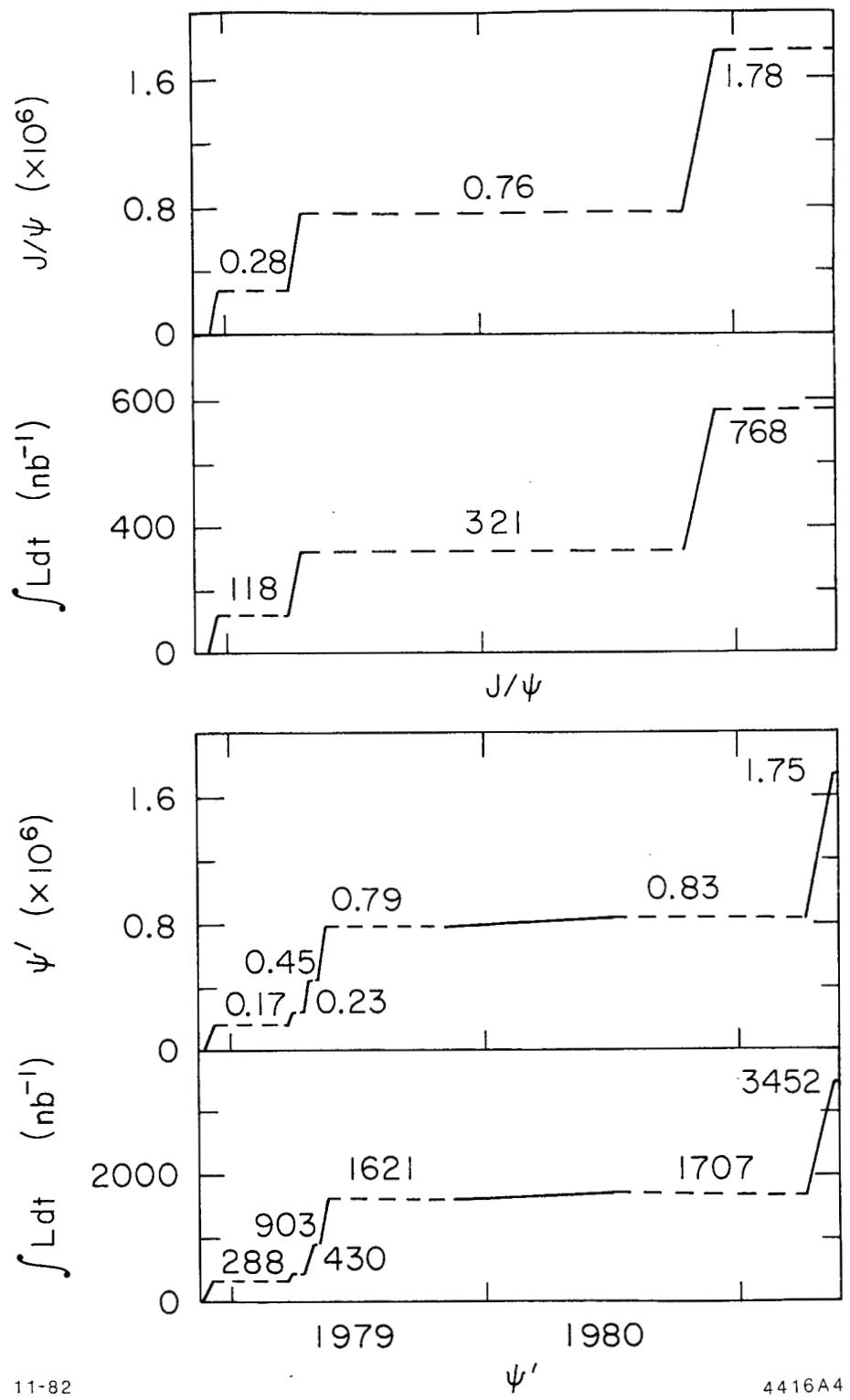
Figure 5: J/ψ and ψ' Data Acquisition Histories.
The integrated luminosities and observed numbers of hadronic decays at
the J/ψ and ψ' resonances are shown versus time.

TABLE 1

Typical SPEAR Beam Currents and Luminosities after Injection.
Also shown is the SPEAR wiggler magnet status, the trigger rate, and the
corrected resonance production yield.

RUN	WIGGLER CONDITION	BEAM CURRENT (ma)	LUMINOSITY $(cm^{-2}sec^{-1})$ $(\cdot 10^{30})$	TRIGGER RATE (Hz)	RESONANCE YIELD RATE (Hz)
J/ψ 1	off	4.8	0.48	2.6	1.08
J/ψ 2	off	5.1	0.52	2.4	1.01
J/ψ 3	off	4.9	0.31	2.4	0.74
ψ' 1	off	8.4	1.2	2.1	0.52
ψ' 2	on	11.8	1.9	3.5	0.72
ψ' 3	on	11.3	1.8	3.2	0.66
ψ' 4	on	11.4	1.8	3.2	0.66
ψ' 5	off	9	1	2.5	0.44
ψ' 6	on (85%)	12.2	1.4	4.0	0.70
ψ' 6	off (15%)	7.6	0.7	2.8	0.45

2.3   THE CENTRAL BALL

As shown in Figure 3, the central ball[10] consists of two hemispheres

of 336 NaI(Tl) crystals each, positioned one above the other around the

SPEAR beam pipe. During normal data taking the two hemispheres are

closed to within about 2 mm. Two tunnel regions on opposite sides of

the ball, where 48 crystals have been removed, allow for the insertion

of the beam pipe. A central $\simeq 50$ cm diameter hollow dome surrounds the

beam pipe and central tracking chambers.

To understand the ball and crystal geometries,[2] begin with a hollow

sphere. Figure 6 shows how the surface is divided into an icosahedron.

Each of the 20 triangular faces (major triangles) is subdivided into 4

triangles (minor triangles). These in turn are subdivided into 9

crystal triangles. Their vertices are projected back onto the surface

of the sphere to obtain the final crystal geometry.

GEOMETRY AND JARGON

ICOSAHEDRON

"MAJOR TRIANGLE"   <u>20</u>

"MINOR TRIANGLE"   <u>80</u>

INDIVIDUAL "MODULES"
OR "CRYSTALS"   <u>720</u>

"EQUATOR"

"TUNNEL REGION"

11-82
4416A55
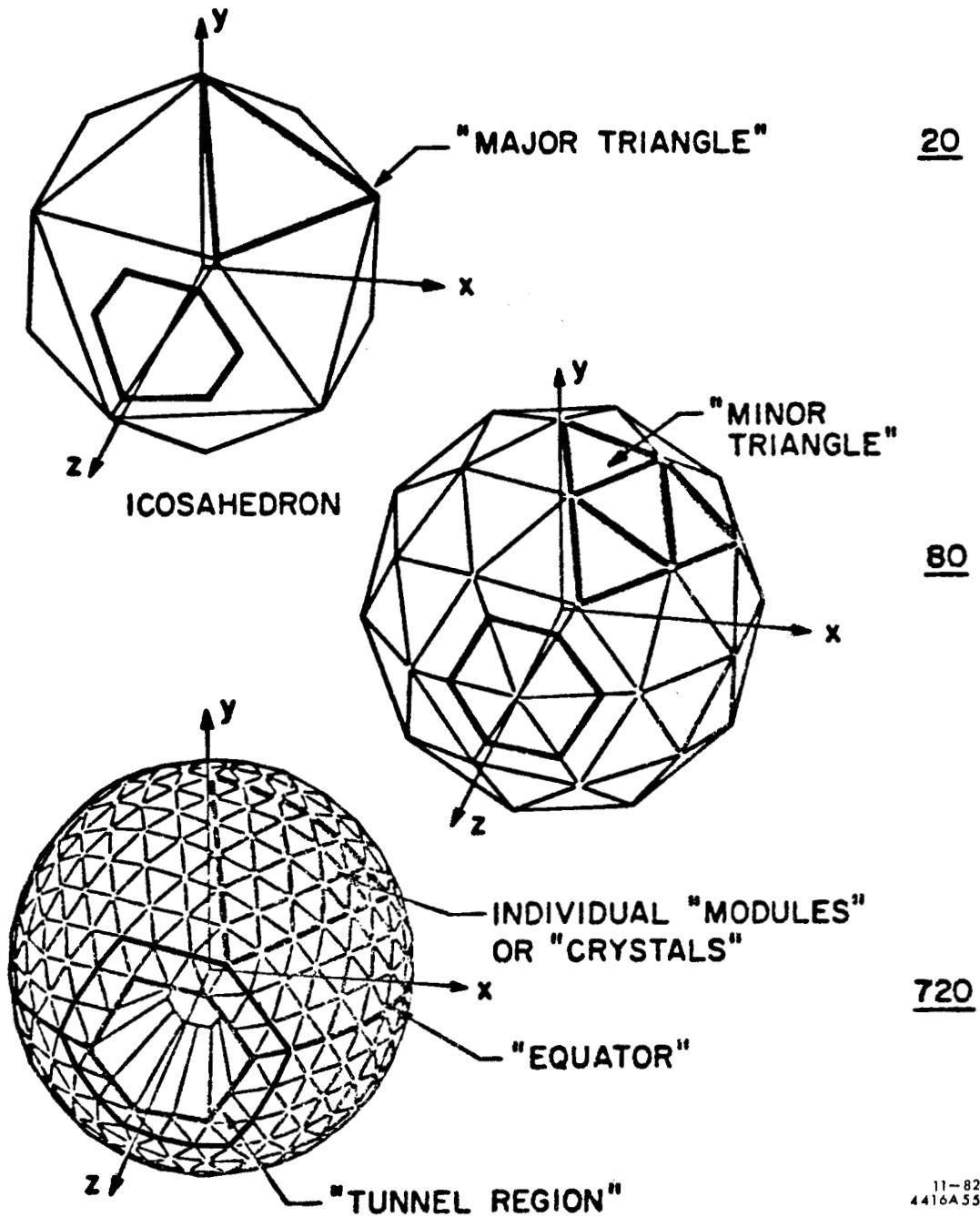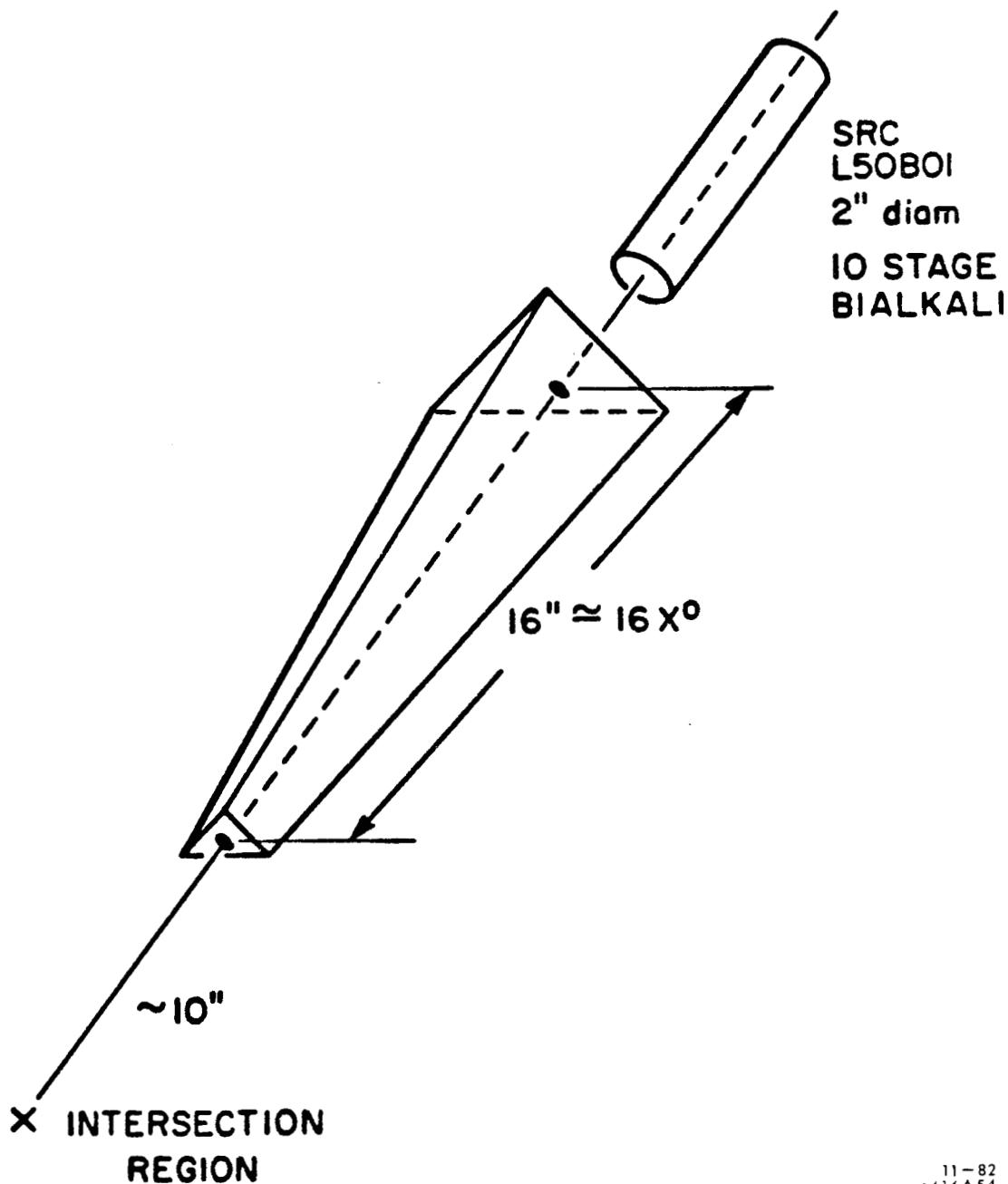
Figure 6: Construction Geometry for the Central Ball.
Note the single layer of crystals surrounding the tunnel opening.

As shown in Figure 7, each crystal has three longitudinal edges constructed from radii extending from the interaction point. The crystals are 16 inches long with triangular cross sections tapering towards the IR. An inscribed (circumscribed) circle subtends a full cone angle of $\approx 6.5°$ ($\approx 12°$) with respect to the IR. To ensure proper internal light propagation and inter-crystal optical isolation, each crystal was individually wrapped in reflector paper and aluminized foil (aluminum foil for the bottom hemisphere and aluminized Mylar foil for the top hemisphere). The scintillator light output traveled through a ≈ 1 inch air gap, glass window, and another 2 inch air gap before entering a two inch diameter PMT.[11]

After the crystals were fabricated, they were individually compensated for longitudinal linearity by sanding the crystal sides. This was done to control the scintillator light propagation inside the crystal. The goal was to achieve a uniform pulse height from an attached PMT as a ^{137}Cs source was moved longitudinally along the crystal side. The depth of maximum shower development for photons increases with the log of the photon energy. Although this compensation removed a logarithmic bias in the photon energy, it introduced random inter-crystal energy dependent calibration errors. Based on the known compensation curves, signal output versus longitudinal position of the ^{137}Cs source (a few typical examples are shown in Figure 8), these errors are known to be $\pm(2-3)\%$.

The resulting configuration provides 94% of 4π solid angle coverage. Those crystals immediately surrounding the tunnels were shaved to smaller dimensions than the remaining standard crystals, to allow

SINGLE CRYSTAL SCHEMATIC

SRC
L50B0I
2" diam

IO STAGE
BIALKALI

$16" \cong 16 X^0$

$\sim 10"$

X INTERSECTION
REGION

11-82
4416A54

Figure 7: Individual Crystal and Photomultiplier Tube.
Each crystal is individually wrapped in reflector paper and aluminized
foil (not shown). The small triangular end is typically $\cong 2$ inches on a
side, and the large end is typically $\cong 5$ inches on a side. Due to the
construction technique there were 11 different sizes of crystals.
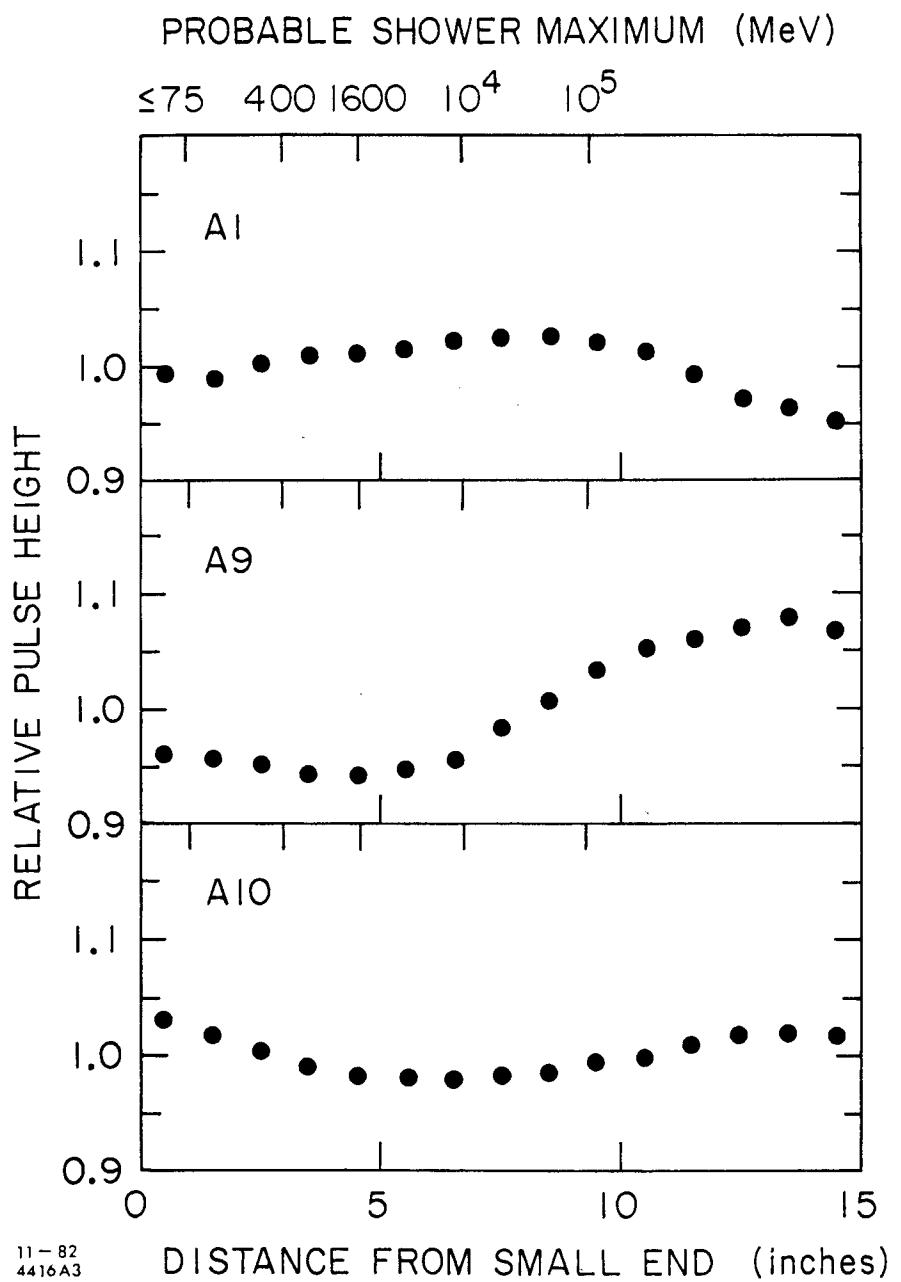
Figure 8: A Few Typical Crystal Compensation Curves.
The signal output from a ^{137}Cs source positioned along the side of a
crystal is plotted versus the longitudinal position of the source. The
signals were normalized by their averge value.

adequate cable access to the central chambers. Taking this into account, plus the finite size of the interaction region and the requirement that there be an additional layer of crystals surrounding the central crystal struck by a photon, leads to an acceptance of 85% of 4π solid angle for clean photon detection and the best energy measurement.

2.4 THE CENTRAL TRACKING CHAMBERS

2.4.1 Magnetostrictive Spark Chambers

Two cylindrical magnetostrictive spark chambers (MSSC), each with two spark gaps, provided data for accurate charged particle trajectory reconstruction. Appendix B gives a detailed description of the central MSSC. Basically, the construction details for the MSSC and multiwire proportional chambers (MWPC) cylindrical shells were the same. The conductive surfaces were formed from etched copper (MSSC) or aluminum (MWPC) coated Mylar. For the MSSC 1.5 and 2 mil copper on 5 mil Mylar was used, while for the MWPC 0.5 mil aluminum on 2.5 mil Mylar was chosen. Laminated cylindrical shells made from the metallized Mylar, epoxy, and Styrofoam were used as the basic chamber building blocks. Different diameter shells were concentrically connected using spacers at their ends to form the chambers. The final structure was extremely rigid, even though the shells were only $\simeq 1.5$ mm thick and up to $\simeq 15$ cm in radius, as shown Figure 9.

Both MSSC had a similar design except for dimension and cross plane angles. The following structures are noted when moving from the inner to the outer surfaces:
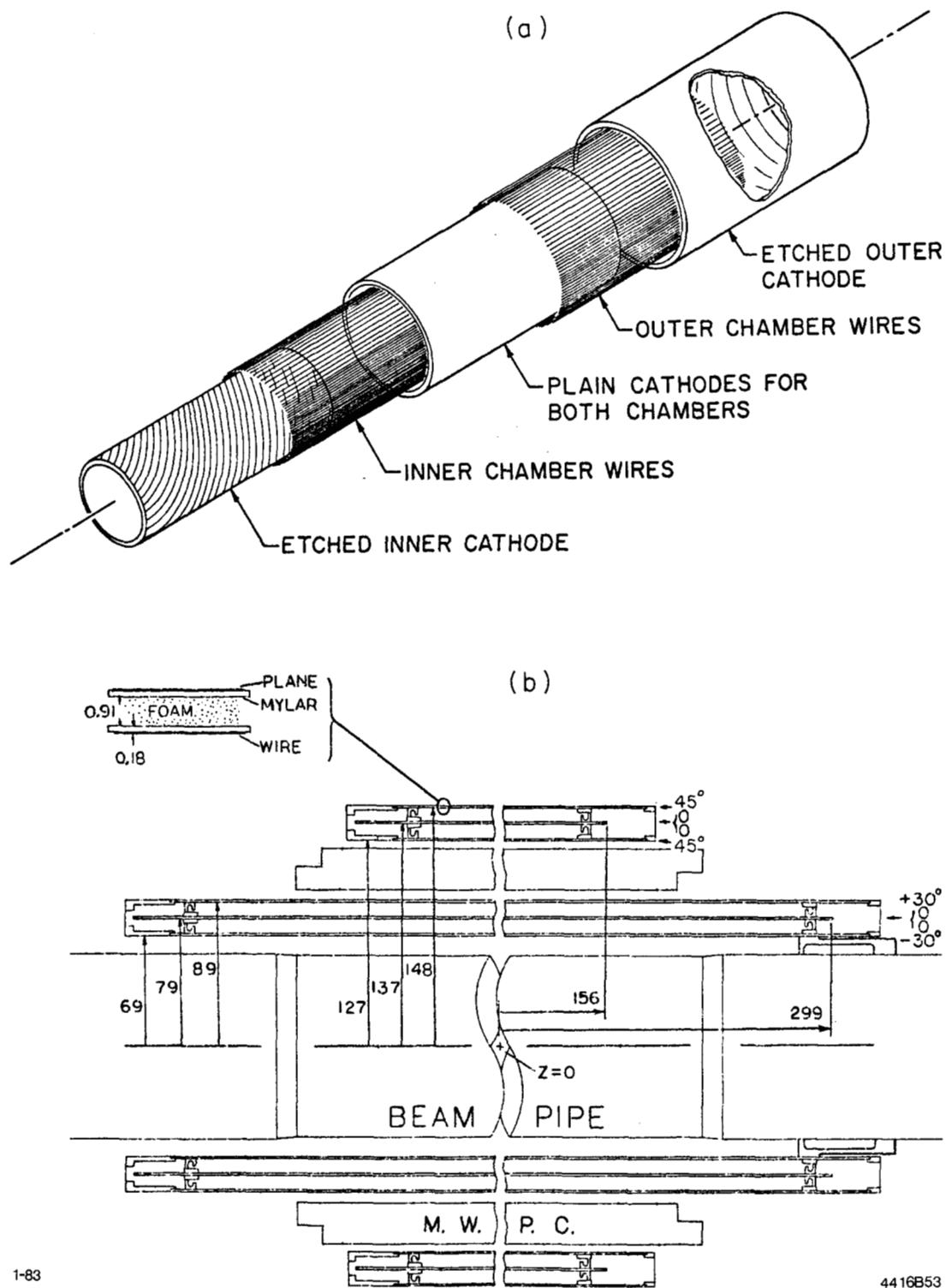
Figure 9: Central Tracking Chamber Dimensions.
The MWPC construction is shown in figure (a), which exemplifies the cylindrical geometry used for the central chambers. Figure (b) shows a cross section schematic of the chamber system as it was installed at SPEAR.

1) inner shell.
   a) shield ground plane (1.5 mil Cu).
   b) H.V. return ground etched cross plane gap 1 (1.5 mil Cu).
2) spark gap 1 (90% Ne and 10% He).
3) middle shell
   a) H.V. etched straight plane, gap 1 (1.5 mil Cu).
   b) two non-etched H.V. return current planes (2 mil Cu each).
   c) H.V. etched straight plane, gap 2 (1.5 mil Cu).
4) spark gap 2.
5) outer shell.
   a) H.V. return ground etched cross plane gap 2 (1.5 mil Cu).
   b) shield ground plane (1.5 mil Cu).

The etched copper tracings were 0.012 inches wide with a 1.0 mm center to center spacing. In general, the two cross planes were of opposite helicity to reduce ambiguities in track reconstruction. The chamber cross planes were inclined 30° for the inner chamber and 45° for the outer chamber. Both chambers, including the end cap MSSC, used the same gas mixture. The inner chamber covered 94% of 4π, while the outer chamber covered 71% of 4π solid angle.

Since the spark chambers had to be pulsed, their data were not used by the trigger logic. Information from the central ball and MWPC was used for trigger determination. Once a trigger was asserted, a high voltage pulse to the spark chambers was initiated. If an ionization track was present in one of the MSSC gaps due to a charged particle, then a spark in that gap might occur. The ensuing current pulse along the chamber's etched wires was detected using the magnetostrictive effect. The resulting acoustic pulses were converted to electrical signals, then amplified, and finally digitized in the control room. The raw data indicated the point on the chamber circumference, projected along the etched wire, where a charged particle had passed.

Following a trigger, by $\simeq 1$ ms, a 350 volt ion clearing field pulse was applied to the chambers for a duration of $\simeq 15$ ms. In addition a constant field of 10 volts was applied at all other times. The combined effect was to remove the uncombined ions resulting from the spark discharge.

2.4.2 Multiwire Proportional Chambers

A single cylindrical multiwire proportional chamber[5] (MWPC) with two gaps was sandwiched between the two MSSC's. The MWPC subtended 83% of 4π sr. Moving from the inner to outer surfaces the structure was as follows:

    1) inner shell
        a) shield ground plane
        b) etched negative H.V. cathode cross plane (62°) for gap 1
    2) inner gap 1 (90% Ar and 10% CO_2)
        a) 5 mm gap
        b) 144 signal anode wires at H.V. ground
        c) 5 mm gap
    3) middle shell
        a) plain negative H.V. cathode plane for gap 1
        b) plain negative H.V. cathode plane for gap 2
    4) outer gap 2
        a) 5 mm gap
        b) 144 signal anode wires at H.V. ground
        c) 5 mm gap
    5) outer shell
        a) etched negative H.V. cathode cross plane (90°) for gap 2
        b) shield ground plane

The anode wires were 0.02 mm gold plated tungsten with a spacing of $\simeq 4.5$ mm. The MWPC data consisted of a list of wires with signals above the noise level, and the analog signals from the etched cathode strips. In general the MWPC spatial resolution was coarser than for the MSSC, although the MWPC anode wires had a substantially better efficiency (see

Table 2). For these reasons the MWPC information was only used for identifying (or "tagging") charged particles and not for reconstructing charged particle trajectories.

TABLE 2

Central Tracking Chamber Performance.
The values given are for a single MSSC plane, MWPC anode wire plane, or MWPC cathode strip plane and pertain to inclusive hadronic decays of J/ψ and ψ'. The resolution for a track crossing N gaps would be $\simeq N^{-1/2}$ better. Also, the polar angle resolution contains a contribution due to the uncertainty in the measured interaction z vertex ($\sigma_z \simeq 0.8$ cm ; ranges from 10-100 mr at the chambers).

CHAMBER	FWHM AZIMUTHAL RESOLUTION (mr)	FWHM POLAR RESOLUTION (mr)	EFFICIENCY (%)
Inner MSSC	25±5	150±20	70-75
Outer MSSC	25±5	115±15	70-75
MWPC gap 1	35±2	95-180	90-98 (anode only)
MWPC gap 2	35±2	75-137	90-98 (anode only)

2.5 END CAPS

The end caps were intended to increase the solid angle coverage of the detector, providing both energy deposition information and charged particle tracking. Fifteen standard Harshaw manufactured hexagonal 20 L_{rad} NaI(Tl) crystals were used in each of the end cap quadrants (see Figures 3 and 4). Two gaps of magnetostrictive spark chamber[12] were placed directly in front of the crystals. This brought the solid angle coverage to 98% of 4π sr.

End cap data were used in the selection of hadronic decay events, and as an additional source of candidate photons for π⁰ reconstruction. No end cap particle information was included in the inclusive photon spectra.

2.6   DATA ACQUISITION

The PMT analog pulses were fed to the counting house, where they were integrated and held on capacitors for digitization.[13]   Using CMOS switching, the integrate and hold pulses were sequentially connected to a 200 MH_z Tracor Northern 1213 rundown 13 bit ADC (8192 channels) for digital processing.   To accomodate the desired dynamic range in photon energies and not permit the ADC to limit the detector's resolution, required each PMT signal to be digitized at two gains.   The low channel corresponds to a low energy deposition and is fed from the higher gain circuit.   The high channel is best suited for high energy deposits and is fed from the lower gain circuit.   This way a single ADC can handle both channels, increasing its dynamic range.   For this experiment the high gain was set for 0-200 MeV and the low gain was set for 0-4 GeV. Fast-out analog sums of 9 crystals (corresponding to minor triangles) were available for trigger purposes.

Two independent hardware trigger systems, both using the fast-out analog signals from the central ball in coincidence with the beam cross and MWPC information, evaluated the trigger assertion.   The tower trigger system,[7,14] which was a compact TTL logic system, performed analog summations corresponding to various geometries with in the ball; e.g., i) the total ball energy excluding the tunnel modules (E_{tot}) and ii) a count of the number of major triangles with energy above $\simeq110$ MeV (NMT), the near minimum energy deposition due to minimum ionizing particles traversing 16 L_{rad} of NaI.   In addition the tower trigger hardware interrogated the MWPC readout hardware to obtain the number of groups of 8 contiguous wires, with at least one hit in coincidence from

each gap (NL_{PWC}).   Table 3 gives a list of tower triggers and their

thresholds used for   the data in this study.   The primary trigger

consisted of an "OR" of these two   triggers,   in addition to   one and

sometimes two other triggers which were not used in this study.

TABLE 3

Primary Trigger Scheme

NMT, NL_{PWC}, and E_{tot} are explained in the text.   A small part of the
early running for both J/ψ and ψ' had the total energy threshold set at
1.7 and 2.0 GeV, respectively.   This trigger had an active solid angle
of 84% or 92% of 4π sr, depending on whether or not the tunnel boarder
crystals were included in the trigger hardware energy summations.

TRIGGER	LOGIC	E_{tot} J/ψ	THRESHOLDS (GeV) ψ'
Total Energy:	$E_{tot} >$	1.1	1.1
Multiplicity:	$(NL_{PWC} > 0) \cdot (NMT = 2) \cdot E_{tot} >$	0.14	0.14
	$(NL_{PWC} > 0) \cdot (NMT = 3) \cdot E_{tot} >$	0.14	0.14
	$(NMT \geq 4) \cdot E_{tot} >$	0.14	0.14

The other trigger system[2] was constructed from modular NIM logic.

This system, which was somewhat redundant to the tower trigger in

function, made hardware analog sums for the top, bottom, and full ball.

The top and bottom were each required to pass a 140 MeV discriminator

and the total energy had to be $\geq$ 650 MeV.   Constant fraction

discriminators were used to provide timing information.   To satisfy the

timing requirement, the signals had to be present within 8 ns of the

beam cross.   The NIM trigger, with an active solid angle of 94% of 4π

sr, was combined as an "OR" with the primary tower elements to make the

highly redundant and thus dependable final trigger.   Studies of the

trigger requirements using Monte Carlo simulated events (see Appendix C)

show the trigger efficiency to be ≈99% for inclusive hadronic decays of the J/ψ and ψ'.

Following a trigger assertion a general event hold pulse is issued by the primary trigger logic.   This signals the pending acquisition of the processed data by the Data Acquisition Program[8] running on the PDP 11/T55 computer.   By way of a CAMAC interface[15] the information from each element of the detector is read into the computer memory. The data are stored both i) in internal buffers to be written to magnetic tape for offline analysis, and ii) in common block areas for online program analysis. Two Digital Corporation tape drives handled the data I/O.

2.7   CALIBRATION

Periodic calibrations[6] using i) ^{137}Cs as a 0.661 MeV gamma ray source and ii) a Van de Graaff to generate 0.34 MeV protons for the reaction $^{19}F(p,\alpha)^{16}O^*$, resulting in a 6.31 MeV gamma ray from the $^{16}O^*$ decay, were made on approximately two week intervals during the runs.   The pedestals for each crystal were sampled at the same time.   The results of the calibration led to a determination of the high and low channel pedestals and the low channel slope.   It was convenient to parameterize the high channel slope as a ratio of the high channel slope to the low channel slope.   The ratios were set by comparing the ADC values for crystal energy depositions within the range of both the high and low channels simultaneously (120-200 MeV).

Using Bhabha events, γγ events, and direct e⁺e⁻ decays of J/ψ and ψ', collected over the two week period corresponding to the ^{137}Cs and Van de Graaff data, it was possible to correct the initial calibration and

substantially improve the resolution. These events yielded a clean sample of monoenergetic pairs at the known beam energies, 1.5475 GeV at the J/ψ and 1.8420 GeV at the ψ'.

Each major run was preceeded by a careful scan of the resonance peak as a function of the SPEAR beam energy. The peak set point was easily held to within ±0.2 MeV. The chromatic dispersion in the beams has a sigma of $\simeq$ 1.2 MeV. This will broaden the Bhabha contribution to the peak, but not the direct resonance decay contribution. However this statistical broadening is negligible compared to the NaI(Tl) resolution which is $\simeq$30 MeV at these energies. It was found that about two weeks running on resonance produced enough e^+e^- and $\gamma\gamma$ events to make statistically significant calibrations of each crystals slope value. The Bhabha calibration improved the resolution at 1.84 GeV by $\simeq$34% over the ^{137}Cs and Van de Graaff calibration alone.

There are several important consequences to this calibration procedure. First, the calibrations are parameterized in a way that assumes a linear relationship between the digitized value for the crystal signal and the energy deposition in the crystal. This may not be the case. For example the masses of slow π^0's and η's, calculated from the invariant mass of their two photon decay products, are both slightly but significantly below their known masses ($\simeq$3% for the π^0 and $\simeq$2% for the η). However, this result is complicated by possible correlations between the γ energies and/or directions. Second, calibration variations with a time constant of less than two weeks but longer than a few hours, would be averaged over in the Bhabha calibration measurement, and entirely missed by the short duration

^{137}Cs/Van de Graaff runs. A discussion of the detector's energy

resolution may be found in Appendix F.

REFERENCES

1. K. Köningsmann and F. Bulos, Crystal Ball memo CB-NOTE 154 or 251
    (1980).

2. M. Oreglia, Ph.D. thesis, Stanford University Report No. SLAC-236,
    1980, (unpublished).

3. M. Oreglia et al., Phys. Rev. D25, 2259 (1982).

4. Y. Chan et al., IEEE Trans. on Nucl. Sci. NS-25, 333 (1978).

5. J. Gaiser et al., IEEE Trans. on Nucl. Sci. NS-26, 173 (1979).

6. I. Kirkbride et al., IEEE Trans. on Nucl. Sci. NS-26, 1535 (1979).

7. E. D. Bloom, "Initial Studies of the Charmonium System Using the
    Crystal Ball Data at Spear," in Proc. of the XIVth Rencontre de
    Moriond, Les Arcs-Savoie, France, March 111-23, 1979, SLAC-PUB-2598,
    August, 1980; E. D. Bloom, "Results from the Crystal Ball Detector
    at Spear," in Proc. of the 1979 International Symposium on Lepton
    and Photon Interactions at High Energy, Batavia, Illinois, August
    23-29, 1979, SLAC-PUB-2425, November, 1979.

8. R. Chestnut et al., IEEE Trans. on Nucl. Sci., NS-26, 4395 (1979).

9. M. Sands, Stanford University Report No. SLAC-121, 1970.

10. Fabrication of the hemispheres was performed under a joint effort
    by the Crystal Ball Collaboration and the Harshaw Chemical Company,
    Solon, Ohio.

11. C. Peck and F. Porter, Crystal Ball memo CB-NOTE 010 (1976).

12. J. Tompkins, Crystal Ball memo CB-NOTE 232 (1977).

13. G. Godfrey, Crystal Ball memo CB-NOTE 121 (1976).

14. G. Godfrey, Crystal Ball memo CB-NOTE 131 (1978).

15. G. Oxoby and J. Bernstein, Crystal Ball memo CB-NOTE 113 (1977).

Chapter III

DATA SELECTION

3.1 INTRODUCTION

The data acquisition at SPEAR resulted in $\simeq 5.7 \cdot 10^6$ J/ψ and $\simeq 9.3 \cdot 10^6$

ψ' triggers written to tape.   Of these triggers only $\simeq 1.9 \cdot 10^6$ and

$1.8 \cdot 10^6$ are hadronic decays of J/ψ and ψ', respectively.   The remaining

triggers resulted from a combination of background processes:

Removable Backgrounds

1) Cosmic rays intersecting the ball within the trigger timing window
    (termed cosmic ray events).

2) Degraded e^+/e^- from the beams which shower in the NaI(Tl), or e^+/e^-
    in the beams interacting with residual gas atoms in the vacuum pipe
    (termed beam gas events).

3) QED reactions, $e^+e^- \to e^+e^-$, $\mu^+\mu^-$, or $\gamma\gamma$, including single photon
    radiative additions to these reactions (termed QED events).   Direct
    resonance decays to lepton pairs are also included in this category
    (ie. J/ψ or $\psi' \to \ell^+\ell^-$).

Non-removable Backgrounds

4) Non-resonance hadron production, $e^+e^- \to$ hadrons not via J/ψ or ψ'
    (termed non-resonance events).

The goal in the data selection process was to efficiently retrieve the

hadronic decays while minimizing the inclusion of the background events.

It was found that each of the above backgrounds, except the

non-resonance events, had a characteristic signature allowing it to be

effectively removed.   The residual contamination due to backgrounds 1)

through 3) above amounted to 0.8% for the J/ψ sample and 1.5% for the ψ'

sample. The number of non-resonance background events was calculated to

be 17·10^3 at J/ψ and 53·10^3 at ψ', and no attempt was made to remove

them from the sample. The characteristics of the inclusive hadronic

decays were sufficiently different from the backgrounds to allow for a

94% efficiency in the data selection. A description of the parameters

characterizing the classes of events and the details of the selection

criterion will be discussed below. During this discussion, the use of

the term "background" shall refer to the first three classes of events

only.

3.2   INTERPRETATION OF THE CRYSTAL ENERGIES

To minimize the event selection bias and to simplify the Monte Carlo

simulation of the inclusive hadronic decays of J/ψ and ψ', it was

decided to use only the crystal energy data and some properties derived

from this in the event selection. No information was required from the

central or end cap tracking chambers. Cosmic ray and beam gas events

were removed solely on the basis of their spatial energy deposition

pattern in the NaI(Tl). The QED event selection required the more

sophisticated determination of particle track information (i.e., the

number of tracks and their energies). Note that the use of the word

"track" in this study refers to both neutral and charged tracks.

Aside from the analysis which leads to the isolation of the

individual final state particles, to be described below, each event may

be analyzed as a unique pattern of energy. This leads to two

interpretations of an event: i) a mixture of isolated and sometimes

overlapping energy depositions produced by the final state particle interactions in the detector, and ii) a pattern of energy deposition characteristic of a particular class of event. Three parameters were used to quantify the patterns. These were the event's total multiplicity, total energy, and asymmetry, as will be discussed in Section 3.4. Following is a description of the particle identification and track reconstruction techniques. This information is pertinent to the QED event subtraction and to the inclusive photon analysis in Chapter IV.
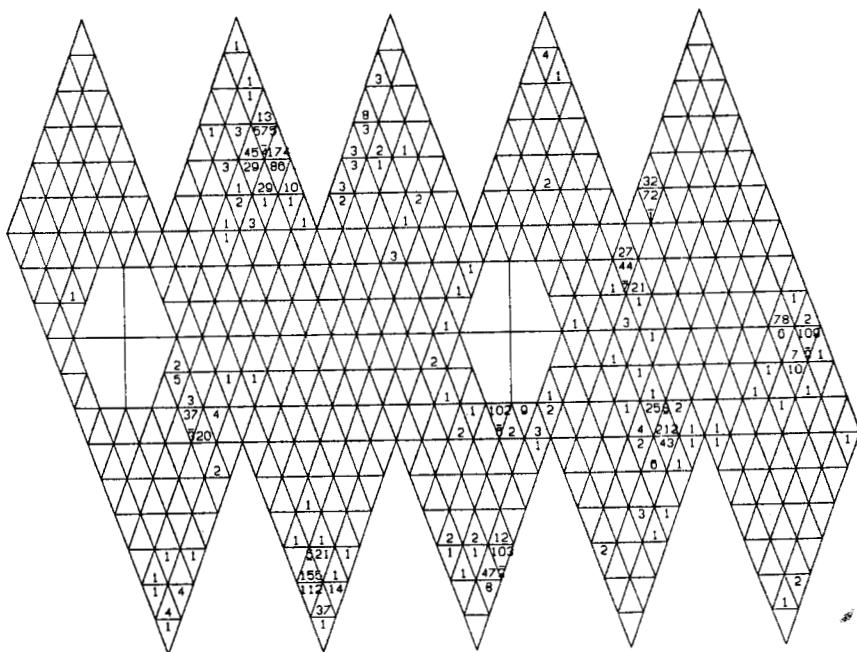
The crystal map has proven to be a useful mode of graphically displaying the energy deposited in each event. Figures 10 and 11 show a J/ψ hadronic decay, a cosmic ray event, a beam gas event, and a J/ψ radiative QED event. The map projections are made by dividing the ball along it's major triangle boundaries, and then unfolding it. Each crystal is projected as a small triangle, with it's energy inscribed. The tunnel regions appear as hexagonal holes. Any energy deposited in the end caps is indicated in these holes. Readily visible are clusters of crystals with non-zero energies, corresponding to points of impact by the reaction products. Also apparent to the eye are the widely different patterns of energy distribution in these typical events.

It is clear from Figures 10 and 11 that most clusters appear to result from a single particle. This means that there is one central crystal with the maximum energy, surrounded by crystals with lesser energies which can be attributed to the shower of a single particle striking the central crystal. Some examples of energy clusters (connected regions) are shown in Figure 12. An isolated minimum

RUN # 1217   EVENT #   27   ETØT=   2485   ECM=   3095

#	ECR	ETRK	TYP
1	57	105	CIR
2	950	162	CIR
3	338	74	N
4	102	1018	N
5	162	381	N
6	92	102	CG1
7	281	102	N
8	105	332	N
9	197	197	CG2

(a)
J/ψ
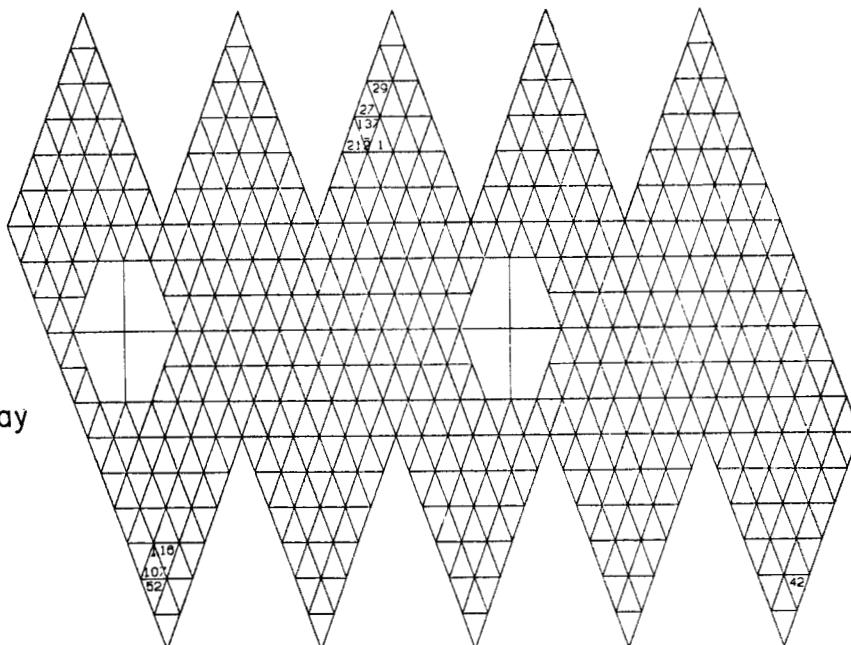
RUN # 2305   EVENT #   58   ETØT=   406   ECM=   3684

#	CR	TRK	T
1	217	218	N
2	215	215	N

(b)
Cosmic Ray

11-82
4416B32
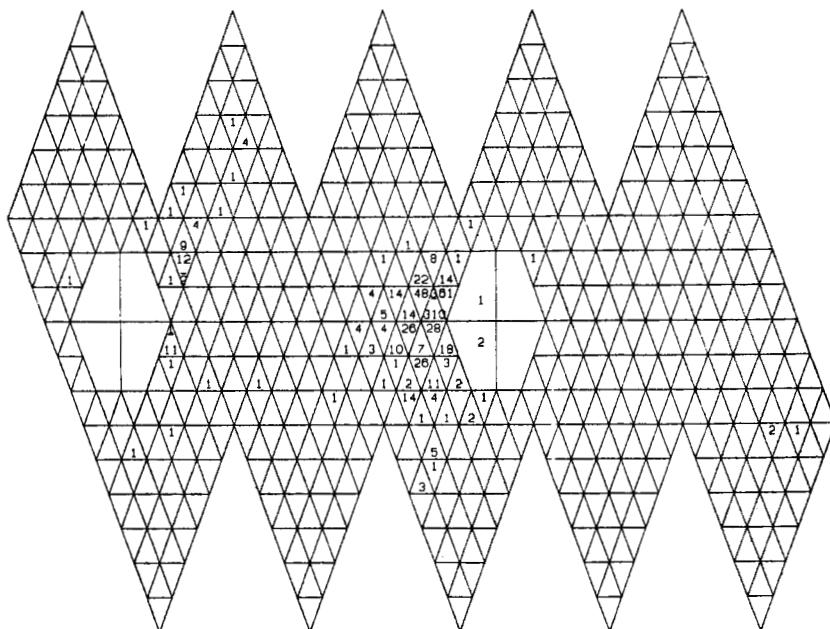
Figure 10: Crystal Energy Maps-I.
The top figure (a) indicates a typical J/ψ hadronic decay.   It is not
possible to distinguish this event from a ψ′ decay.   The bottom figure
(b) illustrates a cosmic ray traversing two lines of crystals separated
by the inner hollow dome of the detector.   Tracks identified by the
standard production analysis are printed at the left.

– 39 –

RUN # 2305   EVENT #   66   ETØT=   721   ECM=   3684

#	CR	TRK	T
1	11	17	N
2	12	27	N
3	606	683	N

(a)
Beam Gas

RUN # 1091   EVENT #   3002   ETØT=   3516   ECM=   3683

#	CR	TRK	T
1	123	1708	C
2	1734	140	N
3	1525	1919	N

1040 IN 351

(b)
$e^+e^-\gamma$

11-82
4416B33   1040 IN 351
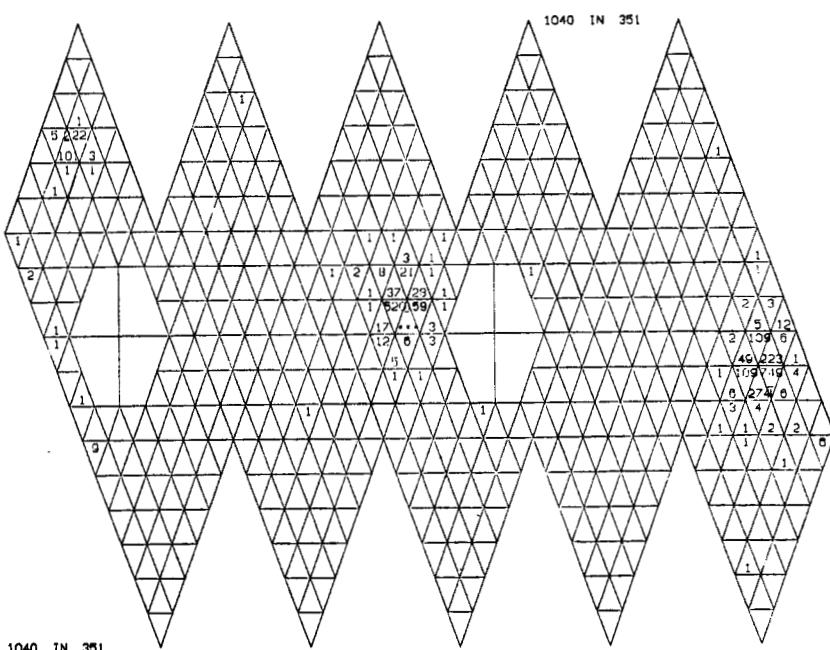
Figure 11: Crystal Energy Maps-II.
A typically asymmetric beam gas event is shown in the top figure (a),
while a radiative QED event at J/Ψ is shown in the bottom figure (b).
The energy of the crystal indicated by "***" is shown above the map.

ionizing particle sometimes provides an extreme example of the single

bump connected region, where all the energy of the cluster is contained

in one crystal. Electromagnetic showers are examples of very regular

energy deposits, both in the longitudinal and lateral development of the

shower. Their fluctuations are relatively small, though occasional

large fluctuations do occur. As a contrast, interacting hadrons produce

extremely varied energy patterns in the NaI(Tl). Their fluctuations are

large and irregular when compared to electromagnetic showers.

In addition there are multiple bump clusters, where the energy

depositions of several particles may overlap (see Figure 12). In these

cases the individual bumps had to be unfolded from the main clusters

using the bump discriminator algorithm.[1] The analysis began by finding

connected regions of energy defined as follows:

> A connected region is a cluster of contiguous crystals all
> with an energy greater than 10 MeV. Contiguous means
> crystals touching at either their vertices or their sides.
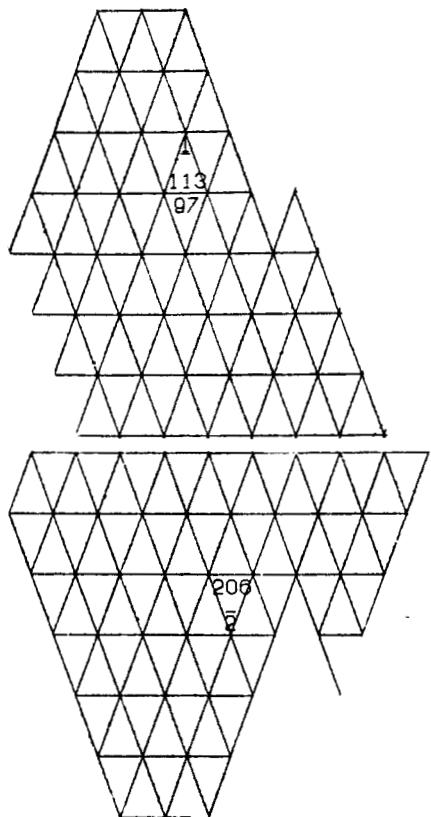
The bump discriminator algorithm was then applied to each connected

region to determine the number of particles within the region.

Initially there is only a single identified particle (bump), which is

associated with the crystal containing the maximum energy in the

connected region. Each crystal in the connected region was tested to

see if it's energy could be explained as a probable shower fluctuation

of this bump. An empirically derived envelope function was fine tuned

on the data to most effectively discriminate true particle bumps from

shower fluctuations by hand scanning events. This necessarily required

walking a fine line between, on the one hand, finding too many fake

bumps due to fluctuations, and on the other hand, introducing a large detection inefficiency by radically suppressing fake bumps and real bumps. In the search for new bumps the energy of the i_{th} crystal is compared to the empirically estimated maximum energy for the i_{th} crystal resulting from a fluctuation of a showering particle striking the bump crystal. The envelope function is parameterized by the intercrystal opening angle, ϕ, as follows:
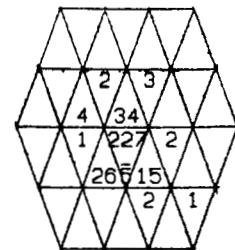
$$f(\phi) = \begin{cases} E_b & , \text{ for } \phi < 12° \\ E_b \cdot 0.72 \cdot \exp(-9.4 \cdot (1 - \cos\phi)), & \text{ for } 12° < \phi < 45° \\ 0 & , \text{ for } \phi > 45° \end{cases} \qquad \text{(III-1)}$$

where E_b is the energy of the particle striking the bump module (the $\sum 4$ was used for estimating E_b, see below). The i_{th} crystal is considered another bump if $E_i > f(\phi_i)$. This process is repeated until each of the modules in the connected region has been explained as either a bump or a fluctuation of an existing bump.
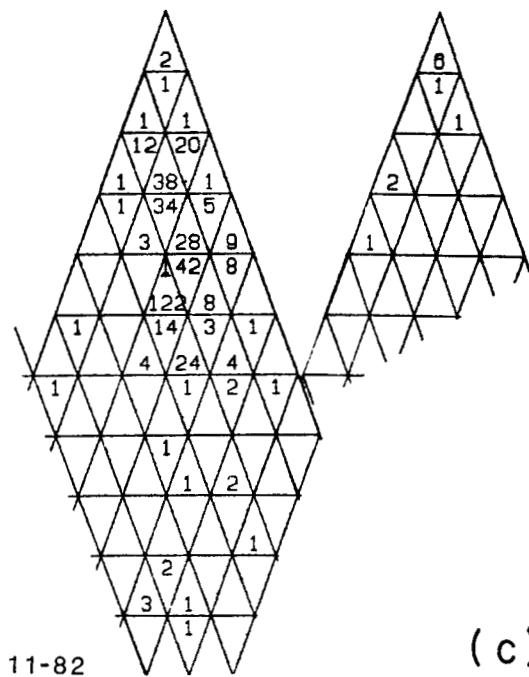
The multiplicity of the event refers to the number of observed discrete energy bumps. Each bump became an impact site for a particle candidate and was associated with a track in the event track bank. On occasion, the charged particle trajectory reconstruction programs, which used only the central spark chamber data, would find a track which was not associated with any energy bump in the detector. A hand scan of some of these events revealed the cause: charged particle trajectories were fit individually to roads of spark chamber hits. Only after all the tracks were fitted was the common interaction vertex determined. The trajectories were then displaced to intersect the vertex. Sometimes a poor initial vertex determination would move the trajectory far enough
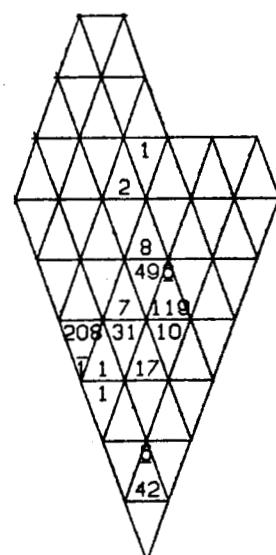
Figure 12: Connected Regions.
Figure (a) illustrates two minimum ionizing energy clusters, while an electromagnetic shower is shown in Figure (b). Figure (c) shows an interacting charged hadron connected region. A two bump complex connected region is shown in Figure (d).

away from it's true energy bump to destroy the correspondence. The result was a charged track with zero energy. As a consequence the true charged particle energy deposit became a fake "photon." To remove the overcounting bias the multiplicity was defined as the number of bumps rather than the number of tracks.

Two generically different methods for measuring the particle's energy deposition were employed in the standard event analysis. The energy sort algorithm[2] (ESORT) was the more sophisticated method in that it attempted to unscramble overlapping showers. It sorted each crystal's energy, determining what fraction belonged to each particle. In most cases each crystal's entire energy was attributed to a single particle. With regard to multiple bump energy clusters, the ESORT method achieved the maximum possible spatial resolution which was set by the resolution of the bump discriminator. The algorithm was fine tuned on electromagnetic showers, since their energies were the most reliably measured.

In contrast, the much simpler $\sum 13$ algorithm estimated the particle's energy as the sum of a geometrically fixed pattern of crystals surrounding the bump module; usually 13 crystals were involved (see Figure 13), although bumps at the major triangle vertices involved only 12 crystals. In practice, the distribution of the number of crystals with an energy $>$ 0.5 MeV used in the $\sum 13$ energy calculation, peaked at 8 crystals with a standard deviation = 3 crystals. This method made no attempt to unscramble overlapping energy deposits. On the one hand, it systematically underestimated the energy of electromagnetic showers, by not including the average $\approx 2.2\%$ of energy deposited outside the $\sum 13$. On

the other hand, it suffered from a systematic overestimate of the
particle's energy, if another particle impacted sufficiently close by.
In this case there was a double counting of the deposited energy since
the two $\sum 13$'s overlapped. This was remedied by requiring that the
interparticle opening angle, θ_{ij}, satisfy $\cos\theta_{ij} < 0.85$. With this cut,
the $\sum 13$ energy estimate yielded a slightly better resolution than the
ESORT mesurement, but at the expense of a reduced acceptance for
particle detection.

Since obtaining the best resolution is critical to the analysis of
the inclusive photon spectra and the search for small signals, the $\sum 13$
energy estimate was chosen. The final particle energy was calculated
using the following equation:

$$E_{track} = \sum 13 \cdot PCORR / 0.978 \qquad (III-2)$$

where the factor 0.978 corrects for the $\sum 13$ underestimating bias and the
PCORR term represents a position correction[3] to the energy based on the
estimated impact point of the photon relative to the crystal sides and
vertices. On the average, showers near a crystal vertex have a
proportionally larger energy loss than showers near a side or a center.
The PCORR correction improved the resolution at 1.84GeV by $\simeq 26\%$ over the
resolution resulting from the ^{137}Cs, Van de Graaff, and Bhabha
calibrations alone (see Section 2.7).

The photon directions were calculated using the energy weighted
average of the bump module neighbor crystal centroids (a modified
centroid estimate), plus a correction for the known bias[2] in this
estimate. From Monte Carlo studies the centroid estimate alone is known
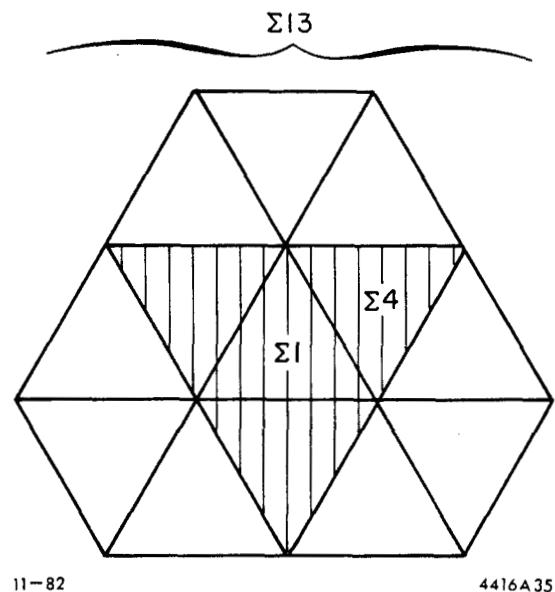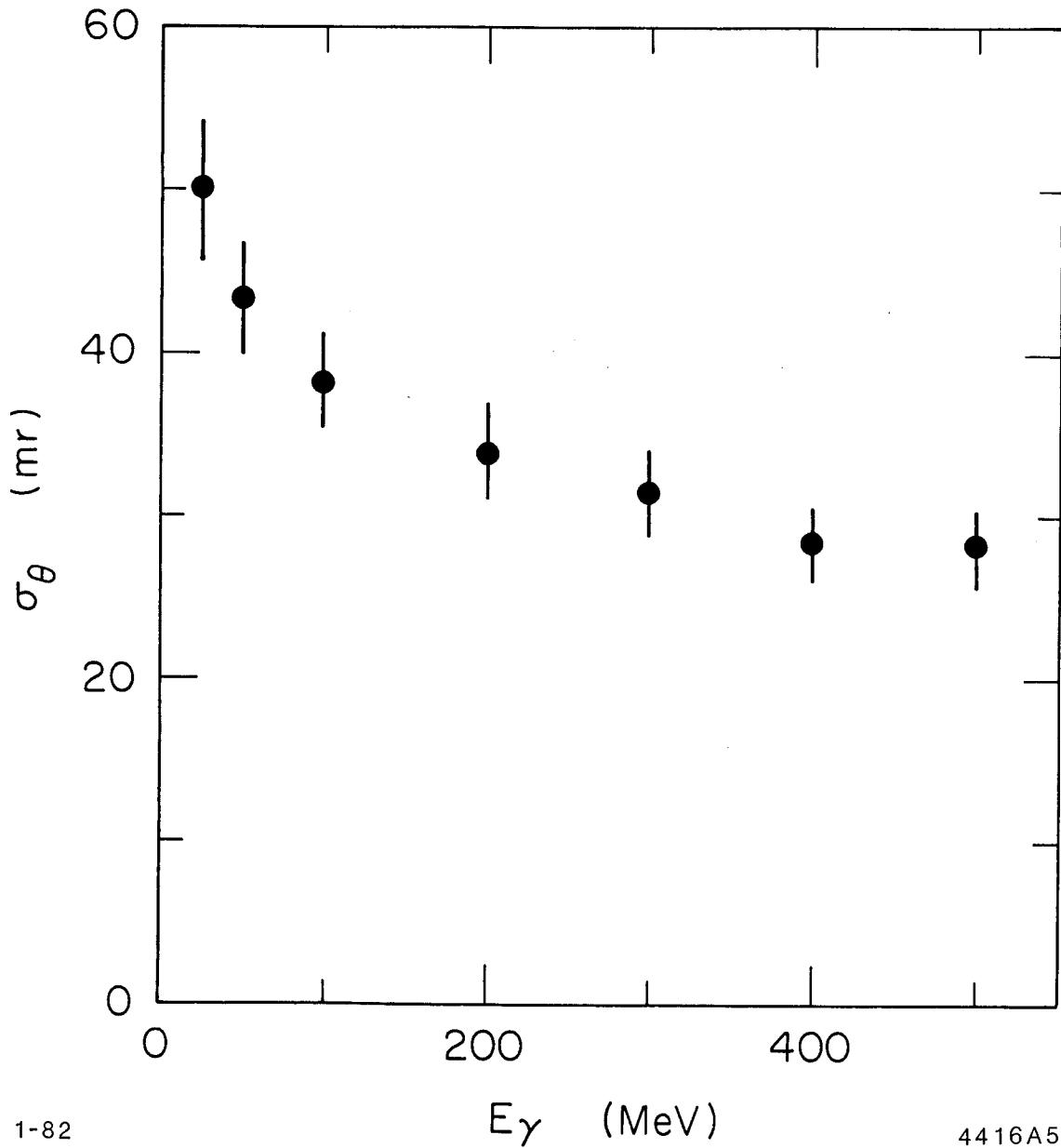
Figure 13: Geometry of the $\Sigma 13$ Crystal Pattern
Also indicated are the bump module ($\Sigma 1$) and the $\Sigma 4$ modules. The $\Sigma 2_{max}$ modules includes the bump module plus whichever module is the next highest in energy with in the $\Sigma 13$, which may or may not be in the $\Sigma 4$.

to be biased towards the center of the bump module, away from the vertices. An empirical correction was added which shifted the centroid γ direction towards the nearest vertex parallel to the nearest crystal side. The resulting photon trajectory reconstruction algorithm[4] was tested by adding Monte Carlo photons, at various energies, to real J/ψ events and then comparing the analyzed Monte Carlo γ direction to the dialed γ direction. See Appendix C for a discussion of the Monte Carlo technique. The photon angular resolution obtained in this way is plotted in Figure 14.

4416A5

Figure 14: Neutral Tracking Resolution.
The photon tracking resolution, for the algorithm SHOWER,[4] is plotted as
a function of the Monte Carlo γ energy, for γ's generated at z = 0.0 in
an environment of inclusive J/ψ hadronic decays.   An additional $\simeq$15%
degradation in resolution is expected to result from a distributed
interaction vertex (z $\neq$ 0.0).   Comparable results were obtained for the
standard production analysis photon tracking routines.
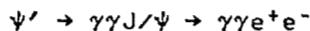
3.3   BACKGROUND DATA SAMPLES

The event selection criterion were tuned on a combination of data samples and Monte Carlo simulated events (for the latter see Appendix C). Special runs were made at SPEAR with the e^+ and e^- beams separated, to produce a data sample including only cosmic ray and beam gas events. This was done several times during the data acquisition to average over slight variations in SPEAR performance and the trigger conditions. These special runs were set up with the following procedure: Electrons and positrons were injected into the SPEAR ring and made to collide as during the normal data acquisition. After colliding for a short time to allow the SPEAR operators to stabilize the orbits, the beams were separated and the data acquisition begun.   In addition, a few runs were made without beams present.   These cosmic ray data precisely duplicated cosmic rays logged during the data acquisition, since the trigger timing coincidence came from the R.F. oscillator at SPEAR, and did not require the presence of beams.

As the QED process $e^+e^- \rightarrow \mu^+\mu^-$ and the direct decays J/ψ and $\psi' \rightarrow \mu^+\mu^-$ produce events very similar to cosmic rays penetrating the central hollow sphere of the ball, they were studied with the data samples mentioned above.   A second class of events involving $e^+e^- \rightarrow e^+e^-(\gamma)$, $e^+e^- \rightarrow \gamma\gamma(\gamma)$, and the direct decays J/ψ and $\psi' \rightarrow e^+e^-$ were lumped together in a category termed showering QED events.   Generally they deposit about twice the beam energy in two symmetric energy patterns. The non-radiating two body final state channels were easily removed with a multiplicity cut, which rejected events with $\leq$ 2 tracks, as discussed
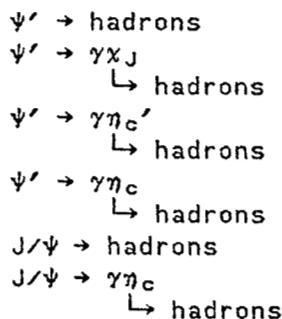
below.   The difficulty arose in selecting out the radiative 3 and

occasionally 4 body final states, without also removing interesting

decays of the ψ', eg. $\psi' \rightarrow XJ/\psi \rightarrow Xe^+e^-$.   The electron and positron in

the J/ψ decay are energetic and so, resemble a QED event.

The effectiveness of the showering QED event selection criterion was

studied using a variety of enriched data samples and Monte Carlo events.

Compared to the J/ψ and ψ' resonances,   the data taken at E_{beam} = 1.835

GeV, just below the ψ' resonance, and at E_{beam} = 2.0-2.5 GeV, above the

open charm threshold, showed a relatively stronger showering QED signal.

These off resonance events had proportionally far fewer hadronic decays.

In addition a select sample of events fitted to the channel,[5]

$$\psi' \rightarrow \gamma\gamma J/\psi \rightarrow \gamma\gamma e^+e^-$$

was used to tune the QED criterion and reduce the loss of this signal.

The rejection efficiency was evaluated using a J/ψ $\rightarrow$ 3γ,   QED Monte

Carlo.

To   evaluate   the   overall   inclusive   hadronic   decay   selection

efficiency, Monte Carlo events were generated for each of the processes:

$$
\begin{aligned}
&\psi' \rightarrow \text{hadrons} \\
&\psi' \rightarrow \gamma\chi_J \\
&\qquad\quad \hookrightarrow \text{hadrons} \\
&\psi' \rightarrow \gamma\eta_c' \\
&\qquad\quad \hookrightarrow \text{hadrons} \\
&\psi' \rightarrow \gamma\eta_c \\
&\qquad\quad \hookrightarrow \text{hadrons} \\
&J/\psi \rightarrow \text{hadrons} \\
&J/\psi \rightarrow \gamma\eta_c \\
&\qquad\quad \hookrightarrow \text{hadrons}
\end{aligned}
$$

The term "hadrons" refers to a phase space distribution of pions, etas,

and kaons in relative proportion to the known hadronic decays of J/ψ and

ψ'.   In addition, the channels with significant branching fractions were

explicitly included. The generation procedure and details of the Monte Carlo program are given in Appendix C. The simulated events were analyzed identically to real data. The number of events passing the event selection cuts was used to determine the efficiency for each channel. Similar efficiencies were measured for all the channels in the range (94-95)% except for $\psi' \to \gamma\eta_c$ and $\psi' \to \gamma\chi_J \to \gamma\gamma J/\psi$ where a value of (95-97)% was obtained.

3.4   BEAM GAS AND COSMIC RAY SUBTRACTION

A loose set of minimal cuts was applied to all the raw data during the standard production analysis (see Table 4) to remove the most glaring cosmic ray and beam gas backgrounds. These cuts resulted in a ≈30% reduction in the number of raw triggers and are included for completeness, although they are far outside the much tighter criterion used in the hadron selection. All further discussion of the data sample selection refers to those events which had passed the minimal cuts.

TABLE 4

List of Minimal Cuts Applied to All Data.
These cuts were imposed on the raw data early in the production analysis to remove the most obvious cosmic ray and beam gas backgrounds. E_{half+z} and E_{half-z} are the total energies in the +z half and -z half of the detector, respectively, including the end cap energies. A connected region is defined in the text.

REJECTION CRITERION

Standard Production Analysis Minimal Cuts:
1) $E_{tot} >$ 10 GeV, or
2) $E_{half+z} <$ 20 MeV, or
3) $E_{half-z} <$ 20 MeV, or
4) Number of Connected Regions ≤   1

As mentioned previously, three quantities were found to adequately classify the event patterns. These were: i) the event's total multiplicity, ii) the event's total energy, E_{tot}, and iii) the event's asymmetry, A_{sym}. Figure 15 shows the multiplicity distributions for uncut J/ψ and ψ' data, separated beams data, and enriched QED data at $E_{beam} > 2$ GeV. The total energy is calculated by summing all the crystal energies:

$$E_{tot} = \sum E_i \qquad (III-3)$$
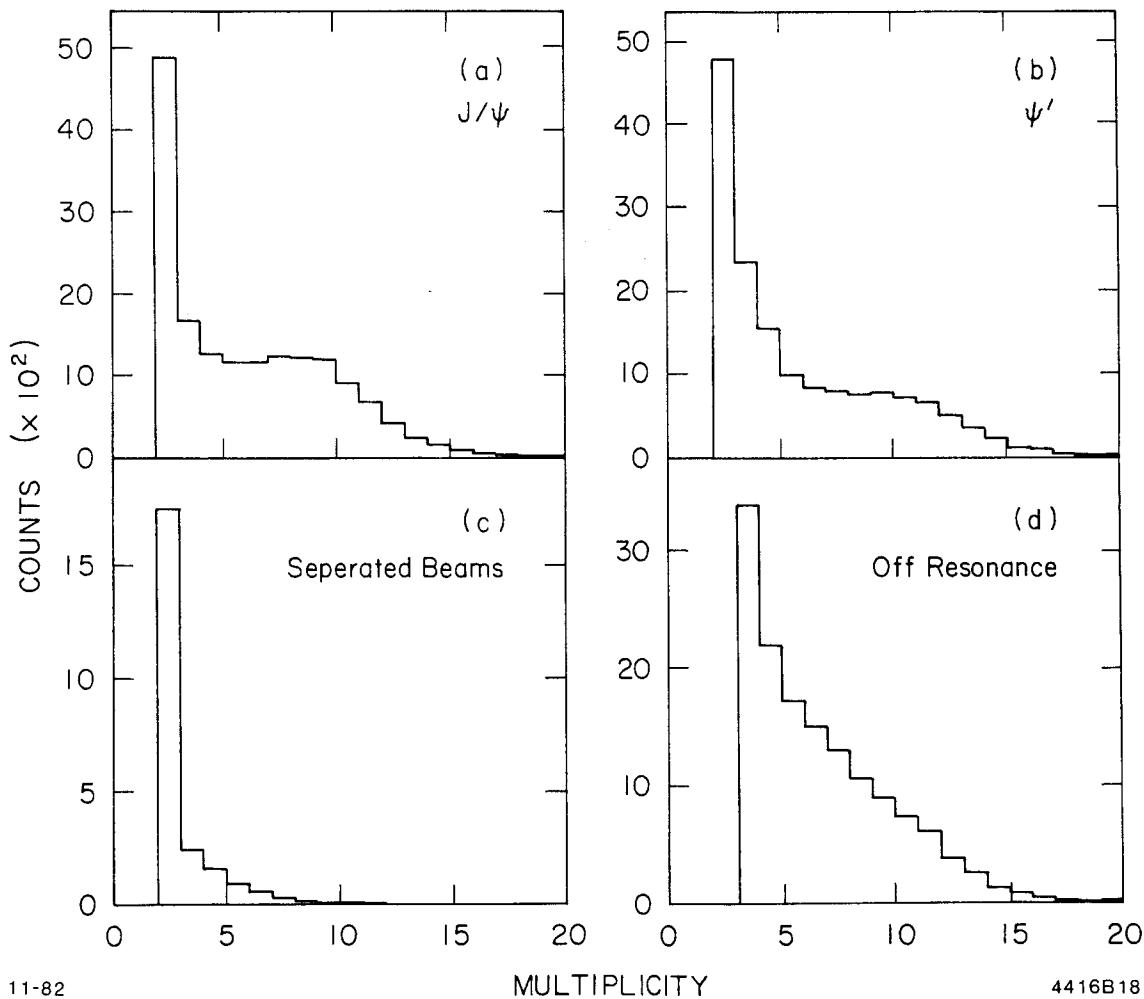
where the sum runs over all the central and end cap crystals with an energy $E_i > 0.5$ MeV. Figures 16(c) and (d) contains histograms of E_{tot} for the separated beams data, and the enriched QED data. These may be compared to Figures 16(a) and (b) showing the E_{tot} distributions for unselected J/ψ and ψ' events. The principle features in the spectra are indicated in the figure captions.

Coarse background rejection cuts were applied to remove the bulk of the showering QED, beam gas, and cosmic ray events. These cuts were near but outside the final cut windows. They are summarized in Table 5.

The asymmetry parameter, A_{sym}, is defined as:

$$A_{sym} = \frac{|\sum \hat{n}_i E_i|}{E_{tot}} \qquad (III-4)$$
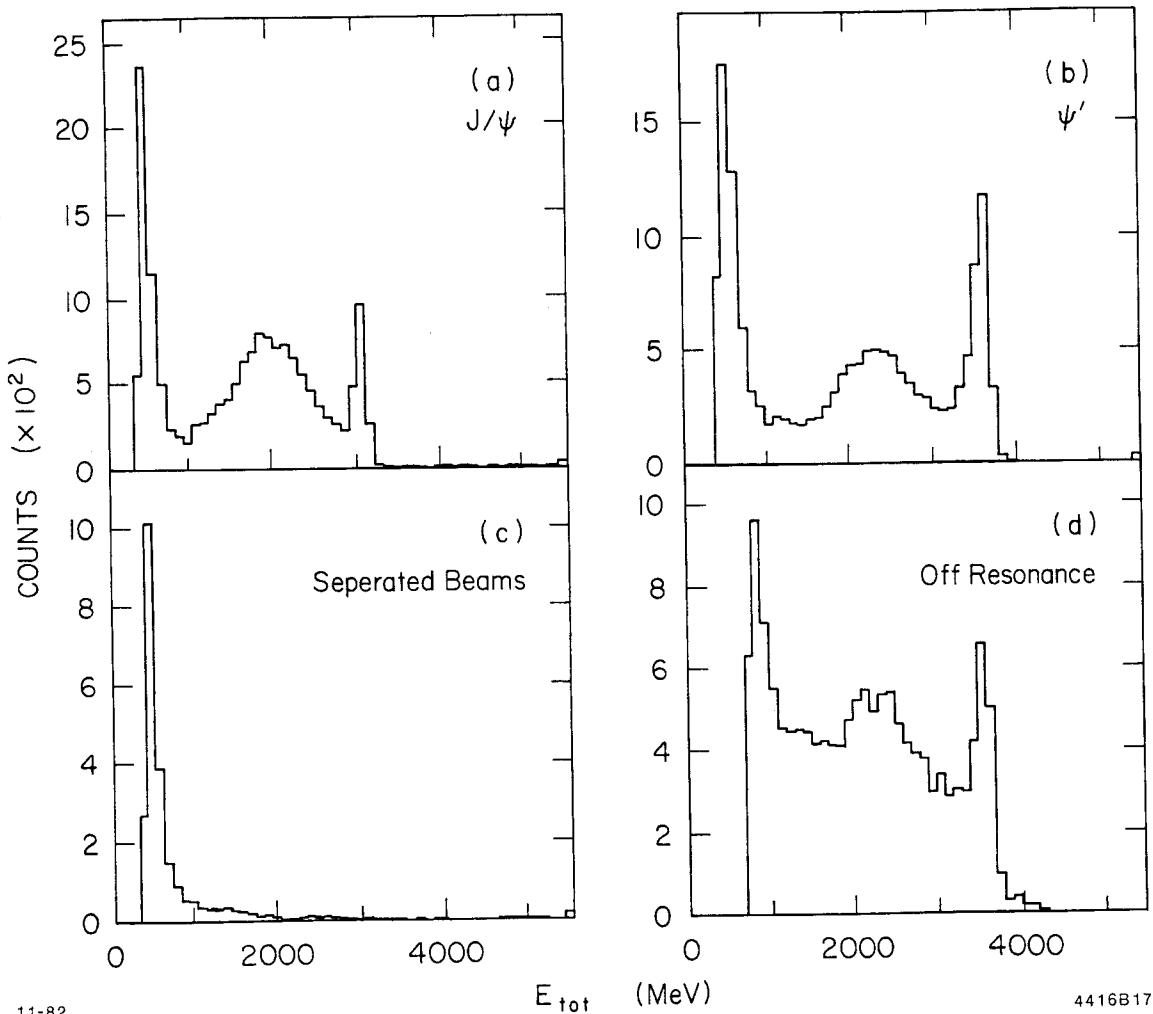
where $\hat{n}_i$ is the unit vector pointing to the center of the i_{th} crystal, and the sum runs over all the crystals with an energy $E_i > 0.5$ MeV. Alone, the asymmetry does not adequately separate the event classes. Also the A_{sym} parameter was not used in the removal of QED events.

Figure 15: Multiplicity Distributions.
The event multiplicities are shown for the unselected data in Figures
(a) and (b), the separated beams events (c), and the enriched QED data
(d). Note the high preponderance of background events in the low
multiplicity channels and the broad bump centered at a multiplicity of
≈8 in the resonance data indicative of the hadronic signal. A cut was
made on events with a multiplicity ≤ 2.

Figure 16: Total Energy Distributions for J/ψ and ψ′ Decays
Figures (a) and (b) give the E_{tot} distributions for unselected J/ψ and ψ′ events. The background data is shown in figures (c) and (d). The peak at the low energy end is produced by the trigger threshold acting on a sharply rising beam gas and cosmic ray background. The hadronic signals are clearly seen in the resonance data centered at ≃1800 MeV. The peaks at $2 \cdot E_{beam}$ are due to $e^+e^- \to e^+e^-$, $e^+e^- \to \gamma\gamma$, radiative contributions to these channels, and all neutral final states. At ψ′ there is an addtional contribution from $\psi′ \to XJ/\psi \to Xe^+e^-$, where X is an all neutral combination of particles.
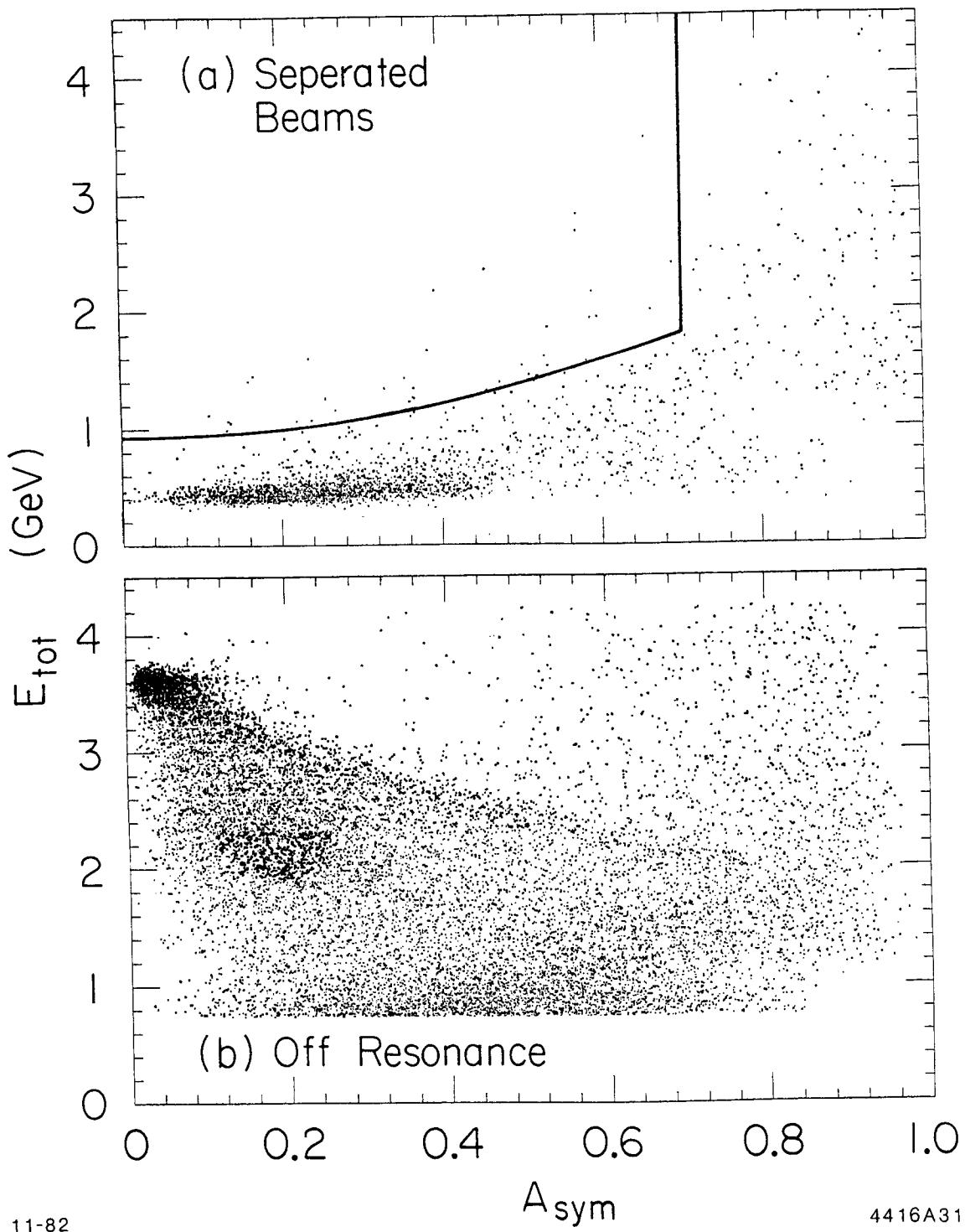
TABLE 5

Coarse Background Rejection Criteria

REJECTION CRITERION	J/ψ	ψ'
Coarse Background Rejection Cuts:		
1) Number of Tracks $\leq$	2	2, <u>or</u>
2) $E_{tot} >$	3445 MeV	4100 MeV, <u>or</u>
3) $E_{tot} <$	656 MeV	800 MeV.

The pattern cut best suited for the removal of beam gas and cosmic ray events at the J/ψ and ψ' resonances is clearly seen in the two dimensional energy-asymmetry space. Figure 17 shows a scatter plot for the separated beam events and for the off resonance data. The quantity E_{tot} is plotted on the vertical axis and the A_{sym} on the horizontal axis. Two regions are populated by the cosmic rays. The first region is at a total energy of $\simeq$420 MeV and a range of asymmetry values between 0.0 and 0.4 corresponding to cosmic rays traversing the center of the detector. The second region is at a total energy of $\simeq$600 MeV and at a larger asymmetry of 0.5 to 0.9. These are cosmic rays with trajectories missing the hollow inner dome of the detector. Their longer flight path in the NaI results in a heavier energy deposition. Also evident are energetic showering cosmic rays, most of which are highly asymmetric. The beam gas events are concentrated in the region $E_{tot} < E_{beam}$, since they result from a single beam particle. They cover a wide range of asymmetry. Both backgrounds are seen to contribute a small contamination in the 1-2 GeV, moderate asymmetry portion of the plot, which is within the hadronic event selection window.

The two dimensional energy-asymmetry decision function was chosen to strongly suppress the backgrounds. It can be seen as the curve and lines drawn on the scatter plot. The selection function was scaled by the beam energy to accomodate both the J/ψ and ψ' data. For comparison, the unselected resonance data is shown in Figure 18. The hadronic signal is centered in the region 2-3 GeV and $A_{sym} < 0.4$. Also evident is the strong showering QED signal at $E_{tot} = 2E_{beam}$ and $A_{sym} < 0.1$. Table 6 summarizes the explicit form of the final energy-asymmetry cut.

Approximately 1% of the retained events were found to have been triggered by the NIM trigger alone. A single energy cut was found to be sufficient for selecting a clean sample of these events. In addition, ψ' events from the 1981 data acquisition which failed the selection cuts were kept anyway if they contained the inclusive process $J/\psi \rightarrow \ell^+\ell^-$. This contributed an additional $\simeq 2\%$ to the retained data sample, mostly from $\psi' \rightarrow \pi\pi J/\psi \rightarrow \pi\pi\mu^+\mu^-$, which were otherwise removed by the energy-asymmetry cut.

Figure 17: Energy-Asymmetry Plot for Background.
The top figure (a) shows the distribution of separated beam events in
the two dimensional energy-asymmetry space used for the selection of
hadronic decays. The cut is indicated by the drawn curve and lines.
The bottom figure (b) is the same distribution for off- resonance data.
Note the concentration of QED events at high energy and low asymmetry,
with a tail leading to lower energies and higher asymmetries due to the
tunnel crystals being included in the trigger energy summation.
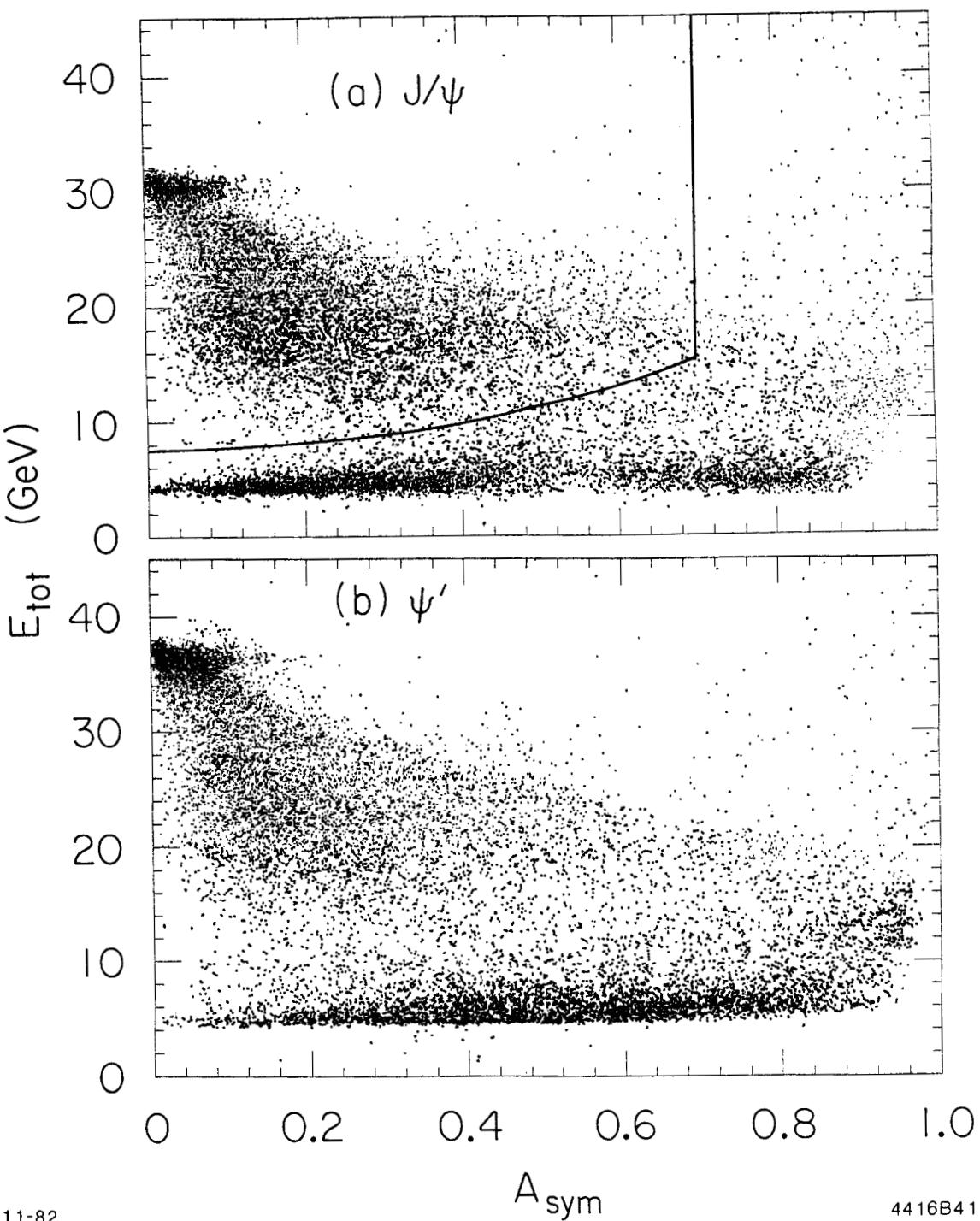
Figure 18: J/ψ and ψ′ Energy-Asymmetry Scatter Plots.
The energy-asymmetry distributions for J/ψ and ψ′ colliding beam data is shown in the top (a) and bottom (b) figures respectively. The drawn curve and lines indicate the cut chosen to optimize the rejection of backgrounds and the acceptance of hadronic decays.

11-82

4416B41

TABLE 6

Beam Gas and Cosmic Ray Event Rejection Criteria
The typically low energy and/or highly asymmetric background events were
removed with the following cuts. Different cuts were applied to those
events which triggered the NIM trigger and not the tower trigger. They
contributed $\leq$ 1% to final selected event sample.

REJECTION CRITERION

Events Triggered by the Tower Trigger, <u>and</u>:
  1) $A_{sym} > 0.7$, <u>or</u>
  2) $E_{tot} < 0.4888 \cdot E_{beam} \cdot [1 + (A_{sym}/0.7)^{2.02}]$.
Events not Triggered by the Tower Trigger, <u>and</u>:
  1) $E_{tot} < 0.8 \cdot E_{beam}$.

3.5   QED SUBTRACTION

The showering class of QED events can be seen populating the upper
left hand corner of Figure 18(a).   This area is also populated by any
channel with all gammas and/or electron-positron pairs in the final
state, as well as $\psi' \to \pi^+\pi^- J/\psi \to \pi^+\pi^- e^+ e^-$. Of primary concern was
rescuing of the channel $\psi' \to \gamma\gamma J/\psi \to \gamma\gamma e^+ e^-$ from the the QED cut while
still retaining a high efficiency for removing radiative showering QED
events. Of secondary importance was the retention of the $\psi' \to \pi\pi e^+ e^-$
channel as an important contribution to the inclusive decay sample.
Table 7 summarizes the tuned cuts which accomplished this goal.   About
98.3% of the QED Monte Carlo generated $J/\psi \to 3\gamma$ events were rejected,
while only about 7% of the $\psi' \to \gamma\gamma e^+ e^-$ data sample were cut.   The cut
also removed about 25% of the $\pi^+\pi^- e^+ e^-$ data sample.   The efficiency for
accepting some exclusive decay channels, like $J/\psi \to \gamma\pi \to \gamma\gamma\gamma$, was
drastically reduced.

The showering QED class of events would generally be expected to have
$E_{tot} = 2E_{beam}$.   However, there is a small subclass with E_{tot} as low as

$0.7E_{beam}$ due primarily to shower leakage into the empty tunnel region of the detector when one of the energetic e^+ or e^- particles strikes a tunnel boarder module. These events were detected when the tunnel boarder crystals were included in the trigger hardware energy summations and were removed by the QED cut.

The quantity $x = E_{track}/E_{beam}$ was used as the basic parameter in the search for the remaining radiative QED triggers. Events having ≥ 3 tracks with $x > 0.5$ were rare, comprising $\approx 0.1\%$ of the unselected data sample. A hand scan of these events revealed that they were mostly $e^+e^-\gamma$ with a hard radiative γ. These events were cut. Events having 2 tracks with $x > 0.5$ and a multiplicity of 3 were removed, since an examination showed that they were dominated by $e^+e^-\gamma$ and $\gamma\gamma\gamma$ radiative QED processes. This cut removed about 75% of the QED 3γ Monte Carlo events and did not fit the topology for $\gamma\gamma e^+e^-$ or $\pi\pi e^+e^-$. The remaining two cuts [3) and 4) in Table 7] were designed to suppress both the hard and soft radiative QED processes where the energetic showers fluctuated sufficiently to produce two or more bumps as recognized by the bump discriminator algorithm.

TABLE 7

QED Event Rejection Criteria.

QED events were removed from the data sample with the following set of cuts. Note that all the two track final states in the QED event class will have been removed by the the preliminary cuts listed in Table 5. The cuts here are designed to remove the radiative QED events. For each track the quantity $x = E_{track}/E_{beam}$ is calculated. The quantity $\sum x_{(x<0.5)}$ is the sum of x for each track with $x < 0.5$. The quantity $x_{max(x<0.5)}$ is the track with the largest $x < 0.5$.

REJECTION CRITERIA

$E_{tot} > 0.7 \cdot E_{beam}$, and:
1) ≥ 3 Tracks have $x > 0.5$, or,
2) 2 Tracks have $x > 0.5$, and the multiplicity is 3, or,
3) 1 or 2 Tracks have $x > 0.5$, and $\sum x_{(x<0.5)} < 0.12$, or,
4) 1 or 2 Tracks have $x > 0.5$, and $\sum x_{(x<0.5)} - x_{max(x<0.5)} < 0.04$.

3.6 RESULTS

The number of events surviving the data selection (N_{obs}) amounted to $\simeq 1.8 \cdot 10^6$ each for both J/ψ and ψ'. Some of these events are due to background triggers not entirely removed by the selection process. The contamination due to cosmic ray events was easily measured by examining the trigger timing relative to the beam cross signal, since cosmic rays were entirely asynchronous and produced a flat background beneath the hadronic signal. The beam gas contamination could not be measured in this way as it was in time with the beam cross. Two estimates of the beam gas contamination were made using information from the separated beam data. The number of retained background events which were in time with the beam cross were scaled by their beam currents and live time up to the full resonance data samples. This gave one estimate of the beam gas contamination. A second estimate used the ratio of the number of kept background events to the number of rejected background events

populating the high asymmetry-low energy portion of the scatter plot which were in time with the beam cross. Since it is virtually devoid of hadronic final states, this region was used as a monitor of the number of beam gas events contaminating the full resonance data samples. Both estimates gave similar values. The QED contamination was estimated by multiplying the ratio of the number of Monte Carlo 3γ events passing the selection cuts to the number removed, by the total number of 3 or more track QED events cut from the full resonance data samples.

To calculate the number of produced resonances the background contaminations were subtracted and a correction was included for the selection inefficiency. The latter factor was composed of two parts: i) a term for inclusive hadronic decays and ii) a term for the leptonic decays of J/ψ and ψ'. The non-resonance backgound was calculated using the formula,

$$N_{nonres} = R \cdot \sigma(e^+e^- \rightarrow \mu^+\mu^-) \cdot \int Ldt \qquad (III-5)$$

where $R = 2.4 \pm 0.3$ is the measured[6] ratio of cross sections, $\sigma(e^+e^- \rightarrow hadrons)$ to $\sigma(e^+e^- \rightarrow \mu^+\mu^-)$, off resonance, and $\int Ldt$ is the total integrated luminosity. This number is necessarily subtracted from the corrected number of hadrons. The following formula was used for the calculation.

$$N_{prod} = \frac{\left\{ \dfrac{(N_{obs} - N_{cosmic} - N_{beam} - N_{qed})}{\epsilon} - N_{nonres} \right\}}{1 - B(Res \rightarrow \ell^+\ell^-)} \qquad (III-6)$$

Where N_{prod} is the number of produced resonances, N_{cosmic}, N_{beam}, N_{qed}, and N_{nonres} are the numbers of retained background events, ϵ is the inclusive hadronic decay selection efficiency determined from Monte Carlo, and $B(\text{Res} \rightarrow \ell^+\ell^-)$ is the resonance branching ratio to lepton pairs. Table 8 summarizes the value for each term in Equation III-6 for J/ψ and ψ'.

TABLE 8

Resonance Subtraction and Correction Factors
An explanation of the terms is given in the text. Also see equation III-6.

RESONANCE	ϵ ±5%	$B(\text{res} \rightarrow \ell^+\ell^-)$ Ref. 6	N_{obs} (	N_{cosmic}	N_{beam} $\cdot 10^3$	N_{qed}	N_{prod})
J/ψ	0.941	0.148	1779	10	3	2	2180
ψ'	0.944	0.017	1753	13	8	5	1806

RESONANCE	$\int L dt$ (nb^{-1})	N_{nonres} $(\cdot 10^3)$
J/ψ	768	17
ψ'	3452	53

The net inefficiency for selecting hadronic decays of the J/ψ and ψ' resonances amounted to $\approx 6\%$. About 1% each was due to the trigger inefficiency and to the QED cut. The remaining $\approx 5\%$ was due to the energy-asymmetry cut. A cross check was made by monitoring the number of π^0's found in the $\gamma-\gamma$ mass distribution for the rejected events. Both the data and the Monte Carlo agreed, yielding about 0.008 π^0's cut per hadronic event retained. This suggests that hadronic events failing the selection cuts are dominated by a low π^0 multiplicity (≈ 0.16).

REFERENCES

1. R. Partridge, Crystal Ball memo CB-NOTE 6 (1979).

2. A. Liberman and F. Bulos, Crystal Ball memo CB-NOTE 233 or 127 (1977).

3. The PCORR algorithm was developed by J. Tompkins and a description may be found in: M. Oreglia, Ph.D. thesis, Stanford University Report No. SLAC-236, 1980 (unpublished).

4. The photon direction finding algorithm, called SHOWER, was written by T. Burnett, and was not the standard production analysis photon tracking routine.

5. M. Oreglia et al., Phys. Rev. D25, 2259 (1982). This is the data sample prepared by M. Oreglia in his study of the decays $\psi' \rightarrow \gamma \chi_J \rightarrow \gamma \gamma J/\psi$ and $\psi' \rightarrow X J/\psi \rightarrow \gamma \gamma J/\psi$, where the X is either an η or a π^0.

6. M. Aguilar-Benitez et al., "Review of Particle Properties," Phys. Lett. 111B, April (1982).

Chapter IV

INCLUSIVE PHOTON DATA ANALYSIS

4.1   INTRODUCTION

The primary goal of this study is to examine the inclusive photon

spectra observed in decays of the J/ψ and ψ' resonances. The previous

chapter dealt with the selection of a clean data sample. This chapter

will report on the fitting techniques and the results obtained from the

inclusive γ spectra. A preview of the main features in this

investigation is presented in Figure 19, showing a final inclusive

photon spectrum from ψ' decays. Radiative transitions to all the lower

lying charmonium states, except the $^1P_1$ state, are readily apparent.

The analysis breaks down into several tasks listed below, and more

fully described in the following sections.

1) Based on the crystal and track information for each entry in the
    track bank, how are photons to be defined? The Crystal Ball
    detector provides a lot of information about each photon candidate.
    In order to check the bias associated with the photon selection
    criteria, several widely different criteria were used and the final
    results were compared.
2) Since all the experimental measurements are to be derived from the
    spectra, what is the best way to fit them? In particular this
    amounted to determining what information is known and may be fixed
    in the fitting process, and what parameters are to be measured and
    allowed to vary in the fit.
3) To extract branching ratios from the fitted signals it is necessary
    to measure the efficiency for observing the particular decay being
    studied. What is the best method available for determining the
    photon detection efficiency in this experiment? Does the determined
    efficiency have a bias depending on the photon selection criteria?
4) As seen in Figure 19, all the signals sit on top of a large
    continuum. How can the bias associated with the photon background
    be checked?
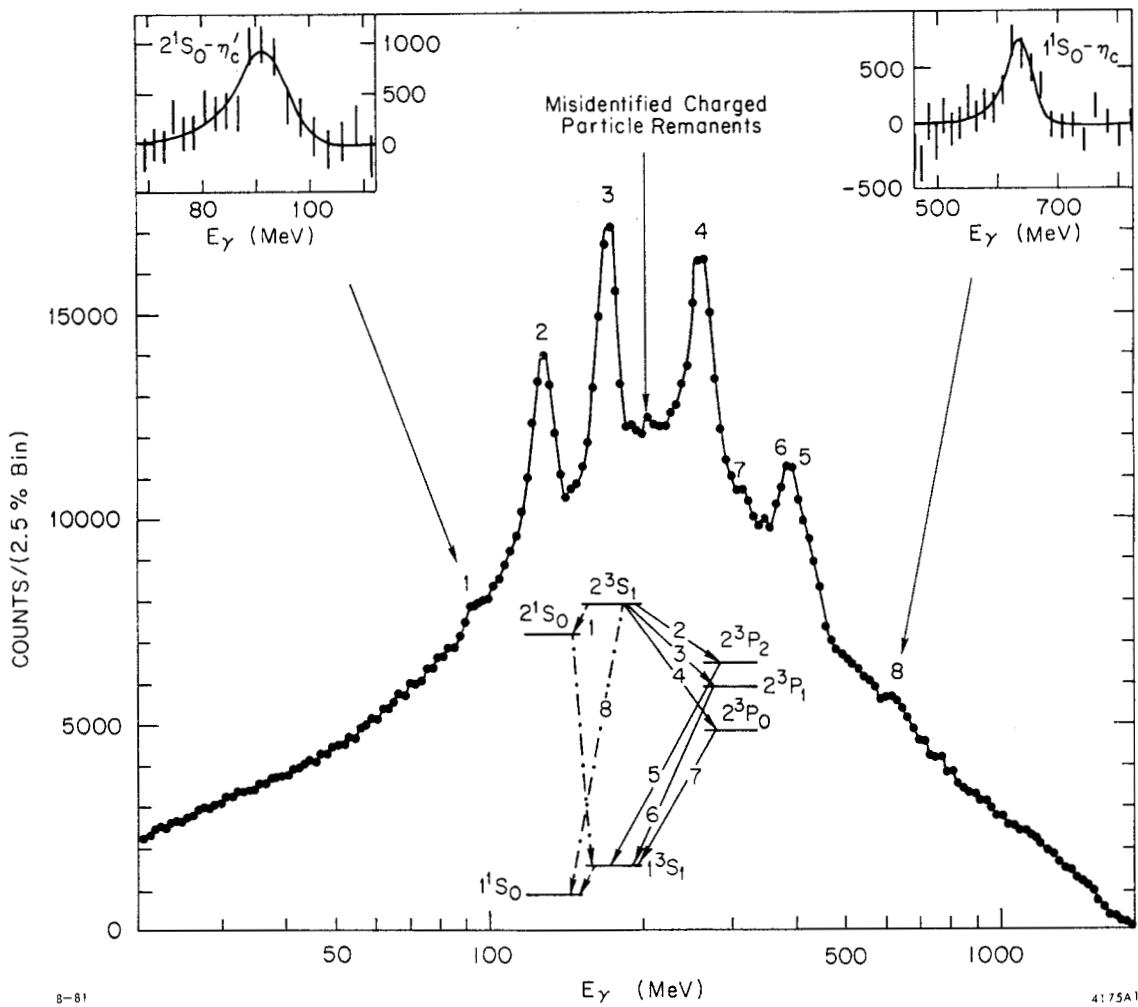
Figure 19: A Preview of the Ψ′ Spectrum

The charmonium level scheme and observed transitions are shown in the diagram. The numbers above the signals correspond to the transitions indicated. Local fits to the pseudoscalar states are shown in the insets. This spectrum resulted from roughly half of the available data sample.

4.2   PHOTON SELECTION CRITERION

4.2.1 $\psi' \rightarrow \gamma\chi_J$ and $\chi_J \rightarrow \gamma J/\psi$

To check the impact of the photon selection process and it's interaction with the background shape on the resulting branching ratio and natural line width measurements, a variety of neutral track selection criteria (cuts) were used. For the transitions $\psi' \rightarrow \gamma\chi_J$ and $\chi_J \rightarrow \gamma J/\psi$, the study was done with four spectra, shown in Figures 20(a)-(d). These spectra result from the application of successively tighter requirements on the particle selection spanning the range from virtually no cuts to a full range of cuts designed to remove backgrounds and enhance the signals. A description of these cuts follows:

A) Figure 20(a) contains a spectrum of all tracks, whether called neutral or charged by the analysis programs. The only requirement is that $|\cos\theta_{track \cdot z}| < 0.85$. The angle $\theta_{track \cdot z}$ is the angle between the track and the positron direction. Figure 21 shows the distribution for $\cos\theta_{track \cdot z}$ and indicates the cut used. As mentioned earlier, this solid angle cut ensures that the particle energy is not degraded by edge effects near the tunnel regions in the central NaI(Tl) detector. The most prominent feature in this spectrum is the enormous peak at $\simeq 210$ MeV produced by minimum ionizing charged particles traversing the 16 L_{rad} of NaI(Tl). Here the transitions to and from the χ_J states appear only as shoulders above a huge background of mainly charged particles and photons. These shoulders however, are highly significant and measurable, as

will be seen below. For reference, inclusive charged particle spectra are shown in figures at the end of Appendix E.

B) In the second spectrum, Figure 20(b), charged particles are removed using information from the central tracking chambers. Only a small remnant of the telltale minimum ionizing peak remains, as evidence of the inefficiency in the central chambers.

C) Figure 20(c) shows the third spectrum containing two additional requirements on the photon selection. Using the entire acceptance of the detector, including end caps, all the neutrals in each event which reconstruct globally to $\pi^0 \to \gamma\gamma$ decays are removed (see Appendix D). This considerably reduces the number of background gammas in the spectrum. However, about half the time the π^0 subtraction algorithm removes non π^0 gammas, so there is also some loss in the signals. The second cut removes neutrals too close to charged particles which interact or shower (the cosine of the opening angle must be < 0.85). A bulge below $\simeq 50$ MeV due to split-off fragments from hadron-nuclear interactions in the detector is clearly seen (see Appendix E). These split-offs are frequently far enough away from the parent charged particle to escape charge tagging and the opening angle cut mentioned above. Figure 22 shows the distribution for $\cos\theta_{neutral \cdot interacting\ charge}$ and the cut at 0.85 applied.

D) The fourth spectrum, Figure 20(d), includes a pattern cut on the lateral shower energy deposition of the particle (see Appendix E). Those neutrals retained are required to have an energy depositon pattern typical of single photon showers in the NaI(Tl). The cut is sufficiently stringent to remove virtually all the remaining minimum

ionizing charged particles, as seen by the absence of the peak at $\simeq 210$ MeV. Compared to the other three spectra this cut has dramatically enhanced the signal to noise. The χ_J transitions are seen as sharp peaks on a much gentler background. The $\psi' \rightarrow \gamma \eta_c$ transition is now clearly visible at $E_\gamma \simeq 640$ MeV.
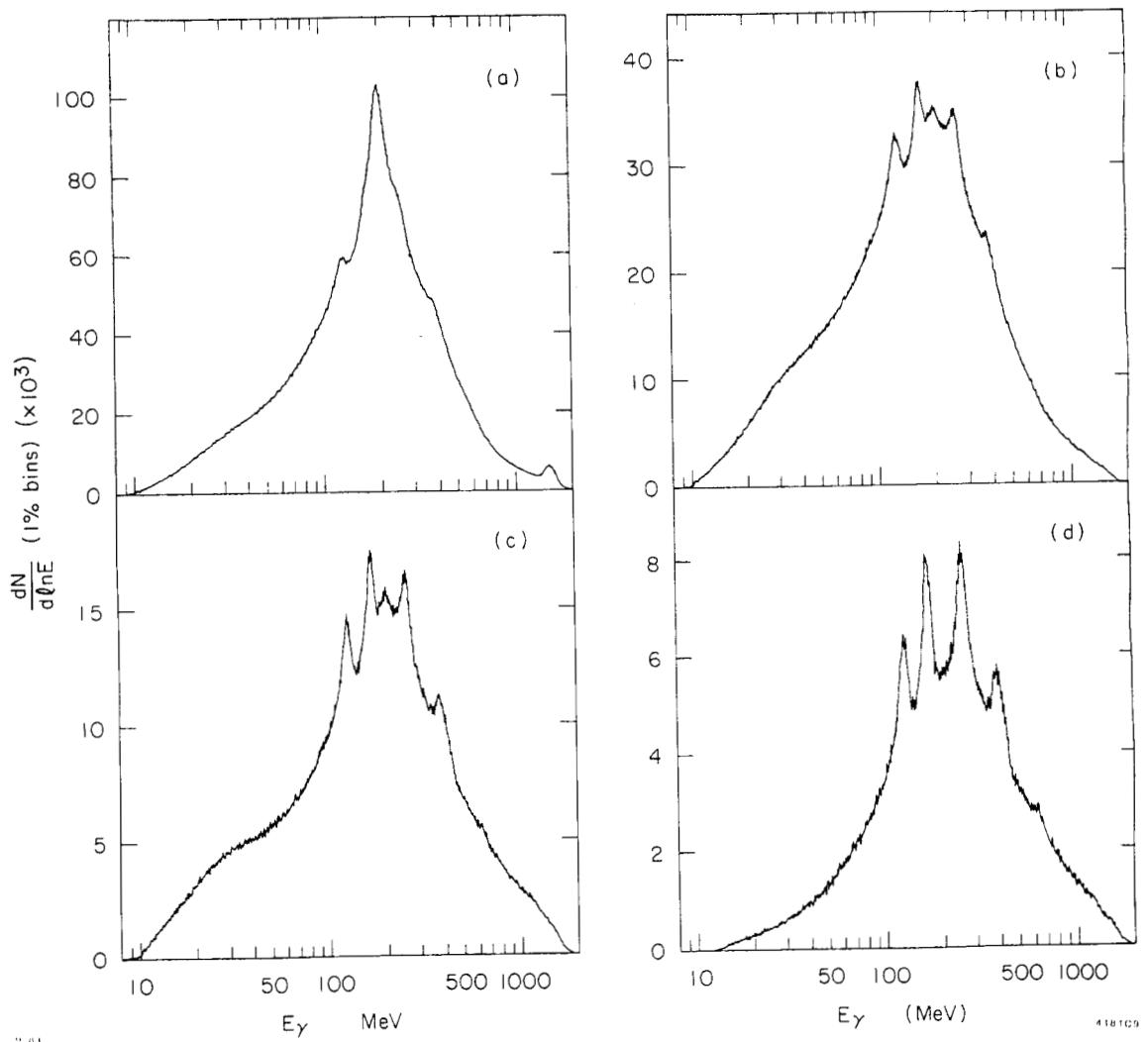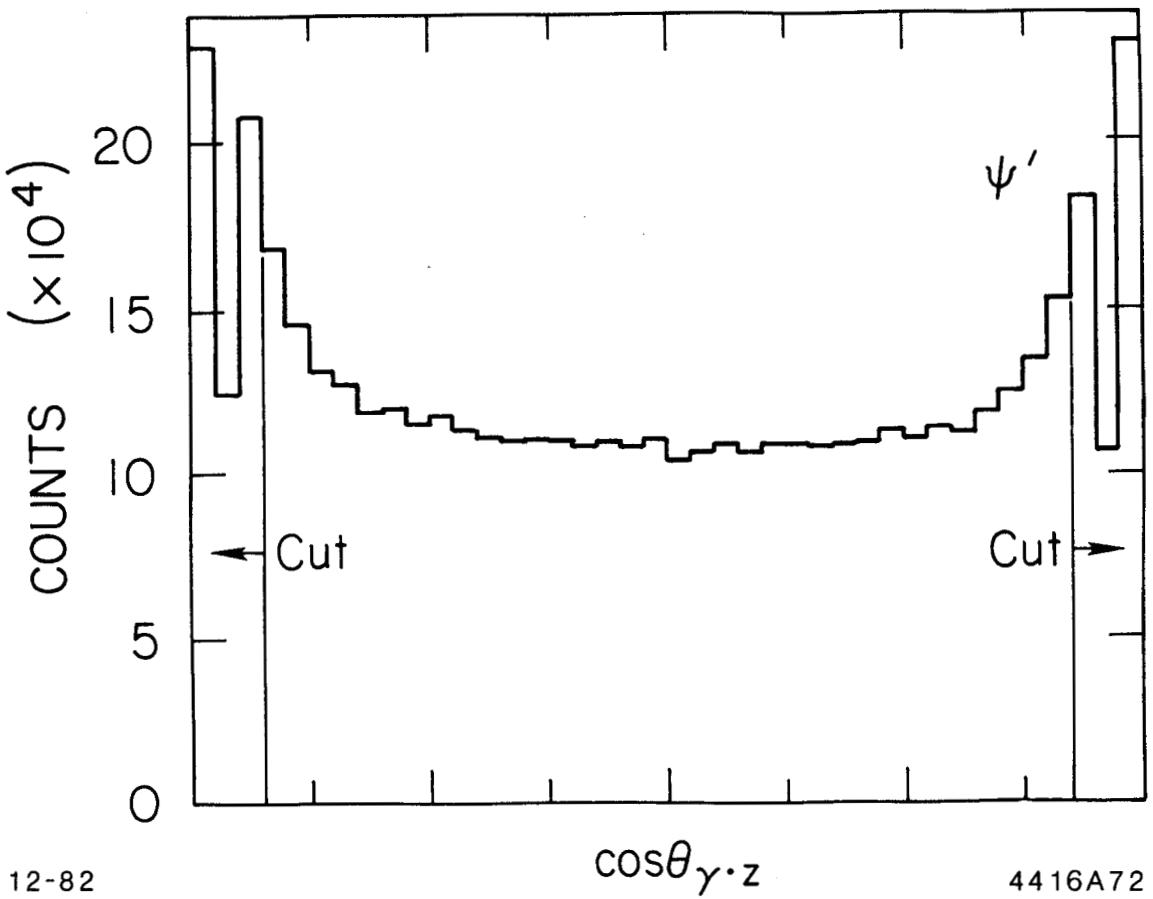
Figure 20: A)-D) Ψ' Inclusive Photon Spectra.
In figure (a) the particle energy E_{track} is plotted for all tracks with $|\cos\theta_{track\cdot z}| < 0.85$ in 1% energy bins. In figure (b) the energy is plotted for each particle identified as a neutral by the central tracking chambers, in addition to the solid angle cut used in (a). The inclusive γ spectrum, after subtracting γ-γ pairs which reconstruct to a π^0 mass, is shown in figure (c). In addition, neutrals too close to interacting charged particles are removed. Figure (d) shows the γ spectrum with pattern cuts applied to remove non-photon like showers, in addition to the cuts used in the previous figures. The best signal to noise ratio is achieved here.
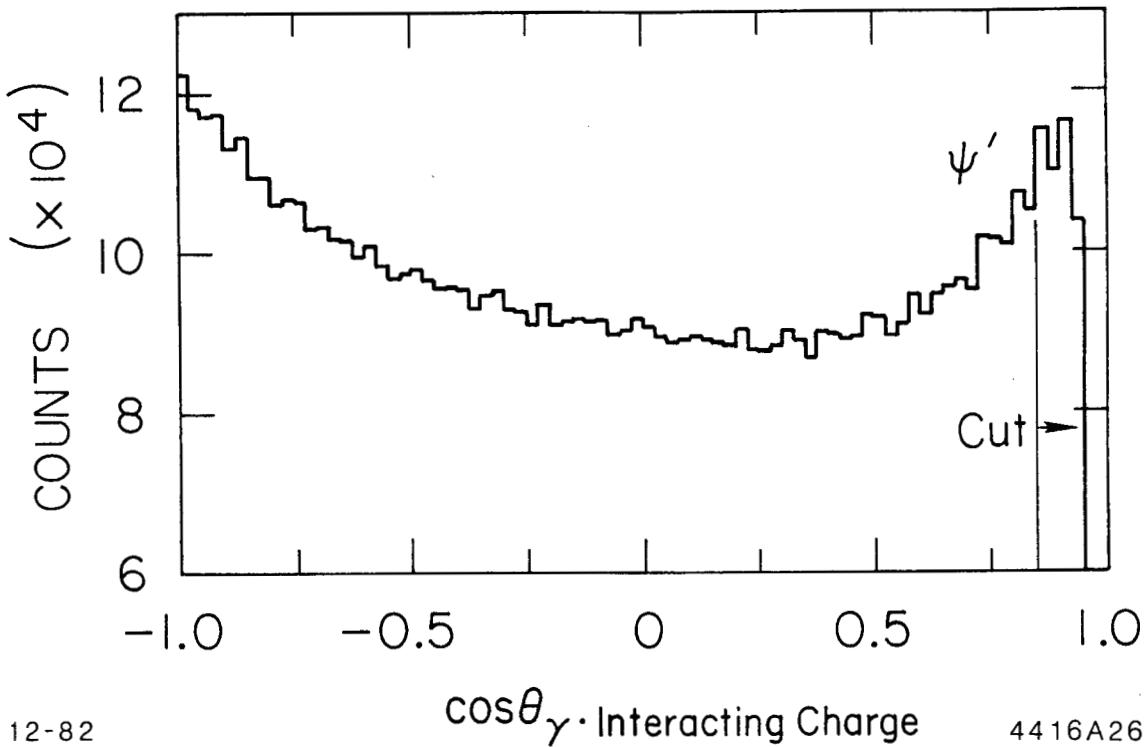
Figure 21:   Inclusive Neutral Angular Distribution
The distribution of $\cos\theta_{track \cdot z}$ for all the neutrals identified by the
central and end cap tracking chambers is plotted. The angle $\theta_{track \cdot z}$ is
the polar angle between the track and the $+z$ axis (e^+ direction).   The
rise in the distribution towards $\cos\theta = +1$ and -1 is due to a decrease
in the charged particle identification efficiency in these regions.   The
symmetric dips in the distribution within both cut regions result from a
lowered particle acceptance in the spaces between the end cap NaI and
the Ball NaI.

Figure 22: Neutral-Interacting Charged Particle Opening Angle.
The cosine of the opening angle between each neutral and each
interacting charged particle is plotted. Interacting charged particles
are identified by their lateral energy deposition pattern, as discussed
in the text, and in Appendix E. The acceptance is 0. for $\cos\theta > 0.95$,
which is the particle resolving limit for the bump discriminator
algorithm. The rise in the distribution for $\cos\theta > 0.5$ is at least
partially due to clustering of hadron-nuclear fragments, identified as
neutrals (split-offs), near the interacting charged particle. The
gentle increase for $\cos\theta < 0.0$ may be due to a phase space bias
associated with the charged particle direction.

4.2.2 $\psi' \to \gamma\eta_c(2984)$ and $J/\psi \to \gamma\eta_c(2984)$

The radiative transitions to the $\eta_c(2984)$ candidate state from ψ' and J/ψ were studied with three photon selection criteria to evaluate the sensitivity of the measured branching ratios and the η_c natural line width to the cuts and the background shape. The same set of cuts, B) and C), as described above for ψ' were used here. Also the pattern cut D) was divided into two parts, only one of which was used here. Figures 23(a) and (b) correspond to Figures 20(b) and (c). Figures 23(c) and (d) show the J/ψ and ψ' spectra resulting from a partial application of the cut D). The selection is as follows:

B) Same as above.

C) Same as above.

E) The pattern cut described in D) above, removes a particle with a lateral energy distribution both too narrow to be a photon shower and too wide to be a single photon shower. The narrow energy deposition is typical of minimum ionizing charged particles which deposit their energy in only a few crystals. That part of the cut was not applied here. Rather, in addtion to criteria A)-C), Figures 23(c) and (d) show the result of requiring that the particle showers merely not be too broad (see Appendix E). This has the effect of removing energetic π^0's ($E_\pi > 600$ MeV) where the showers from the decay γ's have merged, and is responsible for the improved signal to noise seen at the J/ψ spectrum end point. More important to the present application, interacting charged particles also tend to have broad energy patterns and are suppressed by this cut.

The η_c signal was also seen in spectra obtained by applying the cuts A)

and D).
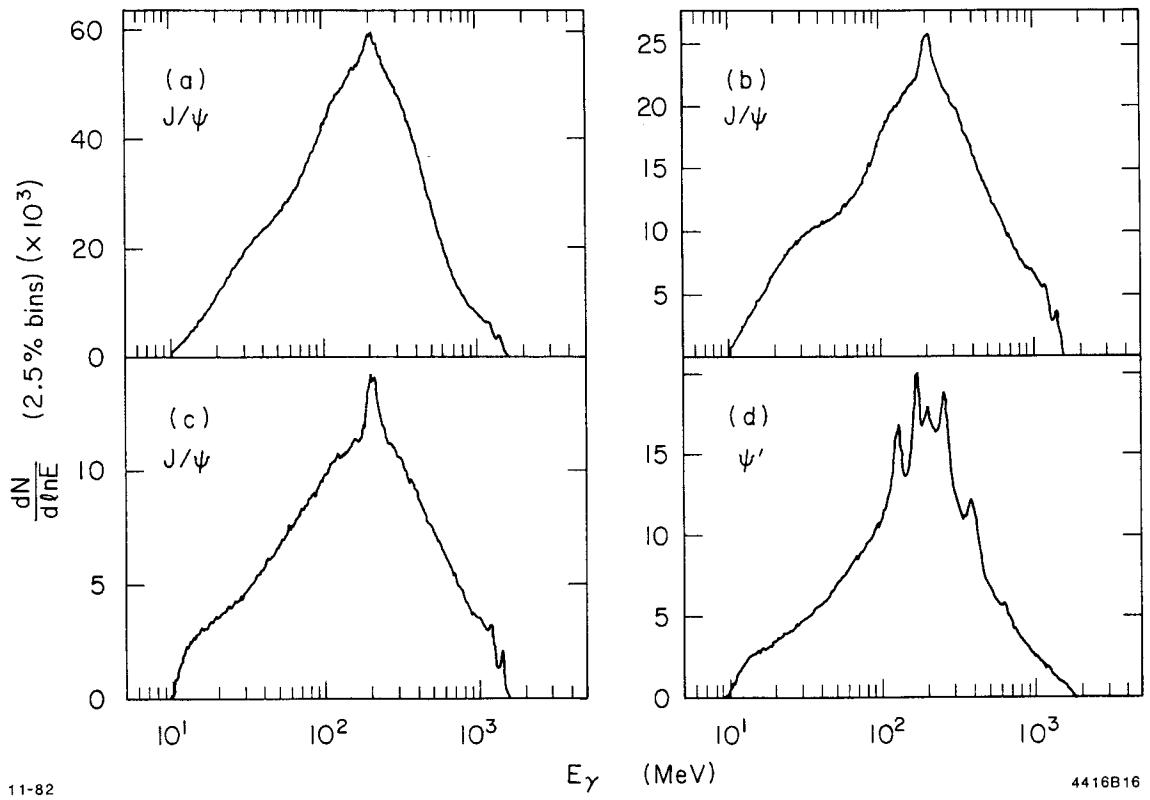
Figure 23: B), C), and E) J/ψ and ψ' Inclusive γ Spectra.
The J/ψ spectra (a) and (b) result from the same cuts as used for
Figures 20(b) and (c). Figures (c) and (d) show J/ψ and ψ' spectra
obtained by applying the pattern cut E) designed to remove energetic
π⁰'s as well as interacting charged particles. The removal of fast π⁰'s
especially enhances the end point structure as seen in the J/ψ spectrum.
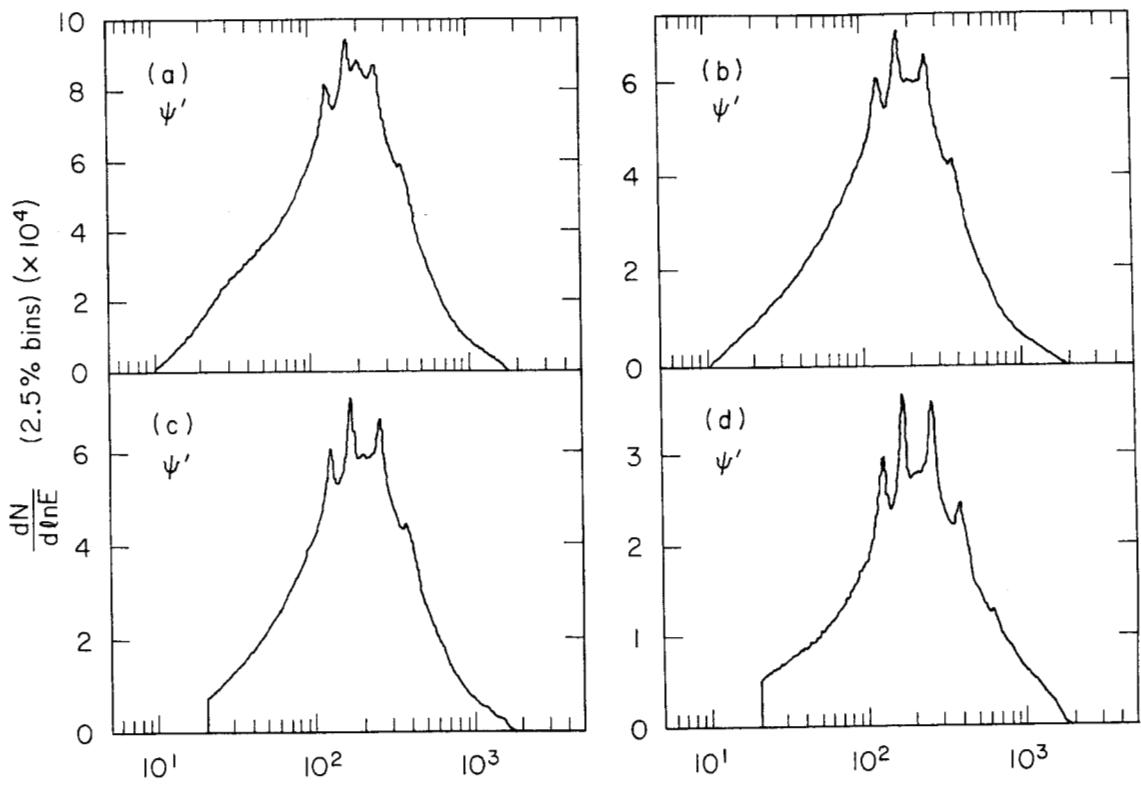
4.2.3 $\psi' \to \eta_c'(3592)$

Slightly different photon selection criteria were used for studying the $\eta_c'(3592)$ candidate state observed in the transition $\psi' \to \gamma\eta_c'$ at a photon energy of $\simeq 92$ MeV. The cuts are summarized here:

B) Same as above.

G) In addition to B) the particles were required to pass a pattern cut which rejected energy depositions too broad to be consistent with a single photon shower. The cut was similar to E), but less stringent. In the region of $E_\gamma \simeq 92$ MeV, this cut predominantly removed interacting charged particles, misidentified as photons. Neutral tracks too close to interacting charged particles were also removed if $\cos\theta_{track\cdot interacting\ charge} > 0.85.$

H) Instead of criterion G), and in addition to B), an alternate pattern cut was applied. Using a different parameterization for the lateral energy profile, a selection criterion similar to but milder than D), was used to suppress both interacting and minimum ionizing charged particles (see Appendix E). Neutral tracks too close to any charged particle were removed if $\cos\theta_{track\cdot charge} < 0.90.$

I) In addition to H), photon pairs reconstructing to a π^0 mass were removed, with the techniques described in Appendix D.

The four ψ' inclusive γ spectra resulting from the above selection criteria are shown in Figure 24 plotted in 2.5% energy bins. All the structure which was evident in the ψ' spectra previously shown, including the signal at $E_\gamma \simeq 636$ MeV due the η_c, is seen in these figures. Two factors are working together to bring out the additional

structure seen at $\simeq 92$ MeV: i) the coarse binning does not wash out the signal, and ii) the milder pattern cuts retain the excellent improvement in signal to background at $E_\gamma = 92$ MeV without severely lowering the efficiency.   No further significant structure, below the end point, is seen in the ψ' inclusive photon spectrum.

Figure 24: F)-I) Inclusive γ Spectra from ψ′ Decays: $\eta_c′$ Study. Four inclusive ψ′ photon spectra used in the analysis of the transition ψ′ → γ$\eta_c′$ are shown. The photon selection cuts are discussed in the text.

4.3 FITS TO THE INCLUSIVE PHOTON SPECTRA

The goal in fitting the spectra is to reliably measure the signal amplitudes, the peak photon energies, and the state's natural line widths. Of primary concern is the effect of the large underlying background on these measurements. Basically there are two approaches to fitting the signals: i) fit only the small local portion of the spectrum surrounding the signal, or ii) perform a global fit to a large portion of the spectrum. The global fit necessarily requires a detailed model for the background, taking into account contributions from misidentified charged particles, the broad photon continuum due to π^0 and $\eta \to 2\gamma$ decays, and the presence of additional photon signals due to near threshold production and decay of π^0's and η's. The latter complication results from the channels $\psi' \to \eta J/\psi$ and $\psi' \to \pi^0\pi^0 J/\psi$, where the phase space of the η's and π^0's are limited.

The shape of the signal itself depends on a variety of factors. First, if the transition is to a narrow state the monochromatic photon will be seen as the line shape response function of the Crystal Ball, with the intrinsic resolution of the apparatus. Studies of Bhabha events, $e^+e^- \to e^+e^-$, at $E_{beam} = 1.547$ Gev, have shown that the detector's response function to monoenergetic showering particles can be adequately described by a Gaussian and a power law tail to low energies, starting at $\simeq 1$ sigma below the peak and joined to the Gaussian with continuous first derivative. If either the parent or the recoil state is broad, the signal will be widened by the Breit-Wigner mass distribution of the broad state, and the line shape will be modified by

the convolution process. In the transition $\chi_J \rightarrow \gamma J/\psi$, the parent state is also Doppler shifted. The corresponding signal shape must reflect the resulting Doppler broadening. Finally, the photon energy dependence in the dipole transition matrix element to wide states (like E_γ^3 for allowed E1 and M1 transitions or E_γ^7 for forbidden M1 transitions) must be included in the convolution integral and will slightly shift the photon signals to a higher energy. A detailed discussion of the detector's intrinsic line shape and the result of folding it with the various broadening and shifting functions may be found in Appendix F.

4.3.1 $\psi' \rightarrow \gamma \chi_J$ and $\chi_J \rightarrow \gamma J/\psi$

For the complicated χ_J state transitions shown in Figures 20(a)-(d), a global fit was made to the photon energy region, 65 MeV < E_γ < 600 MeV. These spectra, with their crowded and overlapping signals sitting on top of a broad thrusting background, became the crucible for cross-checking the entire fitting analysis.

In fitting the signals, the form of the detector's response function was fixed, although the two parameters specifying the joining position and the power law (see Appendix F) were determined globally from the fit. The three χ_J states were assumed to have non-zero widths described by a non-relativistic Breit-Wigner resonance shape. The width of the Breit-Wigner distribution was determined by the fit. The transition matrix elements for the χ_J transitions was taken to be dominantly electric dipole,[1] leading to an E_γ^3 energy dependence in the folded signal shape. The photon peaks and signal amplitudes for the $\psi' \rightarrow \gamma \chi_J$ transitions were also determined from the fit. However, the gamma

energies were fixed for the $\chi_{1,2} \rightarrow \gamma J/\psi$ transitions based on the $\chi_{1,2}$

masses determined from the initial ψ' transition and the masses[2] of the

ψ' and J/ψ. The Doppler broadening (due to the recoil of the $\chi_{1,2}$) was

fixed, based on the gamma energy in the primary transition from $\psi' \rightarrow$

$\gamma\chi_{1,2}$. No signal corresponding to $\chi_0 \rightarrow \gamma J/\psi$ has been observed in the

inclusive photon spectra. The transition has been measured in the

exclusive analysis of cascade decays,[1] but is below the sensitivity of

this study.

Three sources of background to the spectra were included in the fits:
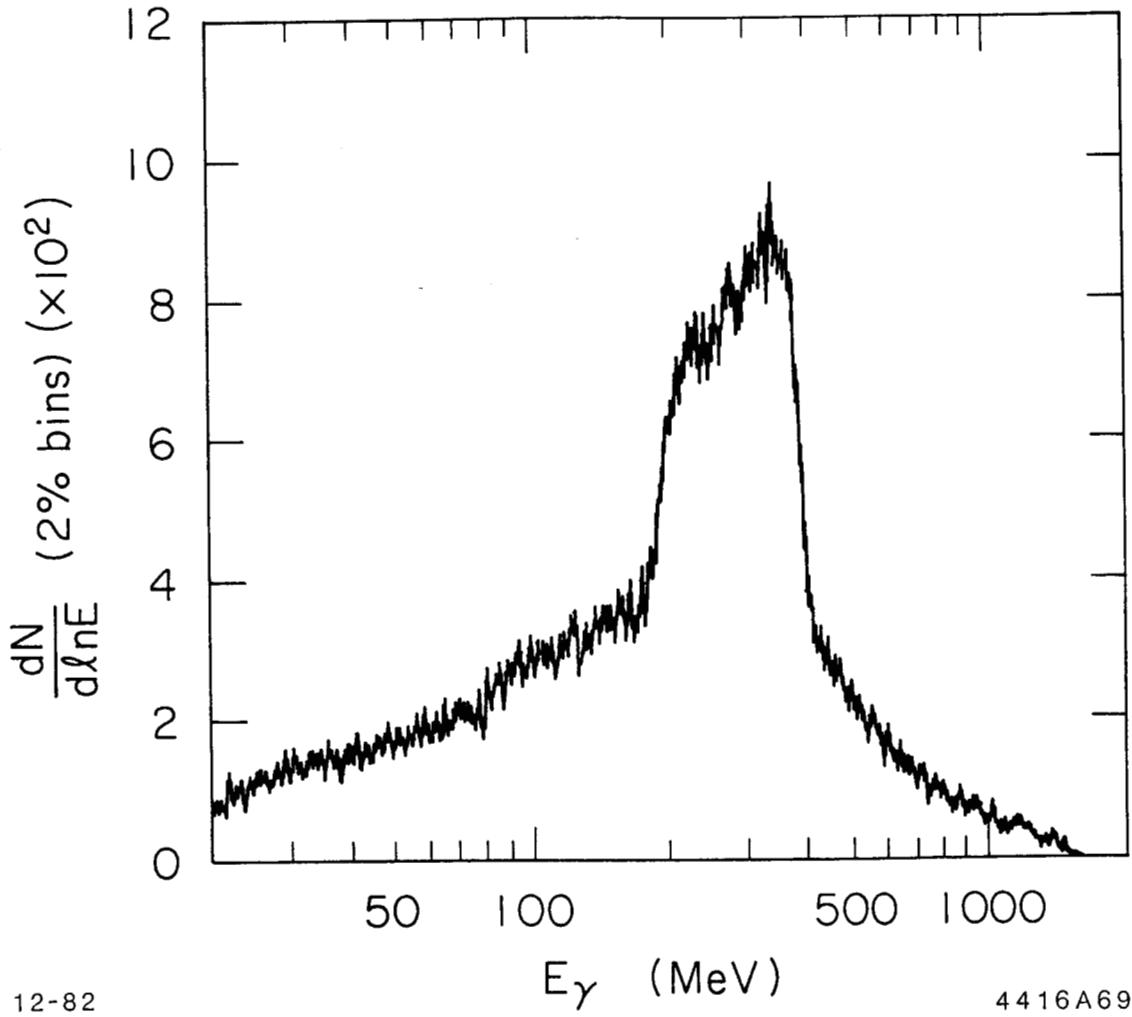
i) The charged particle contribution was taken into account, by

including in the fit the shape of the charged particle spectrum (see

figures at the end of Appendix E). The charged particle spectrum

was prepared by plotting the energy of only reconstructed charged

particle tracks passing through both central magnetostrictive spark

chambers (well-defined charged particles). Each background

spectrum, from which the background shapes were derived, was

tailored by applying the appropriate selection criteria for the γ

spectrum being fit. During the fitting, the charged particle

background shape was fixed and it's amplitude was allowed to vary.

ii) The shape of the photon contribution from the decay $\psi' \rightarrow \eta J/\psi$

$\rightarrow \gamma\gamma J/\psi$ was determined by a Monte Carlo calculation and is shown in

Figure 25 (also see Appendix C). Monochromatic η's were generated

and allowed to decay to $\gamma\gamma$. The photons were propagated through the

apparatus geometry using the EGS (electron-gamma-shower) program.[3]

The resulting Monte Carlo data was added to real J/ψ events (one η

per J/ψ), to simulate the decay $\psi' \rightarrow \eta J/\psi$. The background spectrum

shape was plotted from these simulated events. In fitting the inclusive γ spectra, the amplitude for this background was held fixed, based on the known branching ratio[1] $B(\psi' \rightarrow \eta J/\psi) = (2.18\pm0.38)\%$, and the measured number of background γ's per event. The background photons resulting from the decay $\psi' \rightarrow \pi^0\pi^0 J/\psi$ were found to have a negligible effect on the fitted signal amplitudes and natural line widths, and were not included.

iii) The remaining broad photon background was assumed to be smooth and was fit with a sum of Legendre polynomials. The fits to the spectra in Figures 20(a)-(c) used fourth order polynomials, while the fit to the spectrum in Figure 20(d) needed a fifth order polynomial.

Figure 26 shows the final fits to the ψ' inclusive photon spectra and to the χ_J transitions. The χ^2 confidence levels ranged from 12%-52%, indicating that the signal shapes and backgrounds are consistent with the data. Table 9 summarizes the resulting signal amplitudes and natural line widths, along with their statistical errors from the fit.

As a cross check on the background model and it's possible interplay with the large χ_J transitions, a similar global fit was made to the transition $J/\psi \rightarrow \gamma\eta_c$ in the J/ψ inclusive photon spectrum. The J/ψ spectrum, which does not contain such large signals nor the complex structure as in the ψ' spectrum, provides an excellent test of the background hypothesis. Only background contributions due to i) and iii) above were included in the fit. The background charged particle shape was obtained from a spectrum of well-defined charged particles in J/ψ decays. Figure 27 shows the resulting fits to the J/ψ photon spectra obtained using selection criteria A) and D). The fitted background

Figure 25: B) Monte Carlo Derived Photon Spectrum for $\psi' \rightarrow \eta J/\psi$.
A Monte Carlo generated γ spectrum for the process $\psi' \rightarrow \eta J/\psi \rightarrow \gamma\gamma J/\psi$, obtained from $\simeq 12.4 \cdot 10^3$ events and using the photon selection criterion B) is shown.
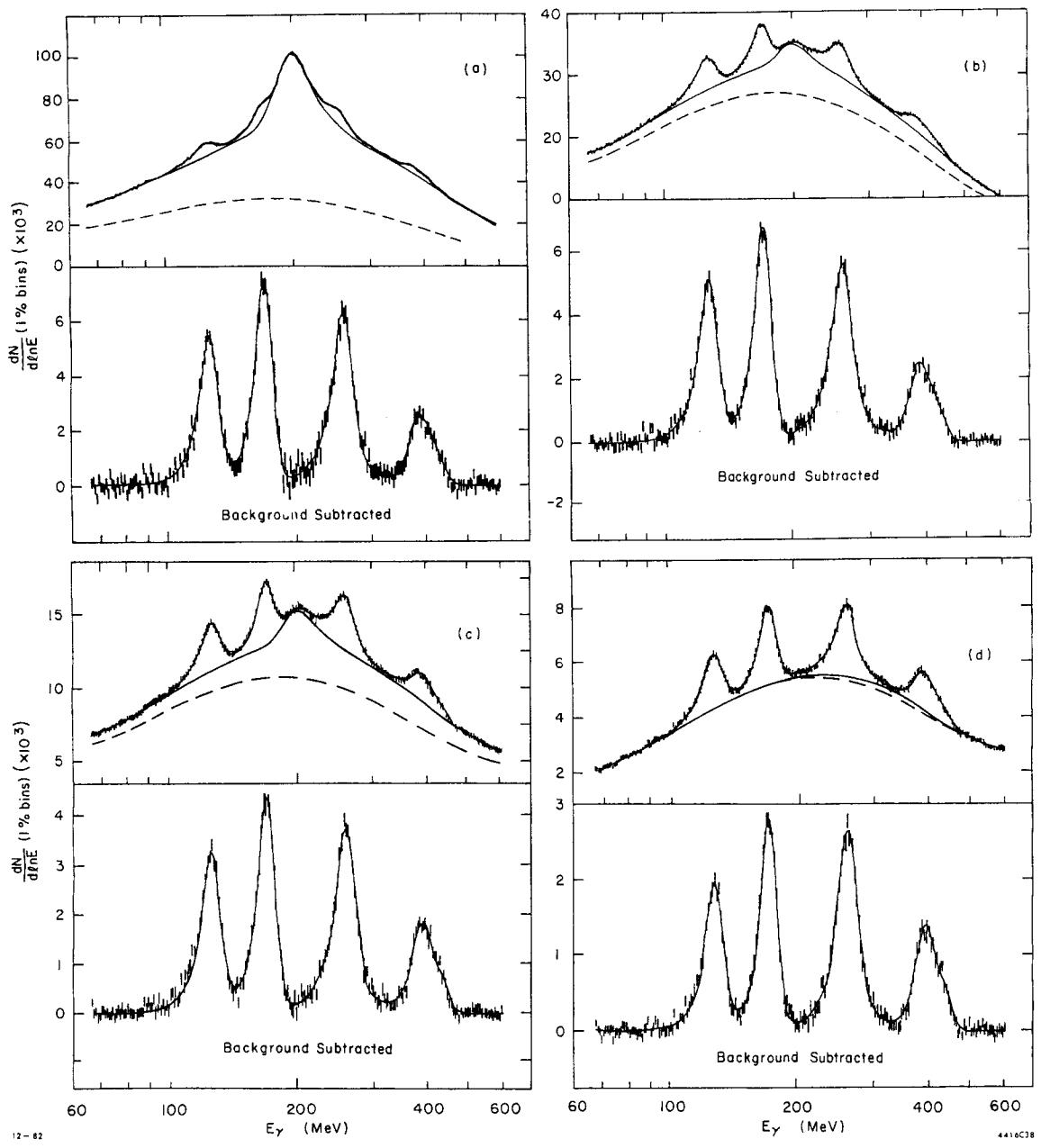
Figure 26: A)-D) Fitted ψ' Inclusive Photon Spectra.
The four ψ' inclusive photon spectra shown in Figures 20(a)-(d), are fit
with the techniques described in the text.   The bottom portion of each
figure shows the result of subtracting the fitted background.

TABLE 9
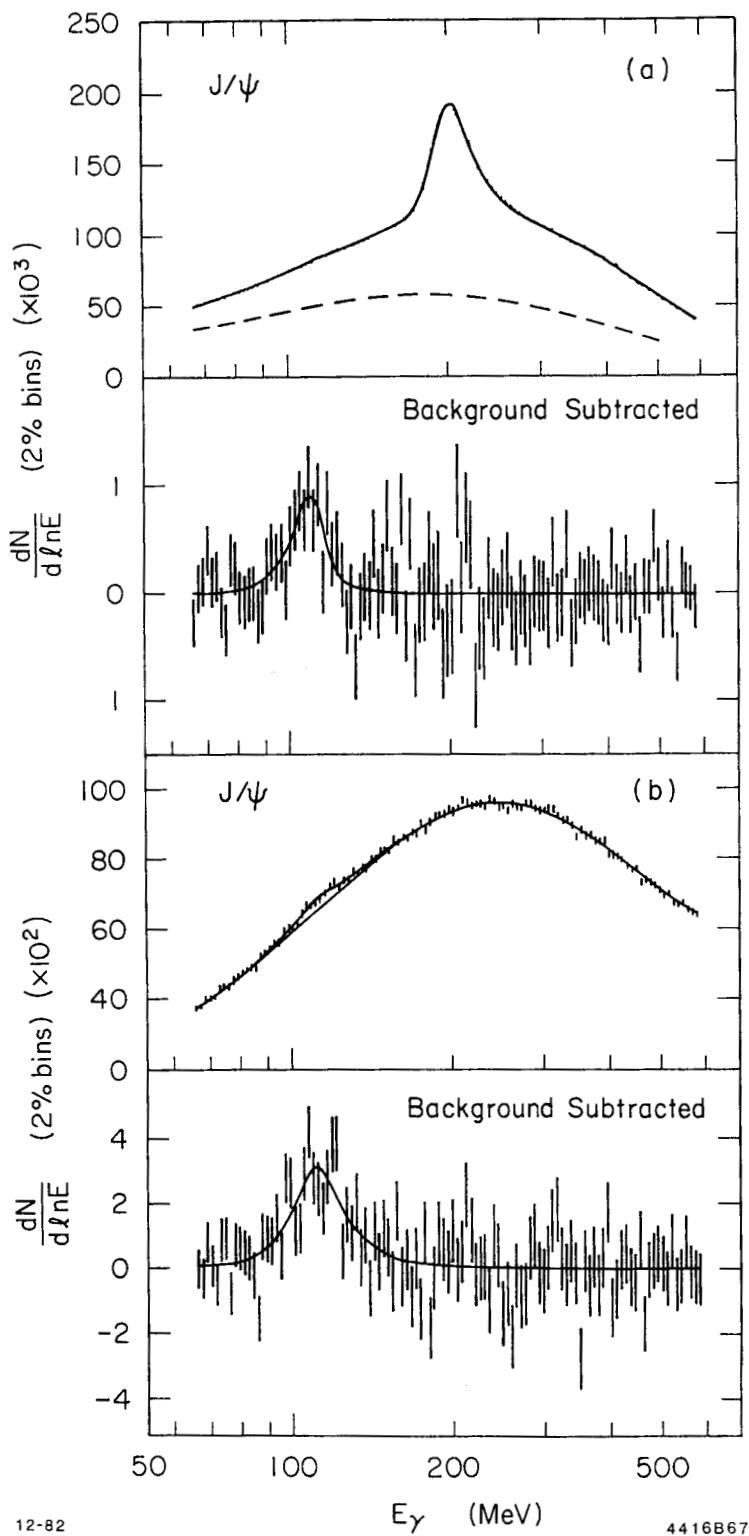
Fit Results for the χ_J States.
The results from the fits to the four ψ' inclusive photon spectra shown in Figure 26 are listed here. The errors are statistical resulting from the fit only, except for the natural line widths where the 90% C.L. interval due to the uncertainty in resolution is also shown.

DATUM	χ_0	χ_1	χ_2
Spectrum A)			
E_γ (MeV)	258.43±0.17	169.91±0.15	126.06±0.07
Γ (MeV)	(14.7-18.1)±1.0	(0-3.1±0.4)	(1.2±0.4-3.4±0.2)
N_γ ($\psi' \to \gamma \chi_J$)	110090±4260	96668±3610	76965±3110
N_γ ($\chi_J \to \gamma J/\psi$)	not seen	30979±1210	10598±1010
Spectrum B)			
E_γ (MeV)	258.73±0.13	169.75±0.08	126.14±0.10
Γ (MeV)	(16.5-20.1)±1.0	(0-3.2±0.4)	(1.7±0.4-4.4±0.2)
N_γ ($\psi' \to \gamma \chi_J$)	101650±2100	87051±2430	73668±2610
N_γ ($\chi_J \to \gamma J/\psi$)	not seen	28649±856	12314±763
Spectrum C)			
E_γ (MeV)	258.59±0.14	169.54±0.15	125.92±0.08
Γ (MeV)	(14.5-18.1)±1.0	(0-3.3±0.4)	(1.3±0.4-3.7±0.2)
N_γ ($\psi' \to \gamma \chi_J$)	66633±1660	57411±1230	47566±1110
N_γ ($\chi_J \to \gamma J/\psi$)	not seen	22317±517	8672±453
Spectrum D)			
E_γ (MeV)	258.00±0.18	169.36±0.07	125.88±0.03
Γ (MeV)	(15.4-18.2)±1.0	(0-3.4±0.4)	(1.7±0.4-4.7±0.2)
N_γ ($\psi' \to \gamma \chi_J$)	45626±1250	34900±537	27786±442
N_γ ($\chi_J \to \gamma J/\psi$)	not seen	16241±393	6086±359

agrees reasonably well with the data ($\chi^2 = 101$ and 112 for 100 degrees of freedom, respectively). More will be said below about the signal at $\simeq 108$ MeV due to the radiative transition to the $\eta_c(2984)$.

Of crucial importance to the natural line width measurements is a knowledge of the detector's intrinsic resolution. The fitted signal amplitudes were found to be fairly insensitive to variations in the resolution, since the signal shape was a convolution of the intrinsic line shape and the Breit-Wigner resonance shape. However, the fitted natural line widths varied inversely to the resolution, and for the more

Figure 27: Global Fits to the J/ψ Inclusive Photon Spectra.
Global fits to the J/ψ gamma spectra selected with cuts A) and D) are
shown (see Section 4.2.1). The fits were performed, as described in the
text, as a cross check on the background model used in fitting the ψ'
gamma spectra, since the J/ψ spectrum in the region 65 MeV to 600 MeV
contains much less structure than the ψ' spectrum. The background is
reasonably well fit when the signal due to the radiative transition J/ψ
→ γη_c is included in the fit.

narrow states ($\chi_{1,2}$), in a nonlinear way. The extracted widths of the narrow states were very sensitive to small changes in the resolution. The photon energy resolution in the region of the χ_J gamma transitions was assumed to follow the empirical function given in Equation (IV-1).

$$\sigma = \frac{\sigma_0}{E_\gamma^{1/4}} \qquad\qquad (IV-1)$$

where σ (σ_0) is the relative energy resolution at a photon energy E_γ (E_γ = 1 GeV). The value taken for the parameter is $\sigma_0 = (2.4-\simeq2.8)\%$ as a 90% C.L. interval. While a more detailed discussion of the resolution and it's uncertainty may be found in Appendix F, a few comments are in order here. The upper error on σ_0 is obtained by fitting the ψ' inclusive photon spectra with the natural line width of the $\chi_1(3510)$ fixed at 0. MeV and letting the resolution parameter σ_0 vary. Strictly speaking, the result of such a fit sets a 90% confidence level upper limit on the resolution for photon energy of 170 MeV at $\simeq2.8\%$, but does not necessarily give information on the resolution at 126 MeV or 260 MeV (corresponding to the transitions $\psi' \rightarrow \gamma\chi_{2,0}$ respectively). The value $\sigma_0 = 2.4\%$ is taken as a reasonable estimate of the detector's lower limit (90% C.L.) resolution based on i) studies of exclusive channels involving low energy photons, and ii) the variation in the χ^2 for fits to the χ_J lines as a function of σ_0. Reasonable pulls on the fitted photon energies were found for resolutions in the range $\sigma_0 = (2.5-2.7)\%$. However, this is an estimate since rigorous quantitative measurements are lacking at this time, although work on this problem is in progress. The results from the fits to the inclusive photon spectra are given in Appendix F.

The power dependence in Equation IV-1 (1/4 power) was empirically derived from studies on a prototype[4] of the Crystal Ball detector containing 54 crystals. The resolution was found to obey the 1/4 power law for photon energies in the range 0.66 MeV to 2.0 GeV. The Crystal Ball detector though, has been unable to obtain the high quality resolution achieved in the 54 test, shedding some doubt on the validity of 1/4 power law for the full detector. An uncertainty in the power law of (0.25+0.05,-0.00) is included in the resolution error.

Figure 28 shows the variation in the fitted natural line widths as a function of the intrinsic resolution given by Equation IV-1. The error in the x_J widths was dominated by the uncertainty in the intrinsic resolution, although relatively less so for the x_0 width.
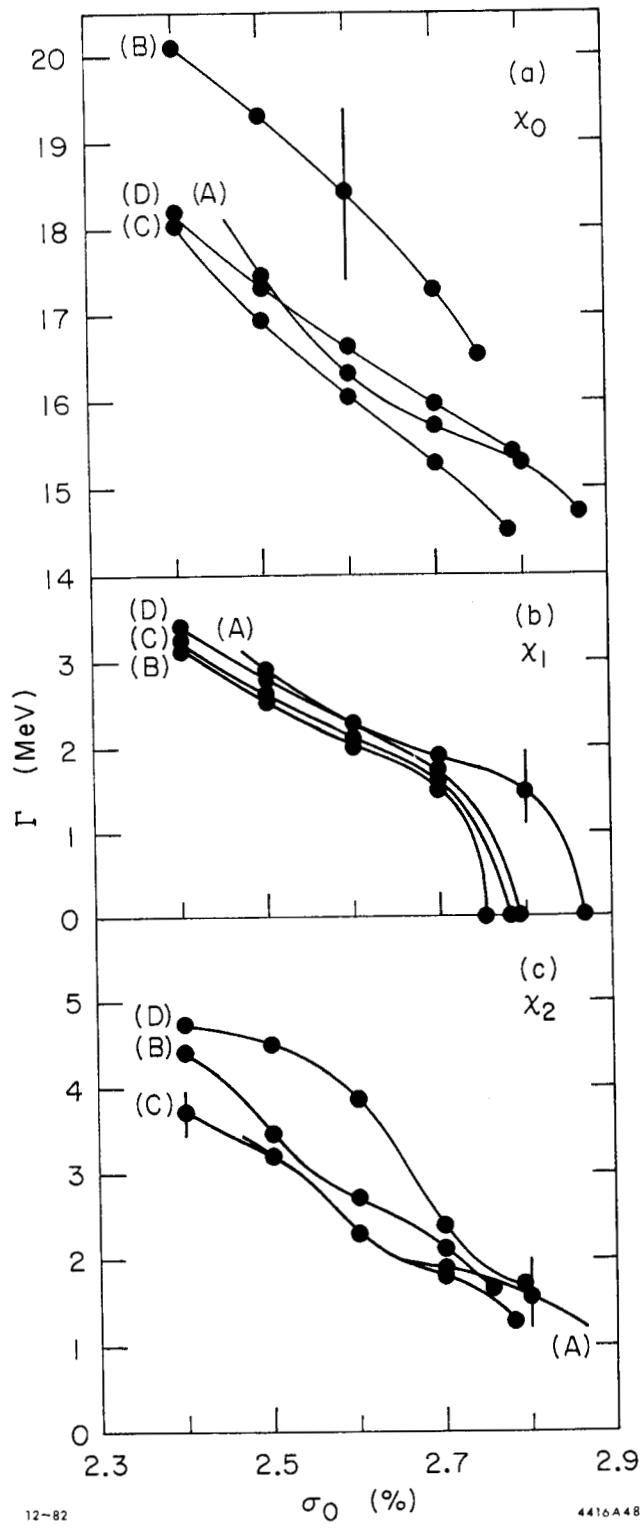
Figure 28: Variation in χ_J Natural Line Widths Vs. Resolution.
The variation in the χ_J natural line width is shown as function of the
intrinsic resolution for fits to the ψ' spectrum shown in Figure 20.
The error bars indicate the magnitude of the statistical error from the
fit. The upper limit on the intrinsic resolution varied slightly among
the spectra.

4.3.2 $\psi' \to \gamma\eta_c(2984)$ and $J/\psi \to \gamma\eta_c(2984)$

The radiative transitions to the η_c candidate state from ψ' and J/ψ were studied simultaneously to check the consistency of the two photon signals and to make a global determination of the state's mass and width. To accomplish this, each pair of J/ψ and ψ' spectra from the three photon selection criteria B), C), and E) were simultaneously fit to an η_c mass and width constrained to be the same in both spectra. The same analysis of the signal shapes as was used for the transitions $\psi' \to \gamma\chi_J$ was also used for the radiative decays to the η_c, except for the energy dependence in the hindered magnetic dipole transition matrix element for $\psi' \to \gamma\eta_c$. A factor of E_γ^7 was included in the convolution of the detector's response function with the η_c Breit-Wigner resonance shape for this transition, while a factor of E_γ^3 was used for the decay $J/\psi \to \gamma\eta_c$. Figures 29(a)-(f) show the results of the simultaneous fits to the spectra in Figures 20(b) and (c), and 23(a)-(d). The numerical results are tabulated in Table 10.

The problem of determining the η_c natural line width is dominated by the statistical uncertainty in the signal $J/\psi \to \gamma\eta_c$, since the signal at $E_\gamma \simeq 636$ MeV in the transition $\psi' \to \gamma\eta_c$ is fairly insensitive to the η_c width. The error introduced due to the uncertainty in the detector's intrinsic resolution for the J/ψ transition is small, since the observed η_c width is about equal to the detector's resolution at $E_\gamma \simeq 108$ MeV. In this regard, the η_c natural width measurement is similar to the χ_0 measurement. Figure 30 gives a plot of the variation in χ^2 versus the fitted η_c width, for each fit shown in Figure 29. The single dot in
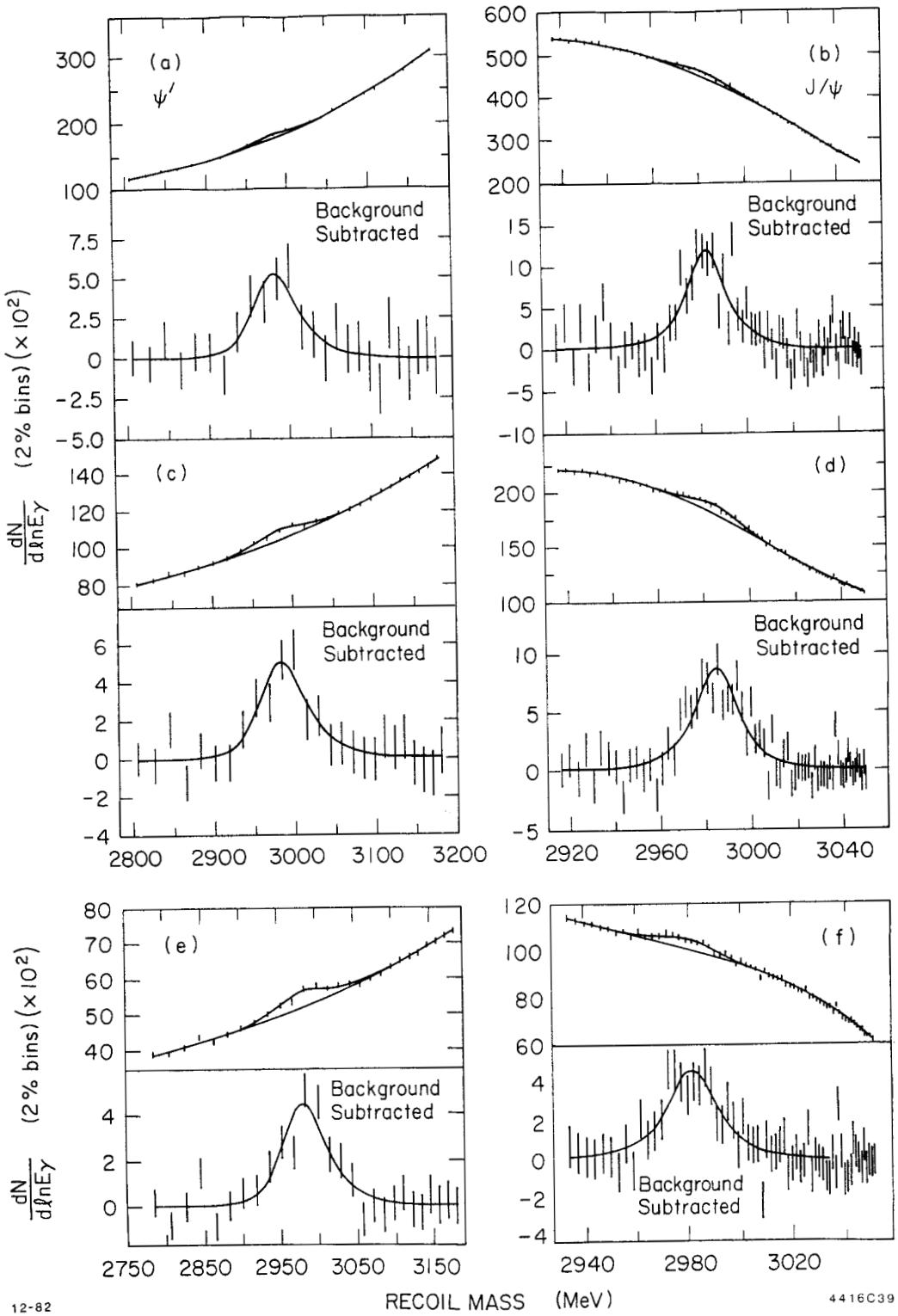
Figure 29: B),C),E) Simultaneously Fitted J/ψ and ψ′ Spectra: η_c. The results of a simultaneous fit to the η_c mass in ψ′ → $\gamma\eta_c$ and J/ψ → $\gamma\eta_c$. The fits (b) and (d) correspond to J/ψ spectra shown in Figures 23(a) and (b), and the fits (a) and (c) to the ψ′ spectra shown in Figures 20(b) and (c). The third fit, (f) and (e), is to the J/ψ and ψ′ spectra in Figure 23(c) and (d), respectively. The preferred resolution value of $\sigma_0 = 2.7\%$ was used here.

Figure 30 represents the fit results for a resolution given by $2.7\%/E_\gamma^{1/4}$. Each half parabola shows the variation in χ^2 obtained from the fit by manually varying $\Gamma(\eta_c)$ for the two extremes in the resolution uncertainty interval. The parabola on the left (right) corresponds to the worst (best) estimated resolution. A symmetric parabola would have resulted if the resolution had been held fixed.

Both the $\psi' \to \gamma\eta_c$ and the $J/\psi \to \gamma\eta_c$ signals were first measured[5] in the 1978 and 1979 resonance data. With the 1980 and 1981 data acquisition, the ψ' and J/ψ data samples were doubled, yielding the results shown here. Several cross-checks were made on η_c signals, verifying that they were present in subsets of the data, and in all regions of the NaI(Tl). In addition, both signals correspond to transitions to a state yielding a consistent mass at 2984±4 MeV. Confirmations[5,6] of the state in exclusive decays of the ψ' and J/ψ have also been reported.
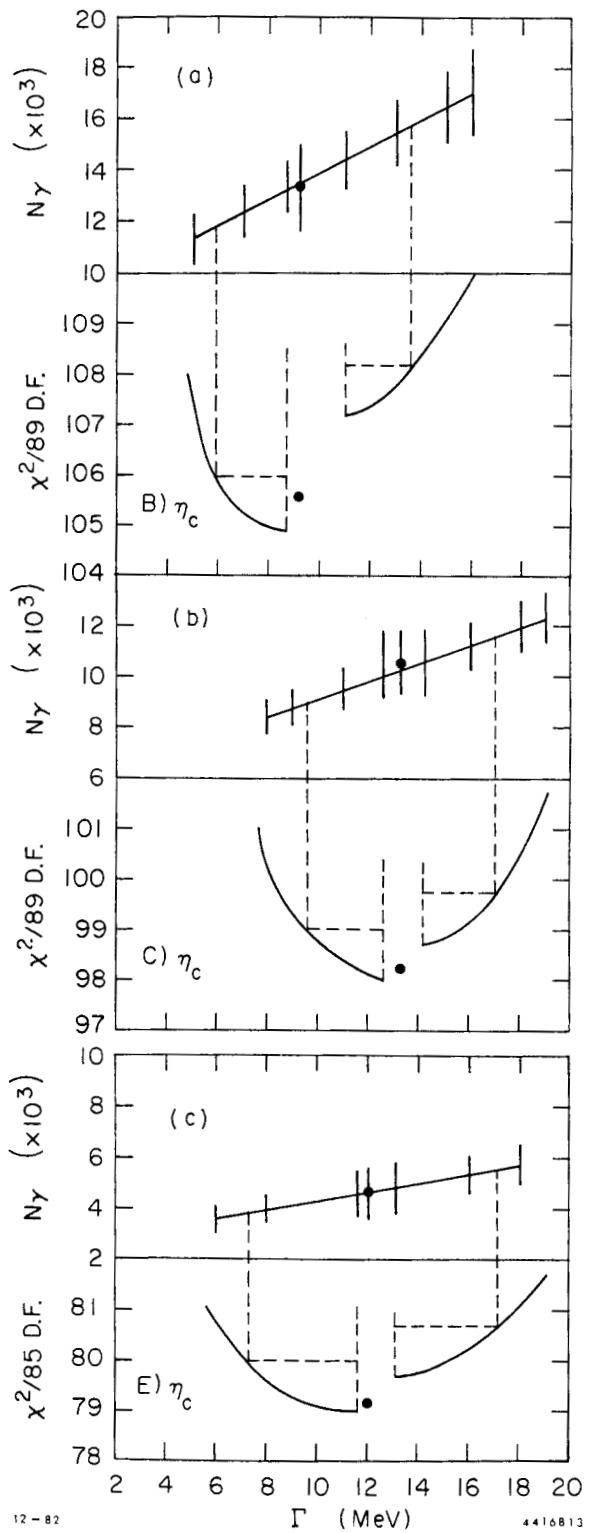
Figure 30: χ^2 Distribution Versus the η_c Natural Line Width.
The variation in χ^2 is shown as a function of the η_c width in the
simultaneous fit to the ψ' and $J/\psi\ \gamma$ spectra shown in Figure 29. The
contributions to the error in Γ (verticle dashed lines) include: i) the
statistical uncertainty traced by the parabolic variations in χ^2 and ii)
the systematic uncertainty in the resolution indicated by the separation
in the vertices for the two half parabola. The half parabola on the
right (left) corresponds to the best (worst) limits in the resolution.
The point in between results from a resolution of $2.7\%/E_\gamma^{1/4}$.

TABLE 10
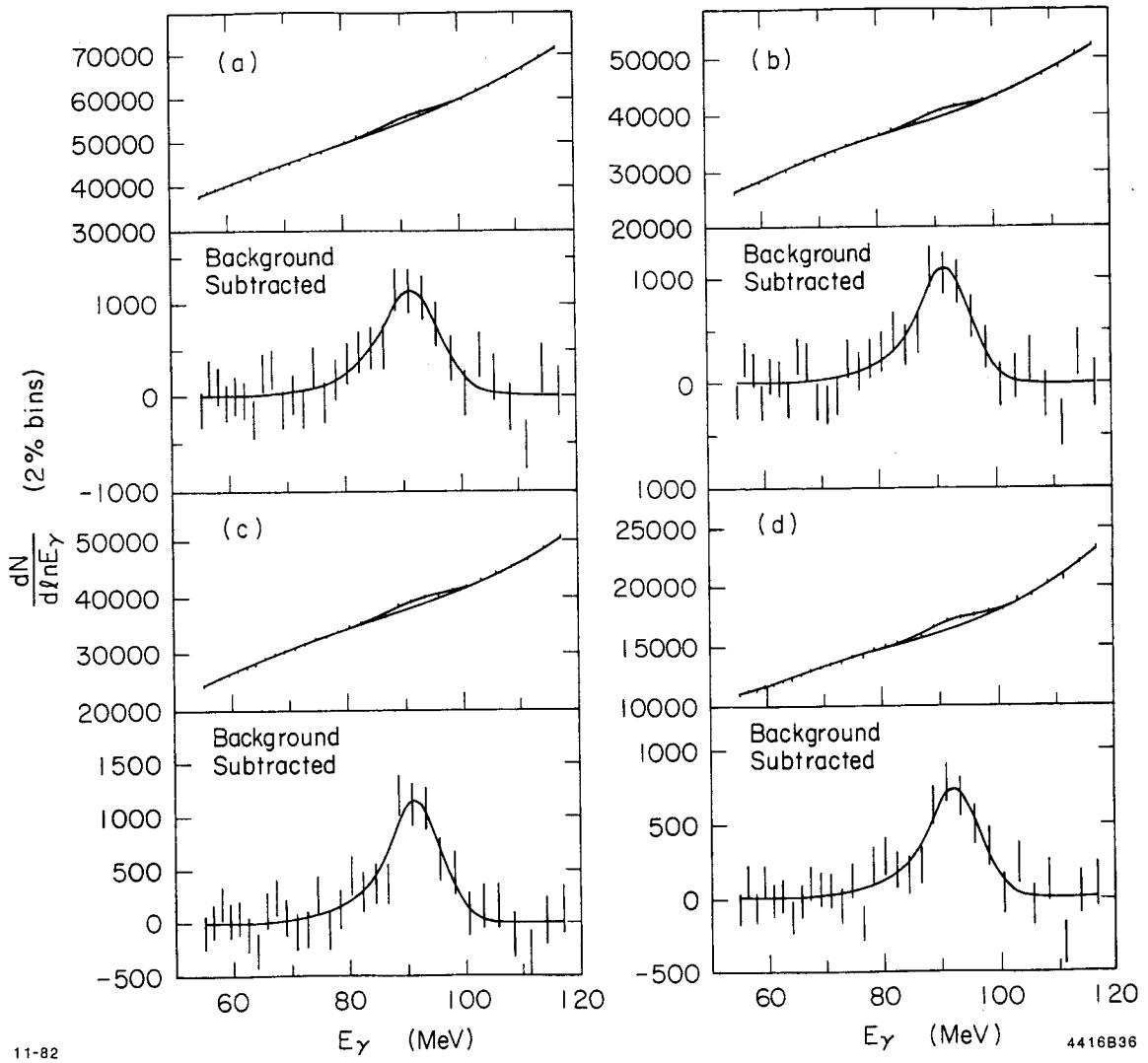
Fit Results for the η_c State.
The results from the simultaneous fits to the three ψ' and J/ψ inclusive photon spectra shown in Figure 29.

SPECTRUM	MASS (MeV)	$N_\gamma(\psi'\to\gamma\eta_c)$	$N_\gamma(J/\psi\to\gamma\eta_c)$	Γ (MeV)
B)	2983.3±1.3	2595±423	13500^{+2642}_{-1887}	$9.2^{+4.4}_{-3.2}$
C)	2986.5±1.2	2538±373	10300^{+1553}_{-1476}	13.3±3.7
E)	2982.1±1.5	2227±277	4600^{+1220}_{-943}	$12.0^{+5.2}_{-4.7}$

4.3.3 $\underline{\psi' \to \gamma\eta_c'(3592)}$

The four ψ' spectra shown in Figure 24 were fit in the region of 92

MeV with an analysis identical to that used for the J/$\psi \to \gamma\eta_c$

transition. The results of the fits are tabulated in Table 11, while

Figure 31 shows four views of the fitted signal using the central value

for the detector's resolution. The signal at $\simeq$92 MeV was first seen in

the inclusive photon spectrum from the 1978-1979 ψ' data. When combined

with the 1981 ψ' data (doubling the data sample), the highly significant

signal shown in the fits was identified[7] as the η_c' candidate state at a

mass of 3592±4 MeV (hereafter referred to as the η_c' for brevity).

The uncertainty in the determined η_c' natural line width is equally

dominated by the statistical uncertainty in the signal and the

systematic uncertainty in the detector's resolution. In this regard the

η_c' width measurement has similar problems when compared to the narrow

χ_1 and χ_2 states. Figure 32 shows the variation in χ^2 and the highly

correlated signal amplitude as a function of the η_c' width. The data

were plotted from fits made while the resolution was fixed at it's lower

uncertainty value, in order to obtain an upper limit on the η_c' width

Figure 31: B),G)-I) Fits to the $\psi' \to \gamma\eta_c'$ transition.
The fitted signal, $\psi' \to \gamma\eta_c'$, from the four ψ' spectra in Figure 24 is shown. These fits were made using the preferred value for the detector's resolution. The data shown in Table 11 were obtained from fits using the best value for the resolution within its uncertainty interval.

and signal strength.   Upper limits at   the 90% confidence level (C.L.) were identified by a change in x^2 of 2.7.   The lower limits for the signal amplitude   were calculated   by subtracting $1.3 \cdot \sigma_{statistical}$ from the amplitude obtained by fixing $\Gamma = 0.0$ MeV,   and   using the narrowest detector resolution.

The   following cross   checks,   in addition   to   some   of the   checks mentioned for the $\eta_c(2984)$ candidate state, were made on the analysis to verify   this interesting   result.   Monte   Carlo studies   ruled out   the possibility of a fake signal resulting from the photon background in decays like $\psi' \rightarrow \pi^0\pi^0 J/\psi$ and $\psi' \rightarrow \eta J/\psi$, where the π^0's and the η are produced close to threshold.   In addition, the charged particle spectrum was examined for structure near 92 MeV, and none was found.
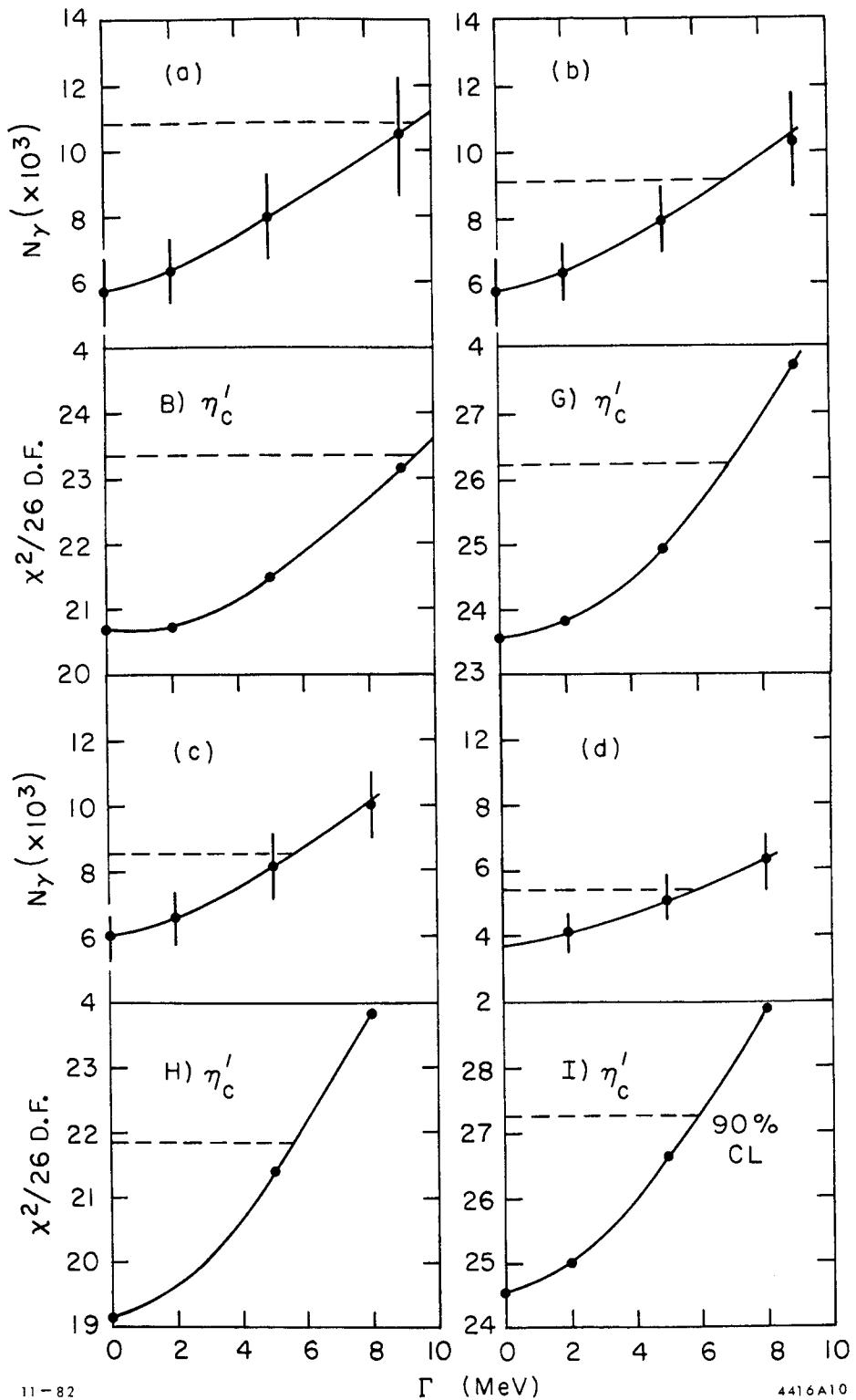
Figure 32: χ^2 Distribution for the η_c' Fit.

The χ^2 distribution and the variation in the signal amplitude for $\psi' \to \gamma\eta_c'$ are shown as a function of the η_c' natural line width for the fits to the inclusive γ spectra shown in Figure 24.   The dashed lines indicate the statistical contribution to the upper limit for the η_c' natural line width for the case with the best detector resolution.

TABLE 11

Fit Results for the η_c' State.
The results from the four fitted inclusive photon ψ' spectra shown in Figure 24 are given below.

SPECTRUM	E_γ (MeV)	$N_\gamma(\psi' \to \gamma\eta_c')$ (90% C.L. Interval)	Γ (MeV) (90% C.L. Upper Limit)
B)	91.09±0.95	[4402-10800]	< 9.5
G)	90.96±0.74	[4484-9100]	< 7.0
H)	91.34±0.69	[5119-8100]	< 5.5
I)	92.07±0.73	[2968-5500]	< 5.8

4.4   PHOTON DETECTION EFFICIENCY IN MULTIHADRON FINAL STATES

As was discussed in Chapter II, the Crystal Ball detector has a near 100% sensitivity to photonic energy above ≃1 MeV. For γ's in the energy region of the radiative transitions studied here, their detection as particles within the fiducial volume $|\cos\theta|$ < 0.85 would also be nearly 100%, if it were not for the following loss mechanisms:

1) The successful detection of a photon requires that: i) a bump is spatially correlated with the photon and ii) the energy measurement for the bump is not too different from the photon's energy. If the photon shower overlaps with another particle's energy deposition, either or both conditions may not be met. This includes overlaps with split-offs from hadron-nuclear interactions in the NaI(Tl). Typically, split-offs deposit < 100 MeV as evidenced by the low energy hump in the spectrum shown in Figure 20(c). A photon might not be detected if it overlaps with some of this hadronic debris. Clearly these loss mechanisms are dependent on the photon energy. The more energetic the photon is, the more robust it is, and the more likely it will be detected.

2) If a photon is misidentified as a charged particle, due to fake combinatorials in the central tracking chamber data, it will be lost, unless all tracks are included in the selection sample.

3) The photon selection criteria themselves are major contributors to the photon detection inefficiency.

4) Finally, there is a finite probability that a photon will convert in the beam-pipe or central chambers and be called charged. This loss mechanism will not apply to the all track selection criterion A).

Items 2) and 4) are not energy dependent for photons with energies between $\simeq100$ and $\simeq600$ MeV. Losses due to the selection cuts, though, are highly energy dependent in a complex way. A Monte Carlo technique (see below) was used to measure the effects of items 1) through 3). The photon conversion probability, ϵ_{conv}, is calculated in Appendix A to be $(3.5\pm0.5)\%$. The resulting efficiency, ϵ_γ, is calculated as a function of energy and the selection criteria according to:

$$\epsilon_\gamma = \epsilon_{mc}\cdot\delta\cdot(1 - \epsilon_{conv}) \qquad\qquad (IV-2)$$

where ϵ_{mc} is the efficiency calculated with the Monte Carlo technique, and δ is a geometric correction factor (see Table 12) for the photon angular distributions, since the Monte Carlo γ's were generated isotropically. The energy dependent uncertainty in ϵ_γ ranges from $\pm2.9\%$ to $\pm4.8\%$ in addition to its overall normalization error of $\pm5\%$.
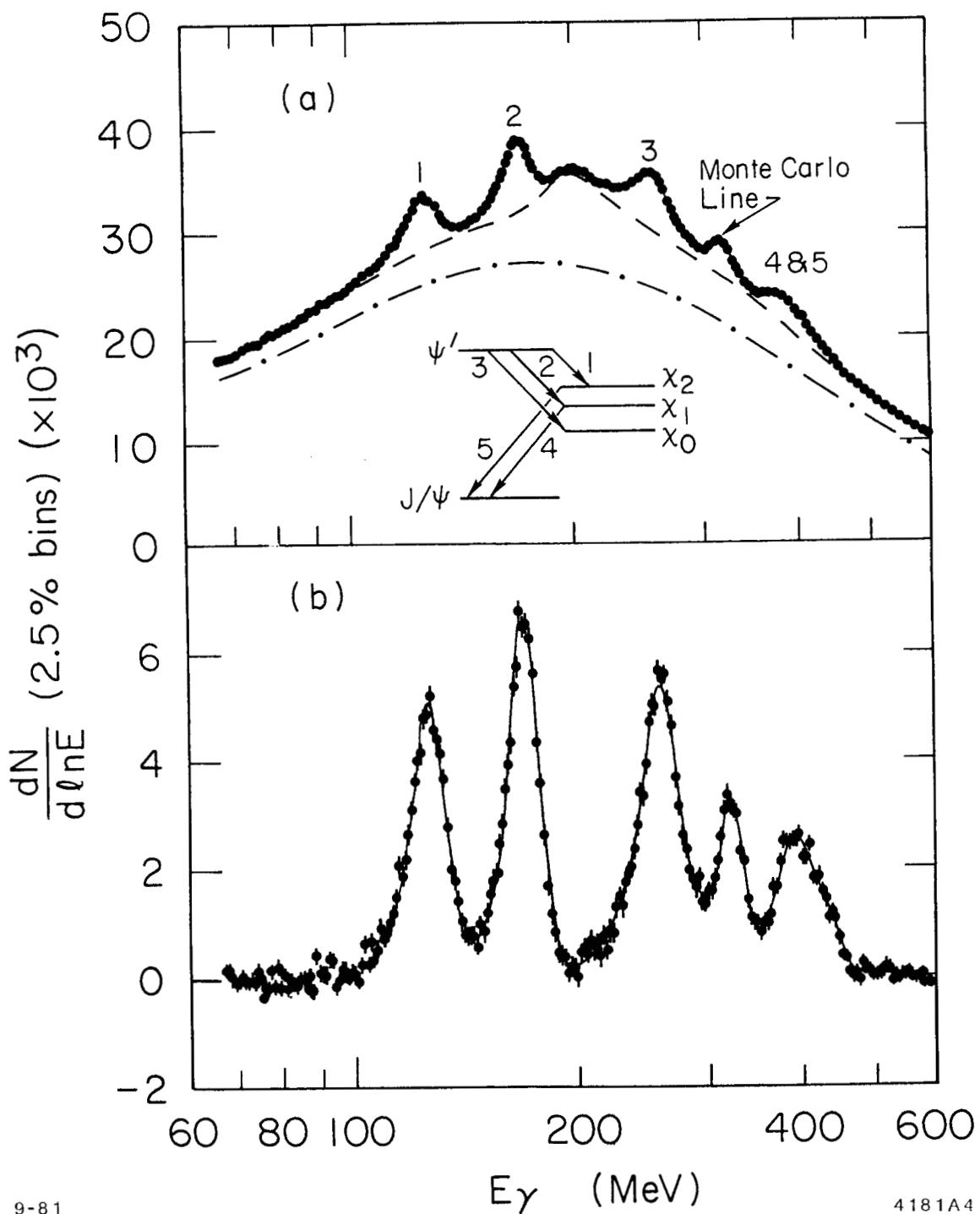
A detailed description of the Monte Carlo technique used to calculate ϵ_{mc} may be found in Appendix C; a summary is presented here. Monochromatic photons were generated with a flat angular distribution at several specific energies in the range 90 MeV to 500 MeV. The photons were propagated through the Crystal Ball detector geometry using the

TABLE 12

Photon Angular Distribution Correction Factor
Geometric correction factors based on the known or assumed photon
angular distributions for the transitions studied is given. The
correction factor, δ, is relative to a flat distribution.

TRANSITION	ANGULAR DISTRIBUTION	δ	COMMENT
$\psi' \to \gamma \chi_0$	$(1+\cos^2\theta)$	0.931	Ref. 1
$\psi' \to \gamma \chi_1$	$(1-0.189\cos^2\theta)$	1.014	
$\psi' \to \gamma \chi_2$	$(1-0.052\cos^2\theta)$	1.005	
$\psi' \to \gamma \eta_c'$	$(1+\cos^2\theta)$	0.931	Assumed
$\psi' \to \gamma \eta_c$	$(1+\cos^2\theta)$	0.931	
$J/\psi \to \gamma \eta_c$	$(1+\cos^2\theta)$	0.931	

Electron-Gamma-Shower (EGS) code.[3] The shower from each Monte Carlo photon was then added to a real J/ψ event and analyzed with the standard analysis programs. These events simulated the transition $\psi' \to \gamma X$, where X decays similarly to the hadronic decays of J/ψ. About $5 \cdot 10^4$ of these simulated events, at a single photon energy, were added to the real full ψ' data sample. This resulted in one additional signal (simulated) to the structure in the ψ' spectrum, and with an amplitude roughly equivalent to the χ_J signals. Using the photon selection criteria described above for the χ_J transitons, four spectra were generated from the modified data sample. Figure 33 shows a typical fit to one of these spectra containing an additional Monte Carlo transition at $E_\gamma = 320$ MeV. The efficiency, ϵ_{mc}, is extracted by fitting the modified spectra and comparing the fitted Monte Carlo signal amplitude to the number generated. Figure 34 shows the resulting efficiencies for each of the four photon selection criteria. The region near 210 MeV for selection cuts A)-C) is complicated by the presence of the minimum ionizing peak. However, this is not a problem for the pattern cut selection criterion D) (see Figure 20(d)).

Figure 33: A Fitted Monte Carlo Line in the Ψ′ Spectrum.
An example of a 320 MeV Monte Carlo gamma added to J/Ψ events and then
combined with the Ψ′ spectrum is shown. The photon detection efficiency
is determined from the number of fitted Monte Carlo gammas compared to
the number originally generated.

9-81   4181A4
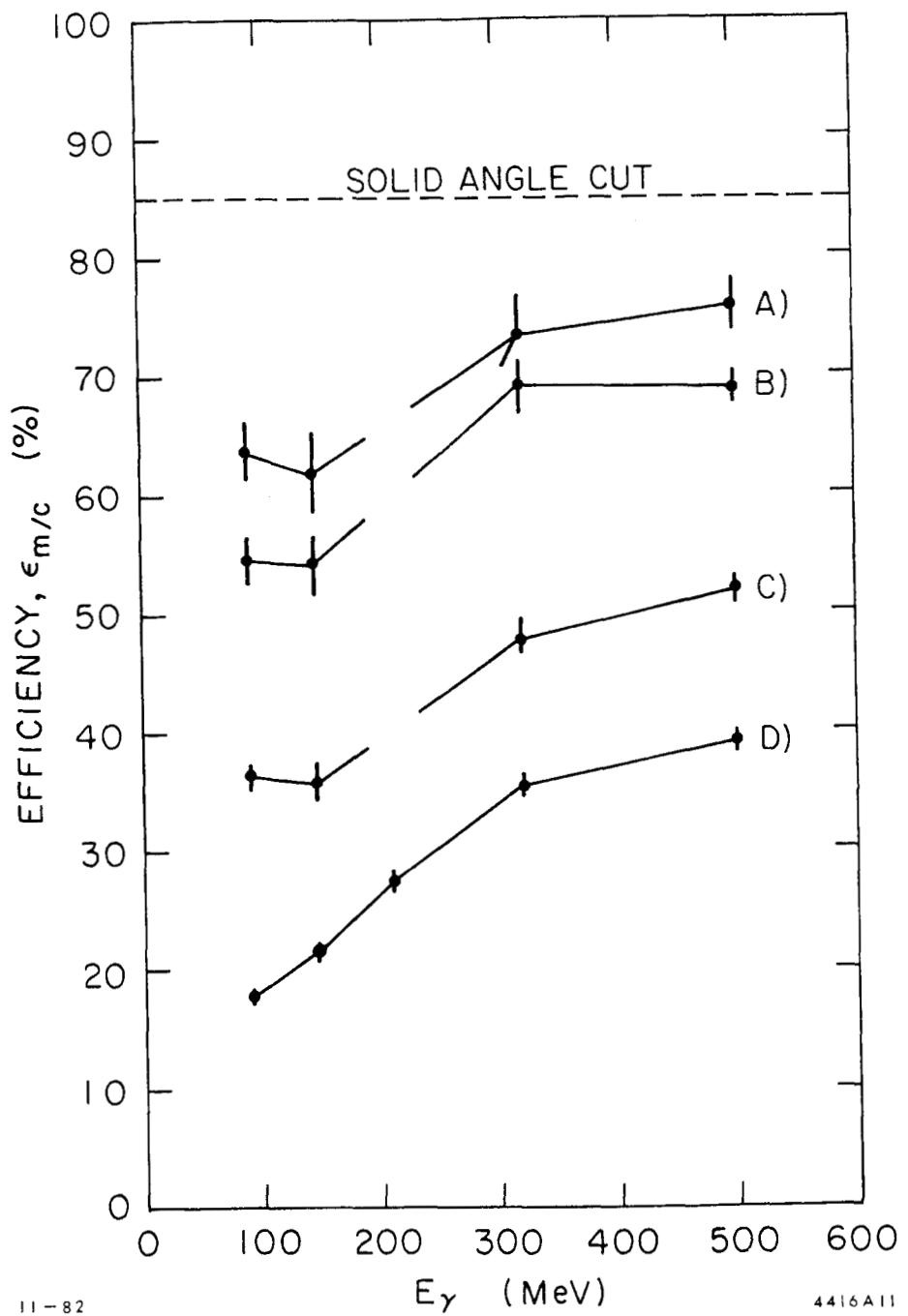
Figure 34: The Photon Detection Efficiency.
The photon detection efficiencies A)-D) corresponding to the four ψ' spectra shown in Figures 20(a)-(d). These values assume a flat photon angular distribution, and do not account for photon conversion in the inner detector. The error bars are from the fits to the Monte Carlo lines. An overall normalization error of ±5% is not shown. The region near ≃210 MeV is complicated by the minimum ionizing charged particle peak for the criteria A)-C) only.

4.5 RESULTS
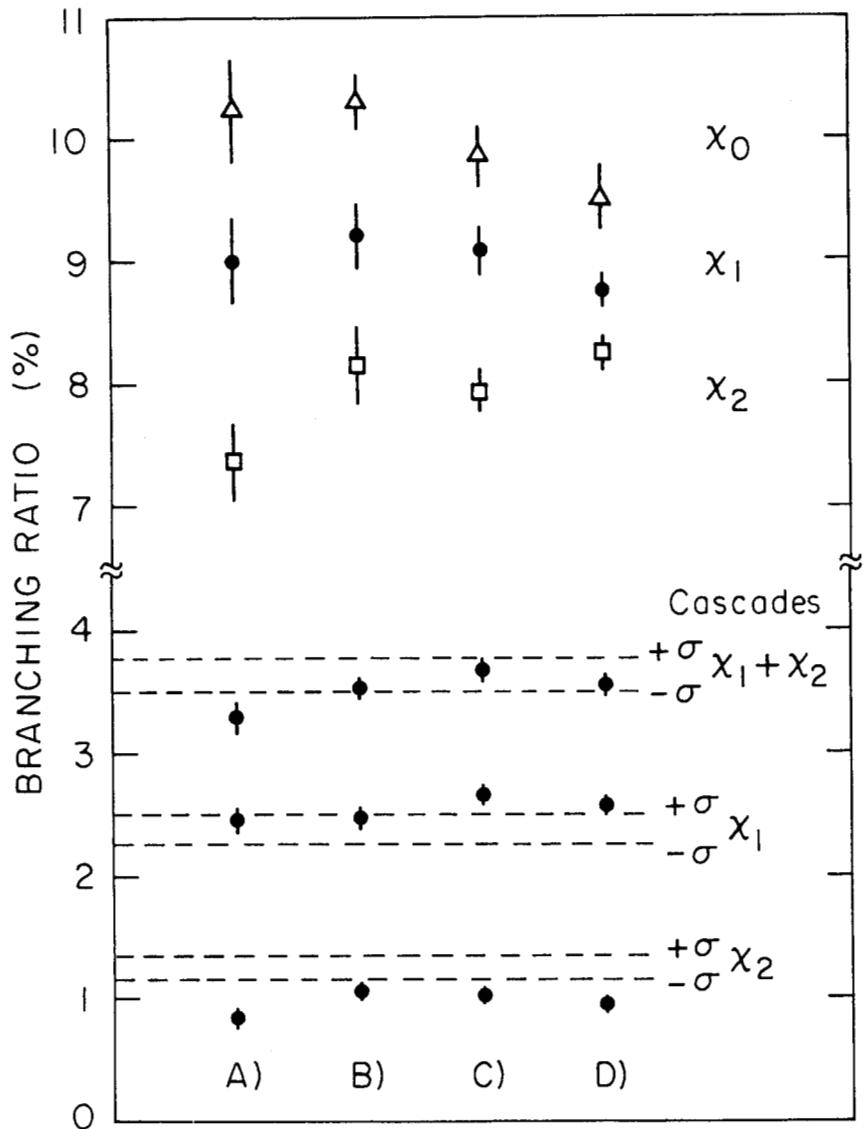
4.5.1 $\psi' \to \gamma\chi_J$ and $\chi_J \to \gamma J/\psi$

For each of the four spectra in Figure 26 and for each of the fitted signal amplitudes, N_γ, a branching ratio was calculated based on the following formula:

$$\text{Branching Ratio} = B = \frac{N_\gamma}{N_{prod} \cdot \epsilon_\gamma \cdot \epsilon_{fs}} \qquad (IV\text{-}3)$$

where N_{prod} is the corrected number of produced ψ' events given in Table 8, ϵ_γ is the photon detection efficiency from Equation IV-2 and Figure 34, and ϵ_{fs} is the final state event selection efficiency. For example, for the transition $\psi' \to \gamma\chi_J$, ϵ_{fs} is the probability of selecting an event containing a χ_J decay and a photon. In determining ϵ_{fs}, it is assumed that the decays of the charmonium daughter states are sufficiently similar to hadronic decays of J/ψ, in terms of the final state multiplicities and angular distributions, to warrant modeling the daughter's decays after J/ψ hadronic decays. A Monte Carlo calculated value of 0.944 is used for ϵ_{fs} for all the transitions, except $\chi_J \to \gamma J/\psi$ and $\psi' \to \gamma\eta_c$ where a value of 0.960 is used (see Appendix C). The overall normalization errors for N_{prod} and ϵ_γ are each $\pm 5\%$. The error in ϵ_{fs} ($\pm 2\%$) reflects the error due to the uncertainty in the dissimilarity between the particular final state and inclusive J/ψ hadronic decays.

Figure 35 presents a graphic comparison of the resulting x_J branching ratios. The errors shown are due to the statistical uncertainties in the fits. An important cross-check is the observed consistency between the same branching ratio extracted from different spectra, seen by reading across the figure from left to right. Considering the wide variation in background shapes and efficiencies (especially seen in Figure 20) the agreement within statistical errors gives confidence to the procedure for extracting the branching ratios, and ultimately to an understanding of the backgrounds and photon detection efficiencies. The bottom of Figure 35 presents another check on the analysis by comparing the product branching ratios $B(\psi' \to \gamma x_{1,2}) \cdot B(x_{1,2} \to \gamma J/\psi)$, from the inclusive photon analysis here with the values obtained from a study[1] of the cascade decays in the exclusive channel $\psi' \to \gamma\gamma J/\psi \to J/\psi e^+e^-$ or $\mu^+\mu^-$, also using the Crystal Ball detector. In the inclusive spectra, the signals corresponding to the x_1 and x_2 cascade transitions are seen to overlap, while in the exclusive channel measurement the product branching ratios are extracted from the first cascade gammas which do not overlap. A slight bias is noted in the inclusive result here, also seen in Monte Carlo studies, where the stronger signal steals some of the amplitude from the weaker signal. However, when the two product branching ratios are added together, removing this bias, agreement is observed.

Figure 35: Comparison of the χ_J Branching Ratio Results.
A comparison is shown for the branching ratios $B(\psi' \to \gamma \chi_J)$ and
$B(\psi' \to \gamma \chi_J \to \gamma \gamma J/\psi)$ among the four fitted inclusive ψ' photon spectra shown
in Figure 26. The error bars indicate the statistical uncertainty from
the fits only. The letters A)-D) below the branching ratios refer to
the photon selection criterion described earlier in this chapter. The
plus and minus one sigma statistical errors on the exclusively derived
cascade product branching ratios[1] using the Crystal Ball detector are
indicated by the dashed lines for comparison with the inclusive values
shown as data points.

4.5.2 ψ' and $J/\psi \to \gamma\eta_c(2984)$

Figure 36 gives a two dimensional comparison of the η_c width and branching ratios, $B(\psi'\to\gamma\eta_c)$ and $B(J/\psi\to\gamma\eta_c)$, obtained from the three fitted spectra in Figure 29. The branching ratios were calculated using Equation IV-3, and the data in Table 10 with a final state detection efficiency, ϵ_{fs}, of 0.944 for the radiative J/ψ transition and 0.960 for the radiative ψ' transition. The photon detection efficiency, ϵ_γ, for the spectra B) and C) were obtained from Equation IV-2 using the results in Figure 34. For spectrum E), ϵ_γ was determined to be $(24\pm5)\%$. Only the statistical error in the branching ratios from the fit is shown, while the width error is a combination of statistical uncertainty from the fit and systematic uncertainty in the detector resolution.
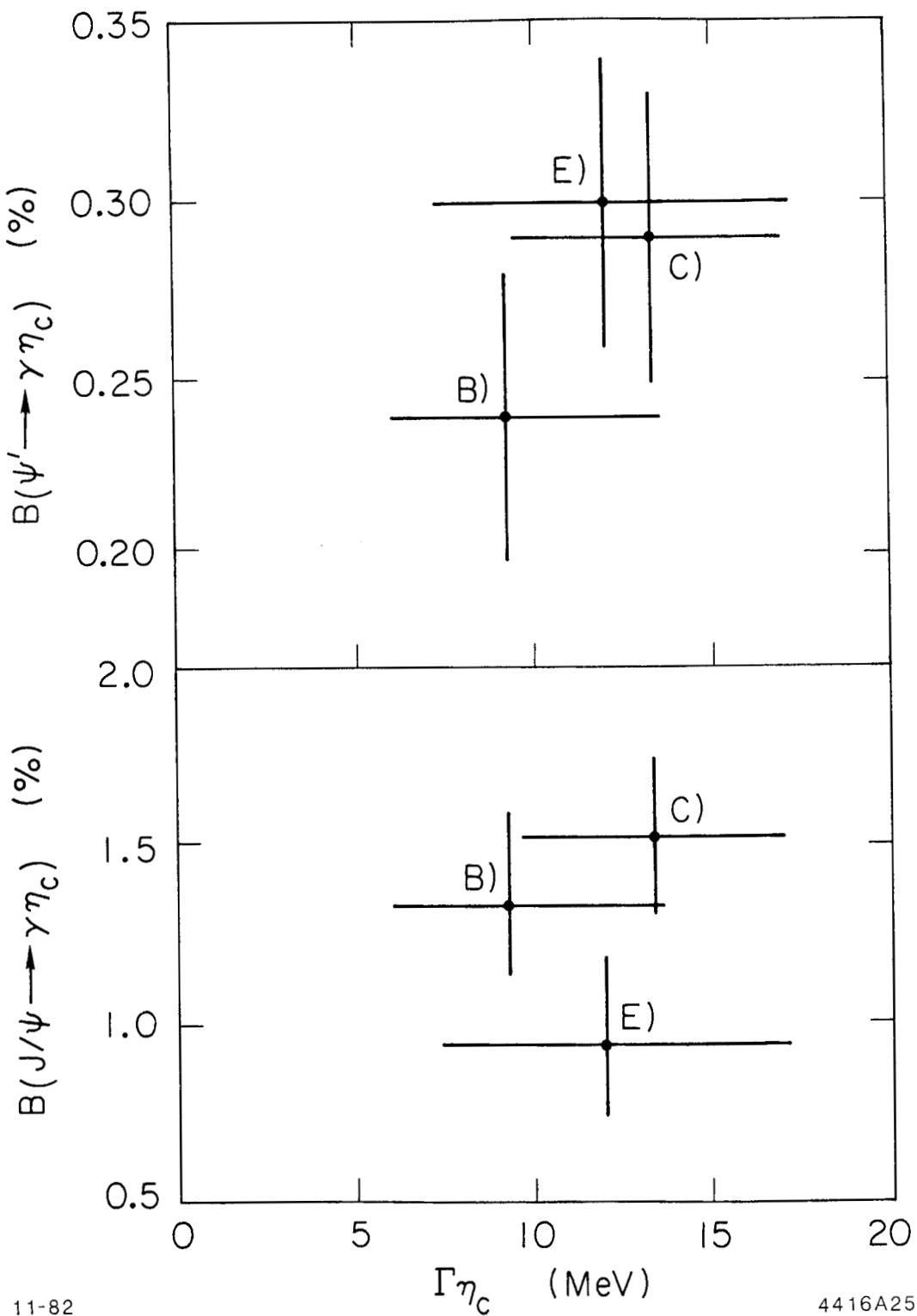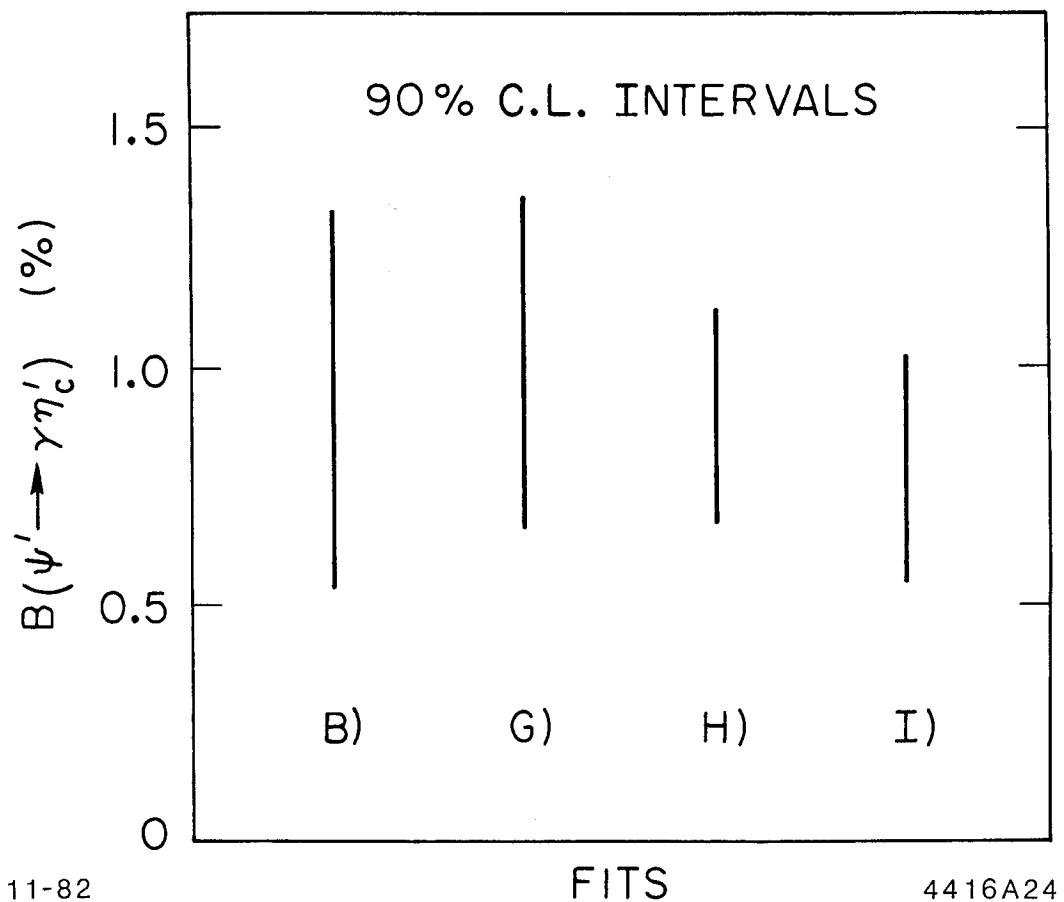
Figure 36: Comparison of the η_c Fitted Widths and Branching Ratios. The η_c natural line width, branching ratio $B(\psi' \to \gamma\eta_c)$, and branching ratio $B(J/\psi \to \gamma\eta_c)$ obtained from the three simultaneous fits shown in Figure 29 are compared. The errors include contributions from the statistical uncertainty and from the systematic uncertainty in the detector's resolution.

4.5.3 $\psi' \rightarrow \gamma \eta_c'(3592)$

A comparison of the branching ratios $B(\psi' \rightarrow \gamma \eta_c')$ obtained from the four fitted spectra in Figure 31, are shown in Figure 37. The photon detection efficiencies, ϵ_γ, at 92 MeV for each spectra B), G), H), and I) were found to be 48%, 39%, 44%, and 32% respectively ($\pm 5\%$). The η_c' natural line width was found to be consistent with zero (90% confidence level upperlimit is $\Gamma < 7$ MeV). The main contribution to it's substantial upper limit is due to the statistical uncertainty in the fitted signal.

Figure 37: A Comparison of the η_c' Branching Ratio Results.
The branching ratio $B(\psi' \to \gamma \eta_c')$ extracted from the four spectra in Figure
31 are compared. The errors result from a combination of the
statistical uncertainty and the systematic uncertainty in the detector's
resolution.

REFERENCES

1. M. Oreglia et al., Phys. Rev. D25, 2259 (1982).

2. During the analysis, the values 3684 MeV and 3095 MeV were used for the ψ' and J/ψ masses, respectively. After the analysis, any measured quantity sensitive to these values was corrected for the known resonance masses at 3686 MeV and 3097 MeV as given in the "Review of Particle Properties" reference following. M. Aguilar-Benitz et al., "Review of Particle Properties," Phys. Lett. 111B, April (1982).

3. R. L. Ford and W. R. Nelson, Stanfor Univ. Report, SLAC-210 (1978).

4. Y. Chan et al., IEEE Trans. on Nucl. Sci. NS-25, 333 (1978).

5. R. Partridge et al, Phys. Rev. Lett., 45, 1150 (1980).

6. T. M. Himel et al., Phys. Rev. Lett. 45, 1146 (1980).

7. C. Edwards et al., Phys. Rev. Lett. 48, 70 (1982).

Chapter V

CONCLUSIONS

5.1   STATUS OF CHARMONIUM SPECTRUM

With the existence of the two strong candidates for the pseudoscalar states, the $\eta_c(2984)$ and the $\eta_c'(3592)$, the measured charmonium bound state spectrum substantially bears out the predictions of the theory. Of the eight excepted states below the $D\bar{D}$ threshold, only the singlet $^1P_1$ state has not been observed experimentally. The resulting charmonium level scheme and radiative transitions are shown in Figure 38 (compare with Figure 2).

The naive QCD potential models without spin and relativistic dynamics cannot predict how the triplet ^3P_J states split about their center of gravity (the fine structure) or the degree of splitting between the singlet $^1S_0$ pseudoscalar states and their triplet $^3S_1$ vector partners (the hyperfine structure).   However, in QCD the triplet ^3P_J center of gravity (c.o.g.) is split from the 2^3S_1 state by the long range confining potential without including the spin structure,   unlike the situation in QED.

Numerous accounts of how the spin dependent forces in QCD should be included have been published. Some of these are reviewed in Appendix A. It will suffice for now to make a comparison between the results presented here and a couple of the standard models.   In the spirit of the success of the "Coulomb plus linear" naive models in predicting the

spectra of triplet S states and the triplet P and D states c.o.g., Buchmüller et al (model-A) have employed a similar approach in obtaining a QCD spin dependent Hamiltonian.[1] They superimposed the one gluon exchange Breit-Fermi Hamiltonian (for the short distance dynamics) with a long distance Thomas precession term defined by the confining potential. They base their model on the hypothesis that at large distances the color fields in the rest frame of the flux tube joining the quark and antiquark are purely electric. Buchmüller points out that their results are also obtainable from the standard non-relativistic reduction of the Bethe-Salpeter equation with a kernel given by an instantaneous interaction and a Lorentz structure corresponding to a vector exchange at short distance and a scalar exchange at large distance. A model[2] of this latter type has been formulated by Byers and McClary (model-B), where in addition they included relativistic corrections to the non-spin part of the Hamiltonian. The corrections in both of these models were up to order $(v/c)^2$ in the quark velocity. Typically $(v/c)^2$ is $\simeq 0.25$.

An alternate approach,[3] formulated by Henriques, Kellett, and Moorhouse in 1976 (model-C) started with the Bethe-Salpeter equation incorporating an instantaneous potential having a scalar confining piece and a one gluon exchange piece. From this they obtained and solved a modified Salpeter equation (they droped the negative energy projections) to all orders of (v/c).

Table 13 compares the model predictions with the experimentally observed values. The SPEAR values for the ψ' and J/ψ resonance masses have been corrected[4] using the recent Particle Data Group

determinations.   A correction has also been included for the estimated

bias in the calibration (see Appendix F), which just cancels the

previous correction (both are $\simeq 2$ MeV). The masses reflect the unfolding

of the skewing in their signals from the γ energy dependence in their

production dipole matrix elements.   The fine structure may be compared

using a parameter first introduced by Schnitzer[5] to characterize the

splitting.

$$R = \frac{M(^3P_2) - M(^3P_1)}{M(^3P_1) - M(^3P_0)} \qquad\qquad (V-1)$$

The model of Buchmüller gives R_{th} = 0.61, while the relativistic

prediction of Henriques et al gives $\simeq 0.5$.   The data yields R_{exp} =

0.48±0.02.   Using a purely vector confining potential in the

Bethe-Salpeter equation leads to the prediction[6] R_{th} = 1.38.   The

theoretical analysis of the fine structure may be complicated by the

long range contribution to the spin-orbit interaction.   Since $\alpha_s \simeq 0.5$

for the $c\bar{c}$ seperation in the triplet P states, perturbation calculations

might be less reliable.

Excellent agreement is seen for the hyperfine splitting when compared

with the Byers and McClary derivation.   Models based on only a scalar

piece to the confining potential (no vector piece) result in a contact

spin-spin interaction.   In this short distance interaction, perturbative

QCD (one gluon exchange) might be expected to work well.   Including a

vector confining piece results in a long range spin-spin interaction,[7]

which can yield quite large hyperfine splittings.
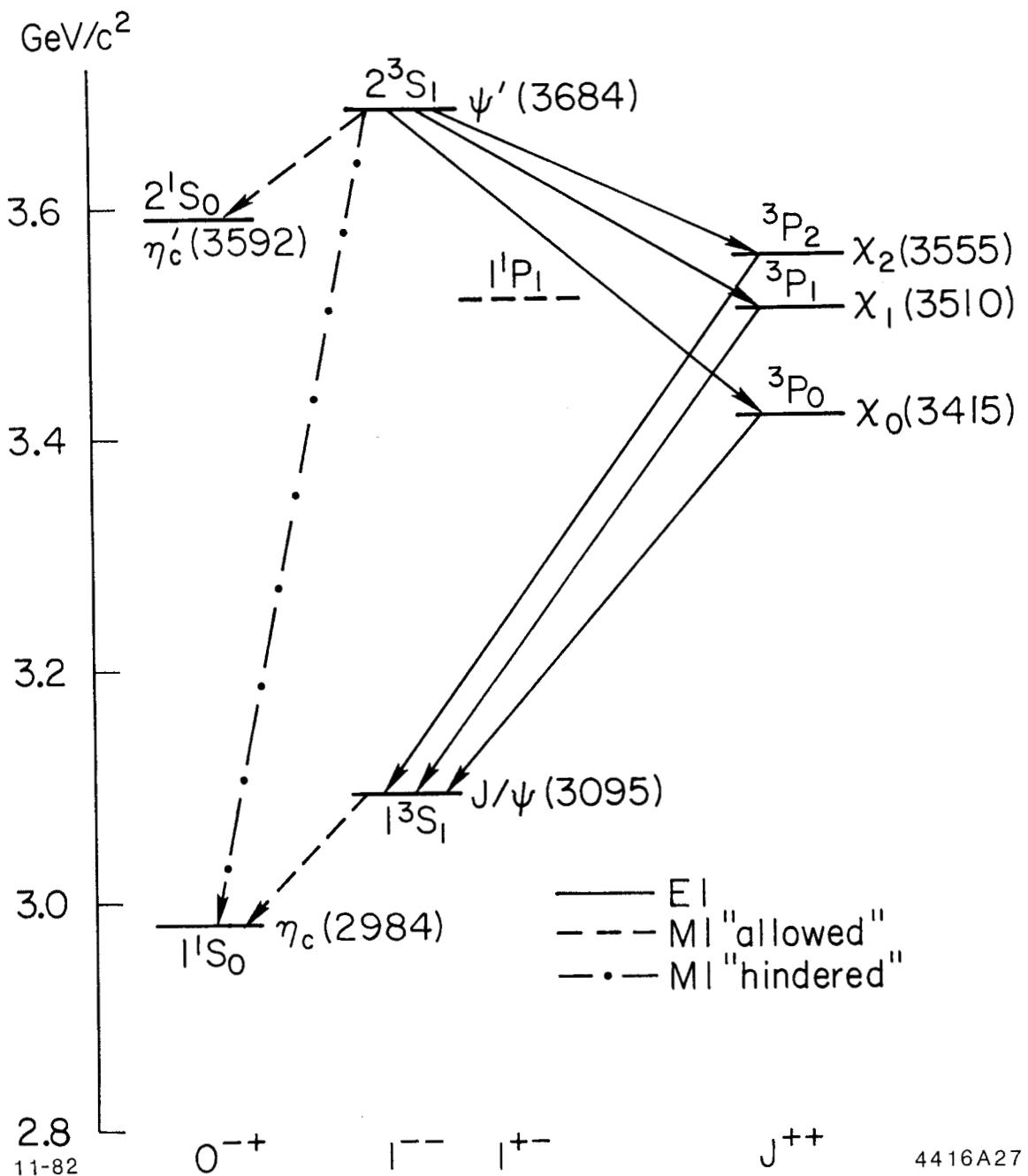
Figure 38: Current Status of the Charmonium Spectrum.
The level scheme for the bound states of charmonium is shown. The only state not yet observed and predicted by the theory is the singlet $^1P_1$ state. The radiative transitions allowed by the theory are indicated by: i) a solid line for the electric dipole transitions, ii) a dashed line for the "allowed" magnetic dipole transitions, and iii) a dot-dashed line for the "hindered" magnetic dipole transitions. The transition $\eta_c' \to \gamma J/\psi$ has not been observed.

TABLE 13

Charmonium Masses from the Inclusive Photon Spectra.
The masses of the charmonium states observed in radiative decays of the
ψ' and J/ψ calculated from the photon energies are given. The first
error is statistical from the fit and the second error is due to the
systematic uncertainty in the detector energy calibration. The
reference to theory is explained in the text.

STATE	MASS: (MeV)	EXPERIMENT	MODEL-A Ref. 1	MODEL-B Ref. 2	MODEL-C Ref. 3
$\eta_c'(3592)$		3591.5±0.9±4.0		3592±5	3.65±.03
$\eta_c(2984)$		2984.0±2.3±4.0		2984±5	3.02±.03
$\chi_2(3555)$		3557.8±0.2±4.0	3553	3523	3.54
$\chi_1(3510)$		3512.3±0.3±4.0	3502	3486	3.50
$\chi_0(3415)$		3417.8±0.4±4.0	3419	3380	3.42

5.2   CHARMONIUM NATURAL LINE WIDTHS

An analysis of the signal widths in the fitted inclusive photon
spectra allows for the possibility of measuring the state's natural line
width contribution. No previous experiment has determined the χ_J or
pseudoscalar widths. Practically speaking, the quality of the natural
line shape measurement depends on two interrelated factors: i) the
statistical significance of the signal, and ii) the relative size of the
state's width compared to the detector's resolution. The convolution
process used in the fitting is explained in Appendix F. For the
present, it is useful to formally express the state's natural line
width, Γ, as a function of the signal's full width, Γ_{sig}, and the
detector's full width resolution, Γ_{res}, as follows:

$$\Gamma = f[g(\Gamma_{sig}) - h(\Gamma_{res})]$$

$$(V-2)$$

where f, g, and h correspond to a functional relationship somewhere between quadratic and linear subtraction. The significance of the Γ measurement results from a complicated relationship between how precisely Γ_{sig} is known (depends on the signal's statistical significance), how precisely Γ_{res} is known (depends on how well the detector is understood) and how large Γ_{sig} is compared to Γ_{res}. As discussed in Chapter IV, in all cases where the natural line width determinations were difficult , an analysis of the fit's χ^2 significance relative to the state's width was used in the final evaluation of the width's error or upper limit. Table 14 summarizes the experimental results.

In the ψ' inclusive photon spectrum, the χ_J signals corresponding to the $\psi' \rightarrow \gamma\chi_J$ transition are highly significant. Based on the statistics of these signals alone it is possible to extract width measurements for the narrower states on the order of $\simeq 1$ MeV. However, the uncertainty in the detector's resolution is also of this order, and so entirely dominates the uncertainty in their natural width measurements or upper limits. For the χ_0 transition, the substantially broader signal width relative to the resolution results in a large value for the χ_0's natural line width relative to either the contribution due to the statistical uncertainty, or due to the resolution uncertainty. The χ_0 width measurement is quite significant.

For similar reasons the η_c width measurement results almost entirely from the $J/\psi \rightarrow \gamma\eta_c$ signal. Here the detector's full width resolution for the $\simeq 108$ MeV γ is $\simeq 12$ MeV, with an uncertainty much less than the purely statistical uncertainty in the resulting η_c width measurement.

However, the full width resolution for the $\psi' \rightarrow \gamma\eta_c$ transition γ is $\simeq 45$ MeV. Aside from the uncertainty in resolution, the low statistics for this transition render the extraction of a roughly 12 MeV natural line width insignificant. Consequently, the η_c natural line width measurement is primarily attributable to the signal width in the $J/\psi \rightarrow \gamma\eta_c$ transition, and the error in the width is dominated by the statistical uncertainty in that fitted signal.

Although the small absolute size in the resolution error for the $\simeq 92$ MeV γ from the $\psi' \rightarrow \gamma\eta_c'$ transition works in favor of a precise natural width determination, the signal's low statistics make it impossible to extract a significant measurement. In this case an upper limit for the η_c' natural line width contains contributions from both the statistical uncertainty in the signal and the uncertainty in the detector's resolution.

On the theoretical side, predictions for the charmonium state's decay rates to hadrons, the principal component[8] to their widths, is hampered by the calculational difficulties in QCD. Lowest order estimates,[9] obtainable from positronium theory after substituting for the QCD coupling constant and color factor, suggest a χ_0 width substantially below the measured value. Although the calculation of higher order QCD contributions to the χ_J state's absolute widths are not now possible, estimates of the corrections to the relative widths have been made,[9] as indicated in Table 14, and are found to be large. The relative χ_J state widths are in fairly good agreement with the higher order QCD corrected theory. Absolute estimates of the pseudoscalar hadronic widths with QCD corrections[9] are also seen to be in agreement with the measured values as shown in Table 14.

TABLE 14

Charmonium Natural Line Widths

The charmonium state's natural line widths extracted from the fitted inclusive photon spectra in decays of the ψ' and J/ψ are given. The errors, or 90% confidence level limits, reflect both the statistical uncertainty from the fit and the systematic uncertainty in the detector's energy resolution. The ratio of measured widths is also given. The reference to theory is described in the text.

DATUM	χ_0		χ_1		χ_2
Γ (MeV)					
Inclusive γ	(13.5-20.4)		< 3.8		(0.85-4.9)
Lowest Order QCD,[9]	$\simeq 2.4$		$\simeq 0.14$		$\simeq 0.64$
Relative Widths					
Inclusive γ	(2.8-24)	:	< 4.5	:	1
Lowest Order QCD,[9]	3.75	:	0.25	:	1
QCD Radiative Corr.[9]	6.8±0.4	:	0.17±0.03	:	1

DATUM	η_c	η_c'
Γ (MeV)		
Inclusive γ	$11.5^+4.5_-4.0$	< 7
QCD Radiative Corr.[9]	8.3±0.5	6.9±0.5

5.3 CHARMONIUM RADIATIVE TRANSITION RATES

5.3.1 $\psi' \to \gamma\chi_J$

Table 16 summarizes the branching ratio measurements obtained for the the $\psi' \to \gamma\chi_{0,1,2}$ transitions. The values shown were derived by averaging the four branching ratio results shown in Figure 35, weighted by their energy dependent errors.[10] The effect of the weighting process was to slightly de-emphasize the results from the uncut spectrum containing charged and neutral particles. Two errors are given for each branching ratio. The first error is dominated by the uncertainty in the photon detection efficiency and the statistical uncertainty from the fitted signals. The second error contains all the uncertainty in the

overall normalization, due mainly to the systematic error in the number of resonances produced (±5%) and to an absolute uncertainty in the photon detection efficiency (±5%). The error attributable to the systematic uncertainty in the detector's resolution is ≅±1%. For the relative ratio of transition rates shown in Table 16 the second error cancels. The ratios were calculated after normalizing by the factor $1/[E_\gamma^3 \cdot (2J+1)]$, yielding the ratio of electric dipole matrix elements as discussed below (see Equation (V-3). Comparison with the earlier SPEAR result[11] from the experiment SP-27 is seen to agree within the experimental error, although consistently lower.

The naive non-relativistic charmonium model predictions[7] for these branching ratios, based on the electric dipole formula [see Equation (V-3)], yield rates about a factor of two larger than observed.

$$\Gamma(\psi' \to \gamma\chi_J) = (4/27)(2J+1)Q^2\alpha|\langle\psi_f|r|\psi_i\rangle|^2 K_\gamma^3 \qquad (V-3)$$

The model of McClary and Byers[2] uses a Breit-Fermi Hamiltonian derived from an instantaneous approximation to a Bethe-Salpeter equation whose kernel contains both a one gluon Coulomb exchange plus a scalar linear confinement piece. They retain leading $(v/c)^2$ corrections to the non-relativistic model which result in additional spin-orbit, spin-spin, tensor, and spin independent forces. In the Byers and McClary model,[2] substantial corrections to the naive predictions were found, stemming from partial cancellations in the dipole matrix element which lowered the predicted rates [see Equation (V-3)]. They found that the matrix element overlap integral was very sensitive to shifts in the χ_J state wave functions due to the spin-orbit interaction. The sensitivity

resulted from the degree of overlap between the peak in the χ_J states radial wave function and the node in the radially excited ψ' wave function. Their final predictions,[12] (model-A) included in Table 16, also incorporated substantial corrections[6] resulting from ψ' coupling to nearby closed decay channels. Considering the factor of two discrepancy with the naive models, the agreement with the Byers and McClary model is substantially better. Included in Table 16 are the relativistic predictions[3] of Henriques, Kellett, and Moorhouse (model-B) which were discussed above. Their prediction agrees with the measurement to within the errors.

TABLE 16

Radiative Transition Rates for $\psi' \to \gamma\chi_J$.

The absolute and relative rates for $\psi' \to \gamma\chi_{0,1,2}$ obtained from the fitted inclusive photon spectra in decays of the ψ' are given here. The first error is the total energy dependent uncertainty used in calculating the errors for the ratio of transition rates. The second error is the systematic uncertainty in the overall normalization, which cancels in the ratio of rates calculation. The reference to theory is discussed in the text. The fitted photon energies are also listed.

DATUM	χ_0	χ_1	χ_2
E_γ (MeV)	258.4±0.4	169.6±0.3	126.0±0.2
$B(\psi'\to\gamma\chi_J)$ (%)			
Inclusive γ	9.9±0.5±0.8	9.0±0.5±0.7	8.0±0.5±0.7
SP-27 Ref. 11	7.2±2.3	7.1±1.9	7.0±2.0
Model-A Ref. 2	7.4±1.4	10.7±2.0	10.2±1.9
Model-B Ref. 3	10±2	9.8±1.8	6.5±1.2
Ratio of Rates (see text)			
Inclusive γ	1 :	1.07±0.08 :	1.39±0.11
Model-A Ref. 2	1 :	1.70 :	2.38
Model-B Ref. 3	1 :	1.14 :	1.12

5.3.2 $\chi_J \to \gamma J/\psi$

As was discussed in Chapter IV, the product branching ratios $B^2(\chi_{1,2})$ = $B(\psi' \to \gamma \chi_{1,2}) \cdot B(\chi_{1,2} \to \gamma J/\psi)$ extracted from the fits to the inclusive photon spectra suffer from a bias attributable to the overlap of the χ_1 and χ_2 signals in the ψ' spectrum. The size of the bias was estimated with a Monte Carlo calculation ($\approx 5\%$) and used to correct the product branching ratio measurements. The results are given in Table 15, where the errors are as described above for the branching ratio $B(\psi' \to \gamma \chi_J)$. Comparison with the other experimental results,[1,13-15] shown in the table is good.

Dividing the product branching ratios $B^2(\chi_{1,2})$ by the inclusive results for the $B(\psi' \to \gamma \chi_{1,2})$, from Table 16, yields the branching ratio $B(\chi_{1,2} \to \gamma J/\psi)$. Note that in these calculations the normalization errors cancel. For the branching ratio $B(\chi_0 \to \gamma J/\psi)$ the Crystal Ball exclusive channel product branching ratio[16] was divided by the inclusive result. In this case only the common normalization error due to the uncertainty in the number of ψ' resonances produced cancels. The results are shown in Table 15.

In order to compare these results with theory, the radiative rates must be calculated. Using the χ_J widths from Table 14 and the formula $\Gamma_{rad} = B(\chi_J \to \gamma J/\psi) \cdot \Gamma$ yields the values shown in Table 15. The quality of the measurements is dominated by the large error in Γ for the χ_J states. Consequently, the best determined radiative width is for χ_0. Virtually all theoretical models, whether corrected or not, are in agreement with the observed rates for $\chi_{1,2} \to \gamma J/\psi$. The naive model predictions for the χ_0 radiative width are slightly higher than the experimental value. For

completeness the Byers and McClary model predictions for these radiative

widths are included in the table.

TABLE 15

Radiative Transition Rates for $\chi_J \rightarrow \gamma J/\psi$.
The product branching ratio cascade rates determined from the fitted
inclusive photon spectra are compared with previous experimental
results. The use of the two errors is the same as explained in Table 16
for the $\psi' \rightarrow \gamma \chi_J$ transitions. Values for the calculated branching ratio
$B(\chi_J \rightarrow \gamma J/\psi)$, were obtained by dividing the product branching ratios
$B(\psi' \rightarrow \gamma \chi_{1,2}) \cdot B(\chi_{1,2} \rightarrow \gamma J/\psi)$ from the table by the inclusive branching
ratios $B(\psi' \rightarrow \chi_{1,2})$ from Table 16. $B(\chi_0 \rightarrow \gamma J/\psi)$ was calculated using the
Crystal Ball exclusive channel product branching ratio value.[16] For
comparison with theory, the absolute radiative rates $\Gamma(\chi_J \rightarrow \gamma J/\psi)$ are
calculated based on the natural line widths in Table 14 and the
branching ratio $B(\chi_J \rightarrow \gamma J/\psi)$. The comparison to theory is explained in
the text.

DATUM	χ_0	χ_1	χ_2
$B^2(\chi_J)$ (%)			
Inclusive γ	not seen	2.56±0.12±0.20	0.99±0.10±0.08
C. B. Exclusive	0.059±0.017	2.38±0.40	1.26±0.22
Mark-II	< 0.56	2.4±0.6	1.1±0.3
Mark-I	0.2±0.2	2.4±0.8	1.26±0.22
DESY-Heidelberg	0.14±0.009	2.5±0.4	1.0±0.2
$B(\chi_J \rightarrow \gamma J/\psi)$ (%)			
Inclusive γ	0.60±0.17	28.4±2.1	12.4±1.5
$\Gamma(\chi_J \rightarrow \gamma J/\psi)$ (KeV)			
Inclusive γ (90% C.L.)	51-167	< 1183	89-703
Model Ref. 2	117	240	305

5.3.3 Radiative Decays to the η_c and η_c'

Table 17 summarizes the pseudoscalar branching ratios obtained by

averaging the results from each spectrum. All contributions to the

uncertainty are given in the single error which includes a contribution

due to the uncertainty in the intrinsic detector resolution and a ±8%

normalization error. The dominant error is attributable to the low

statistics of their signals over a large background which is further

- 122 -

complicated by the correlation of the fitted signal amplitudes and widths (except for the transition $\psi' \to \gamma \eta_c$).

When the naive model prediction for the magnetic dipole transition $J/\psi \to \gamma \eta_c$ is properly corrected, as indicated by Sucher, Feinberg and Kang,[17] a rate is predicted in close agreement with the experimentally observed value, if the confining part of the potential is taken to have a scalar Lorentz structure. Table 17 includes this corrected model estimate given by Martin,[18] which is a factor of 2 below the naive M1 value. Since a similar correction for the transition $\psi' \to \eta_c'$ is lacking, the naive M1 theory prediction[6] is given in the table. A prediction for the hindered magnetic dipole transition $\psi' \to \gamma \eta_c$ obtained using a QCD sum rule,[19] is found to be in agreement with the observed value.

TABLE 17

Radiative Decays to the Pseudoscalar Candidates.
The branching ratios $B(\psi' \to \gamma \eta_c')$, $B(\psi' \to \gamma \eta_c)$, and $B(J/\psi \to \gamma \eta_c)$ obtained from the fitted inclusive photon spectra from J/ψ and ψ' decays are given. The errors reflect the total uncertainty in the branching ratio values. A description of the reference to theory may be found in the text.

DATUM	η_c	η_c'
$B(\psi' \to \gamma^1 S_0)$ (%)		
Inclusive γ	0.28 ± 0.06	$(0.5-1.2)$ 90% C.L.
QCD Sum Rule Ref. 19	0.35	
Naive M1 Theory Ref. 6		0.6 ± 0.1
$B(J/\psi \to \gamma^1 S_0)$ (%)		
Inclusive γ	1.27 ± 0.36	
Corr. M1 Theory Ref. 18	$(1.0-1.3)$	

REFERENCES

1. W. Buchmüller, Phys. Lett. $\underline{112B}$, 479 (1982).

2. R. McClary and N. Byers, UCLA/82/TEP/12, 1982, to be published.

3. A. B. Henriques $\underline{et}$ $\underline{al}$., Phys. Lett. $\underline{64B}$, 85 (1976).

4. M. Aguilar-Benitez $\underline{et}$ $\underline{al}$., "Review of Particle Properties," Phys. Lett. $\underline{111B}$, April (1982).

5. H. Schnitzer, Phys. Rev. Lett. $\underline{35}$, 1540 (1975).

6. E. Eichten $\underline{et}$ $\underline{al}$., Phys. Rev. $\underline{D21}$, 203 (1980). The naive M1 theory prediction obtained from this reference was calculated with a charmed quark mass of 1.6 GeV.

7. For example see: T. Appelquist, R. M. Barnett and K. Lane, Ann. Rev. Nucl. Part. Sci. $\underline{28}$, 387 (1978); W. Buchmüller and S.-H. H. Tye, Phys. Rev. $\underline{D23}$, 2625 (1981).

8. The theoretical gluonic (hadronic) decay rates for the x_J states can be converted into total widths using the data in Table 15. Assuming that the gluonic and radiative widths dominate, $Bh_J(x_J\rightarrow hadrons)$ = (0.994±0.002), (0.716±0.021), and (0.876±0.015), respectively for j=0,1,2. To get the total widths the absolute QCD predicted gluonic widths should be multiplied by $1/Bh_J$. To correct the widths relative to the x_2 width, the x_0 and x_1 QCD estimates should be multiplied by Bh_2/Bh_0 =(0.88±0.02) and Bh_2/Bh_1 = (1.22±0.04), respectively.

9. R. Barbieri, R. Gatto, E. Remiddi, Phys. Lett. $\underline{61B}$, 465 (1976); R. Barbieri, M. Caffo, R. Gatto, E. Remiddi, Phys. Lett. $\underline{95B}$, 93 (1980); R. Barbieri, R. Gatto, E. Remiddi, Phys. Lett. $\underline{106B}$, 497 (1981).

10. The energy dependent error in the branching ratio is mainly a

combination of the statistical error from the fit and the photon energy dependent error in the photon detection efficiency (as opposed to the overall normalization error).

11. C. J. Biddick et al., Phys. Rev. Lett. 38, 1324 (1977).

12. The width of the ψ' is taken to be (215±40) KeV. This error shows up in some of the model predictions, when calculating a branching ratio.

13. T. M. Himel et al., Phys. Rev. Lett. 44, 920 (1980).

14. J. Whitaker et al., Phys. Rev. Lett. 37, 1596 (1976).

15. W. Bartel et al., Phys. Lett. 79B, 492 (1978).

16. M. Oreglia et al., Phys. Rev. D25, 2259 (1982).

17. G. Feinberg and J. Sucher, Phys. Rev. Lett. 35, 1740 (1975); K.S. Kang and J. Sucher, Phys. Rev. D18, 2698 (1978).

18. A. Martin, "Quarkonium Phenomenology," in the Proc. of the XXI International Conference on High Energy Physics, Paris, July 26-31, 1982, Ref.TH.3397-CERN, August 26, 1982.

19. M. A. Shifman, Z. Phys. C4, 345 (1980).

Appendix A

CHARMONIUM THEORY

The model for a strongly bound system of a quark and antiquark is known as quarkonium. The quarkonium model applicable to the J/ψ family is called charmonium, with reference to the flavor quantum number charm, carried by the quark antiquark pair (c$\bar{c}$). The members of the family have a net charm of zero, as it cancels in the particle antiparticle pair. The states are distinguishable by other quantum numbers, such as spin ($\vec{S}$), orbital angular momentum ($\vec{L}$), space parity (P), charge parity (C), and energy (E). Because of the symmetry in fermion-antifermion bound states, not all the quantum numbers are independent. If $\vec{J}$ is the total angular momentum, due to $\vec{L}$ and $\vec{S}$ coupling, then it is known[1] that:

$$C = (-1)^{L+S} \text{ and } P = -(-1)^{L}, \qquad (A-1)$$

where $\vec{J} = \vec{L} + \vec{S}$, $\vec{S} = \vec{S}_c + \vec{S}_{\bar{c}}$, $J = L + S_z$, $L = 0,1,2,...$ or S,P,D,... in spectroscopic notation, $S = 0$ or 1, and $S_z = 0,\pm 1$. These results are independent of the interaction, and predict the following two sets of states:

singlet states   triplet states

    $S=0$ $S=1$

    ^1L_J ^3L_J

where $J = L$ where $J = L-1,L,L+1$, if $L > 0$

                            or $J = 1$ if $L = 0$ (A-2)

    $C = (-1)^L$ $C = -(-1)^L$

    $P = -C$ $P = C$

for $L = 0,1,2,...$, where the spectroscopic notation, $^{2S+1}L_J$, is used for
a state with spin $= S$, orbital angular momentum $= L$, and total angular
momentum $= J$.

The charmonium energy (mass) spectrum within the purely quantum
mechanical constraints given by (A-2), is determined by the details of
the full strong interaction dynamics between the $c\bar{c}$ pair. In this way,
states with different quantum numbers will have different masses to the
extent that the quantum numbers enter into the interaction. For an
interaction which depends only on the separation of the constituents,
the quantized radial excitations constrain the possible values for the
angular momentum. For the radial quantum number, $n = 1,2,3,...$,
indicating $n-1$ nodes in the radial wave function, the angular momentum
is limited to $L = n,n-1,n-2,...,0$. The following states are possible:

3 $^1S_0, ^3S_1$ $^1P_1, ^3P_{0,1,2}$ $^1D_2, ^3D_{1,2,3}$ $^1F_3, ^3F_{2,3,4}$

2 $^1S_0, ^3S_1$ $^1P_1, ^3P_{0,1,2}$ $^1D_2, ^3D_{1,2,3}$ (A-3)

1 $^1S_0, ^3S_1$ $^1P_1, ^3P_{0,1,2}$

---

n L = 0   1   2   3 ...

The ordering of the states in terms of mass will again depend on the details of the interaction.

Understanding spectroscopy viewed as an observable property of the underlying quark structure is essentially a bound state field theoretic problem in the strong interaction. Currently the best candidate for a theory of the strong force is quantum chromodynamics (QCD). It is hoped, but not presently realizable, that in QCD the meson spectroscopies can be calculated precisely. Perturbative calculations in QCD fail to converge for separations roughly $\gtrsim$ 1 Fermi, where the strong coupling constant, α_s, grows larger than 1. The interaction energy between quarks separated a large distance increases linearly with distance, resulting in a constant attractive force of $\simeq$16 tons. In this confinement domain, perturbation theory breaks down. At the other end of the scale for separations roughly $\lesssim$ 1 Fermi, QCD predicts the interaction to be weak, i.e., $\alpha_s < 1$. With small enough separation the quarks are expected to become asymptotically free states. Here lowest order perturbation theory (one gluon exchange) is expected to yield reasonable predictions. Figure 39 shows the QCD value for the strong

coupling constant, α_s, as a function of the momentum transfer squared. The sizes of a few of the charmonium states are also indicated.

Aside from the numerous decay channels of charmonium, two features in the $c\bar{c}$ decay scheme are notable in relation to this investigation. The first is the empirically observed suppression of the annihilation channel, theoretically attributable to asymptotic freedom and the small value of $\alpha_s \simeq 0.25$. The annihilation process involves contact between the quark and antiquark, which then convert into gluons. The second is the threshold for $c\bar{c}$ decays into $D\bar{D}$ pairs, where each D meson is composed of a c quark bound to a lighter u or d antiquark. With reference to (A-3) the 2D and n ≥ 3 states are observed to be above the $D\bar{D}$ threshold (≈3730 MeV) and to have widths ranging from 25 to 80 MeV. Below the threshold, seven states are observed within ≈700 MeV of each other. Their widths range from ≈63 KeV to ≈15 MeV. Extensive experimental investigation of the excitation spectrum below the $D\bar{D}$ threshold has been possible because the two J(PC) = 1(--) triplet states (J/ψ(3095) and ψ'(3684)) produceable in e^+e^- machines, are very narrow relative to the beam energy spread in the storage ring, and possess large production cross sections (their leptonic branching ratios are large).

Since as yet no field theory of the strong interactions has been able to explicitly solve the heavy quark-antiquark bound system problem, a major effort has been directed toward the employment of an instantaneous potential in conjunction with the experience gained from QED as a vehicle to carry out the desired calculations. Inasmuch as the charmonium binding energies are small compared to the c quark mass, by
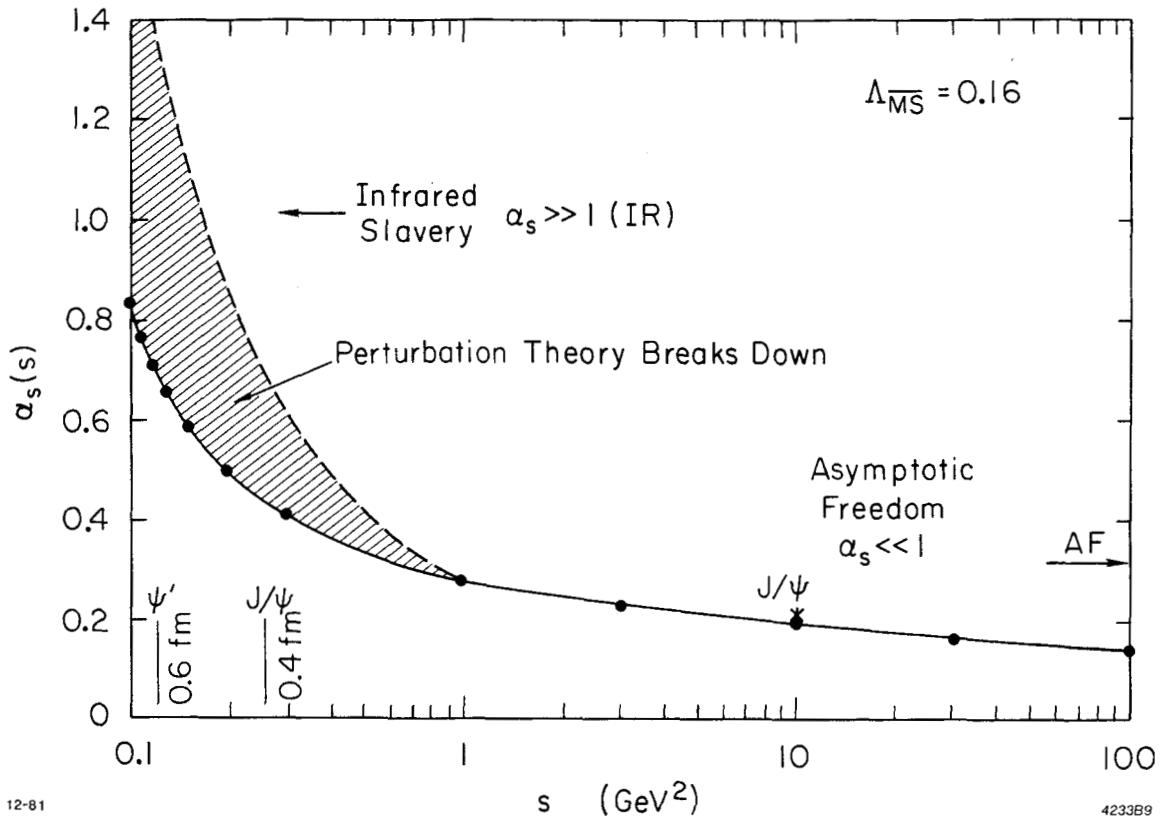
Figure 39: $\alpha_s(S)$ Versus S and the Size of Charmonium.
The radial expectation value, $\langle R^2 \rangle^{1/2}$, for a few of the charmonium bound states is shown along with the value for the strong coupling constant, $\alpha_s(S)$, as a function of $S = q^2$ = the momentum transfer of the strong process squared. The point labeled J/ψ at $S = 10$ GeV^2 gives the α_s value for the J/ψ annihilation into gluons. The sizes of the charmed states equate with a larger value for α_s corresponding to a smaller momentum transfer squared.

far the most powerful approximation in terms of calculating assumes a nonrelativistic system with a spin-independent central potential. All the formalisms of nonrelativistic quantum mechanics and static potential theory can be used. The standard potential includes two terms, one for asymptotic freedom and one for confinement:

$$V(R) = -k/R + R/a^2 \qquad\qquad (A-4)$$

where the first term can be considered due to single gluon exchange and the second term represents confinement. The spectrum and wave functions are obtained by solving the Schrödinger equation. Since QCD suggests only the asymptotic form of the potential (short distance and long distance) a variety of functions (and derivations) for the intermediate region have been tried.[2-7] Figure 40 shows a comparison of a few of the potentials used, along with the corresponding mean square radii of charmonium states. The approach may be modified by including effects due to coupling with nearby states above and below the charm threshold.[3] Spin and relativistic effects may be calculated perturbatively.[9] Uncorrected limits on the E1 rates can also be estimated by using dipole sum rules.[10] For completeness the dipole rate formulae[11,12] for radiative transitions between states with quantum numbers $J_i L_i S_i \rightarrow J_f L_f S_f$ are given below.
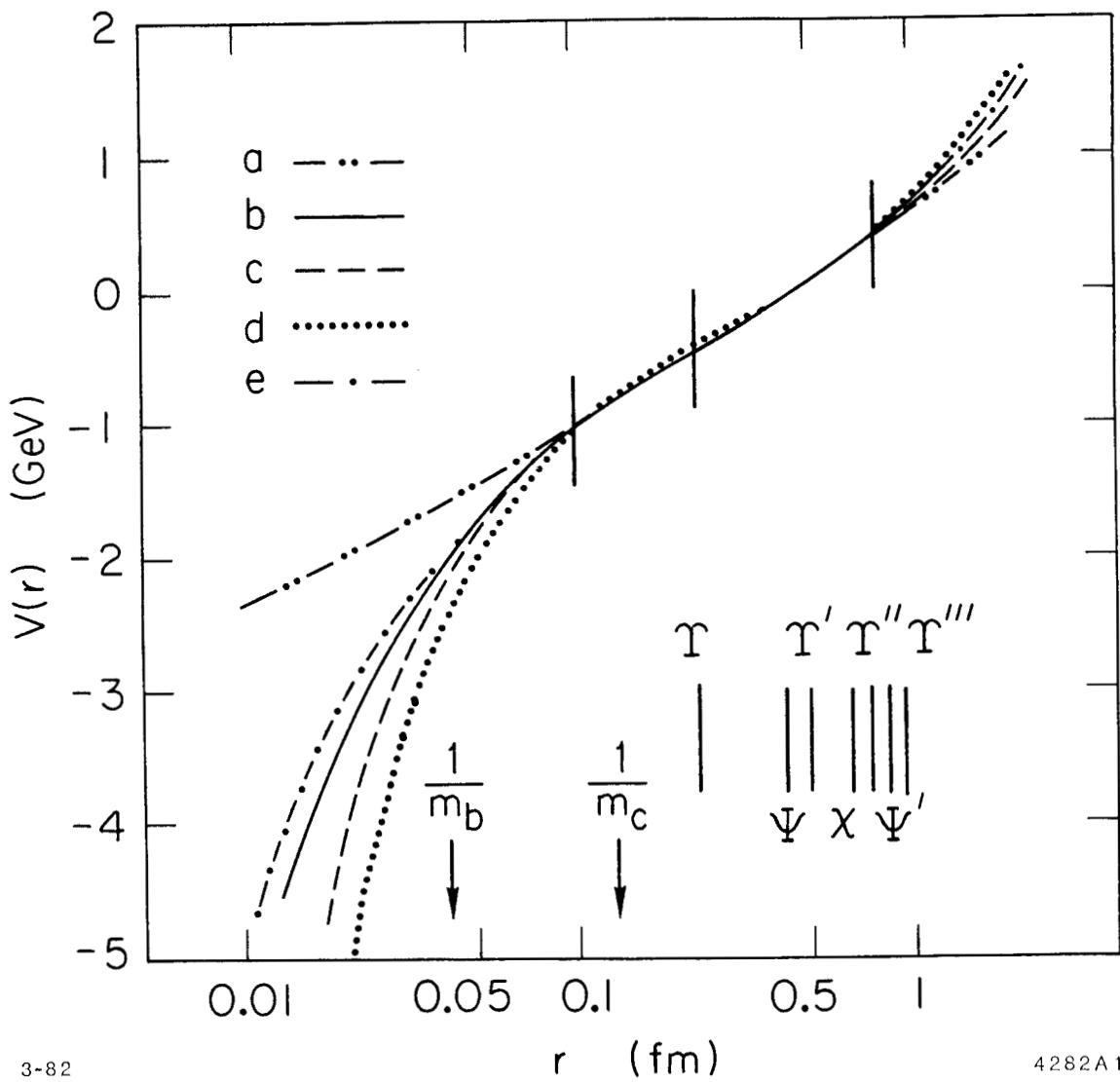
Figure 40: Charmonium Potentials.
A comparison[8] of some of the potentials which have been used to fit the charmonium system: a) $A+B \cdot R^x$ potential[8] with $x \simeq 0.1$; b) QCD inspired potential;[5] c) Coulomb plus linear plus logarithmic interpolation potential;[4] d) Coulomb plus linear potential;[3] e) same as c) but including running coupling constant dependence,[7] $\alpha_s(R)$. The error bars indicate the R independent normalization uncertainty.

E1 (no spin flip, parity flip, $S_i = S_f$) Ref. 11

$$\Gamma_\gamma = (4/3)(2J_f+1)Q^2\alpha|\langle\psi_f|r|\psi_i\rangle|^2 K_\gamma{}^3 S_{fi}$$

where, $S_{fi} = S_{if} = \begin{Bmatrix} S & L_f & J_f \\ 1 & J_i & L_i \end{Bmatrix}\cdot MAX(L_i, L_f)$

is defined interms of the 6j symbol.

M1 (spin flip, no parity flip, $L_i = L_f$) Ref. 12
For transitions between $^3S_1$ and $^1S_0$ only.   (A-5)

$$\Gamma_\gamma = [4/(2S_i+1)](Q^2\alpha/M_q{}^2)|I|^2 K_\gamma{}^3[(M_i{}^2+M_f{}^2)/(2M_i{}^2)]$$

where, M_q is the quark mass,
M_i (M_f) is the initial (final) state mass, and
$I = $ radial matrix element $= I_1 + I_2 + I_3 + I_4$

$I_1 = \langle\psi_f|-j_0(K_\gamma r/2)|\psi_i\rangle$
    is the nonrelativistic amplitude,

$I_2 = \langle\psi_f|2p_q{}^2/(3M_q{}^2)|\psi_i\rangle$
    is the spin-independent relativistic correction,

$I_3 = (\pm)\langle\psi_f|V_{ss}|\psi_i\rangle 4/(M_i-M_f)$
    is the spin-spin interaction effect on the radial
    wave function and applies only to the M1 hindered
    transitions, V_{ss} is the spin-spin interaction
    potential, the $+(-)$ sign is for $S_i = 0(1)$,

$I_4 = \langle\psi_f|V_s j_0(K_\gamma r/2)|\psi_i\rangle/M_q$
    is the virtual quark pair correction, and V_s is
    the scalar part of the potential.

These formulae are good to order $(v/c)^2$ when the eigenvalues and
eigenfunctions used in the calculation are also correct to this order.

    More complex approaches include spin dependence via a Breit-Fermi
Hamiltonian including all relativistic corrections[13] to order $(v/c)^2$ in
the quark velocity. The spin-dependent part of the potential can be
written as:

$$V_{spin} = (3V_v' - V_s')\vec{L}\cdot\vec{S}/(2m^2R)$$

$$+ (\nabla^2 V_v)2\vec{S}_1\cdot\vec{S}_2/(3m^2)$$

$$+ (V_v'/R - V_v'')(3\vec{S}_1\cdot\hat{n}\vec{S}_2\cdot\hat{n} - \vec{S}_1\cdot\vec{S}_2)/(3m^2) \qquad (A-6)$$

where, $\hat{n}$ is the unit radial vector.

The fine structure is given by the first term (spin-orbit interaction) and the third term (tensor interaction). The second term yields the hyperfine structure, where the Laplacian operating on V_v produces a delta function (contact) term. The exact form of Equation (A-6) depends on assumptions regarding the Lorentz structure of the potential. As shown, the scalar part (V_s) contains all of the linear confining piece. The Coulomb exchange part is contained in the vector part, V_v. There is an additional long range dependence in the spin-orbit term which does not exist in QED, resulting from the scalar part of the potential. Setting $V_s = 0$ would give the Breit reduction found in QED. An analog of the Breit-Fermi equation has been calculated for an arbitrary potential from QCD without the necessity of inputing Lorentz structure.[14] This calculation yielded an opposite sign for the long range spin-orbit interaction. The Klein-Gordon equation was used in another approach, with a static potential to gauge the effect of relativistic wave functions on the E1 rates.[15] In addition, relativistic corrections can be applied consistently to the electric dipole rate formula.[16] Relativistic sum rules have provided a corrected estimate of the relative E1 rates.[17] It is possible to avoid the non-relativistic assumption and retain the use of an instantaneous potential with spin dependence and a particular Lorentz structure by solving the Salpeter integral equation of motion.[18] In this case

relativistic wave functions are also obtained. Others have calculated

the leading QCD corrections.[19,20]

An approach independent of potential models, based on the calculable

aspects of QCD such as gluonic vacuum expectation values, perturbative

amplitudes, and dispersion relations,[21] attempts a "first principles"

formulation (QCD sum rules are derived).   The procedure includes

relativistic effects, the non-Abelian and noninstantaneous nature of the

gluonic field, and couplings to mixed states.   Although the methods are

formalized and not ambiguous,   they do not easily lend themselves to

generalizations beyond predictions for the ground states.

A comparison[24] of the predictions among the models listed above and

to some preliminary results from this investigaiton may be found in the

references.

Appendix B

MAGNETOSTRICTIVE SPARK CHAMBERS

Magnetostrictive spark chambers[25] (MSSC) were chosen as the primary charged particle tracking system because of their superior resolution capabilities within the narrow spatial confines of the Crystal Ball's interior, and because of their clean signals and insensitivity to low level beam related backgrounds. A cylindrical geometry was selected as the most compatible with the inner detector space, bound by the cylindrical beam pipe on the inside and by the spherical cavity of the Crystal Ball on the outside. A 1 mm wire spacing yielded a maximum geometrical resolution of about ±5 mr, to be compared with about ±22 mr for the multiwire proportional chambers (MWPC). The MWPC package was included to compensate for the known sag in spark chamber efficiency as the charged particle multiplicity increases. The design philosophy for the central chambers can be summarized as follows: the magnetostrictive spark chambers were responsible for reconstructing a few gold plated charged particle tracks, while the MWPC's were responsible for tagging the charged particles missed due to the MSSC inefficiency.

A reconstructed track refers to the result of a successful straight line fit to a group of spark chamber hits and is constrained to pass through the z-axis. The fits were made independently of any bump information from the NaI. After all the reconstructed tracks were found, the remaining MSSC and MWPC hits not correlated with a fitted

track were used to tag bumps as charged. The tagging scheme was necessarily less precise than the reconstruction technique. The outcome yielded a charged particle detection efficiency of (85-92)% and a photon overtagging probability of ≃10%.

B.1   CONSTRUCTION

A cross sectional schematic of the spark chambers is shown in Figure 9. The basic component in the chamber structure is the laminated cylindrical shell. The shells serve as: i) the plane upon which the etched wires are mounted, ii) the enclosure for the Ne-He gas mixture (90%/10%), and iii) the main structural support for the chambers. Using aluminum mandrels turned on a lathe to the desired OD dimension, the laminated shells were contructed as follows:

1)   The inner conductor/Mylar was wrapped on the mandrel and coated with epoxy.
2)   A thin layer of styrofoam was tightly wrapped around the epoxy which was allowed to set.
3)   The styrofoam was "machined" to the desired OD dimension. (0.036 inches for MSSC and 0.060 inches for the MWPC). A coat of epoxy was applied.
4)   The outer conductor/Mylar was wrapped tightly and the epoxy was allowed to set.

When the epoxy had set, the laminated shell was pulled from the mandrel. The smaller diameter shells were joined to the larger shells with specially machined lucite rings at the ends of the chambers. The rings included provisions for gas inlets and outlets, and machined fingers for holding the magnetostrictive wands tightly against the etched spark planes.

The MSSC package consisted of two chambers. The inner chamber with an ID for the innermost spark plane of 13.98 cm was separated from the

OD of the beam pipe by $\simeq 1$ cm, and was the closest part of the detector to the interaction region (IR). It had an active length in the z direction of $\simeq 57$ cm subtending a solid angle of $\simeq 94\%$ of 4π sr. The chamber was divided into two 9.0 mm spark gaps delimited by a single shell. Two shells formed the inner and outer surfaces. The outer spark chamber was separated from the inner spark chamber by the MWPC. The ID of the outer MSSC was 25.65 cm and it had an active length of $\simeq 28$ cm or $\simeq 71\%$ of 4π sr. It was also divided into two 9.0 mm gaps and was built from 3 laminated shells.

Each of the four spark gaps was formed by a ground plane[26] of etched copper-Mylar facing a negative high voltage plane of etched copper-Mylar. The etched wire tracings were 0.012 inches wide with a 1.0 mm spacing. The two high voltage planes for each chamber were constructed on the middle shell and the tracings were all parallel to the z-axis ($0°$ stereo angle). The ground tracings for the inner (outer) chamber were inclined to a stereo angle of $30°$ ($45°$). For the inner chamber the $30°$ ground planes had opposite helicity, while for the outer chamber they had opposite helicity in the 1978 and 1979 data, but the same helicity in the 1980 and 1981 data, when new chambers were installed.
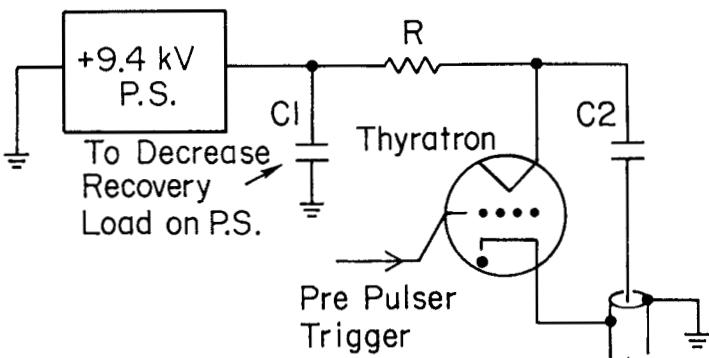
The ground and high voltage spark planes extended beyond the lucite rings outside the spark gaps. The magnetostrictive wands were fastened against the planes at this exterior point. The wands had to be specially designed to allow them physical flexibility, since they were wrapped around the exposed ends of the etched spark planes. The wands were built up with three pieces of teflon spaghetti surrounded with

shrink tubing. The wire was fed through the middle teflon and anchored

at one end with a soft setting epoxy/RTV mixture to provide acoustic

dampening. The other end of the wand was fastened to the pick up coil

and bias magnet head. The four wands in each chamber were held in place

firmly against the etched conductors by machined lucite fingers.

The gas system consisted of two stages of low pressure regulators fed

by a bank of 1A cylinders containing a mixture of Neon(90%) and

Helium(10%). A flow rate of $\simeq$0.2 SCFH per gap was maintained and

monitored by bubbling the return gas from the gaps through a mineral oil

bath. The driving pressure was $\simeq$0.25 inches of water.
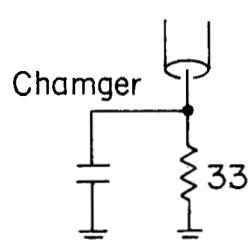
Each gap was driven by three 33 Ohm (source impedance) cables charged

to 9.4 KV and discharged by a Thyratron pulser (see Figure 41). The

Thyratron was fired by a prepulser which was triggered by a signal from

the control room event trigger logic. The 4.5 KV negative going pulse

from the Thyratron had a width of $\simeq$250 ns and was terminated at the gap

with its characteristic 33 Ohm impedance. Spark formation was observed

to require $\simeq$ 150-170 ns, leaving $\simeq$ 80-100 ns for the spark discharge.

During the discharge, about 280 amps of current was available for all

the spark channels formed. The gap termination, as shown in Figure 42,

was distributed between the gap fiducials and resistance to ground. Two

tracings from each plane were isolated as fiducials; one was held as a

spare. Roughly 63 amps of current was allowed for each fiducial during

spark formation period.

When a spark occurred in a gap along the ionized path of a charged

particle, current would flow across the spark and through a pair of

etched tracings, one on the high voltage plane and one on the ground
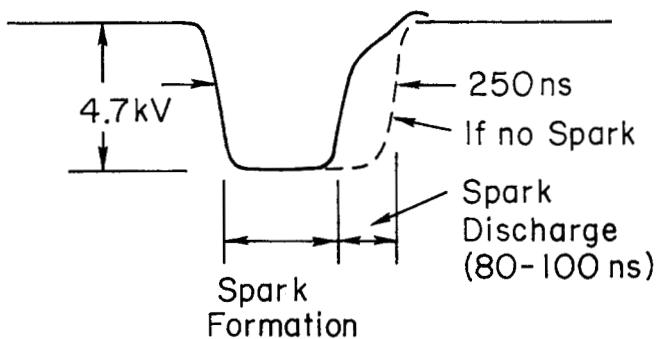
THYRATRON PROPERTIES
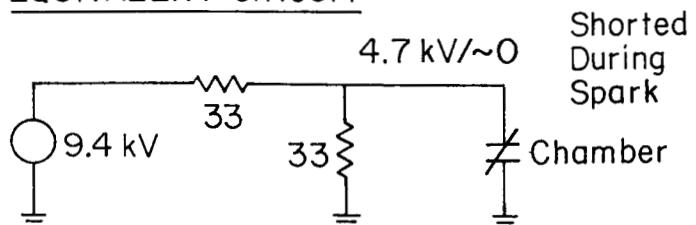
1. Fast Switching.
   Rise Time ~ 20 ns
2. Hi Load Currents.
   ($\geq$ 1000 a)
3. Hi Voltage Isolation

H.V. Pulse

4.7 kV

250 ns

If no Spark

Spark
Discharge
(80-100 ns)

Spark
Formation

EQUIVALENT CIRCUIT

Shorted
During
Spark

4.7 kV/~0

9.4 kV

33

33
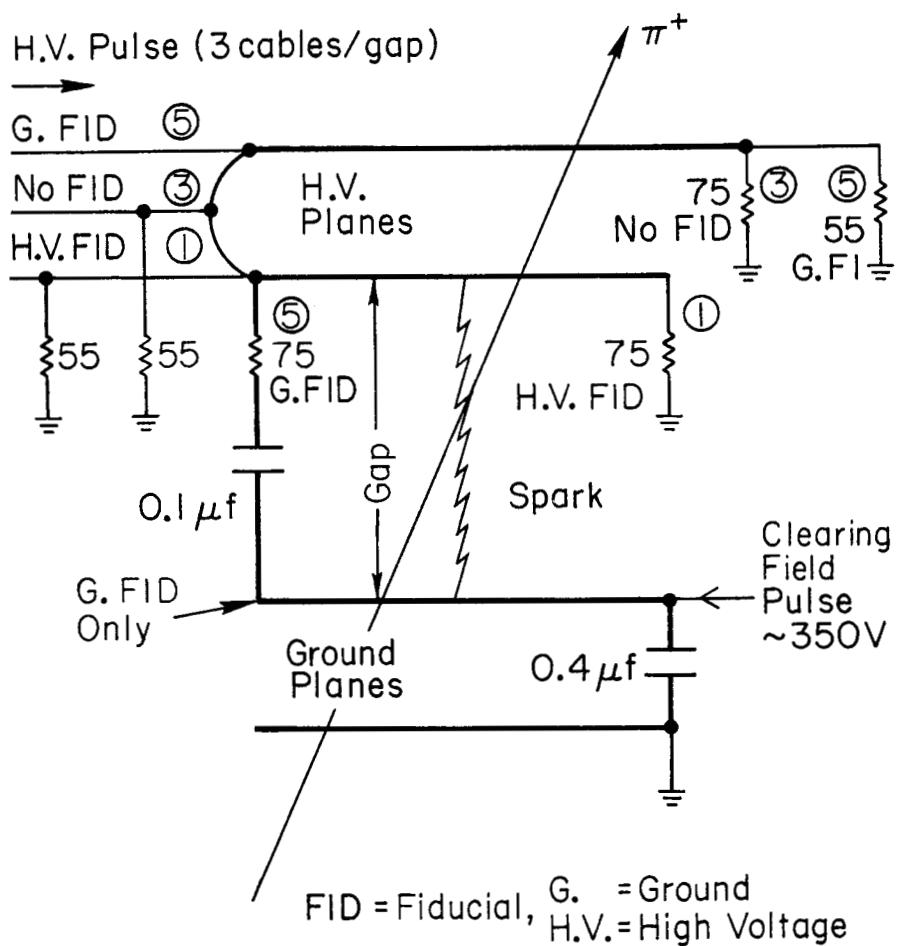
Chamber

$$I_{spark} = \frac{2V}{33} \sim 280 \, a \text{ for } \sim 80\text{-}100 \, ns$$

12-82   4416A58

Figure 41: Spark Chamber High Voltage Pulse.
The general features of the Thyratron high voltage pulser used to fire
the spark chambers is outlined. The MSSC represents a capacitive load
until the spark discharge occurs, when it is seen as a short.

H.V. Pulse (3 cables/gap)

G. FID ⑤

No FID ③ H.V. Planes

H.V. FID ①

75 ③ ⑤
No FID 55
G.FI

⑤
75
G.FID

75 ①
H.V. FID

55 55

0.1 μf

Gap

Spark

G. FID
Only

Ground
Planes

0.4 μf

Clearing
Field
Pulse
~350V

π^+

$FID = Fiducial, \quad \begin{matrix} G. & = Ground \\ H.V. & = High\ Voltage \end{matrix}$

$I_{FID} = \dfrac{4.7\ kV}{75\ \Omega} = 63\ a$

12−82
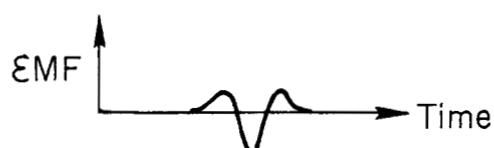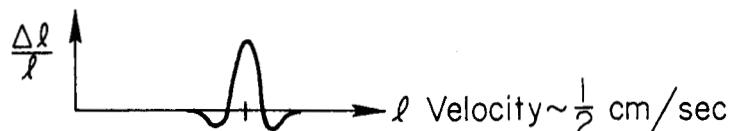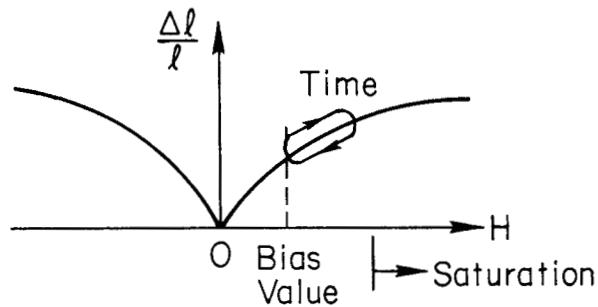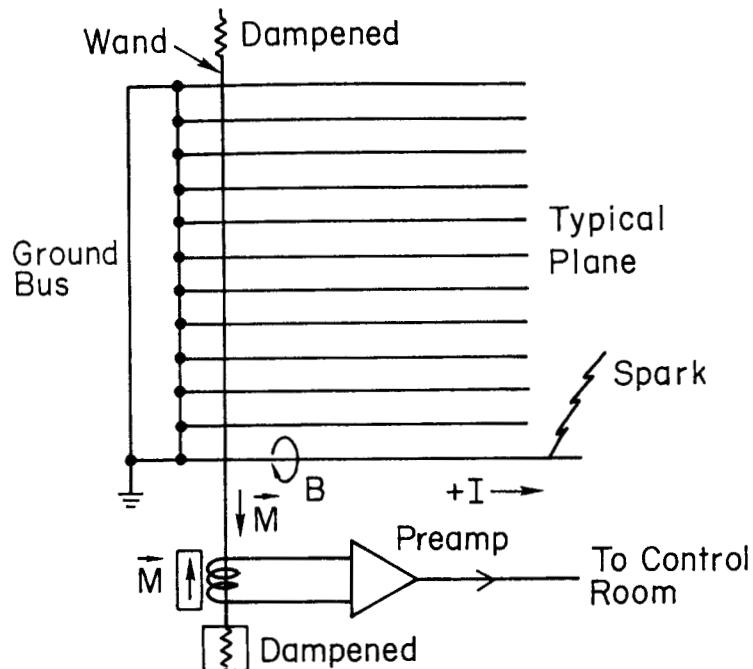
4416A59

Figure 42: Typical Single Spark Chamber Gap Termination.
The schematic shows the fiducials, the distributed terminations, and the
clearing field connection for one gap in the MSSC.

plane, ultimately passing next to the magnetostrictive wands. The process is illustrated in Figure 43. The pulse of current and associated magnetic field would excite an acoustic wave in the magnetostrictive wire. The wave would generate a pulse of magnetic flux through the pick-up coil driven by the bias magnet. The change in magnetic flux through the coil generated a voltage pulse which was preamplified in the dry room and fed differentially to the counting house amplifier, resulting in a $\simeq$ 1.5 volt signal.

The amplified wand signals were passed through a zero-cross detector to remove bias due to a variable pulse amplitude. The zero-cross signals were fed to a time digitizer with memory in a module on a special CAMAC branch of the computer. When the digitization was through, the computer controller would read the data from the memories via a direct memory access (DMA). During the DMA, a 350 volt pulse lasting 15 ms was fed to the ground planes to clear ions left over from any spark discharge. The timing sequence is summarized in Figure 44, and required a total dead time of 40 ms. The data were in the form of channel numbers corresponding to the transit time of the acoustic pulses in the wand wire plus an offset. Using the offline software, the offset could be removed by subtracting the first fiducial time, and the transit times could then be mapped into fractions of a circumference on the appropriate MSSC plane, or into angles. By comparing the overlaps between hits in the various planes, space points corresponding to the sparks were obtained.

Figure 43: Operation of the Magnetostrictive Wand.
The physics of the magnetostrictive wand is illustrated. The spark
current excites an acoustic wave in the wand wire, which induces an EMF
in the pickup coil.
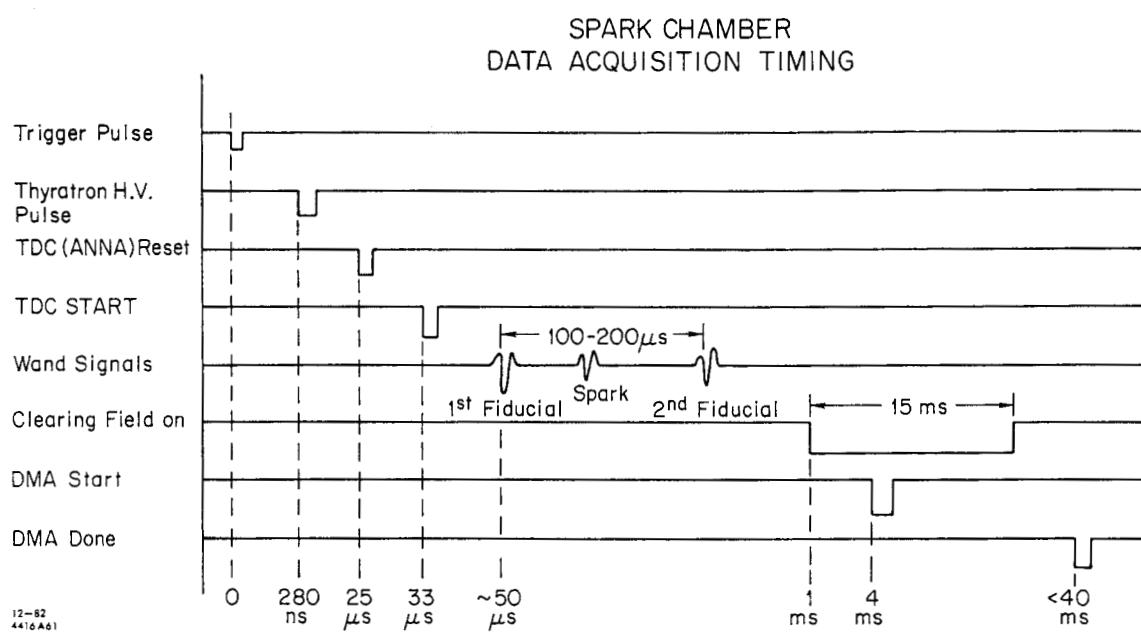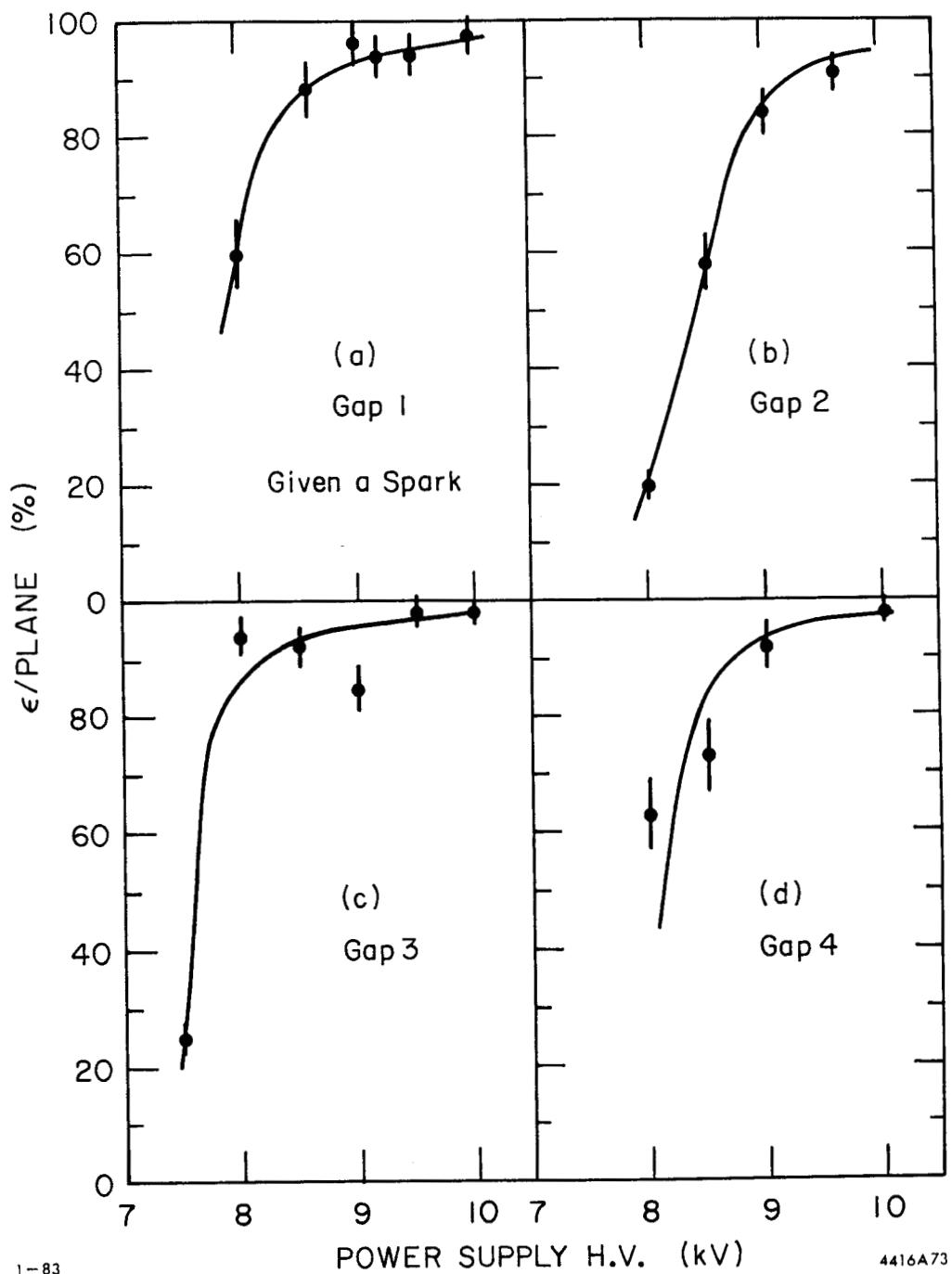
Figure 44: MSSC Data Acquisition Timing.
The sequence of events involved in obtaining the the MSSC data is
illustrated.

B.2   OPERATION AND PERFORMANCE

Information on the MSSC charged particle detection efficiency was
obtained using: i) a pion test beam,   ii) cosmic rays,   iii) Bhabha
events, iv) the number of charged particles found in the photon spectrum
for inclusive decays of the ψ' and J/ψ, and v) the number of π^0's found
in the gamma-gamma,   gamma-charge,   and charge-charge mass spectra.
Figure 45 shows the results of a test using cosmic rays.   Plastic
scintillators were used to define the timing and the presence of cosmic
rays.   After triggering the spark chambers,   the coincident hits within
the expected region of the chamber were counted.   Figure 46(a) shows the
outcome of a similar test using a charged pion test beam.   Both of these
investigations were performed when the spark chambers were isolated from
the rest of the detector.   Figure 46(b) was obtained by studying the
chamber's response to Bhabha events using the full detector at SPEAR.
The events were defined by back-to-back energy deposits in a narrow
window about the e^+e^- beam energy.   A clear plateau in efficiency is
seen at ≈ 9.4 KV, which is where the MSSC were operated. During the data
acquisition period at SPEAR the back-to-back e^+e^- efficiency was
monitored on a run by run basis and was generally found in the interval
(85-95)%.

However, a substantially decreased efficiency was observed for events
with more than two charged particles.   Studies using the Monte Carlo
simulation of the MSSC and MWPC indicated that spark chamber
efficiencies per plane in the range (70-75)% were necessary in order to
obtain plane occupancies for fitted and tagged tracks comparable to what
was seen in the inclusive hadronic data.
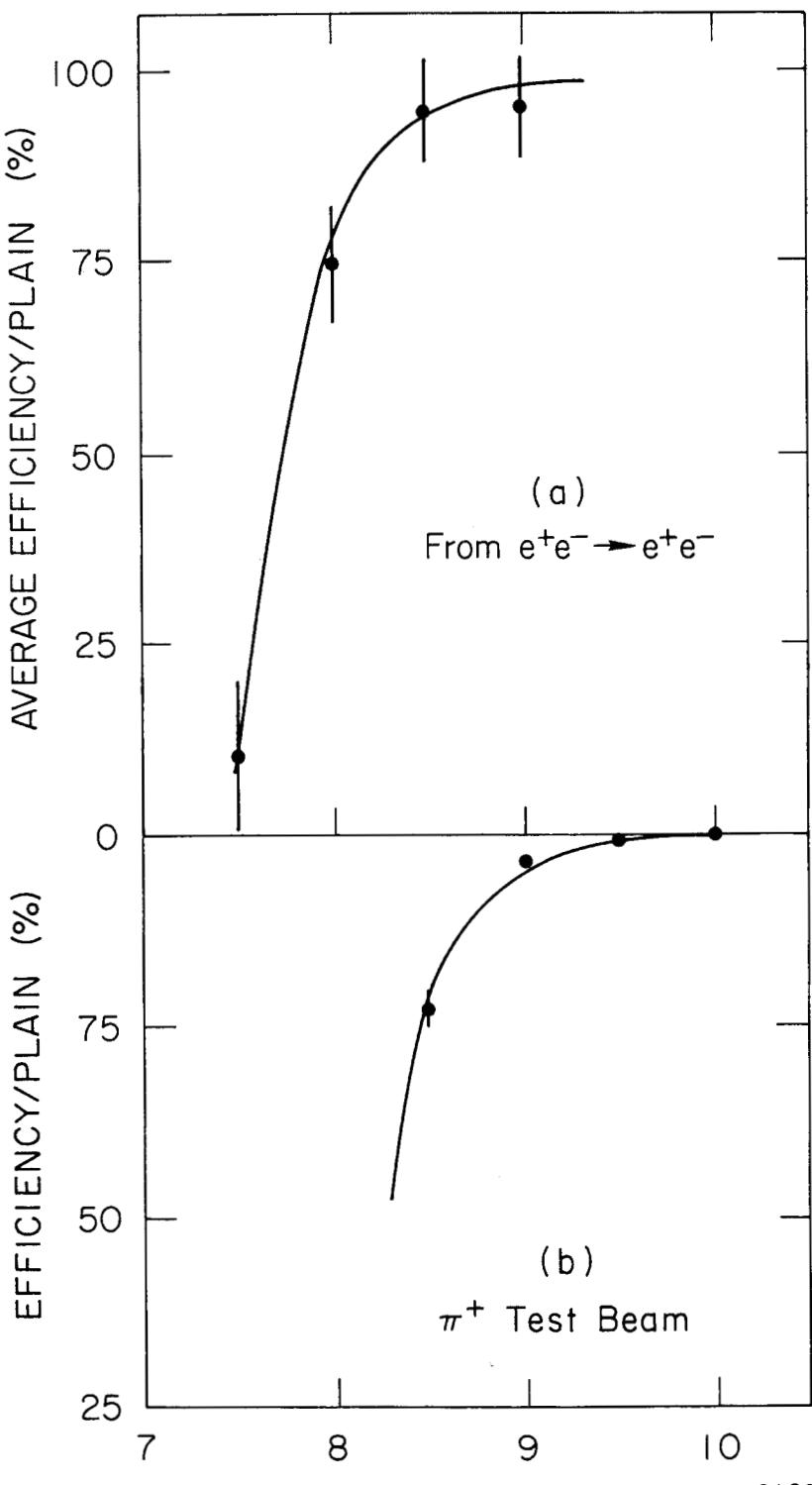
Figure 45: Spark Chamber Efficiency from Cosmic Rays.
A plot of the cosmic ray detection efficiency per gap for the ground
planes versus the charging voltage is shown. Figure (a) shows the
efficiency for detecting a cosmic ray on the inner most gap ground plane
given that a spark was detected on the high voltage plane in the region
of the track for the same gap. Essentially this checks the sensitivity
of the wand and electrical instrumentation for detecting a spark.
Figures (b)-(d) give true cosmic ray detection efficiencies.

Figure 46: MSSC Pion and Bhabha Efficiency.
Figure (b) plots the spark chamber efficiency per plane typical of the charged pion test beam results. The efficiency for detecting individual e^+ or e^- tracks per plane is shown in figure (a), for candidate events selected using the Crystal Ball energy information.

B.3 PHOTON CONVERSION PROBABILITY

Part of the photon detection inefficiency is attributable to the probability that the photon converts to a e^+e^- pair in the material preceeding the NaI and is then labeled charged. Since the probability is only a few percent, several approximations were made. The conversion probability was assumed to be independent of photon energy in the range 100 MeV to 650 MeV (this is $\simeq\pm10\%$ effect). The probability was averaged over the central tracking chamber's acceptances for a flat photon angular distribution. The uncertainty due to these assumptions is included in the error. Table 18 lists the L_{rad} for the various central components of the apparatus.

TABLE 18

The Radiation Thickness of the Inner Detector.
Values given are for 100 to 600 MeV photons at normal incidence.

DETECTOR ELEMENT	SOLID ANGLE COVERAGE (% OF 4π)	% RADIATION LENGTH (L_{rad})
Beam Pipe	100	1.9
Inner MSSC	94	2.0
MWPC	83	0.35
Outer MSSC	71	2.0

Based on the software requirements for identifying a particle as charged, the photon was required to convert in the Beam pipe, the inner MSSC, or halfway through the MWPC. The overall inefficiency in photon detection due to conversion was found to be $(3.5\pm0.5)\%$.

Appendix C

MONTE CARLO STUDIES

The Crystal Ball Monte Carlo program[27] has two main parts: i) the event generator[28] and ii) the detector hardware simulator.[29] Any configuration of final state particles can be prepared by the event generator. In this experiment, the inclusive hadronic decays of the charmonium states were simulated in order to calculate the event selection efficiency. In the determination of the photon detection efficiency, events were prepared by the Monte Carlo program with only one photon, later to be combined with real J/ψ events to simulate the radiative charmonium decays.

C.1   THE CHARMONIUM MODEL FOR GENERATING FULL EVENTS

The purpose in simulating full events was to measure the detector's trigger efficiency and the hadronic event selection efficiency for inclusive final states. With this in mind, only the gross features of the hadronic decays were input to the event generator, while the significant decays from one charmonium state to another were included explicitly.

The Monte Carlo model for ψ' decays contained the following branching fractions: i) $B(\psi' \to \pi\pi J/\psi) = 0.54$, ii) $B(\psi' \to \eta J/\psi) = 0.024$, and iii) $B(\psi' \to \gamma \chi_{0,1,2}) = 0.07$ each. The mass of the ππ system was forced to reproduce the the measured distribution.[30] The angular distributions

for the radiative decays were fixed at $(1+\cos^2\theta)$, $(1-0.33\cos^2\theta)$, and $(1+0.077\cos^2\theta)$ for $\chi_{0,1,2}$, respectively. A 0.1% and 0.3% branching ratio was included to the η_c' and η_c respectively, both with $(1+\cos^2\theta)$ angular distributions. The singlet $^1P_1$ state was not included in the model.

The known charmonium masses were used, except at that time the η_c' mass was guessed to be 3.62 GeV. The two pseudoscalars were assumed to have widths of 20 MeV each, while the $\chi_{0,1,2}$ widths were input as 7, 0, and 2 MeV, respectively. The χ_J states were radiatively decayed to J/ψ 0.7%, 28%, and 16% of the time for J = 0, 1, and 2. A branching ratio of 0.069 was included for each of the leptonic decays of the J/ψ to $\mu^+\mu^-$ or e^+e^-.

All the remaining branching fractions were assumed to be purely hadronic. A general state of pions, etas, and kaons was generated with Poisson distributed multiplicities. The momenta of the final state particles were distributed according to phase space. Table 19 lists the species multiplicities input to the general hadronic decay mode for each charmonium state. The experimentally observed net charged particle multiplicity[31] was used to fix the number of $\pi^+\pi^-$ and K^+K^- pairs.

For the J/ψ model, only the radiative decay to the η_c was included, all the remaining decays were assumed to be hadronic. The decay of the parent resonance into lepton pairs was not allowed in either model. The η's, π^0's, and K_S^0 were all allowed to decay, according to their known properties. Ten thousand events were generated at ψ' and J/ψ each, along with smaller samples of events for specific channels, such as $\psi' \rightarrow \gamma\eta_c$ and $\psi' \rightarrow \gamma\gamma J/\psi$.

TABLE 19

Monte Carlo Species Multiplicities.

The mean number of $\pi^+\pi^-$ pairs, π^0's, η's, and $K\bar{K}$ pairs per event that was input to the Monte Carlo for the inclusive hadronic decays of the charmonium states is listed.

STATE	$N(\pi^+\pi^-)$	$N(\pi^0)$	$N(\eta)$	$N(K\bar{K})$
$J/\psi(3095)$	1.84	1.84	0.25	0.1
$\psi'(3684)$	2.03	2.03	0.06	0.1
$\chi_0(3415)$	1.97	1.97	0.06	0.1
$\chi_1(3510)$	1.99	1.99	0.06	0.1
$\chi_2(3555)$	2.0	2.0	0.06	0.1
$\eta_c(2980)$	1.64	1.64	0.25	0.3
$\eta_c'(3620)$	2.02	2.02	0.06	0.1

C.2   DETECTOR SIMULATION

Only the Ball and central tracking chambers were simulated in the program. The end caps and other detector components were not included. Photon, positron, and electron showers in the NaI were simulated with the Electron-Gamma-Shower (EGS) routines,[32] tailored to the Crystal Ball geometry. Charged pions and kaons were transported through the NaI using the High Energy Transport Code[33] (HETC). Both EGS and HETC directly gave the energy deposition in each crystal generated by the incident particle. Although this procedure was straightforward, it excluded several details found in the real detector: i)   multiple scattering in the beam pipe and central chambers, ii) photon conversion in the beam pipe and central chambers, iii) imperfect light transmission through the crystals and into the phototubes, iv) shower losses due to the paper and aluminized Mylar between the crystals, as well as to the material of the hemisphere cans, v) phototube multiplication statistics,

vi) electronic signal processing and digitization, and vii) the interplay with the calibration process. In addition HETC treated kaons by scaling to pions, with the same velocity as the kaon. In a later version approximate corrections for the pion-kaon mass difference were made to the energy released in nuclear interactions.

Regarding the omission of the end caps, this did not affect the trigger efficiency calculation since they were not part of the trigger criterion. However, the absence of $\simeq 4\%$ of the total energy ($\simeq 4\%$ loss in solid angle) would lead to a slight underestimate for the inclusive hadronic event selection efficiency. This was included as part of the $\pm 5\%$ overall uncertainty in the event selection efficiency.

The central magnetostrictive spark chambers and multiwire proportional chambers were simulated in great detail. The raw data output was of the same form as for the real experiment. Although simulated central chamber data were not used in this study, they are included in the discussion for completeness.

The Monte Carlo technique actually used for calculating the photon detection efficiency was designed to remove as much bias as possible resulting from the simulation process. The method used combined single photons generated isotropically over the entire 4π solid angle, with real J/ψ events obtained using the hadron selection algorithm. The number of γ's generated was used to normalize the number detected at the end to yield an efficiency. Samples of $\simeq 50 \cdot 10^3$ gammas each were prepared at $E_\gamma = 90$, 145, 210, 320, and 500 MeV. An immediate loss of $\simeq 7\%$ resulted from applying the EGS code, since the end caps were not in the simulated geometry package. This did not bias the final result, as

all candidates for the inclusive photon spectra were required to pass a solid angle cut of $|\cos\theta_{track \cdot z}| < 0.85$. The array of crystal energies for each Monte Carlo photon was summed with the existing crystal energy data of a single J/ψ event. The result was a typical J/ψ event with an extra monochromatic photon.

With the assumption that on the average all the bound charmonium states have similar multibody hadronic decays, these mixed events were used to simulate either $\psi' \rightarrow \gamma X$ or $J/\psi \rightarrow \gamma X$, where X is any charmonium-like state. The number of Monte Carlo gammas surviving the loss mechanisms mentioned in Chapter IV, divided by the number generated is the photon detection efficiency (after including a correction for the photon conversion probability in the beam pipe and inner chambers). This technique contains a slight underestimating bias due to neglecting the decay recoil against the radiative gamma. The bias should be largest for the highest Monte Carlo photon energies. The uncertainty due to this effect is included in the ±5% overall normalization error for the photon detection efficiency.


C.3   MONTE CARLO PERFORMANCE

About 42% of the energy deposited by HETC charged hadronic particles came from the primary particle ionization on the average. An additional 20% (9%) was generated by secondary proton (charged pion) ionization. The two photon decay of π^0's contributed 14%. Secondary muons and their electron decays yielded 1.9%. The remaining $\simeq$13% of the average energy deposition was attributed to three processes known to produce split-offs in the Monte Carlo: i) ionization by heavy nuclear fragments were

responsible for 2.5% of the total energy, ii) prompt γ's from the decay of excited nuclei gave 3.5%, and iii) low energy neutrons from the decay of excited nuclei gave 7.1%. In the HETC code, the heavies, photons, and neutrons from the last three mentioned sources were not transported. All their kinetic energy was deposited at the point where they were generated. This is only correct for the nuclear fragments where a short path length would be expected from their strong ionization. It was observed that HETC produced far more split-offs than were seen in the data. By suppressing the last three processes HETC was made to closely reproduce the real split-off distributions.

The quality of the Monte Carlo data was checked by making several comparisons to the real resonance data. Figures 47-50 show the total multiplicity and energy distributions, γ and charged particle spectra, neutral and charge multiplicities, and γ-γ mass plots for ψ' and Monte Carlo data resulting from the standard production analysis programs.

As can be seen in Figure 47, the Monte Carlo's total energy distribution is shifted slightly higher than seen in the data. This is believed to result from two main sources: i) charged particles in HETC deposit slightly more energy ($\simeq$260 MeV) on the average than in real events ($\simeq$204 MeV) and ii) the model used to generate the decays is not exact. This is expected to lead to a slight overestimate for the event selection efficiency, but well within the ±5% error. The charged particle spectrum produced by HETC deviates from the data mainly in the minimum ionizing peak and in the continuum below 200 MeV (populated mostly by charged particles which have ranged out). The continuum above 200 MeV contains mostly interacting hadrons, and good agreement is seen there.
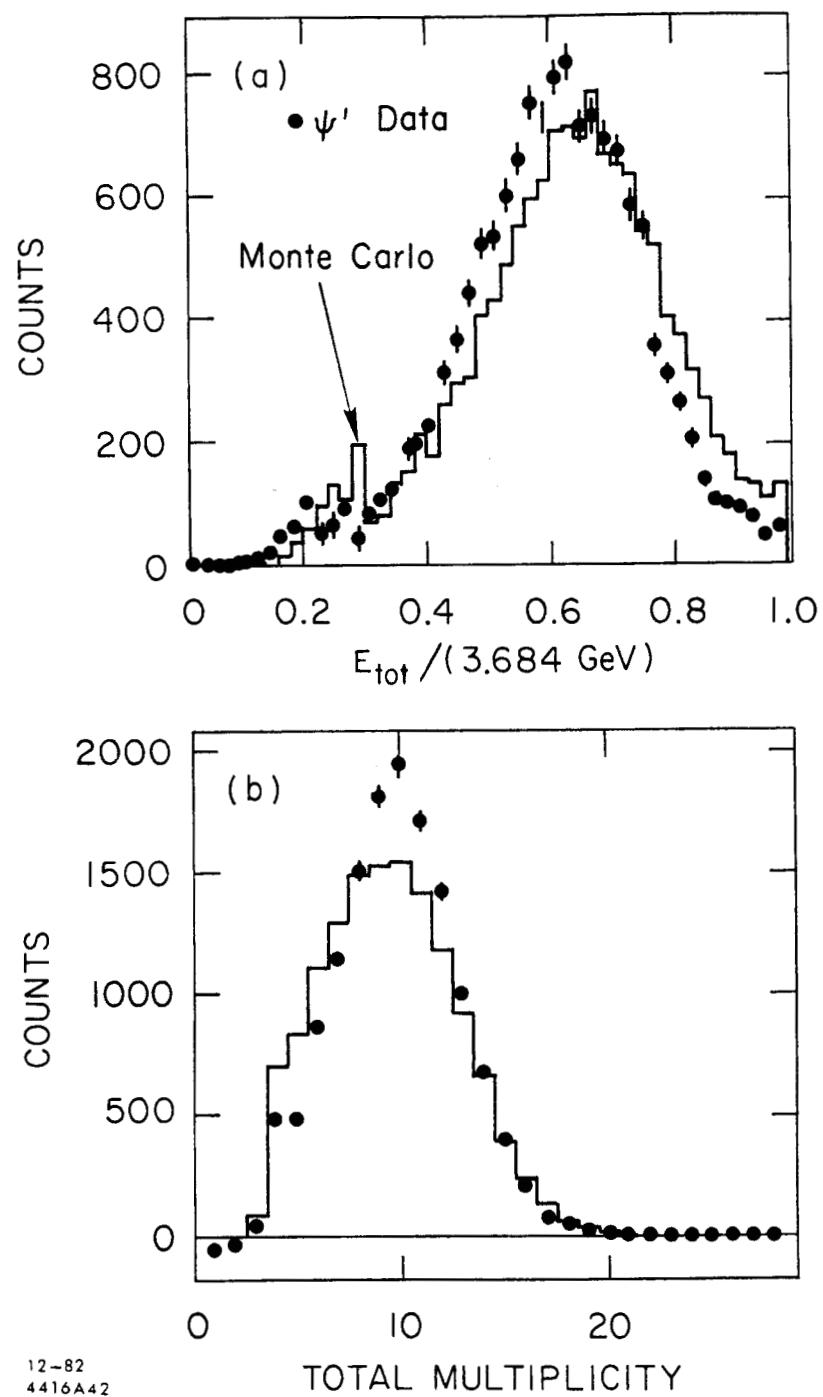
Figure 47: Total Energy and Multiplicity for ψ' Monte Carlo and Data.
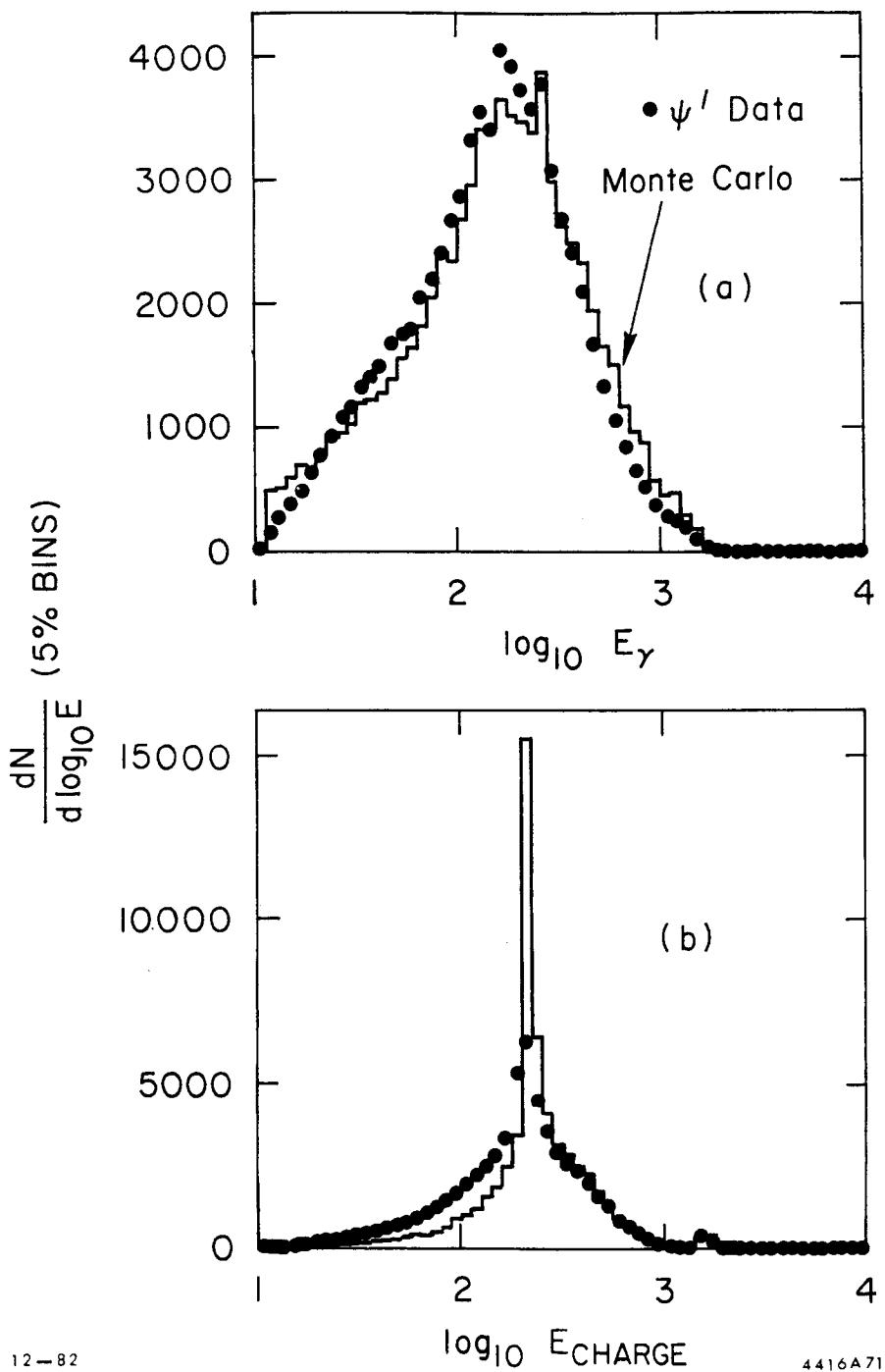
Figure 48: γ and Charged Particle Spectra for Monte Carlo and Data. Figure (a) compares particles identified as neutrals from the data and from the Monte Carlo. The dominant contributions are from real photons in the data and EGS generated showers in the Monte Carlo. Charged hadron cascades generated by HETC are compared with real charged particles in figure (b). The bump at 3.2 GeV is due to real and EGS showered e+ and e− from ψ′→XJ/ψ→Xe+e−.
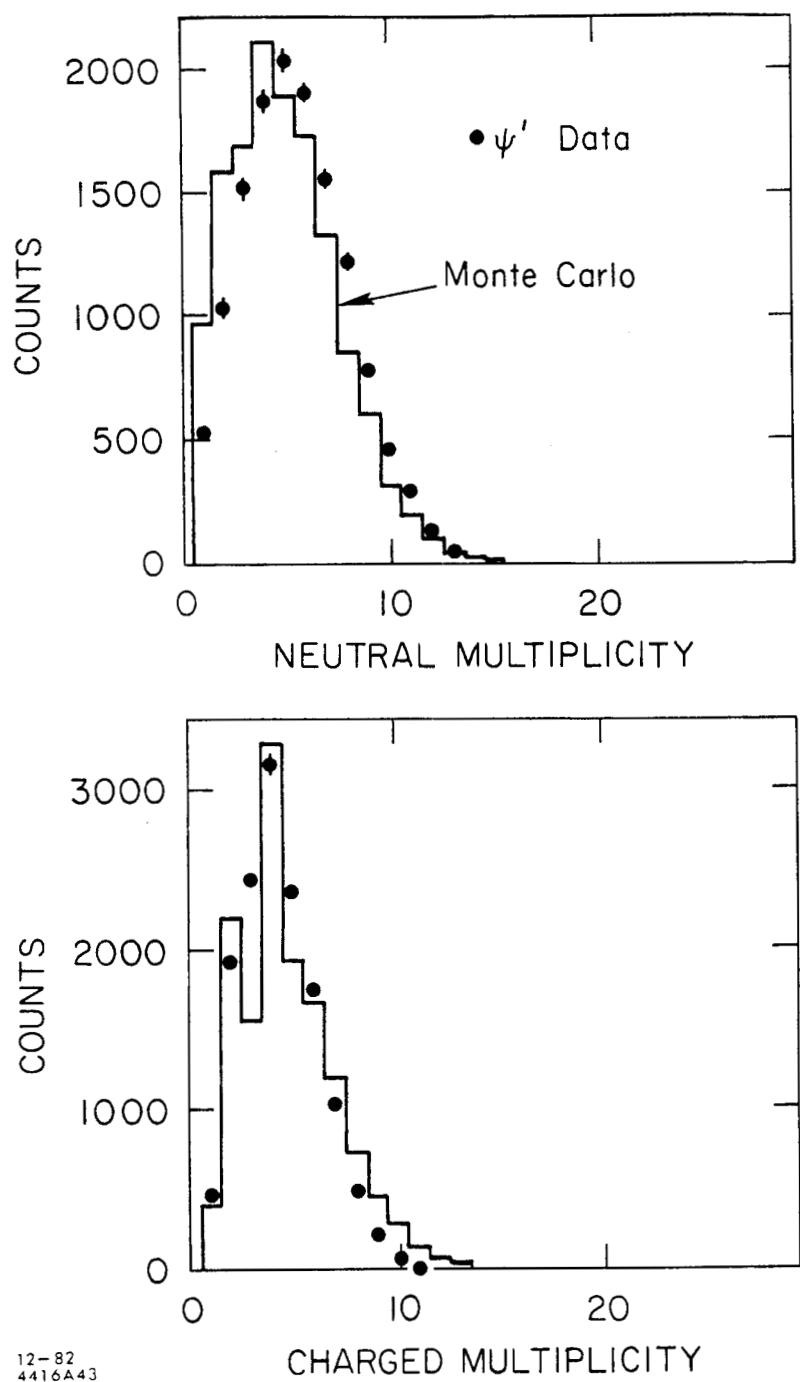
Figure 49: Neutral and Charge Multiplicities for Monte Carlo and Data.
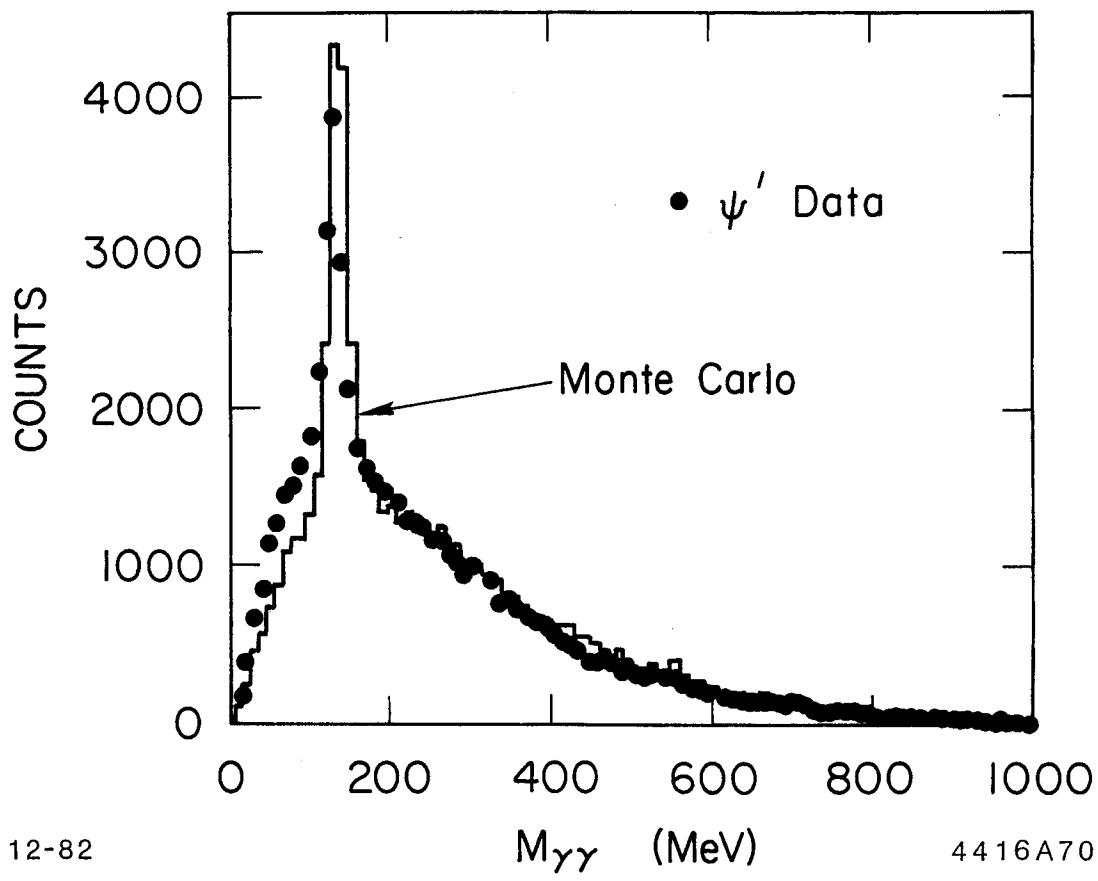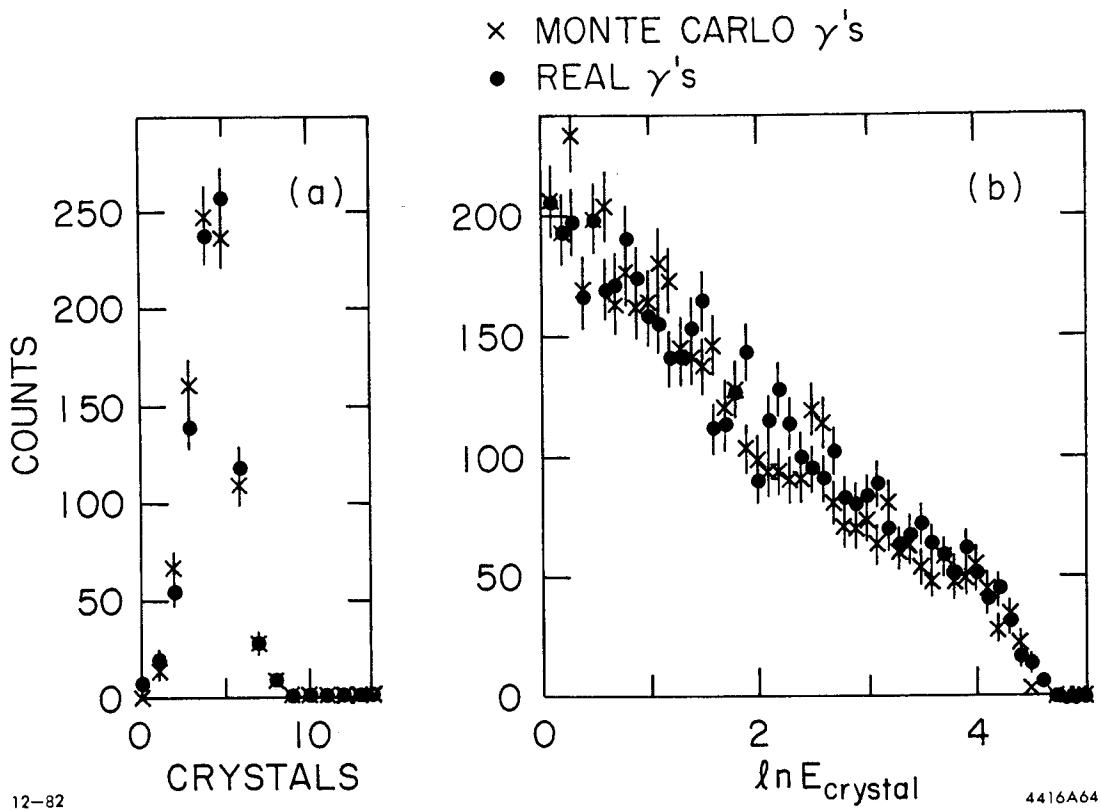
Figure 50: γ-γ Mass Plot for Monte Carlo and Data.

Since Monte Carlo photons were used to measure the photon detection efficiency under a variety of selection criteria, including pattern cuts, the EGS generated shower profiles were compared with real photons. The source of real γ's was from the fitted data sample $\psi' \rightarrow \gamma\gamma J/\psi \rightarrow \gamma\gamma\ell^+\ell^-$, although in the comparison, unfitted quantities were used. The following shower quantities were checked: i) the number of crystals in the $\sum 13$ geometry with an energy $> 1\%$ of the photon energy (Figure 51(a)), ii) the spectrum of energies deposited in each crystal (Figure 51(b)), iii) the $\sum 1/\sum 4$ energy ratio (Figure 52(a)), iv) the $\sum 2/\sum 4$ energy ratio (Figure 52(b)), and v) the $\sum 4/\sum 13$ energy ratio (Figure 52(c)). Very good agreement is seen between the EGS produced photon showers and the real gamma showers.

Figure 51: Crystal Energies for Monte Carlo and Real Photons.
Monte Carlo and real photon showers are compared. Figure (a) shows the
distribution of the number of crystals within the $\sum 13$ which have an
energy > 1.0% of the track energy for 175 MeV < E_{track} < 250 MeV. The
natural log of the inclusive energy depositon in each crystal within the
$\sum 13$ is plotted in figure (b) for the same energy photons.
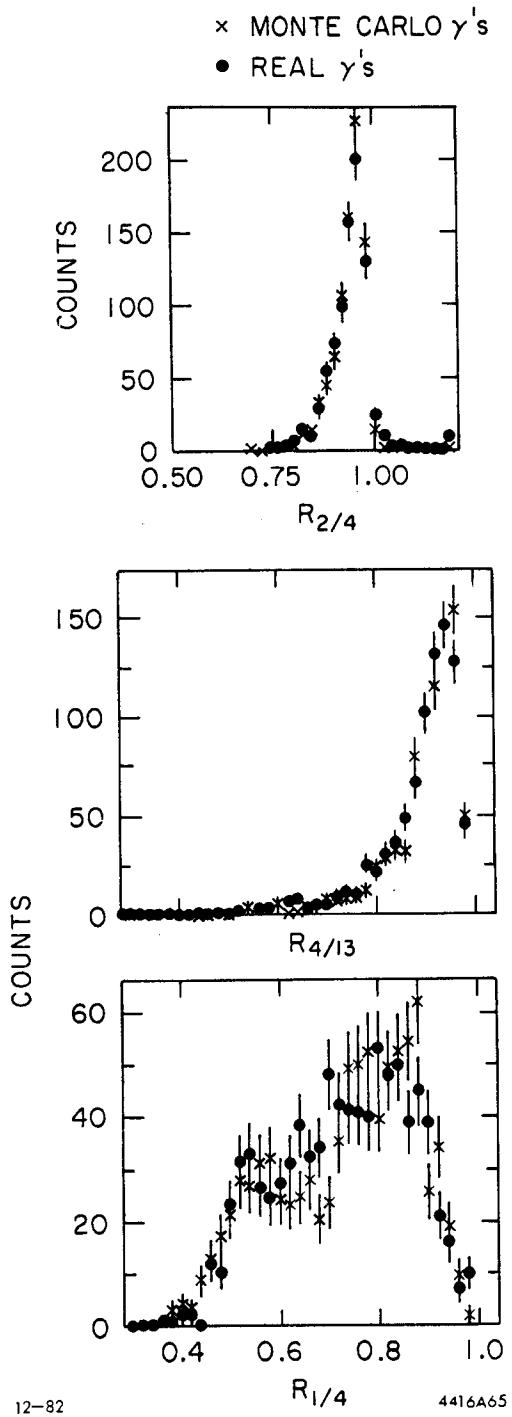
Figure 52: Monte Carlo and Real Photon Shower Patterns.
Monte Carlo and real photon shower patterns $R_{2/4}$, $R_{1/4}$, and $R_{4/13}$ are compared.

Appendix D

SUBTRACTION OF RECONSTRUCTED π^0'S

Neutral pions were identified[34] in the events by selecting the best combination of all fitted γ-γ mass pairs with the lowest global x^2 statistic. The result of this best combination was stored for later subtraction of γ's resulting from π^0 decay in the photon spectra. Photon candidates from the entire detector's acceptance (98% of 4π sr) were included in the combinatorial search. Neutral tracks were identified on the basis of the end cap and central tracking chamber data alone (no pattern cuts were used). Also the algorithm was not intended to find the class of energetic π^0 decays (E_π roughly > 600 MeV), where the two γ showers overlap due to their small opening angle. The discussion which follows excludes this class of π^0 decay.
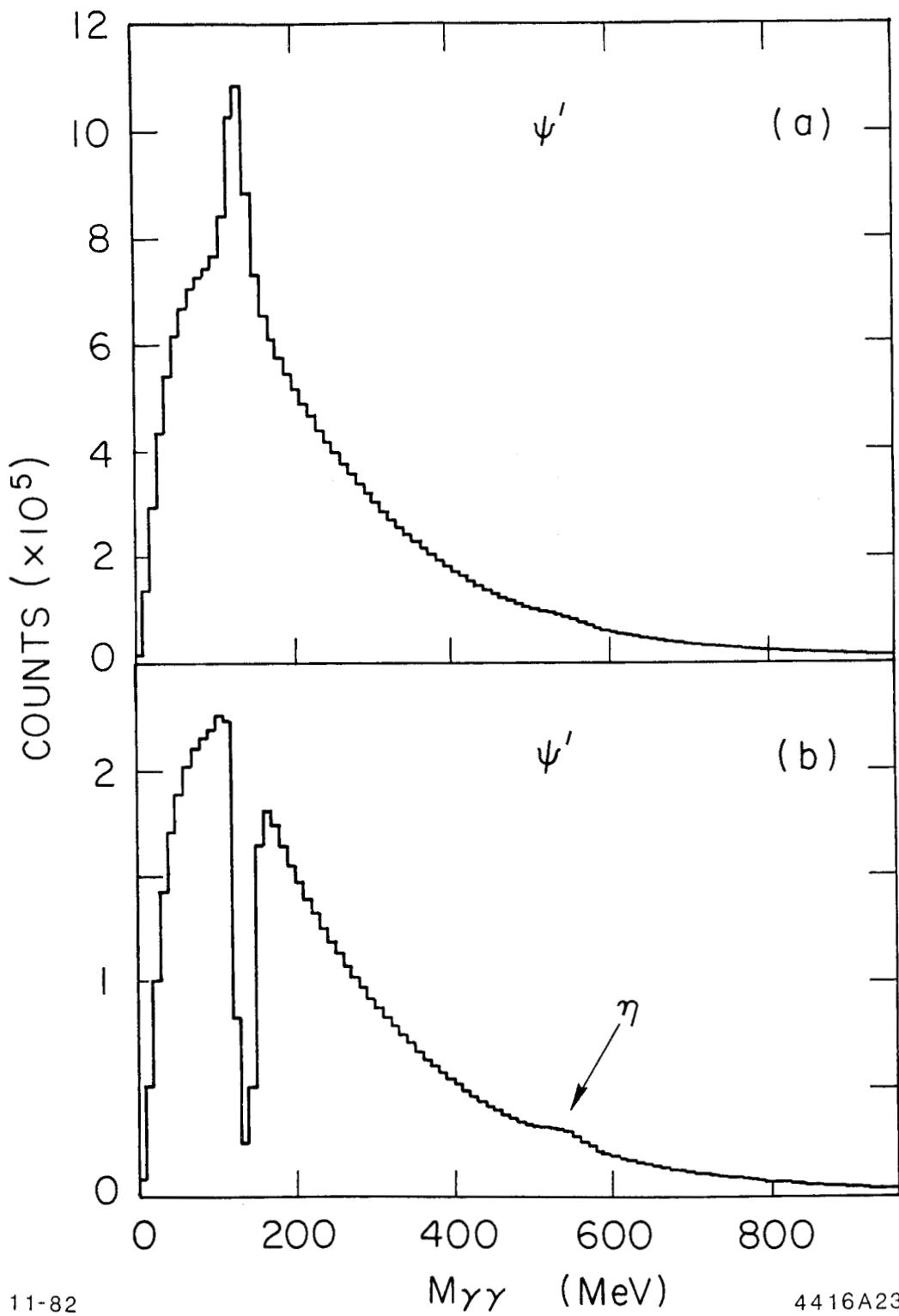
First the routine TGFIT operated on each γ-γ pair. In the fit[35] the photon pair opening angle ($\theta_{\gamma\gamma}$) and energies ($E_{\gamma 1}$ and $E_{\gamma 2}$) were varried to minimize the x^2 statistic subject to the constraint that $M^2_{\gamma\gamma}$(fitted) $= M^2_{\pi 0}$, where x^2 is defined as:

$$x^2 = [E_{\gamma 1}(\text{fitted}) - E_{\gamma 1}(\text{measured})]^2/\sigma_{e1}^2 +$$
$$[E_{\gamma 2}(\text{fitted}) - E_{\gamma 2}(\text{measured})]^2/\sigma_{e2}^2 +$$
$$[\theta_{\gamma\gamma}(\text{fitted}) - \theta_{\gamma\gamma}(\text{measured})]^2/\sigma(\theta)^2 +$$
$$2\alpha \cdot (M^2_{\gamma\gamma}(\text{fitted})-M^2_{\pi 0})$$

(D-1)

The uncertainties in the measurements were taken to be: $\sigma_e = 2.4\%/E_\gamma^{1/4}$ and $\sigma(\theta) = 37$ mr. The minimization[35] was obtained by linearizing the constraint function, $M^2_{\gamma\gamma} = 2E_{\gamma 1}E_{\gamma 2} \cdot (1-\cos\theta_{\gamma\gamma})$, and iterating the solution. The process would converge in less than 5 iterations and the contribution from the last term in Equation D-1 would be neglegable. For each combination of neutrals the χ^2 and the fitted γ-γ momentum 4-vector were saved. Figure 53(a) shows the unfitted γ-γ mass distribution input to TGFIT.

The confidence level (CL) for each pair was calculated from the χ^2 for one degree of freedom and those pairs with a CL < 0.001 were rejected from further consideration. The routine GPAIR evaluated the total χ^2 for each possible global combination of γ-γ pairs within the event. The combination giving the least overall χ^2 was selected as the best hypothesis for that event.

Figure 53(b) shows the γ-γ mass plot after removing the best combination of pairs. Monte Carlo studies indicate that the maximum possible efficiency for reconstructing π^0's is $\simeq 38\%$, owing to the photon detection inefficiency for individual photons. Almost all of the intact π^0 decays in the event are removed by the reconstruction algorithm, yielding an overall π^0 detection efficiency of $\simeq 36\%$ (for π^0's where the decay γ showers do not overlap). The algorithm oversubtracts, removing almost as many non π^0's gammas as real ones. Figure 54 shows the fitted π^0 energy distribution for the best combination of reconstructed π^0's.

Figure 53: γ-γ Mass Distributions at ψ'
The mass distribution for all γ-γ pairs input to the π^0 reconstruction algorithm is shown in figure (a). Figure (b) shows the result after subtracting the best combination of π^0's. Note the strong enhancement in the η signal at $\simeq 545$ MeV.
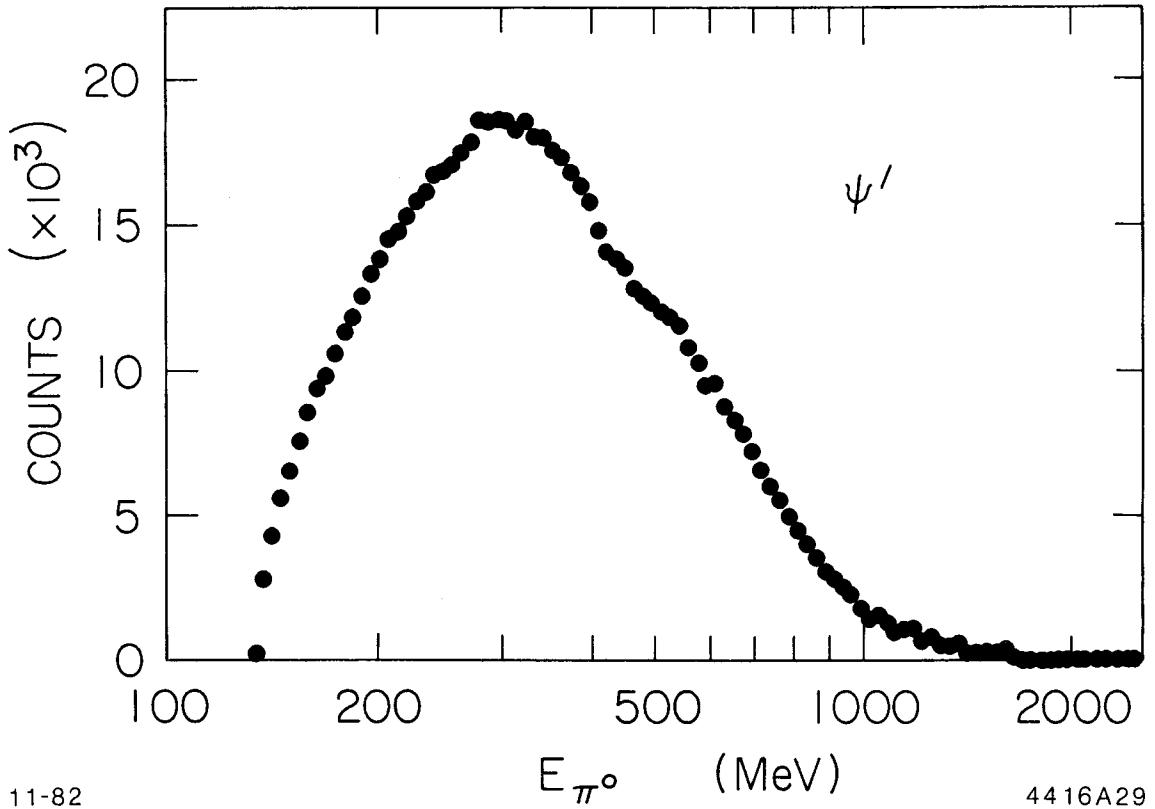
Figure 54: Energy Distribution for Reconstructed π⁰'s.
The shoulder at 540 MeV corresponds to the energy expected for π⁰'s from
ψ' → π⁰J/ψ,   in addition to a contamination resluting from ψ' → γγJ/ψ
where the two γ's combine to form a fake π⁰ mass.   Energetic π⁰'s with
an energy > ≈600 MeV are not well detected with this π⁰ reconstruction
algorithm owing to the frequent overlap of the decay γ's.

Appendix E

ELECTROMAGNETIC SHOWER PATTERNS

The identification of particles, based on their lateral energy deposition profiles (pattern cuts), were chosen empirically from studies of the energy distributions in groups of contiguous crystals. The overall goal was to select particles with energy depositions similar to those of single photon showers. In this study the principal background to be removed was charged particles, misidentified as neutrals. Of lesser importance here, but significant to an analysis of the high energy end-point of the photon spectra, is the rejection of overlapping γ's from the decay of an energetic π^0 ($E_\pi > \simeq 600$ MeV).

Three parameters were used to characterize single photon showers.

$$R_{2/4} = \frac{\sum 2_{max}}{\sum 4}, \quad R_{1/4} = \frac{\sum 1}{\sum 4}, \quad R_{4/13} = \frac{\sum 4}{\sum 13} \qquad (E-1)$$

where the $\sum 1$, $\sum 2_{max}$, $\sum 4$, and $\sum 13$ are energy sums based on the sum of 1, 2, 4, or 13 crystals as shown in Figure 13. The ratios compare the energy deposited in a group of crystals, always including the bump module ($\sum 1$), to a larger group of crystals. In general, $R_{1/4}$ and $R_{4/13}$ are bound in the interval [0,1], while $R_{2/4}$ may be larger than 1.0. This happens when the shower fluctuates across the bump module vertex outside the $\sum 4$ (such that the $\sum 2_{max} > \sum 4$). Values of the parameters near 1.0 indicate a narrow lateral energy profile, while smaller values

indicate a broader profile. The distributions of these ratios were studied for well-defined charged particles and photons.

A variety of pattern cuts were used in the inclusive photon analysis, described in Chapter IV, to suppress the charged particle contamination in the neutral particle sample. The details of the photon selection criteria based on the ratio parameters will be discussed below, with reference to the cuts, A)-I), outlined in Chapter IV.
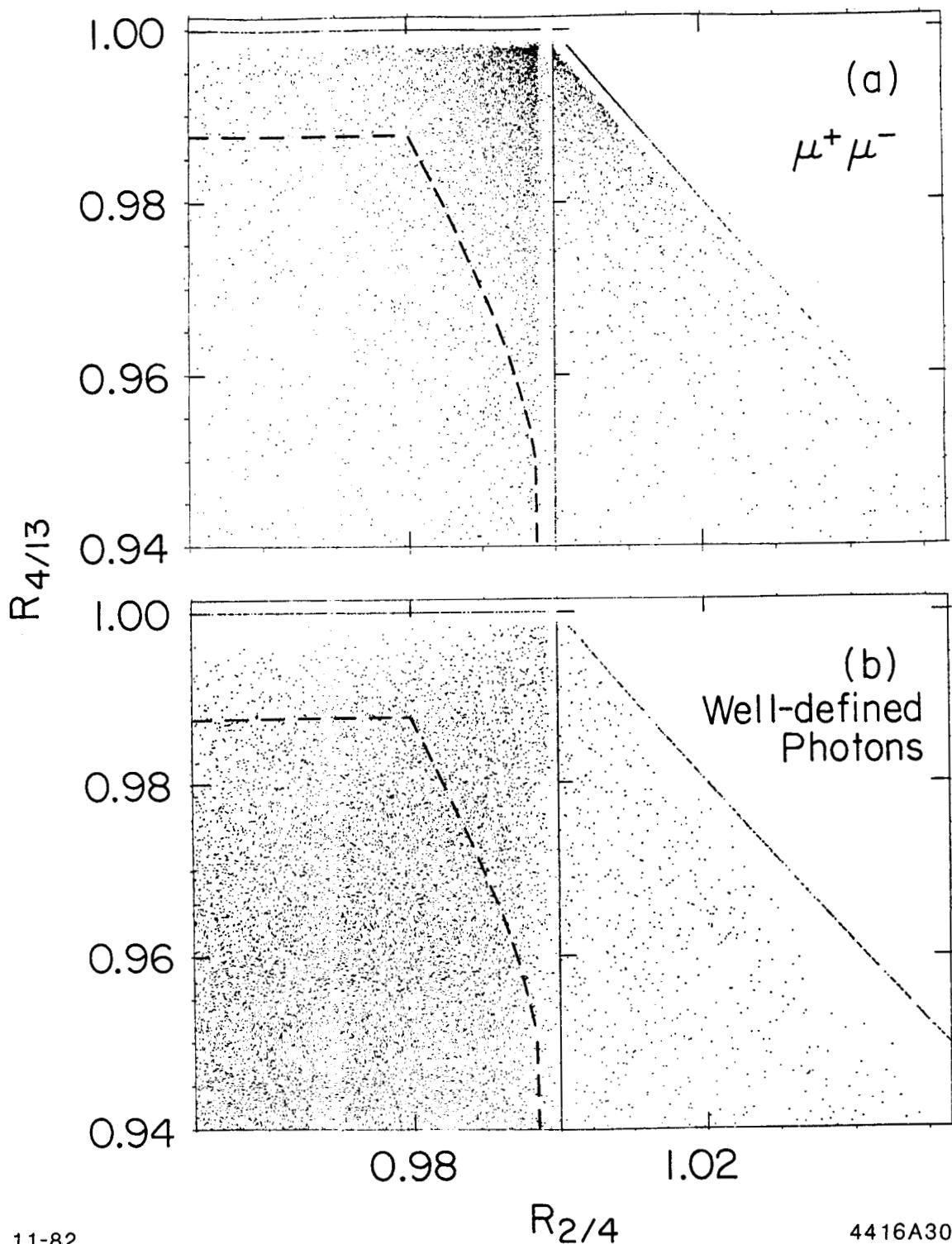
A)-C) No pattern cut was applied.

D) This pattern cut was composed of two parts: i) The narrow energy depositions of minimum ionizing charged particles were removed by rejecting particles with $R_{4/13} > 0.9875$, or $R_{2/4} > 0.9975$, or $R_{2/4} > 0.9975 - (R_{4/13} - 0.95)^{1.23}$. Figure 55(a) shows a scatter plot of $R_{2/4}$ versus $R_{4/13}$ for minimum ionizing charged particles. The curve indicates the cut used to remove this background. Photons also populate the cut region (Figure 55(b)), though their main distribution is centered outside the cut. Referring to Figure 13, this cut selects those photons which shower across the central crystal's side ($R_{2/4} < 1.0$) and rejects those which shower through the vertex ($R_{2/4} > 1.0$). The cut on $R_{4/13}$ requires that the photon shower deposit at least 1.25% of its energy outside the $\sum 4$. The transmission efficiency for both $\mu^+ \mu^-$ pairs and a sample of well-defined photons was measured to ascertain the effect of the pattern cut alone. The results are shown in Figure 56. ii) Photon showers with large fluctuations, interacting charged particles, and overlapping γ showers due to the decay of energetic π^0's, are suppressed by requiring that the particle's energy deposition not be

- 167 -

too broad.   Particles were removed if $R_{4/13} < 0.85$ or $R_{2/4} < 0.90$.

This is a very stringent cut on the photons as is shown in Figures

57 and 58.   Although the combined effect of cuts i) and ii)

effectively suppresses the background,   it introduces a large

inefficiency for low energy γ's, as indicated by curve E) in Figure

34.

E)   The pattern cut used here is identical to D)ii), alone.

F)   No pattern cut was applied.

G)   Only particles with very broad lateral energy profiles were cut, but

not as strongly as in D)ii). This was done to improve the photon

detection efficiency over that cut.   Particles were rejected if

$R_{4/13} < 0.7$ or $R_{2/4} < 0.8$.

H) and I) A milder version of the cuts used in D)i) and ii) was used to

suppress mainly charged particles.   Instead of cutting on the ratio

$R_{2/4}$,   the ratio $R_{1/4}$ was used.   Particles with lateral energy

distributions too narrow to be consistent with single photons were

removed if $R_{4/13} > 0.995$ or $R_{1/4} > 0.98$. Particles with too broad a

distribution were cut if $R_{4/13} < 0.7$ or $R_{1/4} < 0.4$.   These cuts are

shown for well-defined charged particles and photons in Figures 60

and 59.

Figure 61(a)-(c) illustrates the effect of the cuts D)i) and ii) on

the charged particle spectrum from ψ' decays. Also shown is the charged

particle spectrum resulting from the cuts used in H) and I).   Note the

enhancement of the peak at $\simeq 1525$ MeV produced by the e^+e^- pairs in the

decay $\psi' \rightarrow XJ/\psi \rightarrow Xe^+e^-$,   compared to the considerable suppression of

hadronic charged particles in the spectrum.   This is clear evidence of

the cut's ability to select electromagnetic showers.

Figure 55: $R_{2/4}$ Versus $R_{4/13}$.

In figure (a) a scatter plot distribution is shown for minimum ionizing charged particles in the two dimensional space of the parameters $R_{2/4}$ and $R_{4/13}$. Figure (b) shows the same distribution for well-defined photons from a fitted sample of events, $\psi' \to \gamma\gamma J/\psi \to \gamma\gamma\ell^+\ell^-$. The cut used to remove minimum ionizing charged particles is shown for both figures.
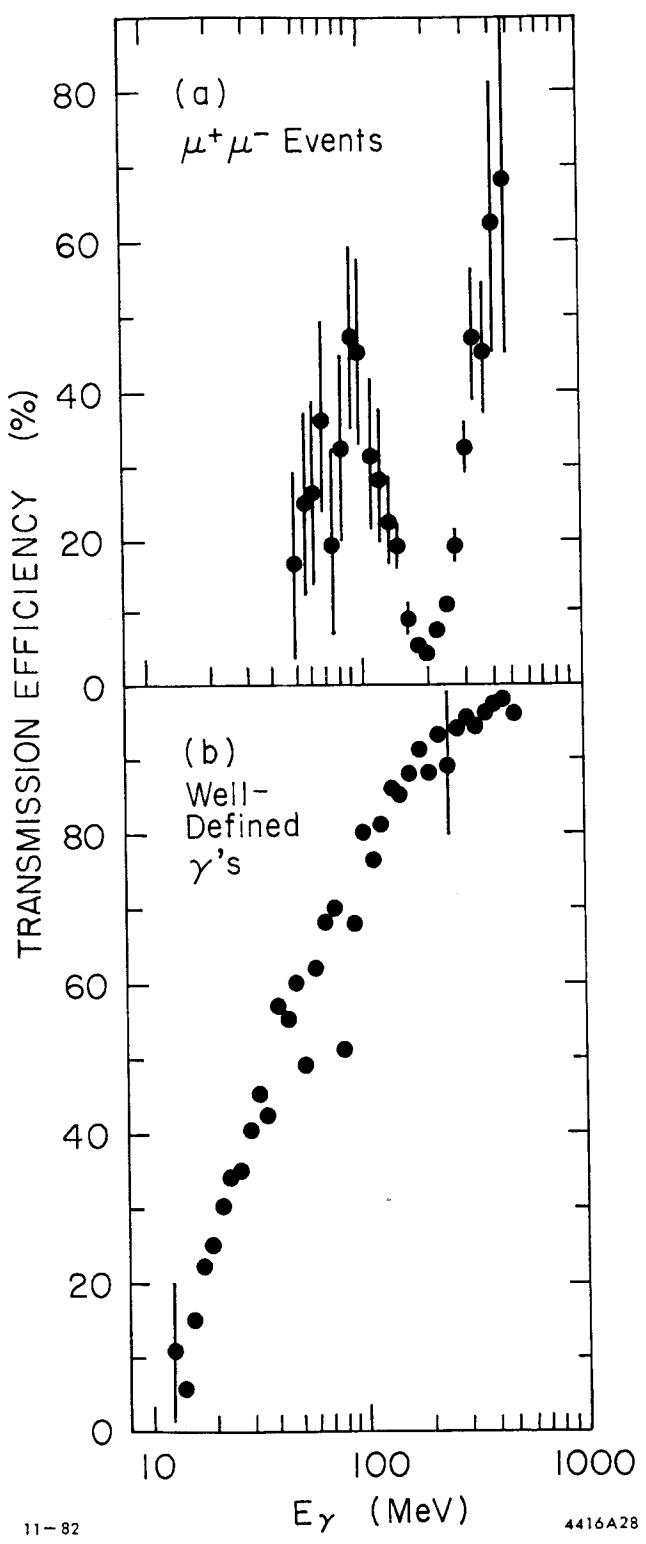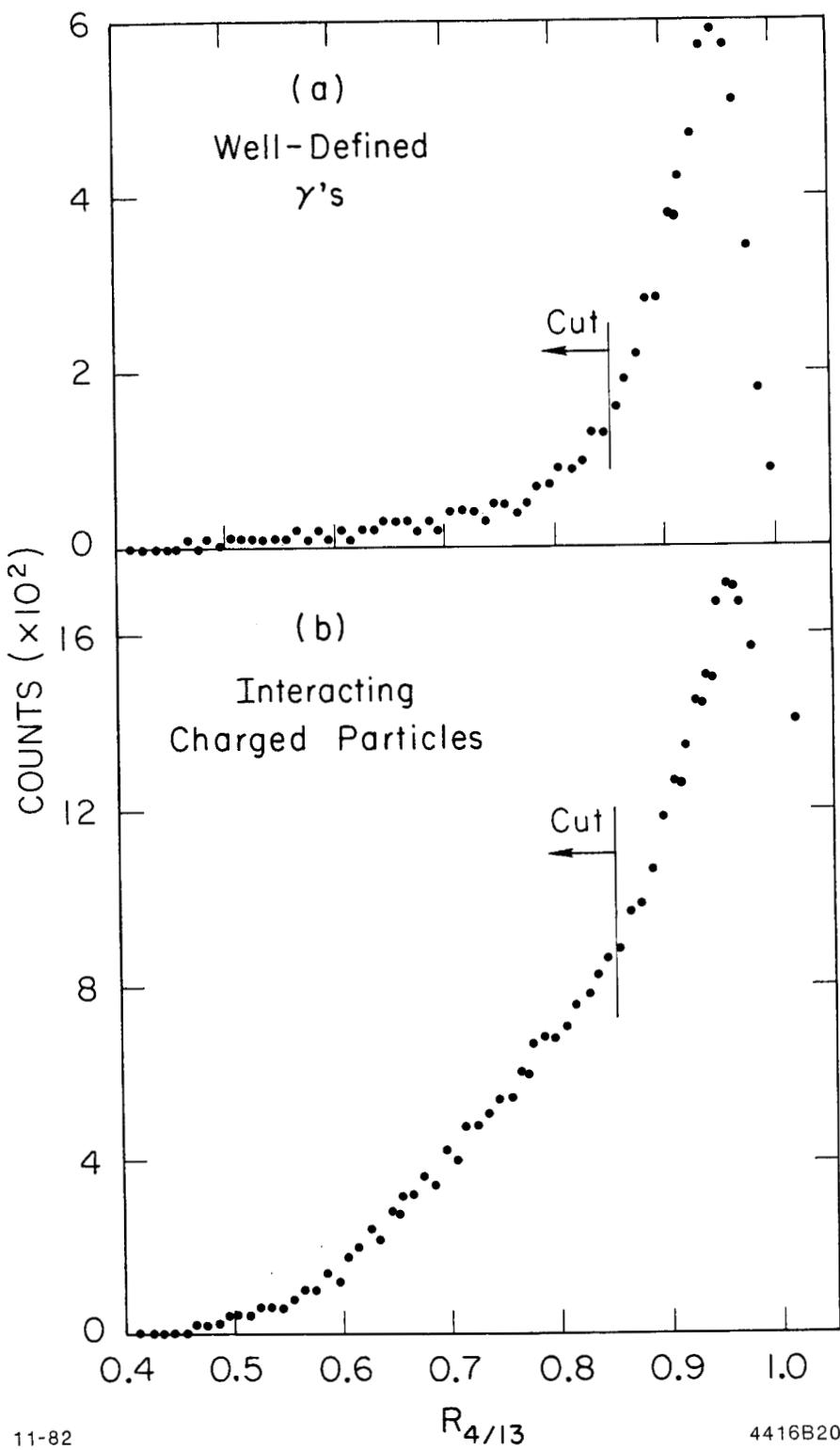
Figure 56: $R_{2/4}-R_{4/13}$ Pattern Cut Transmission Efficiency.
The transmission efficiency for $\mu^+\mu^-$ events (a) and well-defined photons
(b) is shown for the pattern cut designed to remove minimum ionizing
charged particles. Note the dip in figure (a) at $\simeq$210 MeV, indicating a
strong suppression for minimum ionizing particles. The price is a heavy
loss in efficiency for low energy photons as shown in figure (b).

Figure 57: Stringent Pattern Cut Using the Parameter $R_{4/13}$.
The distributions for the parameter $R_{4/13}$ are shown for well-defined
charged particles and photons. The cuts used in the selection criterion
D)ii) are indicated on the plot.
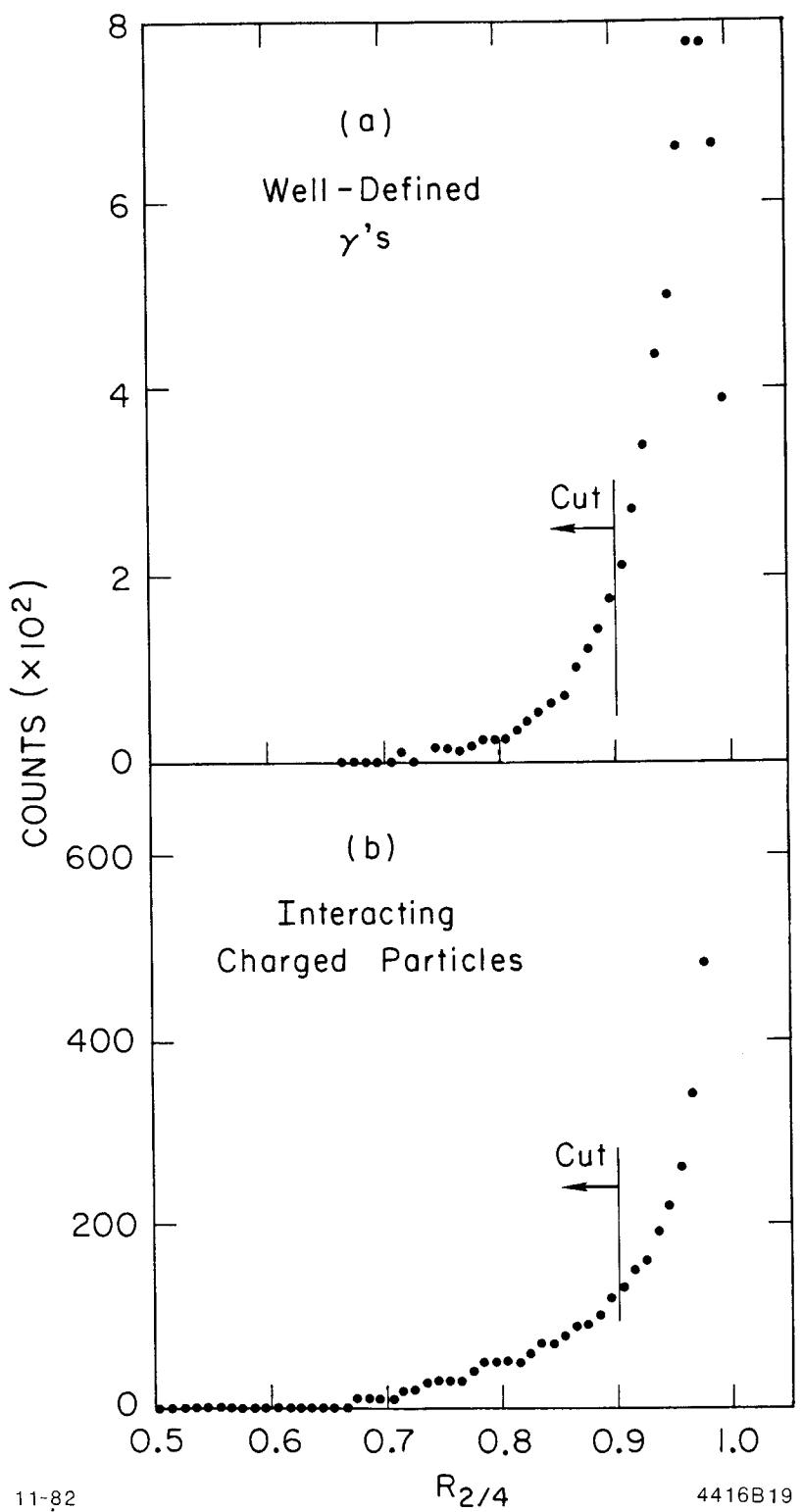
Figure 58: Stringent Pattern Cut Using the Parameter $R_{2/4}$.
The distributions for the parameter $R_{2/4}$ are shown for well-defined
charged particles and photons. The line shows the cut used in the
photon selection criterion D)ii).
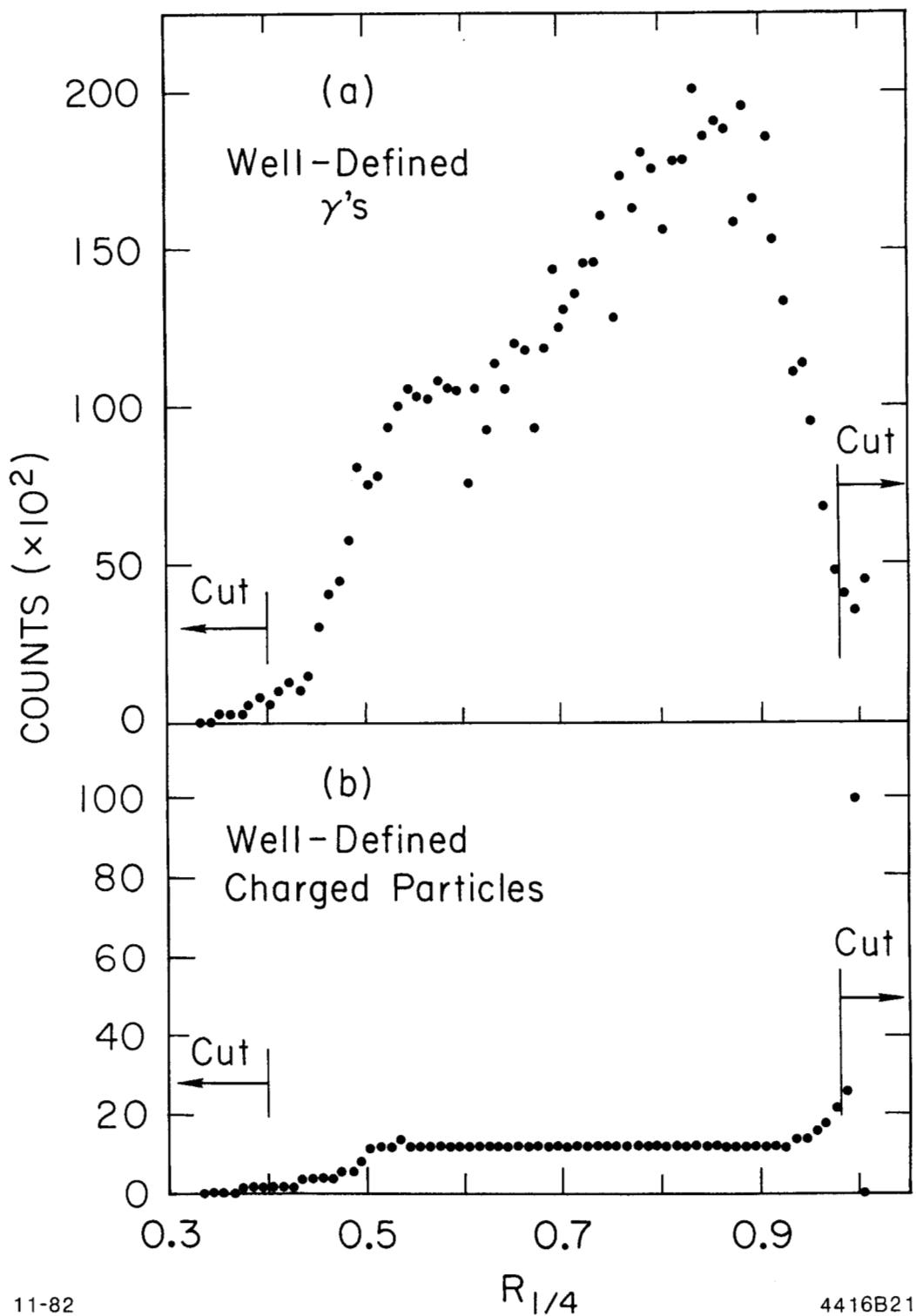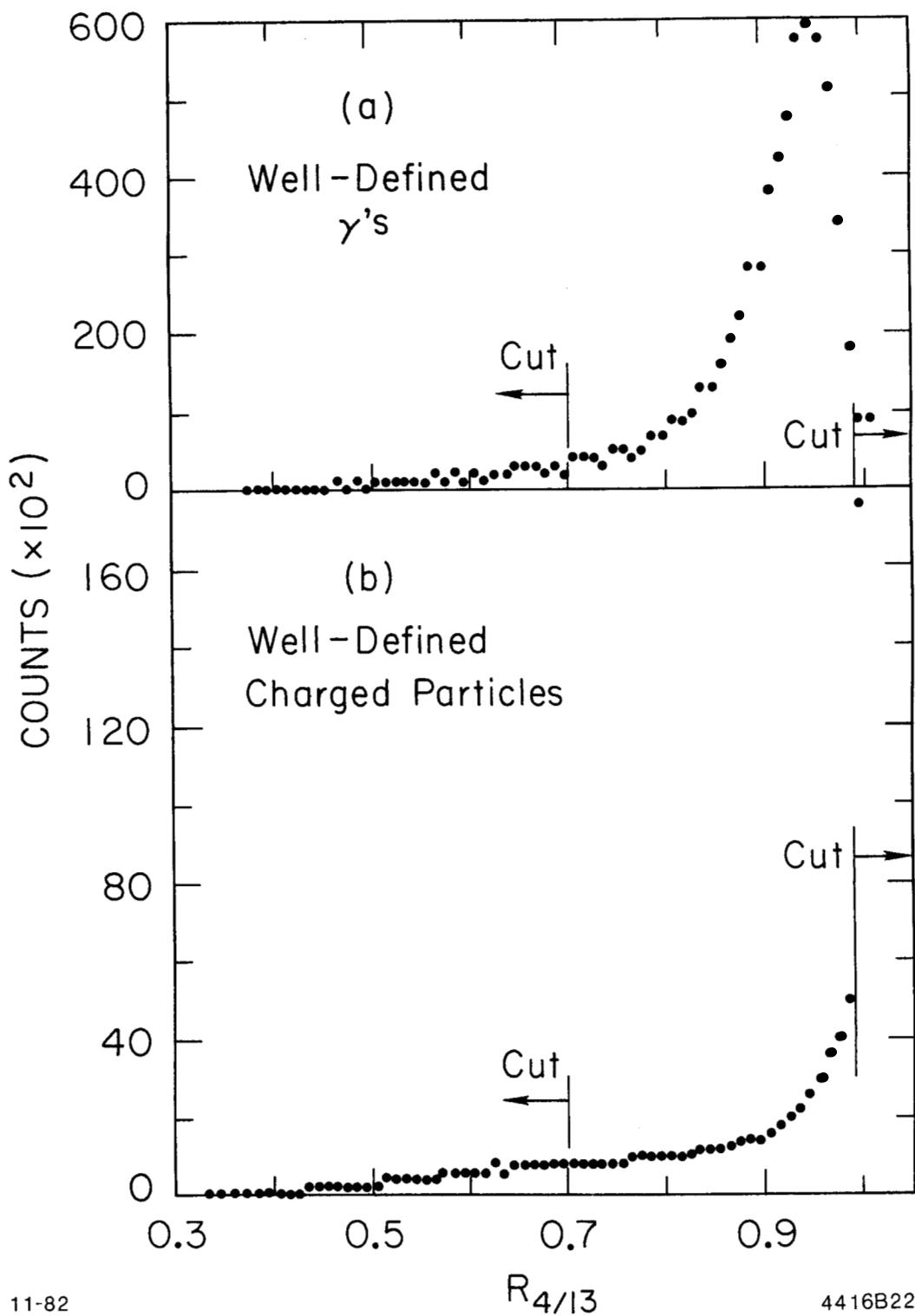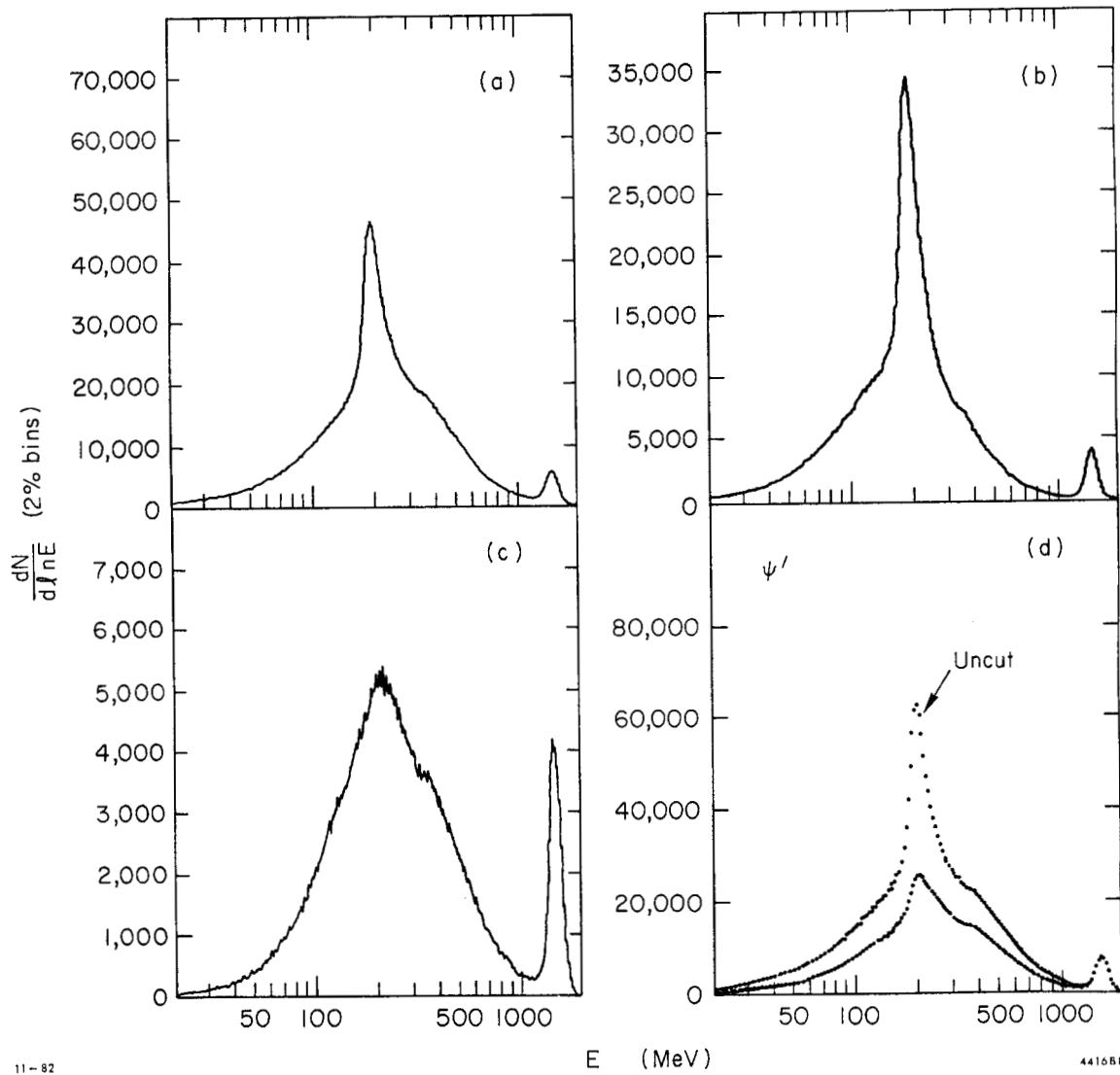
Figure 59: Mild Pattern Cut Using the Parameter $R_{1/4}$.
The distribution of the parameter $R_{1/4}$ is shown for well-defined charged particles and photons. The pattern cut used in selection criterion H) is drawn on the plot.

Figure 60: Mild Pattern Cut Using the Parameter $R_{4/13}$.
The distribution for the parameter $R_{4/13}$ is shown for well-defined charged particles and photons. The pattern cut used in selection criterion H) is drawn on the plot.

Figure 61: Charged Particle Spectra with Pattern Cuts Applied.
An uncut spectrum of charged particles from decays of the ψ' is shown in
figure (a).   Figure (b) is the result after applying the cut described
in D)i), and figure (c) results after the additional cut D)ii).   The
application of the pattern cut H) yields the spectrum shown in the
bottom of figure (d).   The top spectrum in figure (d) is uncut.   Note
the relative enhancement of the showering e^+e^- signal at $\simeq$1525 MeV from
decays of the J/ψ, compared to hadronic charged particles in the
spectrum.

Applying a pattern cut to reject particles with a shower too narrow to be consistent with a single photon also suppresses the hadron-nuclear interaction split-offs usually found in the neutral particle sample. This property of the pattern cut [like D)i] is not noticed in Figure 61, but is readily seen by comparing the photon spectra in Figures 20(c) and (d). The split-offs primarily occupy the low energy (<100 MeV) region of Figure 20(c), where their signal has been enhanced by the subtraction of slow π^0's. The sharp reduction in split-offs seen in Figure 20(d) was traced to the application of the pattern cut D)i alone. The efficiency for detecting low energy real photons (<100 MeV) is also sharply reduced.

Appendix F

LINE SHAPE AND RESOLUTION

The signal shapes observed in the inclusive photon spectra contain
information convoluted from two sources: i) the detector's response
function, which is the distribution of measured energies resulting from
monochromatic quanta of electromagnetic energy striking the detector,
and ii) the physical properties of the states involved in the radiative
transition. Consider the decay taking place in the center of mass of
the radiatively excited parent particle, which has a width (Γ)
essentially zero. If the mass of the daughter state is broad, than the
quantum of electromagnetic energy released in the transition will not be
monochromatic, reflecting the daughter state's mass distribution. The
same result occurs if the parent state is broad and the daughter state
is narrow, or if they are both broad. In this experiment, for all the
transitions studied, either the ψ' or the J/ψ states were the parent or
the daughter particle. Since these resonances are known to be narrow,
215 ± 40 KeV for the ψ' and 63 ± 9 KeV for the J/ψ, their contribution to
the signal shapes can be ignored. By making a detailed analysis of the
observed signal shapes it is possible to extract information about the
width of the other state involved in the transition.

For the two transitions $\chi_{1,2} \to \gamma J/\psi$, the χ_J particle was recoiling
against a photon from the initial transition $\psi' \to \gamma\chi_{1,2}$. The Doppler
broadening of the second photon resulted from the non-zero momentum

distribution of the χ particle in the laboratory center of mass. In this case a Doppler broadening contribution to the signal shape was included solely to enhance the reliability of the single amplitude measurements. Information about the widths of the $\chi_{1,2}$ was not derived from these transitions but from the initial transition.

F.1 THE DETECTOR'S RESPONSE FUNCTION

The form of the detector's response function was measured using the monochromatic e^+ and e^- from the Bhabha reaction $e^+e^- \to e^+e^-$ at the J/ψ resonance ($\simeq 2/3$), and from the direct decay $J/\psi \to e^+e^-$ ($\simeq 1/3$). This is the lowest energy source of well-defined electromagnetic quanta available in the data. Events were selected to suppress radiative Bhabha events by requiring the following: i) only two charged particles in the event with a total energy deposition of, $E_{tot} > 2000$ MeV, ii) both charged track trajectories had to be fully reconstructed from the central spark chamber data and yield an IR vertex with $|z| < 10.$ cm, and iii) the charged particles had to be back to back, such that the charged particle opening angle, θ_{ij}, satisfied $\cos\theta_{ij} < -0.9995$.

The resulting spectrum of e^+ and e^- energies was fit with a line shape calculated from the differential amplitude dL/dw, as follows:

$$\frac{dL}{dw} = \begin{cases} \exp[-(w'-w)^2/(2\sigma_e^2)] & , w \geq w_1 \\ A[\sigma_e/(w''-w)]^x & , w < w_1 \end{cases}$$

where, \hfill (F-1)

w = the observed detector's energy response
$w_1 = w' - \alpha\sigma_e$
$w'' = w' + \sigma_e(x/\alpha - \alpha)$
$A = (x/\alpha)^x \cdot \exp(-\alpha^2/2)$

- 178 -

The intrinsic detector resolution for a quanta of electromagnetic energy, w', incident on the apparatus is σ_e. This function describes a line shape composed of a central Gaussian (mean = w', standard deviation = σ_e), with a power law tail to low energy joined to the Gaussian at w_1 (x is the power). The term w'' corresponds to the infinite asymptote of the inverse power function. Both w'' and the amplitude A are defined by the requirement that the two functions join smoothly (continuous and continuous first derivative). As a result, the detector's response function is specified by four parameters (w', σ_e, x, and α), while the form of the function is fixed to be that of Equation F-1.

Figure 62 shows the result of the fit to the e^+ e^- energy spectrum. Several functional variations to Equation F-1 were tried and rejected, since they all yielded much worse fits. The outcome of the fit is w' = 1.547 GeV, σ_e/w' = 2.2%, α = 1.5, and x = 5.0. For completeness, the detector response function parameters obtained from the fits to the χ_J signals in the ψ' spectra A)-D) are summarized in Table 20.
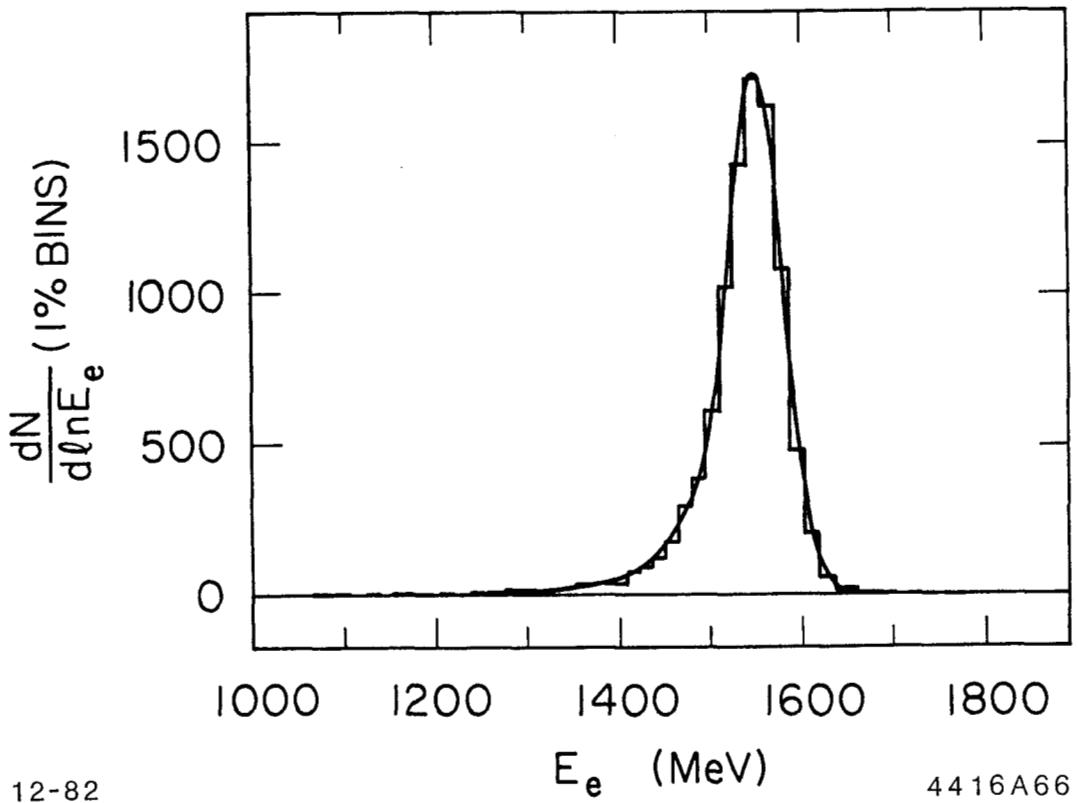
Figure 62: $e^+e^- \rightarrow e^+e^-$ Final State Energy Spectrum.
The energy spectrum for e^+e^- final states is plotted. Also shown is the result of the detector's response function fit to the spectrum. Reasonable agreement is seen (χ^2/D.F. = 64/50). The extracted resolution from the fit was $\sigma = 2.2\%/E_e^{1/4}$ at an energy E_e = 1.547 GeV.

TABLE 20

The Fitted Detector Response Function Parameters.
The parameters x and α, used in equation (F-1) to describe the detector's response function were obtained from fits to the ψ' inclusive γ spectra shown in Figure 26. The fits were found to be very insensitive to the power term in the range of 15.0±7.0, so it was fixed at 15.0.

ψ' SPECTRUM	POWER (x)	JOIN PARAMETER (α)
A) Figure 26(a)	15.0	0.814±0.044
B) Figure 26(b)	15.0	0.744±0.035
C) Figure 26(c)	15.0	0.752±0.029
D) Figure 26(d)	15.0	0.919±0.030

F.2   THE LINE SHAPE FOLDED WITH A BREIT-WIGNER DISTRIBUTION

The signal shape resulting from a transition to a broad state can be expressed as a convolution of a Breit-Wigner mass distribution and the response function as follows:

$$\frac{dA(w_0-w)}{dw} = (1/N_{orm}) \int_0^{m_p/2} dw' \frac{dB(w_0-w')}{dw'} \frac{dL(w'-w)}{dw} (w')^n \qquad (F-2)$$

The response function, $dL(w'-w)/dw$, is given in Equation F-1. The Breit-Wigner distribution, $dB(w_0-w')/dw'$, specifies a state with a width, Γ, and a mean daughter mass, m_0, reached by a photon with a mean energy w_0, from the parent state with a mass of m_p. The term $(w')^n$ is a weight factor obtained from the photon energy dependence in the dipole rate formula. For E1 and allowed M1 transitions, n = 3, while for the forbidden M1 transitions n = 7. This term was dampened to prevent the integral from diverging when w' was far from w_0, by forcing $n \to 0$ for $|w'-w_0| > 4 \cdot \Gamma$. The factor N_{orm} is a normalization obtained by integrating dA/dw. The non-relativistic Breit-Wigner mass distribution, used here, takes the form,

- 181 -

$$\frac{dB(m_0-m')}{dm'} = \frac{K}{(m_0 - m')^2 + \Gamma^2/4} \qquad \text{(F-3)}$$

where m' is the observed daughter mass, and K is a constant independent of m'. The transition photon energy is related to the daughter mass by the relation $m' = (m_p^2 - 2m_p w')^{1/2}$, which is also true for $m' \to m_0$ and $w' \to w_0$. Substituting for m' and m_0, and neglecting terms of order $[w'/(2m'p)]^2$ or smaller yields the result,

$$\frac{dB(w_0-w')}{dw'} = \frac{K}{(w_0 - w')^2 + \Gamma^2/4} \qquad \text{(F-4)}$$

Equation F-4 differs from the corresponding relativistic Breit-Wigner equation by replacing Γ^2 by $(m_0/m_p)^2 \cdot \Gamma^2$. The signal shape was obtained by inserting Equations F-4 and F-1 into Equation F-2, and numerically integrating over dw'. The final result still had to be normalized, requiring an additional integration over dw to obtain N_{orm}. The convoluted signal shape is specified by five parameters, m_0, Γ, σ_e, α, and x. Figure 63 illustrates the result of folding the detector response function at 110 MeV with a 12 MeV wide Breit-Wigner distribution using computer generated curves.
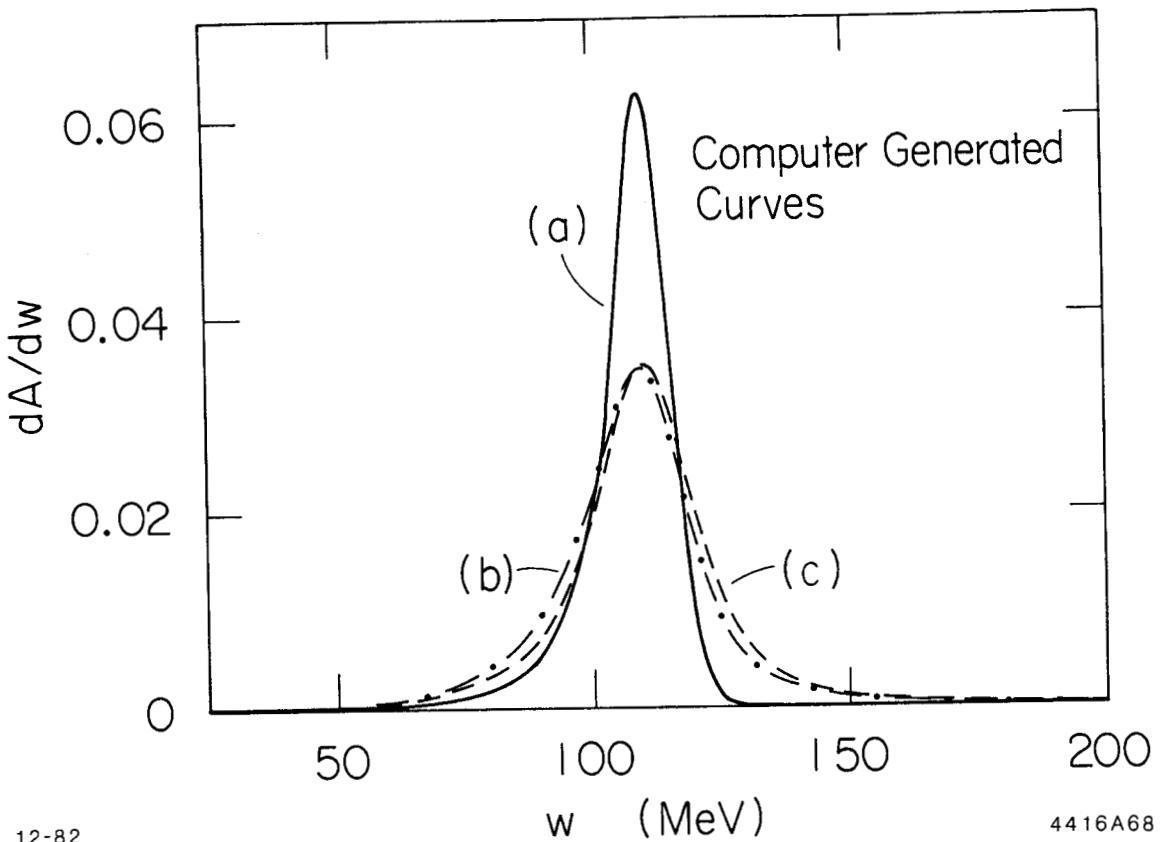
Figure 63: Detector Response Function Folded with a Breit-Wigner. The probability distribution for the detector's response function to monochromatic quanta of electromagnetic energy is shown in curve (a). Curve (b) shows the result of folding (a) with a Breit-Wigner distribution ($\Gamma = 12$ MeV). By including the energy dependence from the dipole rate formula for radiative transitons (E_γ^3 here) the curve is shifted up slightly, as seen in (c).

F.3   THE LINE SHAPE FOLDED WITH A DOPPLER BROADENING

For the transitions $\chi_{1,2} \to \gamma J/\psi$ the signal shape was obtained by replacing the Breit-Wigner function and the $(w')^n$ term in Equation F-2 with a step function of amplitude 1.0 specifying the boost limits of the $\chi_{1,2}$ state.   The first photon energy, $E_{\gamma 1}$, was obtained from the fitted signal, $\psi' \to \gamma_1 \chi_J$, which then yielded the mass, $m(\chi_J)$.   Using the known mass difference, $m(\psi') - m(J/\psi) = 589$ MeV, the second photon's peak energy, in the χ_J center of mass was calculated, $E_{\gamma 2} = [m(\chi_J)^2 - m(J/\psi)^2]/2m(\chi_J)$.   The limits for the integral in Equation F-2 became:

$$w_0' - \delta \leq w' \leq w_0' + \delta$$

where,   (F-5)

$$w_0' = [E_{\gamma 2}/m(\chi_J)] \cdot (E_{\gamma 1}^2 + m(\chi_J)^2)^{1/2}$$

$$\delta = E_{\gamma 1} E_{\gamma 2}/m(\chi_J)$$

Since the natural line widths for the $\chi_{1,2}$ states are small $[\Gamma(\chi_{1,2}) \simeq 0\text{-}5$ MeV)] compared to either the resolution (FWHM $\simeq 31$ MeV) or the Doppler broadening (Doppler box full width $\simeq 34$ MeV), the Breit-Wigner convolution integrals were approximated before the Doppler broadening was folded in.   The response function with a modified σ_e was substituted for the Breit-Wigner convolution integral.   The added width of the $\chi_{1,2}$ states was taken into account by replacing σ_e with $[(2.35\sigma_e)^2 + \Gamma^2]^{1/2}/2.35$.

F.4   ENERGY RESOLUTION

As was pointed out in Chapters IV and V, a knowlege of the detector's intrinsic resolution is a necessary component in unfolding a broad state's width.   The best way to measure the resolution (and response function, for that matter) is to place the apparatus in a test beam of monochromatic photons or electrons.   This was done for a prototype[36] of the Crystal Ball containing 54 NaI(Tl)   modules.   The crystals were of the same design as used in the full detector.   Directly assigning the results of the 54-test to the performance of the Crystal Ball detector in an environment of inclusive hadronic events suffers from four main drawbacks: i) the data for the 54-test at a fixed electron beam energy were collected over a very short time (on the order of an hour); ii) the test beam was usually directed at the center of one particular crystal; iii)   the single particle data of the 54-test do not match the environment of inclusive events populated by many particles and the split-off debris from hadron-nuclear interactions;   and iv) the actual resolution for Bhabha events (which are clean) in the Crystal Ball detector is significantly worse than was found for the 54-test.   The resolution results from the 54-test are shown in Figure 64.

What follows is a review of the Crystal Ball resolution obtained from the data and the numerous calibrations.   The energy data consists of four measurements for each crystal.   The PMT signals are split into a low channel and a high channel.   The low channel incorporates a gain of 20 over the high channel. This feature provides the large dynamic range required, while still using a 13 bit ADC. The four datum consist of the low and high channel pedestals, and the low and high channel digitized
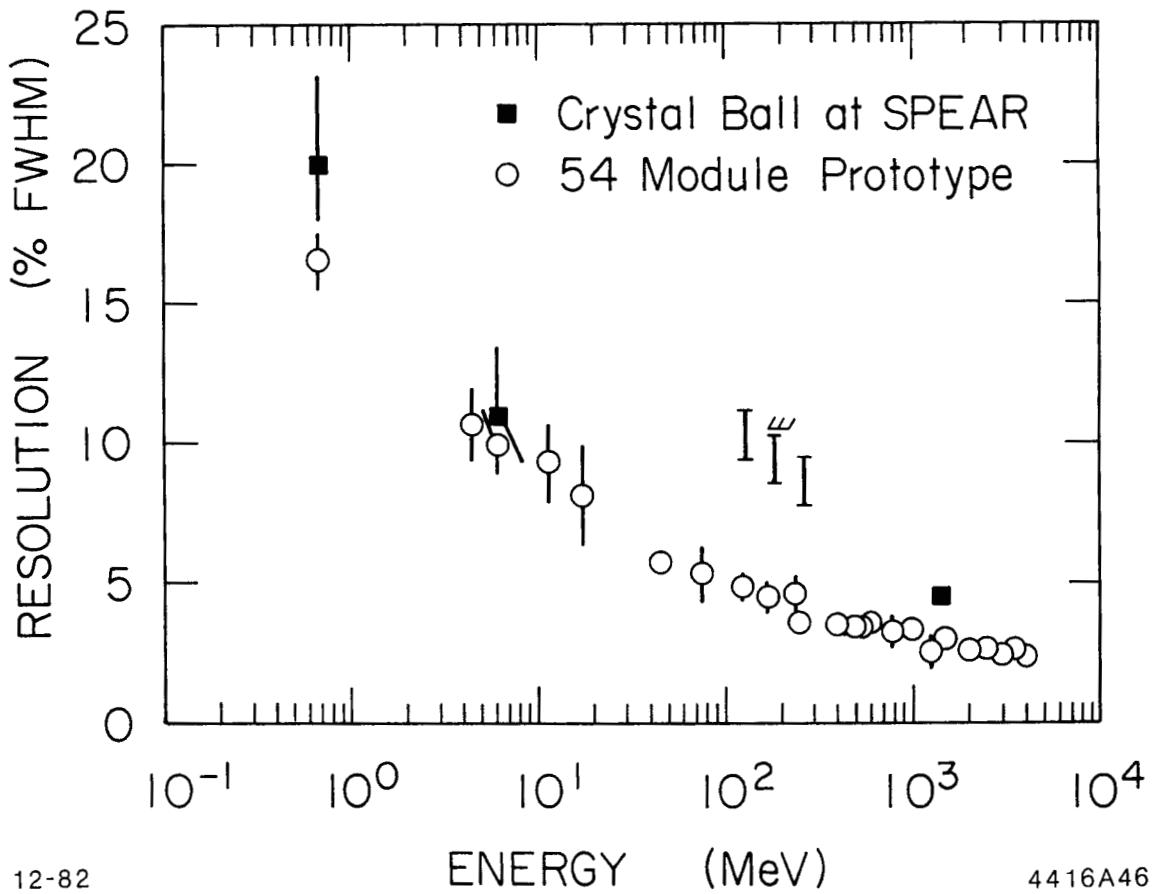
Figure 64: Resolution Obtained from the 54-Test.
The energy resolution measured in the 54 module prototype is plotted as
a function of energy. Also shown is the Crystal Ball resolution for
^{137}Cs, the Van de Graaff produced oxygen line, e^+e^- events at the J/ψ
resonance, and the resolution used in this study (shown as the three
limit bars). The upper limit obtained from the transition $\psi' \rightarrow \gamma \chi_1$ is
also indicated.

signals. By analyzing the trigger pedestal values and pedestal measurements made during the calibrations at $\simeq$2 week intervals, it is known that they fluctuate by about 1-2 counts or $\simeq$30 Kev in the low channel and $\simeq$0.6 MeV in the high channel. The periodic low channel calibrations were made with a ^{137}Cs source (0.661 MeV γ-ray) and the reaction $^{19}F(p,\alpha)^{16}O^* \to \gamma^{16}O$ (6.131 MeV γ-ray), produced with the Van de Graaff accelerator. The calibration of the high channel was parameterized as a ratio of the low to high channel slope. The crystal ratios were obtained by studying the data. When the energy deposited in a crystal was simultaneously in both the low and high channel ranges (120-200 MeV), the known low channel calibration was used to calibrate the ratio. An insignificant variation in the ratio values was seen among the calibrations.

The entire calibration was then corrected using Bhabha and $\gamma\gamma$ events obtained over the $\simeq$2 week period between low channel calibrations. The slope of each crystal was adjusted so that the spectrum of Bhabha events with the given crystal as the bump module peaked at the known beam energy. For any single calibration, the Bhabha corrections modified the slopes by about (4-5)%. The Bhabha calibration significantly improved the resolution for beam energy showers by about 34% over the low channel calibration alone. Variations in the slope among calibrations were found to be (2-3)%.

Variations in the calibration results might be attributed to physical changes in the environment of the apparatus. It was hoped that a xenon light flashing system connected to each PMT by a fiber optic would provide the short term intercalibration data required to correct the

calibrations for fluctuations. However, when the xenon corrections were applied to the 1979 ψ' data, no improvement in the resolution was found. Improvement was defined as a significant reduction in the fitted χ_J signal widths. It may be that variations in the environment were small enough to not contribute significantly to the resolution.

Another area where an improvement in the resolution was made involved a strong correlation between signal strength and where the Bhabha electron hit the crystal face. Impact points away from the crystal center suffer a loss in signal, with the greatest loss occurring for impact near a crystal vertex. The position bias was corrected, in the $\sum 13$ energy estimate, by parameterizing the impact point's deviation from the crystal center with the ratio $R_{1/13} = \sum 1/\sum 13$. Values of $R_{1/13}$ near 1 correspond to a central impact; values less than 1 correspond to an offcenter hit. Correcting for this systematic loss mechanism improved the resolution for Bhabha electrons by $\simeq 26\%$.

Potential improvement in the resolution is expected in the area of non-linear energy-dependent intercrystal variations. The variation in compensation (see Chapter II) is an example of this type of degradation. The light output varies in a nonlinear relation to the photon energy and the differences in this relation among crystals is significant. Work on including the known compensation curves in the calibration is under way, but no compensation corrections were made to the data presented here. It is estimated that compensation corrections could improve the resolution by $\Delta \sigma_e \simeq (1-2.5)\%$.

There is also some evidence for a systematic nonlinearity in the energy calibration. Slow π^0's and η's were selected on the basis of a
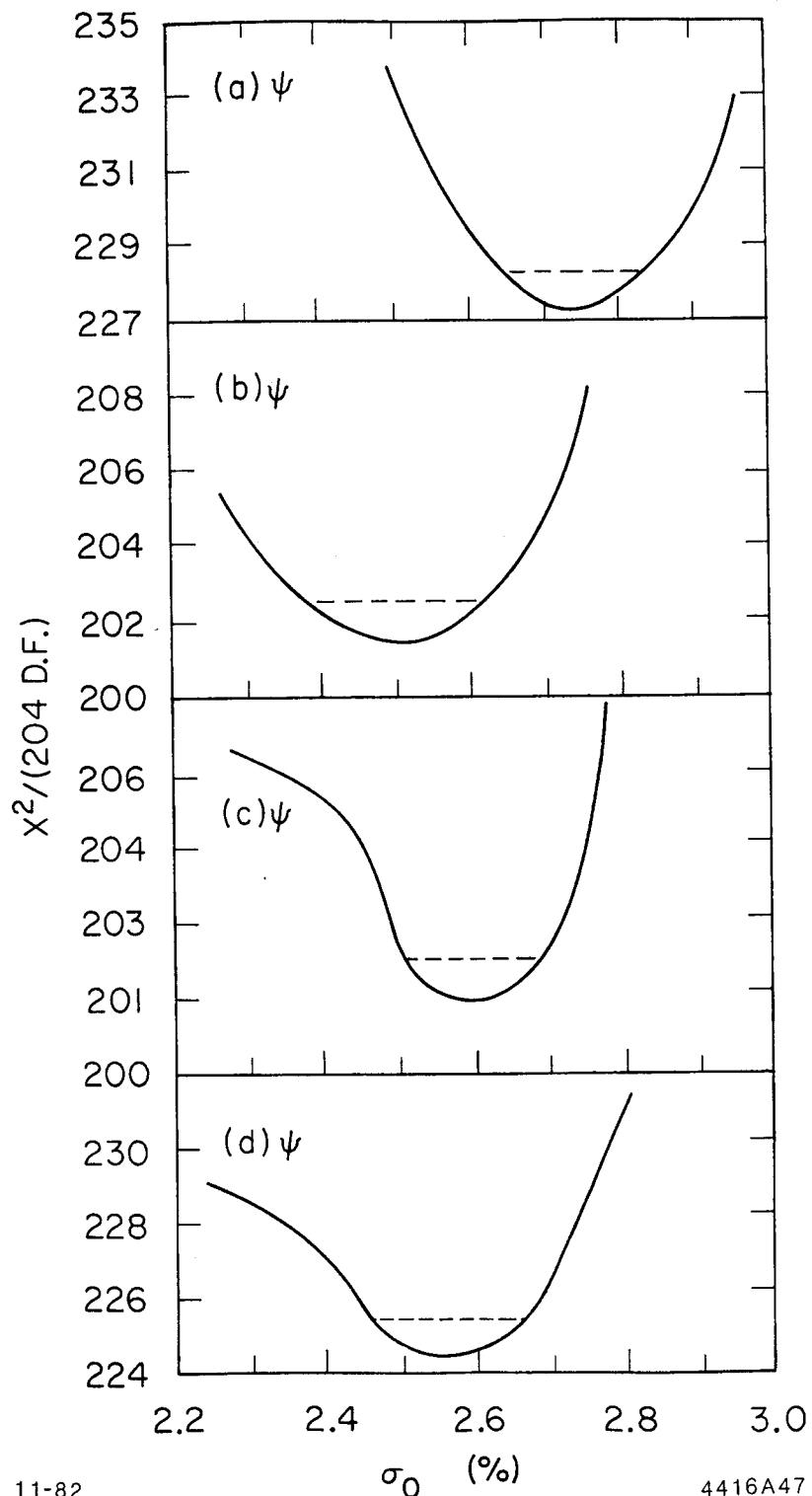
cut in the inclusive $\gamma-\gamma$ mass velocity ($\beta < 0.4$) and plotted. The fitted π^0 and η signal peaks where at 132.0±0.5 MeV and 542±1 MeV respectively. However, these results are complicated by an incomplete understanding of possible correlations in the errors, including the angle measurement.

Figure 64 summarizes what is known about the Crystal Ball resolution from the data and the calibrations. Starting at the high energy end, the point at 1.547 GeV was obtained by fitting the sample of all e^+e^- final states from the 1978 and 1979 J/ψ data after applying a cut designed to remove radiative Bhabha events (see above). This point represents a clean measurement. However, it does not reflect the degrading effects on resolution found in inclusive hadronic final states.

The 90% C.L. upper limit at $E_\gamma = 170$ MeV was obtained by fixing the width of the x_1 state to be 0.0 and allowing the resolution to vary in a fit to the ψ' spectrum. For completeness, the resolutions at 6.131 MeV and 0.661 MeV from the ^{137}Cs and Van de Graaff calibrations are also shown.

To extract as much information as possible from the inclusive photon spectra for ψ' decays and as a check on the calibration interval used in this study, fits to the x_J signals were made for various fixed resolutions. Figure 65 shows the variation in x^2 from the fits versus the resolution. The results assume an energy dependence in the resolution of $1/E_\gamma^{1/4}$. An average of the values obtained for spectra B)-D) is $(0.0255\pm0.0013)\%/E_\gamma^{1/4}$, which is consistent with the spread in resolution used in this experiment [$\sigma_0 = (2.4-2.8)\%$]. The worst

resolution obtained for spectrum A) may be due to the presence of photons missidentified as charged particles because of their overlap with a charged particle. This would degrade their resolution.

Figure 65: x^2 Distribution Versus Photon Resolution.
The x^2 distribution as a function of the input photon resolution is
shown for the fitted ψ' spectra shown in Figures 26(a)-(d).

REFERENCES

1. W. S. C. Williams, *An Introduction to Elementary Particles*, p. 166, Academic Press, New York, 1971.

2. T. Appelquist, R. M. Barnett and K. Lane, Ann. Rev. Nucl. Part. Sci. **28**, 387 (1978).

3. E. Eichten et al., Phys. Rev. **D21**, 203 (1980).

4. G. Bhanot and S. Rudaz, Phys. Lett. **78B**, 119 (1978).

5. W. Buchmüller and S.-H. H. Tye, Phys. Rev. **D24**, 132 (1981); W. Buchmüller, G. Grunberg, and S.-H. H. Tye, Phys. Rev. Lett. **45**, 103 (1981); **45**, 587 (1981).

6. C. Quigg and Jonathan L. Rosner, Phys. Rev. **D23**, 2625 (1981).

7. H. Krasemann and S. Ono, Nucl. Phys. **B154**, 283 (1979).

8. A. Martin, "Testing QCD in Quarkonium Spectroscopy," Proc. of the Second Moriond Workshop, Les Arcs-Savoie, France, January 24-30, 1982; A. Martin, Phys. Lett. **93B**, 338 (1980).

9. Dana Beavis et al., Phys. Rev. **D20**, 743 (1979); and also references 2 and 3.

10. M. Krammer, H. Krasemann, Schladming School 1979:259, Lectures given at 18th Int. Universitatswochen fur Kernphysik, Schladming, Austria, Feb. 28-Mar. 10, 1979; J. D. Jackson, Phys. Lett **87B**, 106 (1979).

11. T. Sterling, Nucl. Phys. **B141**, 272 (1978).

12. J. S. Kang and J. Sucher, Phys. Rev. **D18**, 2698 (1978).

13. R. McClary and N. Byers, UCLA/82/TEP/12, to be published.

14. E. Eichten and F. Feinberg, Phys. Rev. **D23**, 2724 (1981).

15. H. Krasemann, Phys. Lett. **101B**, 259 (1981).

16. K. J. Sebastian, PRINT-79-0636, July, 1979; K. J. Sebastian, Phys.

Lett. 80A, 109 (1980).

17. H. Goldberg, Phys. Rev. D16, 2243 (1977).

18. A. B. Henriques et al., Phys. Lett. 64B, 85 (1976).

19. R. Barbieri, R. Gatto, E. Remiddi, Phys. Lett. 61B, 465 (1976); R. Barbieri, M. Caffo, R. Gatto, E. Remiddi, Phys. Lett. 95B, 93 (1980); R. Barbieri, R. Gatto, E. Remiddi, Ref.TH.3144-CERN, August, 1981.

20. J. Arafune, M. Fukugita, Phys. Lett. 102B, 437 (1981).

21. V. A. Novikov et al., Phys. Lett. 67B, 409 (1977); V. Novikov et al., Phys. Reps. 41C, 1 (1978); M. Shifman et al., Nucl. Phys. B147, 385, 448 (1979).

22. M. A. Shifman, JETP Lett. 30, No. 8, 513 (1979); M. A. Shifman, Zeit. Phys. C4, 345 (1980); M. A. Shifman and M. I. Vysotsky, Zeit. Phys. C10, 131 (1980).

23. A. Yu. Khodjamirian, EFI-427-34-80, 1980.

24. J. Gaiser, "Charmonium Spectroscopy from Inclusive Photons in J/ψ and ψ' Decays," in Proc. of the XVIIth Rencontre de Moriond: Workshop on New Flavours, Les Arcs, France, January 24-30, 1982, SLAC-PUB-2887, March, 1982.

25. F. Bulos, Crystal Ball memo, CB-NOTE 117 (1976); J. Gaiser, Crystal Ball memo, "Crystal Ball Magnetostrictive Spark Chambers," in C. Peck's Crystal Ball Summer School (1980).

26. Note that the term "plane" is slightly misleading since the actual surfaces being described are cylinders. At times it is useful to imagine the chambers unwrapped, transformed into the two dimensional space of the azimuthal angle, ϕ, and the z-axis. In this view the surfaces are planes.

27. J. Gaiser, Crystal Ball memo, "The Monte Carlo Method and the Crystal Ball Simulator CBSIM," in C. Peck's Crystal Ball Summer School (1980).

28. J. Gaiser and C. Kiesling, Crystal Ball memo CB-NOTE 128 (1977); J. Bagger, Crystal Ball memo CB-NOTE 406 (1979).

29. J. Gaiser, Crystal Ball memo CB-NOTE 132 (1978).

30. For example see: T. M. Himel, Ph.D. thesis, Stanford University Report No. SLAC-223, October, 1979.

31. J. L. Siegrist, Ph.D. thesis, Stanford University Report No. SLAC-225, October, 1979.

32. R. L. Ford and W. R. Nelson, Stanford Univ. Report, SLAC-210 (1978).

33. Neutron Physics Division, RSIC Computer Code Collection, Monte Carlo High-Energy Nucleon-Meson Transport Code (HETC), Oak Ridge National Laboratory, CCC-178; T. A. Gabriel et al., Oak Ridge National Laboratory Report, ORNL/TM-7123, January (1981).

34. The algorithms used to reconstruct π^0's, called TGFIT and GPAIR, were written by T. Burnet, with slight modifications by the author.

35. Joseph C. H. Park, "Fit70 - A Kinematic Fitting Routine," SLAC Report 150 or UC-34, June 1972.

36. Y. Chan et al., IEEE Trans. on Nucl. Sci. NS-25, 333 (1978).